Direct observation of Rydberg-Rydberg transitions via CPmmW spectroscopy

by

Yan Zhou

Submitted to the Department of Chemistry
in partial fulfillment of the requirements for the degree of

Doctor of Philosophy

at the

MASSACHUSETTS INSTITUTE OF TECHNOLOGY

September 2014

Author .....
Department of Chemistry
August 29, 2014

Certified by .....
Robert W. Field
Haslam and Dewey Professor of Chemistry
Thesis Supervisor

Accepted by .....
Robert W. Field
Chairman, Departmental Committee on Graduate Students

This doctoral thesis has been examined by a Committee of the Department of Chemistry that included

Professor Keith A. Nelson .....
Chairperson, Thesis Committee

Professor Robert G. Griffin .....
Member, Thesis Committee

Professor Robert W. Field .....
Thesis Supervisor

Direct observation of Rydberg-Rydberg transitions via CPmmW spectroscopy

by

Yan Zhou

Submitted to the Department of Chemistry
on August 29, 2014, in partial fulfillment of the
requirements for the degree of
Doctor of Philosophy

Abstract

Rydberg-Rydberg transitions of BaF molecules have been directly observed in our lab. The key to the experimental success is our ability to combine two powerful and new technologies, Chirped-Pulse millimeter-Wave spectroscopy (CPmmW) and a buffer gas cooled molecular beam source. CPmmW spectroscopy is a form of broadband (20 GHz bandwidth), high-resolution (50 kHz), free induction decay-detected (FID) spectroscopy with accurate relative intensities (10%), which is successfully applied to record Rydberg-Rydberg spectra of Calcium and Barium atoms. To extend CPmmW spectroscopy to a molecular system, I have constructed a new setup, a 20 K Neon buffer gas cooled molecular beam system, which generates of beam containing >1000 times more molecules and 10 times less translational velocity than a Smalley-type laser ablation supersonic beam source. Hundreds of molecular Rydberg-Rydberg transitions with high resolution and high dynamic range can now be recorded in a few hours. The success of this experiment suggests many applications in the near future, such as developing a user-friendly experimental method to study and manipulate Rydberg molecules, preparing a single molecular beam pulse that contains 10^8 state-selected core-nonpenetrating Rydberg molecules/molecular ions, and studying the electronic structure (dipole and quadrupole moments and polarizability) of the molecular ion core with unprecedented precision and completeness. In addition, strong collective effects (superradiance) have also been observed.

Thesis Supervisor: Robert W. Field
Title: Haslam and Dewey Professor of Chemistry

Acknowledgments

There are many people I wish to thank for their advice and collaborations in the past seven years. The first among them is my adviser, Bob Field. In one hand, Bob is not different from most PhD advisers I have heard. He has extreme enthusiasm on research, works hard and loves his students. He has a unique vision of small molecule spectroscopy and is good at conveying his ideas to us. However, in another hand, Bob is unlike any PhD advisers I have heard. He has seldom answered my questions directly, but always listens to me very carefully, and then give me his guidance through many instructive questions. He has never criticized my ignorance, but always encourages me to be an expert through carefully learning and thinking. He has never gave me a job list to do, but always encourages me to think what is the most important. I have never felt any pressure from him, but always benefit and enjoy the light he shines in the front. In addition, he always set up a filter to shield out most of the bureaucratic things and leave me a freedom and relax research environment. At the same time, he always tries his best to leave opportunities to me of reporting our work and express our ideas at the center of the academic arena. I am very lucky to join Bob's lab. Here, I have not only learned knowledge and improved research ability, but also experienced an unique joy in the lab. Without Bob, I would treat research as work. With Bob, I am treating research as life.

During my seven years at MIT, Dr. Steve Coy has gave me many important suggestions and guidance in both theoretical and experimental aspects. For any questions, as large as our research direction, or as small as a detailed problem in Mathematica software, his sensitive intuitions and deep thoughts are always the key to the solution. Prof. John Muenter, who visits our lab for a week every three months, plays an important role in my experiments in the past three years. He is an encyclopedia of almost all experimental techniques. In addition, his humor, optimism and interesting daily quiz make the lab atmosphere even more relax. To John, my only complain is that his visiting frequency is too low.

I must also thank my undergraduate adviser, Xinsheng Zhao, for his advice and

encouragement. He is an excellent teacher and scientist, and teach me how to combine the knowledge from books and from independent research. My two years training and working in Xinsheng's lab provides a solid preparation for my work at MIT. I hope that I have made him proud.

I would like to express my gratitude to all current and former Field group members. Dr. Vladimir Petrovic and Dr. Kirill Kuyanov, as my second advisers, teach me a lot of knowledge of Rydberg spectroscopy, and how to design and operate an experiment hand by hand in my early time. Dr. Tony Colombo and I have worked together more than three years. He is not only my collaborator, but also is my English teacher and help me to adapt the life at Boston. Barratt Park is a super star in the lab. Without his revolutionized CPmmW technique and his generous support, I would spend much longer time on my research. I will memorize the pleasant experience of collaborations with David Grimes, Tim Barnum and Ethen Klein. And I hope that I could be back frequently in near future and collaborate with you continuously. The limited space of this section prevents me to tell all stories of Dr. Josh Baraban, Dr. Carrie Womack, Dr. Adam Steves, Dr. Josh Middaugh, Dr. Kyle Bittinger, Dr. Wilton Virgo, Prof. Bryan Lynch, Jun Jiang, Bryan Changala, Cathrine Salagas, Anelise Beck, Celina Bermudez ,Monika Ciuba, Sam Lippoff, Erika Robinson and Jessica Lam. The experience of studying and working with you is beautiful memory.

I am also grateful to many collaborators:

- Prof. John Doyle, Prof. Dave DeMille, Dr. Dave Patterson, Dr. John Barry. Without your help, I cannot enjoy the wonderful buffer gas cooling technique.
- Prof. Brooks Pate. Your revolutionized CPMW technique has opened a new door for me.
- Prof. Keith Nelson and Prof. Sharly Fleischer. You teach me how to perform ultrafast experiments and think as a time-domain spectrosopist. Many long conversations in the hall way with Sharly are exciting and memorable.
- Prof. Susanne Yeline. Only a few meetings with you improves my understanding of superradiance significantly.

- Dr. Gang Liu. Without your help, I cannot make my apparatus run smoothly. You are not only a senior technician, but also my electronics adviser.

Thank you, Peter Giunta, for all that you have done for everybody in the group.

Last but certainly not least, I wish to thank my parents. Your constant support and encourage in the past thirty years keep me going forward.

Contents

List of Figures

List of Tables

Chapter 1

Introduction

In Section 1.1, I discuss the unique properties of Rydberg states, especially core-nonpenetrating molecular Rydberg states, as well as our current research strategies and goals. In Sections 1.2 and 1.3, I briefly describe two advanced techniques, Chirped Pulse millimeter Wave (CPmmW) spectroscopy and a buffer gas cooled molecular beam. The goal of a large part of this thesis is to show how significant improvements in these two techniques carry us toward our larger research goals. In Section 1.4, I list possible connections between our current progress and applications in other research groups. In Section 1.5, I outline each chapter of this thesis.

1.1 Properties of Rydberg states

The Rydberg states of an atom or a molecule are highly electronically excited states[12]. The loosely bound Rydberg electron has an orbit radius far larger than the Bohr radius and spends most of its time far from the ion core. The electron/ion-core interaction can be described in zeroth order by the Coulomb interaction,

$$V(r) = -\frac{Ze^2}{4\pi\varepsilon_0 r} \tag{1.1}$$

where e is the electron charge, Z is the effective charge of the ion-core, ε_0 is the vacuum permittivity, and r is the distance between the electron and the ion-core.

Table 1.1: n-dependent scaling rules of the atomic Rydberg states

Property	n-dependence	Typical values in n=40
Binding energy	n^{-2}	10 meV
Transition Energy with $\Delta n = 1$	n^{-3}	0.4 meV
Orbital Radius	n^2	1600 a_0
Geometric Cross Section	n^4	$8 \times 10^6 a_0^2$
Electric Dipole Transition Moment	n^2	1600 ea_0
Polarizability	n^7	3 GHz cm^2/V^2
Radiative Lifetime	n^3	5 ms
Fine Structure Interval	n^{-3}	-1.5 MHz

The energies of the Rydberg states follow the Rydberg formula,

$$E = IP - \frac{Ry}{(n-\delta)^2} \tag{1.2}$$

where IP is the ionization potential, Ry is the Rydberg constant, n is the principal quantum number, and δ is the n-independent quantum defect, which is zero for all states of the Hydrogen atom. The energies and wavefunctions of the Rydberg states that belong to one Rydberg series can be calculated with well-known equations and have obvious periodic structures with n-dependent scaling rules. Table 1.1 summarizes several useful scaling rules for Rydberg states[13]. Since many properties scale very non-linearly in n, Rydberg states with moderately high principal quantum numbers (n$\sim$40) have much larger or smaller properties than low-lying excited states. For example, the gigantic electric dipole transition moment and polarizability provide a large handle for control of the internal and external degrees of freedom of the atoms by interactions with an external field or atom-atom collisions. The long radiative lifetime provides a large time-window for precise control and measurement [14, 15, 16, 17, 18].

In addition to atomic Rydberg states, molecules also have Rydberg states, which provide more valuable information[19]. Different from the closed-shell alkali atomic ion-core, the molecular ion-core has additional degrees of freedom, such as rotation and vibration, and a permanent electric dipole moment. The collisions between the Rydberg electron and the ion-core are not only elastic, but also can be inelastic with energy and angular momentum exchange, especially when the period of the Rydberg

electron motion is resonant with the period of the ion-core rotation or vibration (Stroboscopic resonance)[20, 21, 22, 23, 24]. Stroboscopic resonances govern intramolecular chemical reactions and reveals the subtle mechanisms of the interactions between a heavy nuclei and a light electron.

Based on the strength of the interactions between the Rydberg electron and the ion-core, molecular Rydberg states can be classified into two categories, core-penetrating Rydberg states (CP) and core-nonpenetrating Rydberg states (CNP). The Rydberg electron in core-penetrating Rydberg states with low angular momentum, ℓ, can penetrate into and collide with the ion-core, as (ii) in Figure 1-1. Due to the strong coupling between the Rydberg electron and the ion-core, the vibration and rotation quantum numbers of the ion-core and the angular quantum number of the Rydberg electron are not "good". The spectroscopy of core-penetrating states should be of special interest to chemists, because important information about chemical reactions can be extracted from the spectrum [25].

Molecular core-nonpenetrating Rydberg states are a unique and neglected class of matter [1, 26, 27, 28, 29]. They are defined as having negligible overlap between the Rydberg electron wavefunction and that of the ion-core. Their energies and wavefunctions can be described a priori by the hydrogenic Rydberg formula. The Rydberg electron is essentially decoupled from its ion-core, leading to an atom-like electronic structure with "almost good" angular momentum quantum number of the Rydberg electron and vibration and rotation quantum numbers of the ion-core. Because molecular core-nonpenetrating states do not interact strongly with the non-spherically symmetric part of the ion-core, they are similar to atomic Rydberg states in the zeroth-order picture. Therefore, the Rydberg electron is extremely sensitive to external electric fields, which can induce gigantic electric dipole moments and polarizabilities. In addition, the molecular core-nonpenetrating Rydberg states are metastable with relatively long lifetimes [13, 30, 19]. Molecules in such long-lived, highly polarizable states are useful to researchers working on molecular slowing, cooling, and trapping [14, 15, 16, 17, 18]. Different from the complicated spectra of molecular core-penetrating Rydberg states, the spectra of molecular

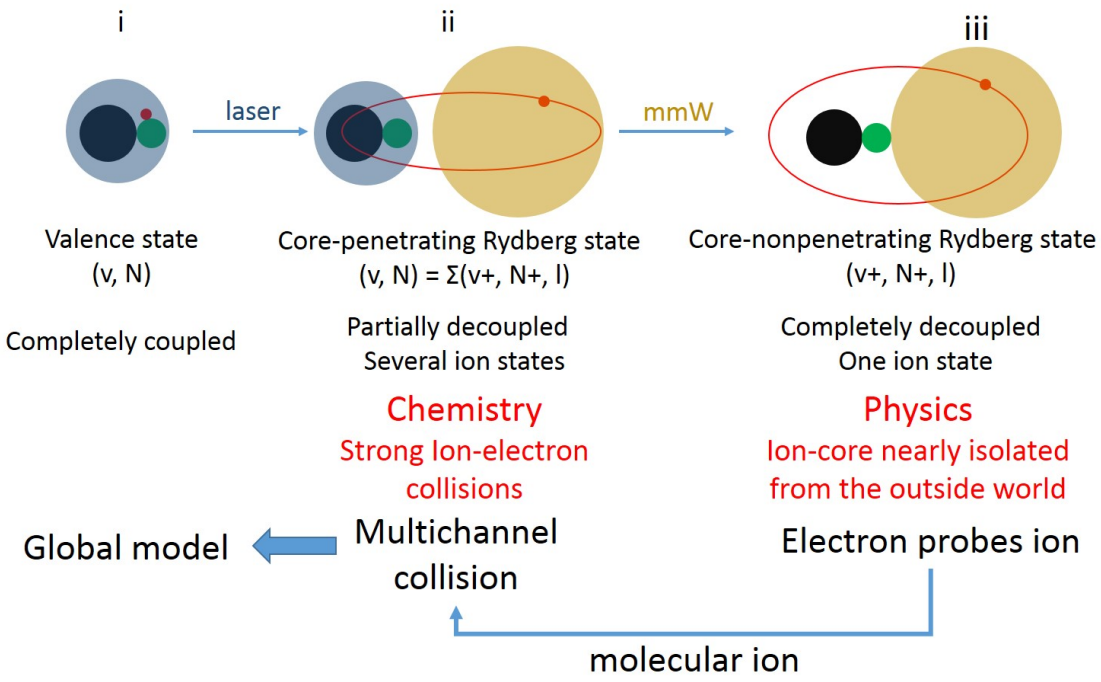

Figure 1-1: Big picture. A diagram of our current and near future research strategy. Step 1, we use lasers to impact on the area near the ion-core (blue area) to populate core-penetrating Rydberg states (ii). Core-penetrating states contain information about ion-electron interactions, which can reveal the information of chemical reactions. However, we do not stop at this step because of the complexity of the spectrum and the fitting model. Step 2, we use millimeter-wave pulses to impact on the area far from the ion-core (yellow area) to populate core-nonpenetrating Rydberg states (iii). In the core-nonpenetrating states, the electron and ion-core are almost decoupled and can be controlled and measured separately. Even better, the Rydberg electron can be used as a sensitive probe to characterize the structures of the molecular ion-core. By fitting the core-nonpenetrating Rydberg spectrum by a perturbative model [1], we can extract the important parameters of the molecular ion-core, such as multipole moments and polarizabilities. Step 3, theorists can implement the precisely measured information of the molecular ion-core into the collisional model of the core-penetrating Rydberg states to reduce the number of fit parameters in the multichannel collision theory [2, 3, 4, 5].

core-nonpenetrating Rydberg states have easily recognizable and predictable patterns that arise from the highly restrictive "pure electronic" transition selection and propensity rules ($\Delta\ell = \pm 1, \Delta N^+ = 0, \Delta v^+ = 0, \Delta N = 0, \pm 1, + \leftrightarrow -$) [19, 30]. With high-resolution spectroscopic techniques and an analytic perturbative model, measured frequency shifts and intensity deviations from the hydrogenic Rydberg formula yield a complete picture of the electronic structure of the molecular ion-core [31, 1]. Molecular core-nonpenetrating Rydberg states are both a central object of scientific study as well as a tool for novel applications in spectroscopy and molecular dynamics [19, 32, 33, 26, 27], quantum chemistry [34, 35, 36], and fundamental physics [37, 38, 39].

Figure 1-1 shows a diagram of our current research strategy. The basic idea is to jump over the complicated molecular core-penetrating Rydberg states to easily controlled and measured molecular core-nonpenetrating Rydberg states, where the Rydberg electron is used as a sensitive probe to characterize the structure of the ion-core. Then, we feedback the precisely measured parameters of the ion-core into the molecular core-penetrating Rydberg states to to reduce the number of fit parameters in the multichannel collision theory. Our ultimate goal is to obtain a complete model that consists of fundamental molecular constants, but without any empirical or *ab initio* calculated parameters. We would hope to apply this model to calculate the "all-spectra and all-dynamics" in a broad range of energy [35, 34, 36, 40, 2, 41].

1.2 Chirped-pulse millimeter-wave technique

Millimeter wave spectroscopy is a powerful tool for performing high precision measurements on atoms and molecules in the gas phase [42, 43, 44, 7, 45, 46, 47]. Compared to laser spectroscopy, millimeter wave spectroscopy can have >1000 times higher resolution and accompanying higher frequency accuracy. Millimeter wave spectroscopy has been widely used to determine molecular structures by the rotational spectrum [48, 49, 50], to detect astronomical and atmospheric molecules [51], and to induce pure electronic transitions in Rydberg states [52, 53, 7, 54, 45, 55]. However, for

a conventional frequency-stepping millimeter wave spectrometer, the dual goals of achieving high resolution and covering a broad bandwidth requires very long data collection times [56]. Fortunately, the recent invention of Chirped-Pulse Fourier-Transform Microwave (CP-FTMW) spectroscopy by Pate and co-workers breaks the limitation of the frequency-stepping spectrometer, and provides a method for obtaining broadband spectra with high resolution in a very short data collection time [57, 58]. Barratt Park in our group has extended the CP-FTMW technique to the millimeter wave region, by designing a Chirped-Pulse millimeter-Wave (CPmmW) spectrometer in the region of 70-102 GHz [59, 60]. Different from the conventional narrow band frequency-stepping spectrometer, CPmmW uses a broadband pulse to polarize all possible transitions with the frequency range of the chirped pulse in a single shot and record the broadband Free Induction Decay (FID) in the time-domain. With advanced phased-locked microwave electronics, all carrier frequency information is preserved and can be transformed into the frequency-domain. Due to the preservation of both amplitude and phase information, and the use of an advanced fast digitizer, the CPmmW technique has a much higher data collection rate (more than 10^5 improvement) than a frequency-stepping spectrometer. In addition, since all frequency components are collected simultaneously, the relative intensities in the frequency-domain are reliable and immunized from shot-to-shot fluctuations of the lasers and molecular beam source. CPmmW spectroscopy provides a combination of high sensitivity, broad single-shot spectral coverage (>20 GHz), high resolution (sub-100 kHz), and accurate (5%) relative intensities. This technique plays a central role in this thesis.

1.3 Buffer gas cooled molecular beam

The atoms or molecules of interest in my experiments are alkaline earth atoms (Calcium, Barium) and alkaline earth monohalide molecules (CaF, BaF). The conventional beam source for such species is a supersonic jet coupled with laser ablation, which has many advantages, such as low translational and rotational temperatures (<5 K),

relatively small gas load (<10 ml/min at one atmosphere and room temperature), and production of a wide range of species [61, 62]. However, fast beam velocities (1800 m/s for Helium, 600 m/s for Argon), large shot-to-shot fluctuations (>50%), and relatively low flux ($<1\times10^8$ molecules/sr/pulse) significantly degrade the resolution, signal-to-noise ratio, and limit the applicability of CPmmW spectroscopy to our interested problems, such as superradiance of a dense atomic Rydberg gas, and pure electronic spectroscopy of molecular core-nonpenetrating Rydberg states.

The buffer gas cooling technique was pioneered by the De Lucia group in the 1980s [63, 64] and has recently been extensively developed by the Doyle group [65, 66, 67, 68, 69, 70, 71] for application to ablated atoms/molecules. Compared to supersonic cooled molecular beam, the buffer gas cooling technique achieves comparable translational and rotational temperatures (<5 K), but obtains a much smaller beam velocity (reduced by a factor of 10) and larger number density (increased by a factor of 1000). Compared to a supersonic cooled beam, the slow beam generated in the buffer gas cooling technique reduces Doppler dephasing, increasing our spectroscopic resolution by a factor of 10. In addition, the high number density not only linearly increases the detected signal in typical experiments, but also provides access to the optically thick regime for nonlinear experiments. Combining the number density and the spectroscopic resolution improvement, the buffer gas cooled molecular beam provides a factor of 10000 improvement.

1.4 Possible collaborations and applications

- Selectively prepared long-lived core-nonpenetrating states
  - Rydberg-State-Enabled Stark deceleration and trapping of cold molecules [14, 15, 16, 17, 18, 72, 73].
  - Preparing molecular cations in a single, selected quantum state by state selective autoionization methods [39, 38, 37].
  - Non-dispersive molecular Rydberg wavepackets, a new coherent control

technique [74, 75, 76, 77, 78, 79].

  - Control of the pendular quantum states by combined permanent and induced electric dipole interactions [80, 81, 82, 83, 84].

- Create an extremely optically thick medium

  - Intermolecular interactions can induce or modify chemical reactions, especially via intermolecular radiative interactions, which is of considerable interest to chemists (e.g. J-aggregate) [85].

  - Study the propagation of a coherent pulse in a highly nonlinear medium [86, 87, 88].

  - Study the dynamics of many-body quantum states [89, 90, 91, 92].

1.5 Thesis overview

In Chapter 2, I describe the experimental setups of two vacuum chambers, including: (1) The upgrade of the supersonic molecular beam system and Time-of-Flight Mass Spectrometer (TOF-MS) with Ramped Pulse Field Ionization (Ramped-PFI); (2) Design and construction of a buffer gas cooled molecular beam system; (3) Design and construction of a 76-98 GHz Chirped Pulse millimeter Wave (CPmmW) spectrometer; (4) A recipe for preparing BaF_2 pellets for laser ablation. The details of the apparatus described in Chapter 2 are not be repeated in other chapters.

In Chapter 3, I outline our progress from PFI detection to FID detection of millimeter wave induced atomic Rydberg-Rydberg transitions. I demonstrates high resolution millimeter wave spectroscopy, quantum state manipulation and evidence of collective effects. After describing the upgrade of the beam source from the supersonic jet to the buffer gas cooled beam, I show the improvement of the signal strength and the spectroscopic resolution. Lastly, I present an observation of collective effects, such as superradiance, in a dense atomic Rydberg gas.

In Chapter 4, I discuss the physical essence of superradiance with a simple two-atom model. Then, two general calculation methods in the Schrödinger picture and

in the Heisenberg picture, are briefly discussed. By simplifying the Heisenberg full quantum mechanics calculation, I perform a semiclassical calculation to predict the behavior of the collective radiation with the practical parameters of our CPmmW spectrometer and buffer gas cooled beam system. In the last part of this chapter, I propose several new experiments based on the calculation results and the preliminary experimental results.

In Chapter 5, I discuss the progress in the extension of CPmmW spectroscopy of Rydberg-Rydberg transitions from atomic systems to a diatomic molecular system. I systematically describe the procedure for populating molecular Rydberg states by lasers, inducing Rydberg-Rydberg transitions in the CPmmW spectrometer, and obtaining a 2D spectrum efficiently. Then I show the developments of several experimental and data processing techniques that can significantly reduce the complexity of the raw data and automatically organize most of the transitions into several Rydberg series. In addition, I demonstrate the capability of separating core-penetrating series and core-nonpenetrating series by a "Stark demolition" experiment, which does not require any pre-assignment. Although the proof of principle experiments are successful, there is a several technical problem preventing systematical collection of the data for analysis. I discuss such problem and propose several possible solutions.

In Chapter 6, I discuss the unique features of the molecular core-nonpenetrating Rydberg states. To extend the preparation of the core-nonpenetrating Rydberg states to other molecules, I propose two different methods, optical-mmW STImulated Raman Adiabatic Passage (STIRAP) and Adiabatically-focused STark-mixed Rydberg Orbitals (ASTRO). By numerical calculations, I demonstrate the capability of moving more than 20% of the population from a valence state to core-nonpenetrating Rydberg states for molecules with a fast nonradiative decay in the core-penetrating Rydberg states. The feasibility and challenge in the experiments is also discussed.

Chapter 2

Experimental setup

Most of the experiments described in this thesis are performed on two independent vacuum chambers, which are designed to be flexible and adaptable to a variety of configurations: (1) A supersonic molecular beam system (named Gertrude) for Laser Induced Fluorescence (LIF), Time-of-Flight Mass Spectrometry (TOF-MS) and preliminary Chirped Pulse millimeter Wave (CPmmW) spectroscopy; (2) A buffer gas cooled molecular beam system (named Buffy) for LIF, high resolution absorption spectroscopy and high resolution CPmmW spectroscopy. Gertrude was built by Jason Clevenger and inherited as a home-built vacuum system [93]. Gertrude has been refurbished and upgraded recently to accommodate the current research in the Rydberg project. The most important upgrades are described in this chapter. Buffy is a completely new system, designed and built by myself with help from the Doyle group at Harvard, the DeMille group at Yale, and the MIT central machine shop. The operating principles, design, and performance are described in detail. A 76-98 GHz broadband CPmmW spectrometer, which was upgraded from the one built by Barratt Park in our group, plays an important role in this thesis. The unique features and optimizations of the CPmmW spectrometer are described. In addition, laser ablation is our primary method to deliver atoms and diatomic radicals into the molecular beam in both Gertrude and Buffy. Several tricks for optimizing the ablation precursor and ablation laser are discussed. The details of this chapter are intended as a reference for future users.

2.1 Vacuum system for supersonic jet-cooled molecular beam

Smalley-type laser ablated supersonic jet-cooled molecular beam sources have been widely used to create cold metal clusters and diatomic radicals in the past fifty years [61, 62]. This technique has many well-known advantages: (1) It is easily implemented in a room temperature vacuum chamber. (2) Synchronized ablation pulse and gas pulse create the target molecules concentrated in a relatively narrow spatial and temporal distribution. Thus, it is possible to obtain a relatively high local signal intensity with very low sample consumption. (3) Relatively high temperature of the laser induced plasma ($\sim 10^4$ K) initiates many chemical reactions that have high activation energy barriers. Through a supersonic expansion, the target molecules can be cooled to below 5 K, which simplifies their spectra and significantly enhances their main spectroscopic features. In my experiment, a laser ablated Smalley-type source is used to create Ca/Ba atomic beams and cold CaF/BaF molecular beams. Figures 2-1 and 2-2 are a photograph and a schematic diagram of Gertrude.

2.1.1 Turbo pumps

Different from the original design of the vacuum chamber, we use two turbo pumps (Source chamber: Varian V1000HT, 1000 L/s, Detection chamber: Varian V360, 360 L/s) to replace two very old diffusion pumps (Source chamber: Varian VHS-10, 3650 L/s, Detection chamber: VHS-4, 1200 L/s). Turbo pumps are oil free. We do not need to worry that residue vapor from the diffusion pumps might contaminate the reactive sample, such as Barium metal. In addition, we can connect the Turbo pump directly to the TOF mass spectrometer, without another buffer chamber or liquid Nitrogen cold traps, which simplifies the vacuum system dramatically. However, the price of the turbo pump is much higher than that of a diffusion pump with the same pumping speed. To avoid paying too much for unnecessary pumping capability of the turbo pump, I estimate required pumping speed carefully. Two parameters that limit

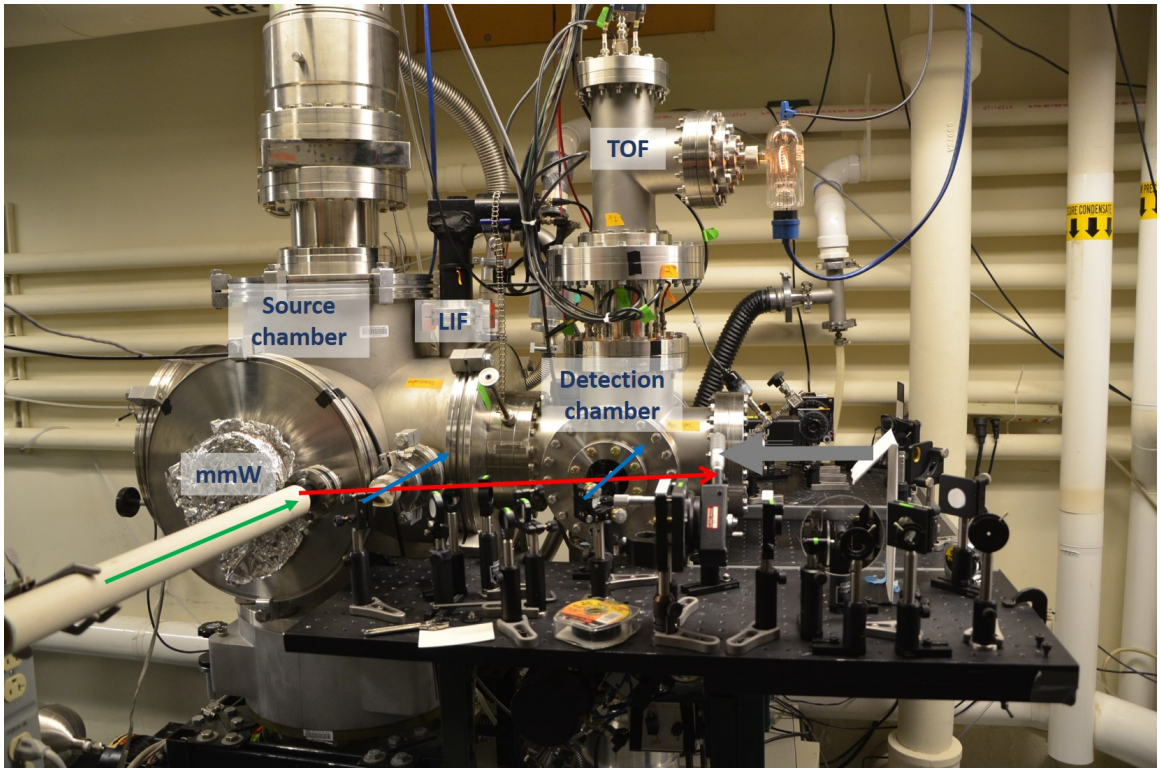

Figure 2-1: A photograph of Gertrude. The red arrow points in the molecular beam propagation direction. The green arrow represents the ablation laser. Blue arrows represent the pump/probe lasers for LIF experiment in the source chamber and TOF-MS experiment in the detection chamber.The thick gray arrow represents how millimeter wave radiation is introduced into the detection chamber. The current settings are for LIF and TOF-MS experiments only. For CPmmW experiments, the front flange of the source chamber needs to be rotated by 180 degrees. The ablation laser entrance port and supersonic nozzle need to be moved back to the end of the source chamber. The large fused silica window, which is covered by aluminum foil in this photograph, is for the entrance of millimeter wave radiation and pump/probe lasers. The Free Induction Decay (FID) is detected from the other side of the source chamber (not visible in this photograph).

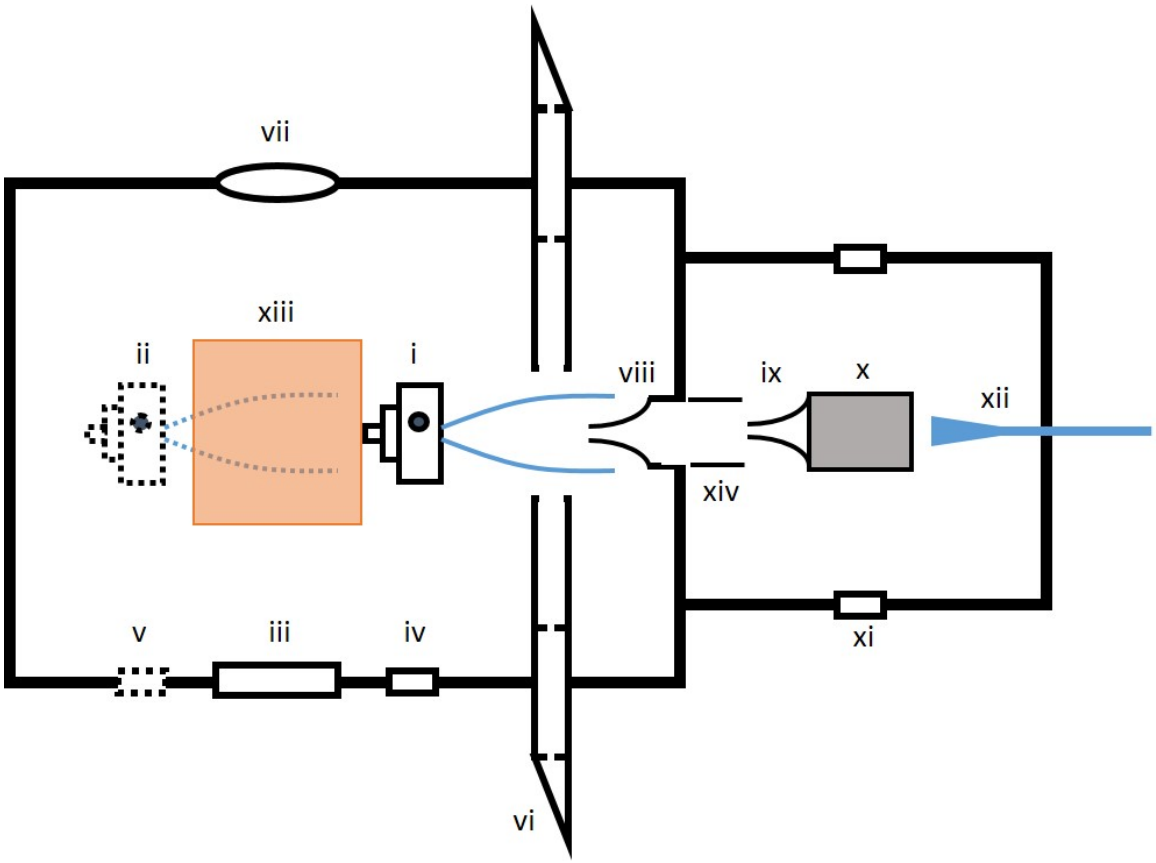

Figure 2-2: Schematic diagram of Gertrude. For LIF and TOF-MS experiments, the target holder attached on the general valve is placed at position (i). For CPmmW experiment, it is placed at position (ii). (iii) is a 4.5" diameter fused silica window, which is used for transmitting millimeter wave radiation and the pump/probe laser beams. The 532nm AR coated window at position (iv) is for transmitting the ablation laser to the target holder at position (i), and the window at position (v) is for transmitting the ablation laser beam to the target holder at position (ii). (vi) is Brewster window and baffle assembly for the LIF experiment. (vii) is Teflon lens/window for transmitting FID in CPmmW experiment. (viii) and (ix) are 0.5 mm diameter and 3 mm diameter conical skimmers that select the center of the molecular beam. (x) are Stark plates and TOF-MS (point out of the page). (xi) is a 2.75" fused silica window for transmitting pump/probe lasers for TOF-MS experiment. (xii) is a W band millimeter wave feedthrough and a 23 dBi rectangular W-band millimeter-wave gain horn. (xiii) represent three pairs of 20 cm $\times$ 20 cm $\times$ 20 cm rectangular Helmholtz coils, whcih are used for canceling the earth's magnetic field in the source chamber for CPmmW experiment. (xiv) is an ion deflector that is used for preventing ions created by the laser ablation from arriving at the TOF-MS detection region.

the pumping speed are the average background pressure and the transient background pressure. The former is determined by the pumping speed only. The latter depends on the volume of the vacuum chamber in additional to the pumping speed. The average background pressure can be calculated by:

$$P_{ba} = \frac{CP_0d^2}{S} f\Delta t, \tag{2.1}$$

where P_{ba} is the average background pressure, P_0 is the backing pressure of the general valve, d is the diameter of the nozzle (cm), f is the experimental repetition rate, Δt is the nozzle opening duration time, S is the pumping speed (L/s), and C is the nozzle conductance (L/cm^2/s). [1] [94].

The transient background pressure can be calculated by:

$$P_{bt}(t) = P_{bt}^{\Delta} e^{-t/\tau} \tag{2.2a}$$

$$\tau = V/S \tag{2.2b}$$

$$P_{bt}^{\Delta} = P_0 \left(\frac{C\Delta t d^2}{V} \right), \tag{2.2c}$$

where P_{bt}^{Δ} is the transient background pressure, τ is the background pressure relaxation time constant, and V is the volume of the vacuum chamber.

I substitute the operating parameters of our source vacuum chamber with turbo and diffusion pumps individually into Eq.(2.1) and Eq.(2.2) to calculate the average background pressure and transient background pressure with four typical buffer gases, as in Table 2.1. The average background pressure with the diffusion pump is much lower than that with the turbo pump. However, their transient pressures are similar. This is due to the volume of our source chamber being large enough to dissipate the gas pulse very rapidly at early time, a rate of which is almost independent of the pumping speed. The 50 ms background pressure relaxation time with the turbo pump suggests that I cannot decrease the transient pressure significantly by increasing the pumping

[1] In our experiment, P_0=40 PSI, d=0.5 mm, f=20 Hz, Δt=150 μs, S=1000 L/s for the turbo pump, 3000L/s for the diffusion pump, C_{He}=45 $L/cm^2/s$, C_{Ne}=20 $L/cm^2/s$, C_{Ar}=14 $L/cm^2/s$, C_{He}=16 $L/cm^2/s$

Table 2.1: Comparisons between the turbo pump and the diffusion pump for the source chamber

	diffusion pump		turbo pump	
relaxation time	15 ms		50 ms	
pressure	average/mtorr	transient/mtorr	average/mtorr	transient/mtorr
He	0.2	0.7	0.7	0.7
Ne	0.1	0.3	0.3	0.3
Ar	0.07	0.2	0.2	0.2
N_2	0.08	0.2	0.2	0.2

speed at our current 20 Hz repetition rate. Because the duration of the molecular beam pulse in the source chamber is <300 μs, the higher average background pressure does not interfere with the beam. Overall, replacing the 3600 L/s diffusion pump by the 1000L/s turbo pump does not degrade the performance of the supersonic molecular beam in the source chamber.

The required pumping speed for the turbo pump in the detection chamber is much slower due to the tiny gas flow through the 0.5 mm diameter skimmer. The pressure of the detection chamber with the turbo pump can be calculated by:

$$P = \frac{P_{eff} d^2}{4S} \sqrt{\frac{2kT_0}{m_0}}, \tag{2.3}$$

where P_{eff} is the effective pressure before the skimmer, which is the local pressure of the molecular beam, and approximately 10 times higher than the transient background pressure (P_{bt}) of the source chamber. For typical experiments, the pressure in the detection chamber is <1 μtorr, which is acceptable for the TOF-MS and the MCP detector.

2.1.2 Cutaway source

The cutaway source was designed by the Duncan group to create metal-Noble gas clusters, as shown in Figure 2-3, Plot (a) [95, 96]. Compared to the regular closed channel source, as shown in Figure 2-3, Plot (b), the molecular beam from the cutaway source is colder, more intense, and more stable. In addition, without the confinement

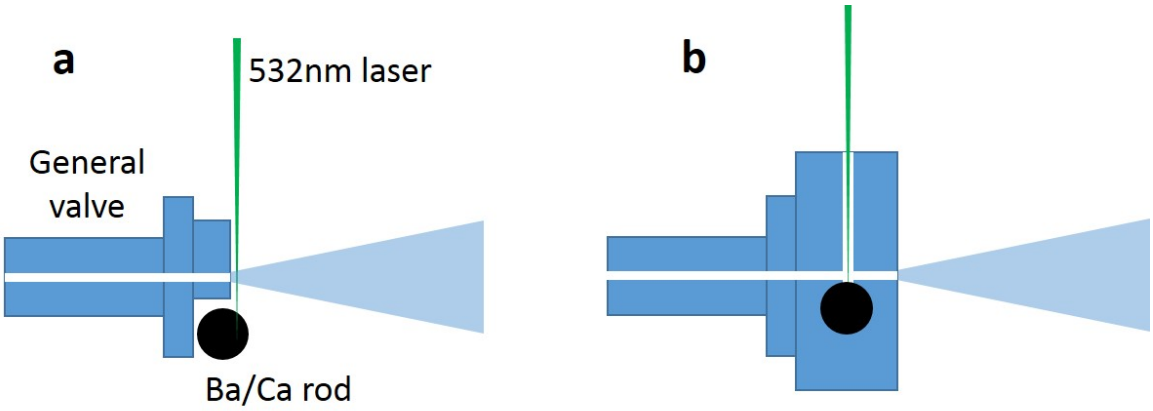

Figure 2-3: Schematic diagram of the cutaway source (a) and the closed channel source (b).

of the growth channel in the closed channel source, the metal-metal collisions are significantly reduced and fewer metal clusters are formed. In my experiment, most properties of the cutaway source are helpful, except for the metal-rare gas clustering. Table 2.2 is a checklist of the cutaway source optimization to increase the beam intensity and decrease the cluster formation. Table 2.3 compares the BaF molecular beams from two different sources. The cutaway source can provide a more intense and confined beam, which is well suited for LIF and TOF-MS experiments with nanosecond pulsed lasers.

2.1.3 Target holder

For typical laser ablation experiments, each spot on the ablating target cannot be ablated by more than 3000 laser shots (2.5 minutes with 20 Hz repetition rate). To extend the experimental duration, the metal rod is mounted on a rotating motor to rotate slowly. Thus, typical experiments can continuously run for more than 5 hours. However, for some soft metals, such as Barium, the ablation speed is much more rapid than for a hard metal, such as Calcium. Thus, the run time of the Barium experiment with a pure rotating target holder is less than 1 hour. To overcome this difficulty, I built a rotating-translating target holder. I directly connect the target rod to a rotating-translating picomotor. A rotating variable resistor is connected to the motor

Table 2.2: A checklist of the cutaway source optimization.

Item	Purpose
Ablation laser power	Above a threshold, the intensity of the molecular beam is constant, but the temperature can be changed. In our BaF experiment, the temperature can be tuned from 3 K to 30 K with different ablation laser powers.
Distance between ablating spot on the rod and the nozzle output	Perpendicular to the ablation laser: as short as possible, no more than 3 mm. Parallel to the ablation laser: 3-5 mm is the best.
Backing pressure of the nozzle	For the experiments without chemical reactions, $\sim$20 PSI. For the experiments with chemical reactions, such as $Ba + SF_6 \rightarrow BaF$, the backing pressure has been optimized with different concentrations of the seed gas.
General valve open time	As short as possible (>10 μs, otherwise, the supersonic expansion cannot be well established). In my experiment, 150 μs, which is limited by the IOTA one pulse controller.
Delay between the ablation laser pulse and gas pulse	Usually, the sweet spot occurs when the ablation laser pulse meets the front edge of the gas pulse. This time delay is quite sensitive, and 30 μs off would decrease the molecular beam intensity by a factor of 5.

Table 2.3: A comparison of BaF molecular beams with Argon buffer gas in the cutaway source and the closed channel source.

	Cutaway source	Standard source
Temperature	3 K - 30 K	> 20K
Pulse length	50 μs	150 μs
Flux	10^9/sr/pulse	10^8/sr/pulse
Number density (in the detection chamber)	10^6/cm^3	3×10^4/cm^3

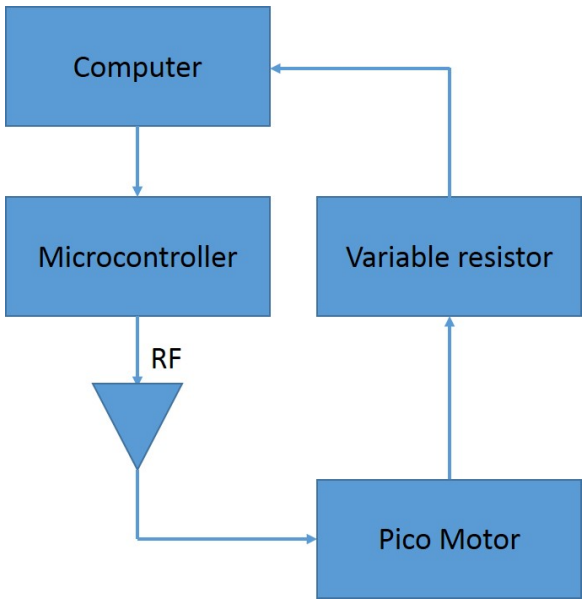

Figure 2-4: Schematic diagram of the motion control system for translation and rotation of the metal rod.

to monitor the rotational position. The schematic diagram of the control system is in Figure 2-4. The picomotor is driven by an amplified RF signal generated by a computer controlled microcontroller. By reading the rotational position in real-time, the rotational variable resistor attached to the picomotor feeds the position and speed back to the computer to control the rotational speed and translational distance. With this new target holder, the Barium experiment can continuously run for more than 10 hours.

2.1.4 Ramped pulser

Most TOF-MS experiments in our lab have been performed with a high speed high voltage pulser, which creates a square pulse that ionizes all Rydberg states above an energy threshold ($n > n_{threshold}$). This fast rising square pulse (rise time < 10 ns) provides high mass resolution. However, it wipes out any possibilities for distinguishing between particles in different Rydberg states in a single measurement. To discriminate among different Rydberg states, I can measure the signal strength as a function of voltage in multiple data collections. However, such a measurement is usually not reliable, due to the fluctuations of the molecular beam intensity. I use

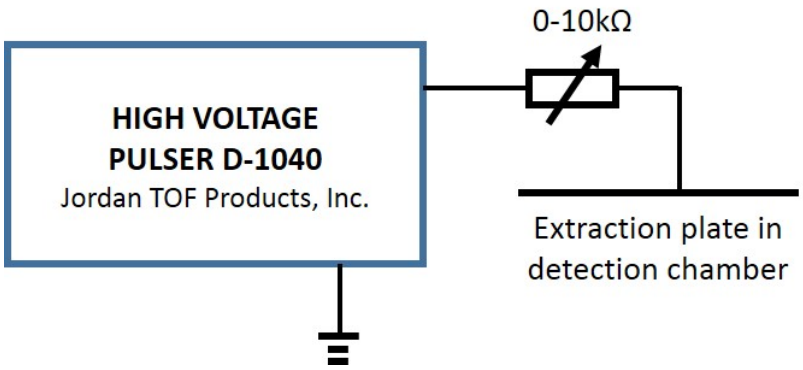

Figure 2-5: Schematic diagram of a modified high voltage ramped pulser based on D-1040 high voltage pulser made by Jordan TOF Products, Inc.

a ramped field pulse to replace the rectangular pulse with constant field amplitude. Thus, different Rydberg states can be ionized with different voltages, which have different delays in the time-domain in a single shot. Their relative intensities are immune from fluctuations in the molecule source.

The modification from a rectangular pulser to a ramped pulser is easy by changing the impedance of the circuit, as shown in Figure 2-5. A variable resistor of 0-10 kΩ is inserted between the high-voltage pulser and the extraction plate. When the variable resistor is set to 0 Ω, a rectangular pulse with 5 ns rise time is added to the extraction plate. When I increase the resistance of the variable resistor, the RC characteristic of the circuit increases and the rising time of the pulse increases continuously from 5 ns to 10 μs. Usually, I set the resistor at 1 kΩ and have a ramped pulse with 1 μs rising time, as shown in Figure 2-6. Although the field ramp is not linear, it is very reproducible and can be calibrated and linearized by data post-processing.

2.1.5 Miscellaneous

Several minor improvements to Gertrude are summarized as follows:

- LIF experiment: To increase the detection efficiency, I built a cage system (LC6W, Thorlabs) with short focued legnth lens (f=5 cm) above and parabolic mirror below (f=5 cm). The detection solid angle is nearly π. In addition, to decrease the laser scattering, two 1' long baffle tubes with four quarter inch irises and two Brewster

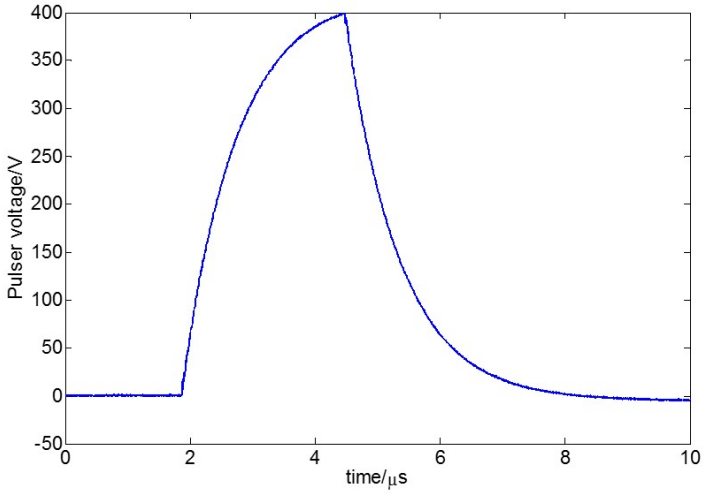

Figure 2-6: The output of the modified ramped pulser. The leading edge and the tailing edge have the same time constant. The maximum amplitude can be changed from 100 V to 400 V, and the time constant can be tuned from 10 ns to 10 μs. In my experiment, I only care about the behavior of the leading edge.

windows are implemented. The number of scattered photons per pulse detected by PMT with typical laser power is less than 3 without any filter.

- Skimmer position: To prevent molecular beam reflections from disturbing the beam propagation, a 0.5 mm diameter conical skimmer is placed 1.5" away from the wall between the source and detection chambers.

- Ion deflector: To prevent the ablated ions from propagating into the detection region of the TOF-MS, a DC ion deflector at 10 V is placed between two conical skimmers in the detection chamber. In addition, to shield the detector region from the stray electric field generated by the ion deflector, a gold shroud is mounted around the high voltage plate stacks.

- Fine tuning power supply: To minimize the stray electric field, two isolated metal plates in the detection region should have the same voltage. The D-603 TOF power supply has very good short-term and long-term voltage stability ($V_{rms} < 10mV$). However, the tuning resolution of the output is 1 V. To achieve better tuning resolution, I connect a high precision, low voltage power supply (HP 6632A) to D-603 power supply in series. This combination power supply can provide up to 3

kV with <20 mV voltage fluctuation and <1 mV tuning resolution.

- millimeter wave feedthrough: I drill a rectangular through-hole (2.54 × 1.27 mm) with sharp corners using an Electric Discharge Machine on a standard 2.75" diameter stainless steel CF flange. Then I insert an acrylic bar (the same size as the hole) into the hole and glue it on maintaining the vacuum. The insertion loss of the home-built feedthrough is 3 dB.

2.1.6 Future improvements

- Stepwise ramped pulser: Although our current continuous ramped pulser can separate different Rydberg states, it significantly degrades the mass resolution in the TOF-MS. A stepwise ramped pulser, with 10 different discrete voltages, might not only have high state selective resolution, but would also retain the mass resolution.
- Faster General Valve controller: Ablated molecules in our cutaway source are typically distributed in a beam of 50 μs duration. The gas pulse, whose duration is longer than 50 μs, is unnecessary to enhance the signal, but degrades the performance of the molecular beam and requires a larger vacuum pump. It would be possible to modify our current IOTA-One General Valve controller to achieve shorter gas pulse duration (<50 μs). Thus, the background gas pressure in the source chamber could be lower, and the molecular beam properties could be improved. It would also give us some freedom to increase the backing pressure of the nozzle far beyond our current limiting pressure of 40 PSI.
- Faraday cage: There are two parallel plates in the interaction region with the same DC voltage (1.5 kV). A ∼2 μs ramped pulse is applied to the bottom plate, but not to the top plate. Our current setup adds the same voltages on both of these two metal plates with two independent 1.5 kV power supplies. The fluctuation of the relative voltages from the two power supplies is more than 20 mV, which is difficult to be decreased by fine tuning either power supply. To decrease such source of stray electric field, the best method is to connect the two plates to form a Faraday cage. A uni-directional electric circuit with multiple diodes might be used to isolate the

ramped pulse on the bottom plate.

2.2 Vacuum system for buffer gas cooled molecular beam

My first atomic Rydberg-Rydberg FID experiments are performed in the laser ablated supersonic beam apparatus, which is described in Section 3.2. The number density of Calcium Rydberg states created in the supersonic beam ($\sim 1\times 10^5 \mathrm{cm}^{-3}$) barely results in sufficient FID radiation signal to be detected by the CPmmW spectrometer. However, due to a factor of ~10 loss for molecule synthesis (eg. Ba + SF_6 $\rightarrow$ 10% BaF) and a factor of 10 loss for the rotational partition function (at 5 K), extension of the FID detected experiments to a molecular system is difficult in the supersonic beam apparatus. In addition, the supersonic beam has several other disadvantages: (1) A fast velocity (for Argon gas, $v_{\parallel,ss}$ = 600 m/s, $v_{\perp,ss}$ = 1000 m/s) results in a broad Doppler linewidth (300 KHz at 100 GHz). (2) Relatively large shot-to-shot fluctuations (>80%) requires a long time average to obtain adequate signal to noise ratio. (3) It is difficult to perform number density-dependent experiments, such as the superradiance, which is discussed in Chapter 4. Therefore, I have spent almost two years to design, construct and test an upgraded molecular beam source to replace the laser ablation supersonic beam apparatus, namely the buffer gas cooled beam apparatus.

The number density of target molecules in a laser ablated supersonic beam source is limited by the low coupling efficiency between the ablated material (ablatant) and the supersonic beam, in which it appears that most of the ablatant is not entrained in the beam but stuck on the wall. In a buffer gas cooled beam source, the ablatant is confined in a cold cell with a cold noble gas (20 K Neon). The mean free path of the ablatant is much shorter than the dimensions of the cell, thus it collides with the buffer gas 50-100 times before either condensing on a wall or being drawn out in a hydrodynamic expansion into vacuum. The ablatant is quickly thermalized through

collisions with the buffer gas and undergoes additional translational and rotational cooling in the hydrodynamic expansion. Compared to the supersonic beam source, the amount of ablatant coupled into the molecular beam, and hence the number density of the target molecules in the beam, can be increased by a factor of 1000. Hydrodynamic cooling effects help reduce the final translational and rotational temperature of the molecular beam to 3 K. Additionally, due to a much smaller pressure difference across the nozzle, the average forward velocity of the buffer gas cooled beam is smaller by a factor of 10 than that of the supersonic beam, and the Doppler broadening is reduced by a factor of 10. Combined number density and linewidth improvement, the buffer gas cooled molecular beam provides a factor of 10000 improvement. In the first section, I briefly discuss the thermodynamics of the beam, which guides me in the design of the apparatus for creating a cold, slow, and intense beam. Most theoretical work on this topic comes from the Doyle group [70]. I apply their work for in my specific experiments. In the second section, I describe important design considerations and key components. In the final section, I characterize the performance of the buffer gas cooled beam source and demonstrate that it indeed provides a huge improvement as we expected.

2.2.1 Characterization of gas flow regimes

The Reynolds number is a dimensionless quantity that is used to characterize the gas flow. It is defined as the ratio of inertial forces to viscous forces:

$$\mathrm{Re} = \frac{F_{inertial}}{F_{viscous}} \approx Kn^{-1} \approx d_{aperture}/\lambda_{mean}. \tag{2.4}$$

By the von Karman relation, the Reynolds number can be related to the Knudsen number (Kn), which is a gas kinetic quantity and can be expressed by the ratio of aperture size $d_{aperture}$ to mean free path λ_{mean}. This relationship clearly interconnects the in-cell buffer gas density, buffer gas flow rate, and Reynolds number. In my experiment, by controlling the buffer gas flow rate via a mass flow controller, I can continuously vary the buffer gas density and Reynolds number in the cell. Typical

flow rates in my experiment are $f_{0,b}$=1-50 SCCM. SCCM (Standard Cubic Centimeter per Minute) is a common unit for gas flow and is approximately 4×10^{17} s^{-1}. Due to the continuous buffer gas flow, the output flow rate, f_{out}, is determined by the conductance of the aperture and is equal to the input flow rate, $f_{0,b}$:

$$f_{out} = (1/4)\, n_{0,b} \langle v_{0,b} \rangle A_{aperture} = f_{0,b} \rightarrow n_{0,b} = \frac{4 f_{0,b}}{A_{aperture} \langle v_{0,b} \rangle} \tag{2.5a}$$

$$\langle v_{0,b} \rangle = \sqrt{\frac{2 k_B T_0}{m}}, \tag{2.5b}$$

where $n_{0,b}$ is the number density of the buffer gas in the cell, m is the mass of the buffer gas atoms, T_0 is the temperature of the cell (4 K for Helium buffer gas, 20 K for Neon buffer gas), $\langle v_{0,b} \rangle$ is the mean thermal velocity of the buffer gas in the cell (150 m/s), and $A_{aperture}$ is the aperture size of the cell output ($d_{aperture}$=3 mm). With a fixed temperature and aperture size, the buffer gas density is proportional to the flow rate, as shown in Figure 2-7, Plot (a).

To evaluate the relationship of buffer gas flow rate and Reynolds number, I need to use collisional cross section (σ_{b-b}), which determines the mean free path of the buffer gas, $\lambda_b = (n_{0,b} \sigma_{b-b})^{-1}$. Typically, σ_{b-b} depends strongly on the temperature at T<10 K and is difficult to measure. Here, I use simulation values created by Timur Tscherbul [97]: $\sigma_{He-He} = 1 \times 10^{-14}$ cm^2 at 4 K and $\sigma_{Ne-Ne} = 2 \times 10^{-14}$ cm^2 at 20 K. By Eq. (2.6), I can approximately evaluate the relationships of the Helium/Neon buffer gas flow rate and Reynolds number, which are plotted in Figure 2-7, Plot (b).

$$\mathrm{Re} \approx \frac{d_{aperture}}{\lambda_b} \approx \frac{4 f_{0,b} \sigma_{b-b}}{d_{aperture} \langle v_{0,b} \rangle} \tag{2.6}$$

Effusive source ($Re \leq 1$)

In this region, the mean free path of the buffer gas (λ_b) is much larger than the aperture diameter, $d_{aperture}$. There are no collisions as the molecules pass through the aperture. The behavior of the beam is completely determined by the thermodynamics in the cell and the geometry of the aperture. The density distribution of the gas in

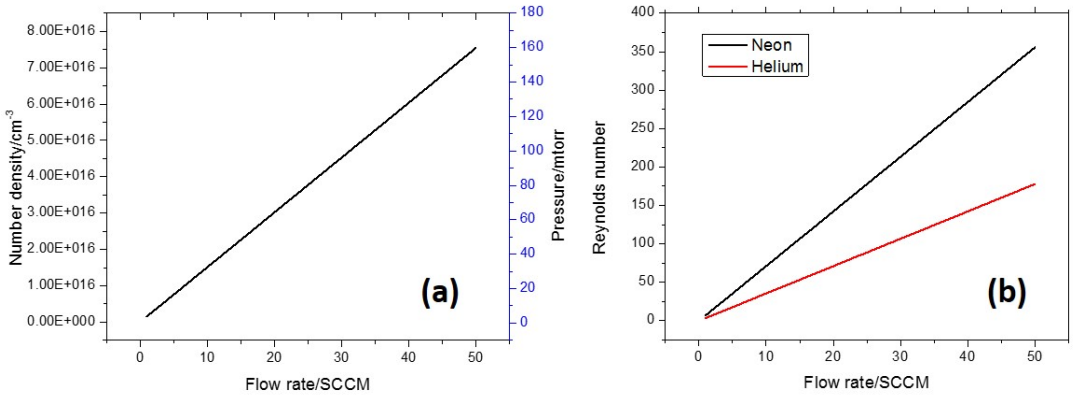

Figure 2-7: Relationships of the buffer gas flow rate vs. buffer gas density, Plot (a), and Reynolds number, Plot (b), in the cold cell.

the beam can be separated into a spatial distribution and a velocity distribution:

$$n_{eff}(R, v, \theta) = n(R, \theta) f(v), \tag{2.7}$$

where $n(R, \theta)$ is the spatial distribution of the number density, f(v) is the normalized velocity distribution, R is the distance from the aperture, and θ is the angle away from the normal to the aperture. The beam temperature is the same as the equilibrium temperature in the cell. The normalized distribution of a classical gas follows the Maxwell-Boltzmann distribution:

$$f(v) = \frac{2}{\langle v_0 \rangle^3} v^2 e^{-4v^2/\pi \langle v_0 \rangle^2}. \tag{2.8}$$

The velocity distribution in an effusive beam and mean forward velocity can be obtained from Eq.(2.8):

$$f_{\parallel,eff}(v) = \frac{v}{\langle v_0 \rangle} f(v) \rightarrow \bar{v}_{\parallel,eff} \approx 1.2 \langle v_0 \rangle . \tag{2.9}$$

Due to the complete thermal equilibrium in an effusive beam, the forward velocity spread and transverse velocity spread are identical and follow the thermal 1D

Maxwell-Boltzmann distribution:

$$\Delta v_{\parallel,eff} = \Delta v_{\perp,eff} = \sqrt{\frac{8\ln(2)k_B T_0}{m}} \approx 1.5 \langle v_0 \rangle . \tag{2.10}$$

The angular part of the number density distribution in an effusive beam can be assumed as a semi-isotropic distribution:

$$n(R,\theta) = \frac{n_0 \cos(\theta)}{4\pi R^2} dA, \tag{2.11}$$

where n_0 is the number density of the gas in the cell. The angular spread (FWHM) and divergence is:

$$n(R, \Delta\theta_{eff}/2) = \frac{1}{2} n(R,0) \rightarrow \Delta\theta_{eff} = 120^\circ \rightarrow \Delta\Omega_{eff} = \pi. \tag{2.12}$$

The above discussion applies not only for the buffer gas, but also for the target molecules, because there is complete thermal equilibrium at temperature T. However, due to the mass difference, the velocity and the velocity spread are different by a factor of $\sqrt{m_t/m_b}$, where m_t and m_b are the masses of the target molecule and buffer gas atom respectively. In addition, all temperatures mentioned above are translational temperatures. In Section 2.2.2, I show that the rotational temperatures of typical heavy diatomic molecules, such as BaF, are approximately the same as the translational temperature. However, the vibrational temperatures can be much higher.

Supersonic source ($Re \geq 100$)

In the supersonic region [61, 94], the mean free path of the buffer gas (λ_b) is much smaller than the aperture diameter $d_{aperture}$. Therefore, the buffer gas experiences thousands of collisions upon passing through the exit aperture. The beam properties are determined not only by the thermal equilibrium in the cell, but also determined by the dynamical flow of the gas, which is well described by the Navier-Stokes equation [94]. Solving the Stokes equation to obtain the beam properties is difficult and beyond

the scope of this thesis. Several empirical formulas, which are fitted to numerical solutions of the Stokes equation with several adjustable parameters, are summarized in the following equations. These equations can guide us in the evaluation of the properties of the supersonic beam.

- The Mach number is a dimensionless quantity that represents the ratio of the speed of the beam and the local speed of sound. Almost all dynamical properties of the supersonic beam are determined by the Mach number. The fitted 1D position-dependent Mach number is:

$$M(x) = A\left(\frac{x - x_0}{D_{nozzle}}\right)^{\gamma-1} - \frac{1}{2}\frac{(\gamma+1)/(\gamma-1)}{A((x-x_0)/D_{nozzle})^{\gamma-1}}, \tag{2.13}$$

  where γ is specific the heat ratio, which, for a monatomic buffer gas, is γ=5/3, D_{nozzle} is the nozzle diameter, and A and x_0 are fitting parameters ($A = 3.26$ and $x_0 = 0.075D_{nozzle}$ in my experiment).

- The temperature of the supersonic beam decreases as the beam isentropically expands. During the expansion, thermal energy is converted into translational kinetic energy. Therefore, the internal energy (velocity spread) of the beam is reduced, but the average velocity of the beam is increased.

$$\frac{T(x)}{T_0} = \left(1 + \frac{\gamma-1}{2}M(x)^2\right)^{-1} \tag{2.14a}$$

$$\Delta v(x) = \sqrt{\frac{\gamma RT(x)}{m}} = \sqrt{\frac{\gamma RT_0\left(1+\frac{\gamma-1}{2}M(x)^2\right)^{-1}}{m}} \tag{2.14b}$$

$$v(x) = M(x)\sqrt{\frac{\gamma RT_0}{m}}\left(1 + \frac{\gamma-1}{2}M(x)^2\right)^{-1/2}, \tag{2.14c}$$

  where T_0 is the temperature of the nozzle, m is the mass of the buffer gas molecules, and R is the gas constant.

- During the expansion, the local pressure and beam density decrease continuously:

$$\frac{P(x)}{P_0} = \frac{n(x)}{n_0} = \left(1 + \frac{\gamma-1}{2}M(x)^2\right)^{-\gamma/(\gamma-1)}, \tag{2.15}$$

where P_0 and n_0 are the pressure and number density in the nozzle.

From Eq. (2.14) and (2.15), I obtain a direct relationship between cooling and expansion for a monatomic buffer gas:

$$\frac{n}{n_0} = \left(\frac{T}{T_0}\right)^{3/2} \tag{2.16a}$$

$$n(R) \propto R^{-2} \tag{2.16b}$$

$$T(R) \propto R^{-4/3}, \tag{2.16c}$$

where R is the distance from the nozzle. The temperature and density of the beam decrease rapidly as the molecules fly away from the nozzle. However, this cooling process terminate where the gas density in the beam becomes sufficiently low that the mean free path is larger than the distance of the neighboring molecules. There, the gas in the beam ceases to behave as a fluid and the Navier-Stokes equation can no longer be used. Following, I estimate the effective cut-off boundary of the cooling process and evaluate the final thermal properties of the beam. This discussion not only can be applied for the supersonic expansion ($Re \geq 100$), but also for the hydrodynamical expansion ($1 \leq Re \leq 100$).

In Figure 2-8, I assume that a collision occurs at position 1 and another collision occurs at position 2. No other collisions occur between positions 1 and 2, or beyond position 2. The mean free path at position 1 is $\lambda_{m,1}(d) = 1/n(d)\sigma$, and the mean free path at position 2 is

$$\lambda_{m,2}(d+L) = \frac{1}{n(d+L)\sigma} = \left(\frac{d+L}{d}\right)^2 \lambda_{m,1}, \tag{2.17}$$

where n(x) is the number density of the beam x cm away from the nozzle, σ is the collisional cross section for Neon-Neon or Neon-target molecule. A very rough but simple approximation of the average mean free path between positions 1 and 2 is:

$$\lambda_{m,average} = \frac{1}{2}\left(\lambda_{m,1} + \lambda_{m,2}\right) = \frac{1}{2}\left(1 + \left(\frac{d+L}{d}\right)^2\right)\lambda_{m,1}. \tag{2.18}$$

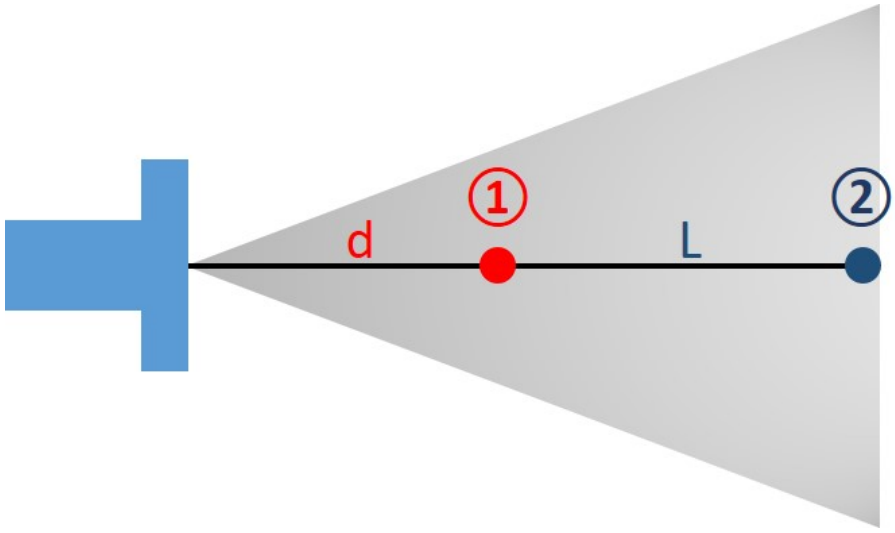

Figure 2-8: A schematic diagram for estimating the cut-off boundary for the isentropic expansion. The distance between the nozzle and position 1 is d, and the distance between position 1 and position 2 is L. The nozzle can be a room temperature General Valve, and also can be a 20 K cold cell.

The time interval between the two successive collisions can be evaluated in the molecular beam translating frame and in the lab frame. In the molecular beam translating frame, the time interval is $\Delta t_1 = \lambda_{m,average}/\Delta v$, where Δv is the velocity spread in the molecular beam.[2] In the lab frame, the time interval is $\Delta t_2 = L/v$, where v is the beam velocity.[3] The time intervals from the two frames should be the same, as $\Delta t_1 = \Delta t_2$. Therefore:

$$\frac{\lambda_{m,average}}{\Delta v} = \frac{L}{v} \rightarrow L^2 + 2\left(d - \frac{\Delta v d^2}{\lambda_{m,1} v}\right) L + 2d^2 = 0, \tag{2.19}$$

where Δv, v and $\lambda_{m,1}$ are independent of L. Therefore, Eq.(2.19) is a quadratic equation of L. The positive solution of Eq.(2.19) is the distance between the two successive collisions in the molecular beam. If I want the collision at position 1 to be the last collision, I should arrange that Eq.(2.19) has no real solutions, as

$$\left(d - \frac{\Delta v d^2}{\lambda_{m,1} v}\right)^2 - 2d^2 < 0 \rightarrow d > \left(\sqrt{2} - 1\right) \lambda_{m,1}(d) \frac{v(d)}{\Delta v(d)}. \tag{2.20}$$

[2] Δv at position 1 and at position 2 are the same, because there are no additional collisions in this region.

[3] v at position 1 and at position 2 are the same. The reason is the same as for Δv.

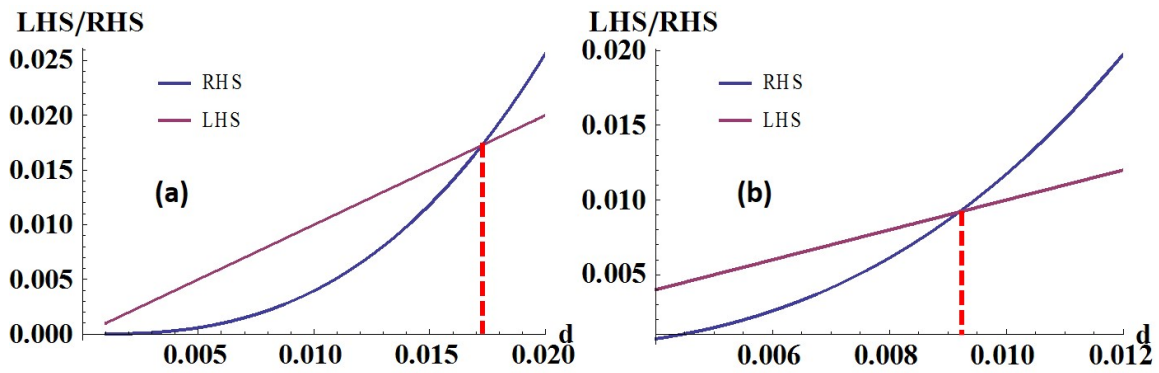

Figure 2-9: Evaluating the cut-off boundary for the isentropic expansion. Plot (a) is for the room temperature Argon supersonic beam from a 1 mm diameter General Valve with 40 PSI backing pressure. Plot (b) is for the 20 K Neon buffer gas cooled beam from a 3 mm diameter cold cell with 10 SCCM flow rate. The vertical dashed lines identify the cut-off boundary.

Δv, v, $\lambda_{m,1}$ are functions of d, and their approximate expressions have been outlined in Eq.(2.13), (2.14), (2.15) and (2.21).

$$\lambda_{m,1}(x) = \frac{1}{n(x)\sigma} = \frac{1}{n_0\left(1+\frac{\gamma-1}{2}M(x)^2\right)^{-\gamma/(\gamma-1)}\sigma}. \tag{2.21}$$

I insert the detailed expressions of $\Delta v(d)$, $v(d)$, $\lambda_{m,1}(d)$ into Eq.(2.20), and evaluate and plot the left hand side (LHS) and right hand side (RHS) of Eq.(2.20) respectively in Figure 2-9. The crossing point of the two curves identifies the cut-off boundary $d_{boundary}$. I submit $d_{boundary}$=17 mm into Eq.(2.14) to calculate that the lowest temperature in the conventional supersonic beam is 3 K, which is consistent with the experimental measurements. In addition, I evaluate all other thermodynamic processes that occurs in the supersonic molecular beam at $d_{boundary}$, such as the velocity and the beam divergence as following:

- Forward velocity

$$v_{\parallel,ss} = \sqrt{\frac{2(H(T_0)-H(T))}{m}} \approx \sqrt{\frac{5k_BT_0}{m}} \approx 1.4\left\langle v_0\right\rangle, \tag{2.22}$$

where $H(T_0)$ is the enthalpy of the gas in the nozzle at room temperature, T_0=293 K. $H(T)$ is the enthalpy of the gas at the cut-off boundary in the beam

at T=3 K.

- Forward velocity spread

$$\Delta v_{\parallel,ss} = \sqrt{\frac{\gamma RT}{m}} = \sqrt{\frac{T}{T_0}}\,\langle v_0\rangle = 0.08\,\langle v_0\rangle\,. \tag{2.23}$$

- Angular spread (FWHM) $\Delta\theta_{ss}$ and beam divergence $\Delta\Omega_{ss}$

$$n_{ss}(R,\theta) = n(R,0)\cos^2\left(\frac{\pi\theta}{2\phi}\right) \rightarrow \Delta\theta_{ss} = \phi \approx 79^\circ, \Delta\Omega_{ss} \approx 1.4. \tag{2.24}$$

- Transverse velocity spread

$$\Delta\bar{v}_{\perp,ss} = 2\tan(\Delta\theta_{ss}/2)\bar{v}_{\parallel,ss} = 1.6\bar{v}_{\parallel,ss} = 2.2\,\langle v_0\rangle\,. \tag{2.25}$$

The above discussions of the gas thermodynamics in a supersonic beam apply to the buffer gas, but not to the target molecules. Different from the effusive beam, the equilibrium condition of the buffer gas and target molecules in the supersonic beam is not having the same translational temperature, but having the same velocity and velocity spread. Therefore, the translational temperatures of the buffer gas and target molecules are different by a factor of $\sqrt{m_t/m_b}$. However, due to the obscured lack of mass dependence of the rotational temperature, the equilibrium rotational temperature of the target molecules is still approximately the same as the translational temperature of the buffer gas. For example, when I seed BaF in a 4 K supersonic beam with Argon buffer gas, the translational temperature of the BaF molecules is ≈8 K, but the lowest rotational temperature of BaF molecules is still 4 K.

Buffer gas source ($1 \leq Re \leq 100$)

Generally speaking, the buffer gas cooled beam source can be operated in the effusive, intermediate, or supersonic regimes. However, for the experimental considerations in our lab, I only concentrate on the intermediate regime, where the hydrodynamic expansion and the number of collisions through the aperture is between the effusive and

supersonic situations. The thermodynamics of the molecular beam is different from the gas in the cell. However, the frequency of collisions is not sufficiently high to make the flow fluid-like. Therefore, most behaviors of the buffer gas cooled beam lie between the effusive and supersonic limits. Their behaviors, include forward velocity, transverse velocity and beam temperature are easy to estimate by interpolation. However, I also show that the angular spread and divergence of the beam is completely different from the background gas in the cell and cannot be interpolated.

In the buffer gas cooled beam, the collision frequency is not sufficiently high to completely boost the target molecules (usually heavier than buffer gas atoms, $m_t > m_b$) to the velocity of the buffer gas. Therefore, the forward velocity of the target molecules should be larger than the effusive beam velocity ($1.2\langle v_{0,t}\rangle$), but smaller than the supersonic beam velocity ($1.4\langle v_{0,b}\rangle$). Intuitively, the interpolation should be linear near the low Reynolds number limit (Re=1), and saturated near the high Reynolds number limit (Re=100). Two functions, (2.26) and (2.27), are usually used for such interpolations and fit the experimental data well. At low Reynolds number, the acceleration (second term in Eq. (2.26)) is linearly proportional to m_b/m_t. One factor of $\sqrt{m_b/m_t}$ comes from the velocity ratio at thermal equilibrium, the other factor of $\sqrt{m_b/m_t}$ comes from the velocity boost due to collisions. At high Reynolds number, the velocities of the buffer gas and target molecules are almost the same. Therefore, such mass ratio dependence does not exist in Eq. (2.27). Figure 2-10 shows how the forward velocity changes ongoing from the effusive limit to the supersonic limit.

- $1 \leq Re \leq 10$

$$v_{\parallel,t} \approx 1.2\langle v_{0,t}\rangle + 0.6\langle v_{0,b}\rangle \,\mathrm{Re}\frac{m_b}{m_t}, \tag{2.26}$$

- $10 \leq Re \leq 100$

$$v_{\parallel,t} \approx 1.4\langle v_{0,b}\rangle \sqrt{1 - 4\mathrm{Re}^{-4/5}}, \tag{2.27}$$

where $\langle v_{0,t}\rangle$ is the average velocity of the target molecules in the cold cell, and $\langle v_{0,b}\rangle$ is the average velocity of the buffer gas molecules in the cold cell.

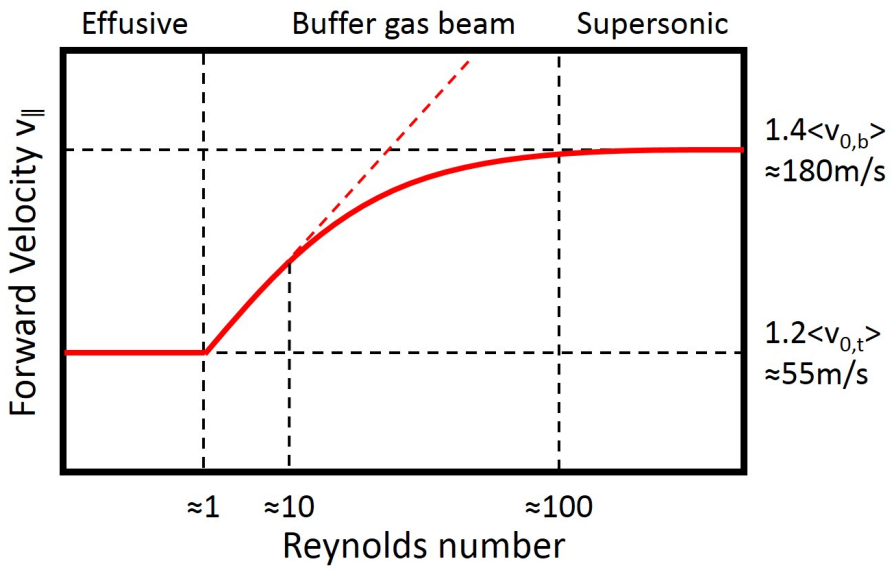

Figure 2-10: A schematic representation of beam forward velocity vs. Reynolds number.

In an isentropic expansion, the forward velocity spread begin to decrease and the temperature of the target molecules in the buffer gas beam is cooled to a lower temperature than the cell temperature. The final temperature is determined by the Reynolds number and lies between the effusive and supersonic limits. The specific dependence is calculated by the method described in Section 2.2.1, and plotted in Figure 2-11. Similar to Figure 2-10, in the intermediate region, the velocity spread decreases linearly in the $1 \leq Re \leq 10$ region, and then saturates to the supersonic limit. Similar empirical formulas can be constructed:

- $1 \leq Re \leq 10$

$$\Delta v_{\parallel,s} \approx 1.5 \langle v_{0,t} \rangle - 0.2 \langle v_{0,b} \rangle \mathrm{Re} \frac{m_b}{m_t}, \tag{2.28}$$

- $10 \leq Re \leq 100$

$$\Delta v_{\parallel,s} \approx 0.4 \langle v_{0,b} \rangle \sqrt{1 + 4\mathrm{Re}^{-4/5}}. \tag{2.29}$$

In the intermediate region, the collisions between the buffer gas and target molecules not only increase the forward velocity, but also increase the transverse velocity spread. In a zero-order picture, the model of transverse velocity spread should not be quite

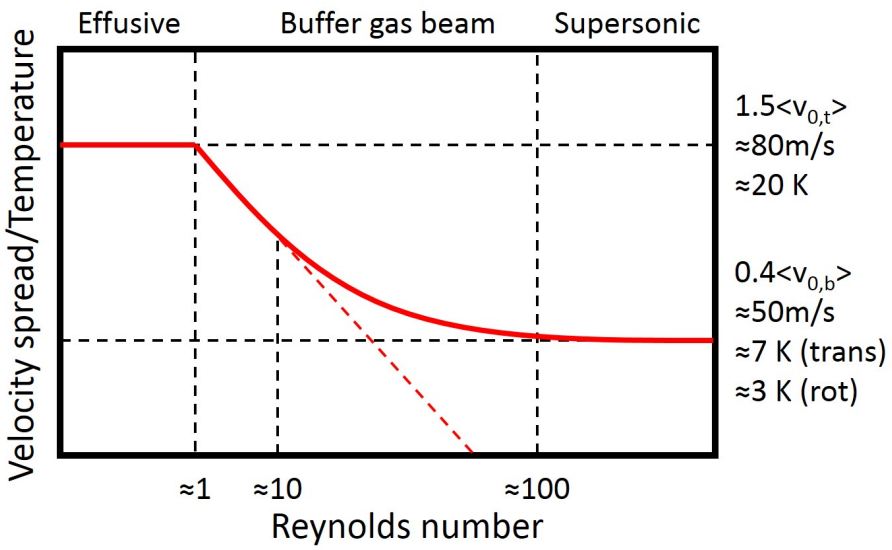

Figure 2-11: A schematic representation of beam velocity spread/translational temperature vs. Reynolds number.

different from that of forward velocity, except for a diffraction effect near the aperture. This diffraction effect modifies the Reynolds number (Re) to an effective transverse Reynolds number ($Re_{tran} = Re \times d_{cell}^2/d_{aperture}^2$). Therefore, the transverse velocity spread is:

- $1 \leq Re \leq 10$

$$\Delta v_{\perp,s} \approx 1.5 \langle v_{0,s} \rangle + (\mathrm{Re}/2) \langle v_{0,b} \rangle \frac{d_{cell}^2}{d_{aperture}^2} \frac{m_b}{m_s}, \tag{2.30}$$

- $10 \leq Re \leq 100$

$$\Delta v_{\parallel,s} \approx 2.2 \langle v_{0,b} \rangle \sqrt{1 - 4\left(\frac{d_{cell}^2}{d_{aperture}^2}\mathrm{Re}\right)^{-4/5}}. \tag{2.31}$$

However, the gas dynamics near the aperture is more complicated than this simple diffraction picture. I perform an FDTD (Finite-Difference Time-Domain) simulation to show that the transverse velocity spread is almost a constant at $1 \leq Re \leq 10$ and then increases significantly. The details of this simulation and development of a more accurate model are beyond the scope of this thesis. Due to the slower rate of

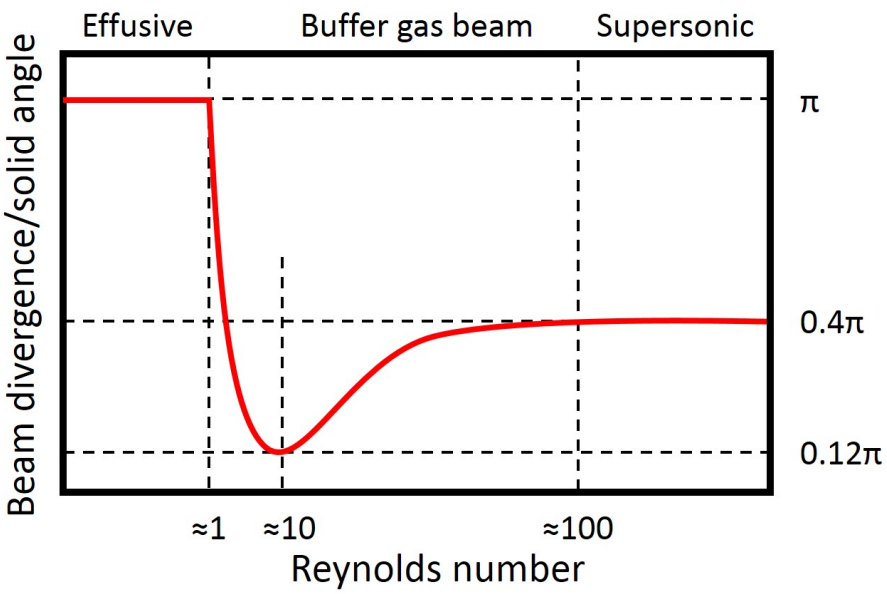

Figure 2-12: A schematic representation of beam divergence vs. Reynolds number.

increase of the transverse velocity spread relative to that of the forward velocity at low Reynolds number, the angular spread or the divergence of the beam decreases at low Re, and increases at high Re. By tuning the Reynolds number carefully, I can collimate the molecular beam and increase the beam density at a position that is far from the output aperture. The simulation predicts the behavior of the beam divergence, as shown in Figure 2-12. At $Re \approx 10$, the minimum angular spread and divergence can be as small as:

$$\Delta\theta = 2\arctan\left(\frac{\Delta v_{\perp,s}/2}{v_{\parallel,s}}\right) \approx 2\sqrt{\frac{m_b}{m_s}} \rightarrow \Delta\Omega \approx \pi m_b/m_s. \tag{2.32}$$

The divergence of the buffer gas beam (0.1π) is significantly smaller than that of the effusive (π) and the supersonic beams (0.4π). In addition, the beam collimation becomes better for heavier molecules.

Comparison of effusive beam, buffer gas cooled beam and supersonic beam

As a conclusion to this section, I plot the expected beam velocities and velocity spreads of three beam sources (room temperature effusive beam source, 20 K Neon

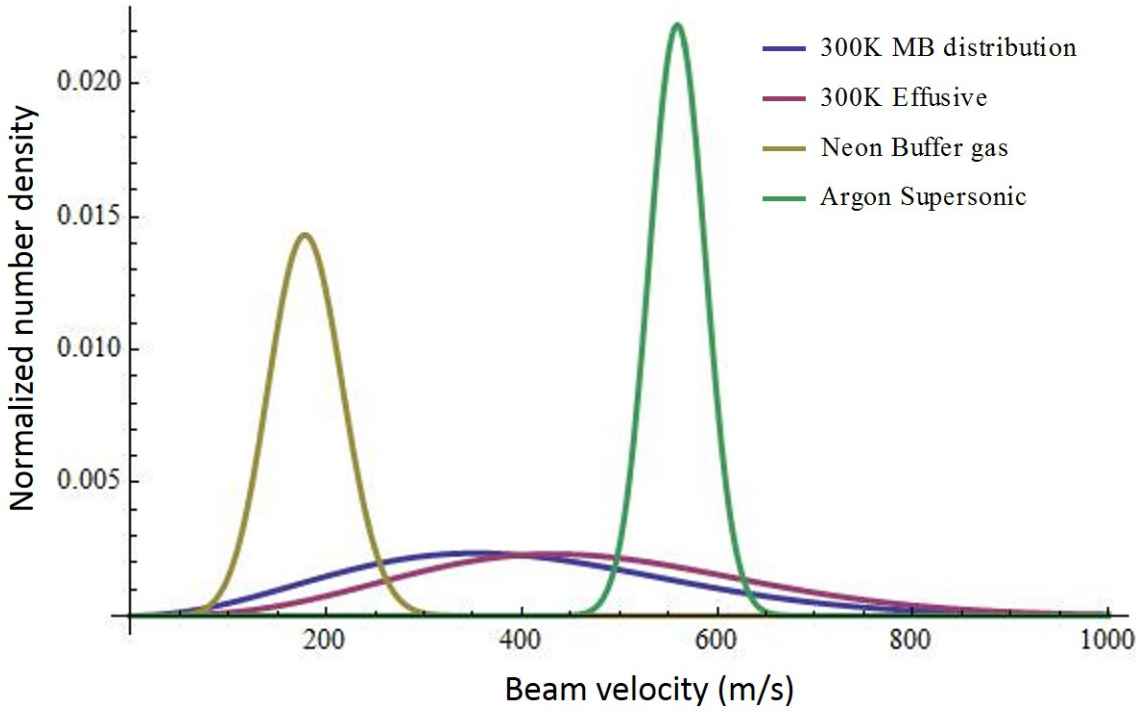

Figure 2-13: Forward beam velocity and velocity spread of the effusive beam, the buffer gas cooled beam and the supersonic beam.

buffer gas cooled beam source and room temperature Argon supersonic beam source) in Figure 2-13. Only the buffer gas cooled beam has both a small forward velocity and a small velocity spread. In addition, I have shown that the divergence of the buffer gas cooled beam is much smaller. The buffer gas cooling technique is best for obtaining a high-flux, collimated, cold, and slow molecular beam.

2.2.2 Introduction of species, thermalization, diffusion and extraction

In the previous section, I have described the gas dynamics through the output aperture and the formation of a beam. In this section, I describe the gas dynamics in the cell. The combination of the dynamics in the cell, through the aperture, and outside of the cell completely determines the properties of the molecular beam in the detection region. The gas thermodynamics in the cell are relatively simpler and effect the beam properties less sensitively. However, the cell design, which is not easily modified

and optimized *in situ*, requires a complete understanding of the thermodynamics.

Introduction of species

There are three usual methods [70] to introduce the target molecules into the buffer gas cooled cell: (1) hot oven; (2) capillary filling; (3) laser ablation. The hot oven method has been widely used for alkali atoms and for some molecules that have high vapor pressure at $\approx$ 500-700 K. Capillary filling is used for molecules that are permanent gases at room temperature. The common advantages of these methods are: (1) formation a continuous beam; (2) a large flux. However, their limitations are: (1) requiring sophisticated thermal isolation between the hot and cold components; (2) not working with unstable molecules, such as radicals. Laser ablation is a method complementary to the hot oven and capillary filling methods, and has been widely used to create a long pulse ($\approx$5 ms) for a variety of diatomic molecules or radicals.

The laser ablation technique requires application of a focused high intensity laser pulse to the surface of the solid precursor, which is located inside the cold cell, to create a dense plasma plume. Multiple chemical reactions occur simultaneously in the plasma. In a very short time, the plasma either recombines to neutral molecules/atoms, or creates free ions. For example, I apply a 25 mJ, 532 nm, 10 ns Nd:YAG laser pulse to ablate a BaF_2 precursor. The final products can be Ba, Ba^+, BaF, BaF^+, BaF_2 or F. Optimizing the yield of the target molecules while suppressing others is nontrivial. I am unaware of a generic and reliable theory that would guide me into optimization of the laser ablation process. Therefore, for a specific molecule, such as BaF, I have spent several months to optimize the precursor preparation and parameters of the ablation laser. This optimization is discussed in detail in Section 2.4.

Thermalization

The initial temperature of ablated molecules is typically 1000 K to 10000 K. Before being pumped out of the cold cell, there should be enough collisions between the hot target molecules and cold buffer gas to decrease the target molecule temperature to the equilibrium temperature (20 K) of the cold cell. The number of collisions should

be larger than:

$$\frac{dT_t(N)}{dN} = -\left(T_t(N) - T_b\right)/\kappa \rightarrow T_t(N) \approx T_b + T_t(0)e^{-N/\kappa} \tag{2.33a}$$

$$\kappa \equiv \frac{\left(m_b + m_t\right)^2}{2m_b m_t}, \tag{2.33b}$$

where $T_t(0)$ is the initial temperature of the laser ablated target molecules (5000 K), T_b is the equilibrium temperature of the Neon buffer gas (20 K), N is the number of collisions, and m_b and m_t are the mass of the buffer gas (20 for Neon) and target molecules (157 for BaF). The minimum number of collisions for cooling BaF with Neon buffer gas is 50. The mean free path of a target molecule in the cold cell is:

$$\lambda_{t-b,0} = \frac{\left(n_{0,b}\sigma_{b-t}\right)^{-1}}{\sqrt{1 + m_t/m_b}} \approx \frac{A_{aperture}\left\langle v_{0,b}\right\rangle}{4f_{0,b}\sigma_{b-t}\sqrt{m_t/m_b}}, \tag{2.34}$$

where σ_{b-t} is the thermally averaged elastic collision cross section and is typically equal to $\sigma_{b-b} = 10^{-14}$ cm^2. If we use $f_{0,b}$=5 SCCM flow rate, the mean free path is $\approx$0.1 mm. The total thermalization length is typically no more than 100 $\times$ 0.1 mm=1 cm. Therefore, the internal diameter of the cold cell should be larger than 1 cm.

The above discussion applies exclusively to translational thermalization. The typical rotational collision cross section is one order of magnitude smaller ($\sigma_{rot} = 10^{-15}$ cm^2) than the translational collision cross section. However, due to the absence of a large mismatch mass factor ($\sqrt{m_t/m_b}$) in the rotational cooling process, the rotational thermalization efficiency of each collision can be higher than that of translational thermalization. Combining these opposing considerations, the rotational cooling almost has the same efficiency as the translational cooling. However, the vibrational cooling is much less efficient, due to a tiny collisional cross section, $\sigma_{vib}/\sigma_{t-b}$<0.1%, where σ_{vib} is the vibrational relaxation cross section and σ_{t-b} is the translational relaxation cross section. Therefore, with typical experimental parameters, the vibrational temperature is similar to the ablation temperature. By measuring the vibrational temperature in the cell, I can approximately obtain the initial plasma temperature.

Diffusion and entrainment from the cold cell

After the target molecules are cooled to the cell temperature, they need to move toward the output aperture. There are two types of gas dynamics in the cell that transport the target molecules from the ablated spot to the aperture: (1) diffusion; (2) entrainment. Diffusion always occurs at equilibrium, and the rate is determined by the diffusion constant, as in Eq.(2.35). With a Brownian motion model, the estimated diffusion time constant is typically 1-10 ms. However, diffusion is not an efficient way to move the target molecules out of the cold cell, and the probability of a target molecule diffusing out of the cell is $A_{aperture}/A_{wall} < 1\%$. Most target molecules impact and freeze on the wall of the cold cell, and are lost.

$$D = \frac{3}{16 n_{0,b} \sigma_{b-s}} \left(\frac{2\pi k_B T_0}{m_b} \right)^{1/2} = \frac{3\pi}{32} \frac{\langle v_{0,b} \rangle}{n_{0,b} \sigma_{b-s}} \rightarrow \tau_{diff} = \frac{16}{9\pi} \frac{A_{cell} n_{0,b} \sigma_{b-s}}{\langle v_{0,b} \rangle}. \tag{2.35}$$

Entrainment of the target molecules out of the cell can be much more efficient than diffusion, and the rate is determined by the conductance of the output aperture:

$$\frac{dN_b}{dt} = \frac{1}{4} N_b \langle v_{0,b} \rangle A_{aperature}/V_{cell} \rightarrow \tau_{pump} = \frac{4 V_{cell}}{\langle v_{0,b} \rangle A_{aperture}}, \tag{2.36}$$

where V_{cell} is the internal volume of the cold cell. The dynamics of the entrainment process is a single exponential decay with time scale τ_{pump} in Eq.(2.36). The pumpout time is also typically 1-10 ms. Except for very high or very low buffer gas flow rate, these two processes occur simultaneously. The ratio of their contributions not only determines the extraction efficiency, but also determines the beam velocity and velocity distribution. I define a dimensionless parameter to characterize their contribution:

$$\gamma_{cell} \equiv \frac{\tau_{diff}}{\tau_{pump}} = \frac{4}{9\pi} \frac{n_{0,b} \sigma_{b-s} A_{aperture}}{L_{cell}} \approx \frac{\sigma_{b-s} f_{0,b}}{L_{cell} \langle v_{0,b} \rangle}. \tag{2.37}$$

To enhance the entrainment contribution, I can increase the buffer gas flow rate. To enhance the contribution of diffusion, I can design a larger cell. A simulation to predict the extraction fraction of the target molecules and the beam velocity vs. γ_{cell}

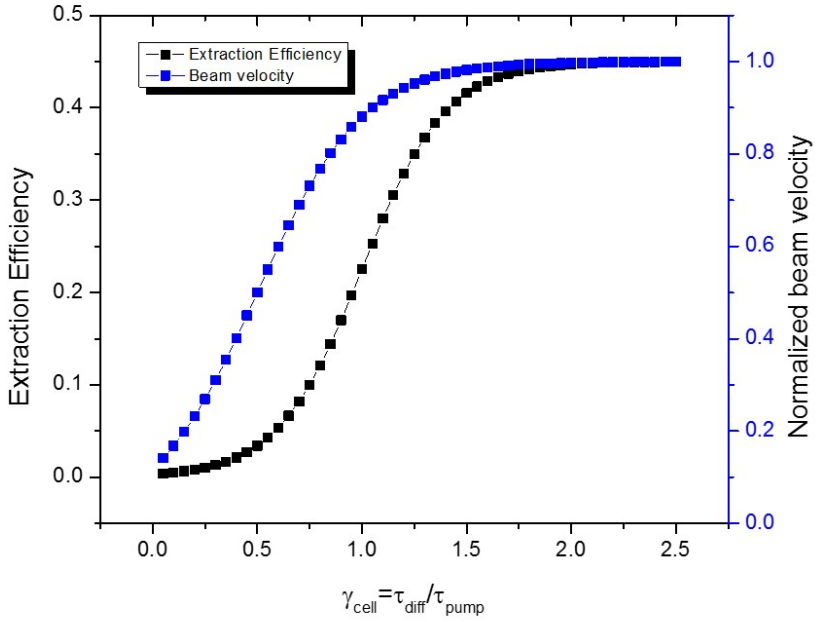

Figure 2-14: Simulated extraction efficiency and beam velocity vs. γ_{cell}.

is plotted in Figure 2-14. The maximum extraction efficiency can be as high as 40%. In typical experiments, this efficiency is usually around 10%.

2.2.3 Design of the buffer gas cooling chamber

Based on my understanding of gas dynamics, introduction of species, thermalization, diffusion, and extraction as discussed above, I have designed and constructed a Neon buffer gas cooling source to form a slow, high density, and cold molecular beam. In addition to the scientific considerations, the chamber is designed based on several other practical principles: (1) If possible, using stainless steel instead of aluminum, because of its strength and resistance to oxidization. (2) Using less welding, but more flat rubber O-ring sealed flanges, because of cost and flexibility. (3) Leaving extra ports, especially on the detection chamber, for future upgrades. (4) Leaving more tapped holes inside the chamber for mounting optics inside. (5) Hanging the chamber instead of placing it on the table, so that I have an additional access from the bottom. Figure 2-15 is the 3D design picture of the buffer gas cooling chamber,

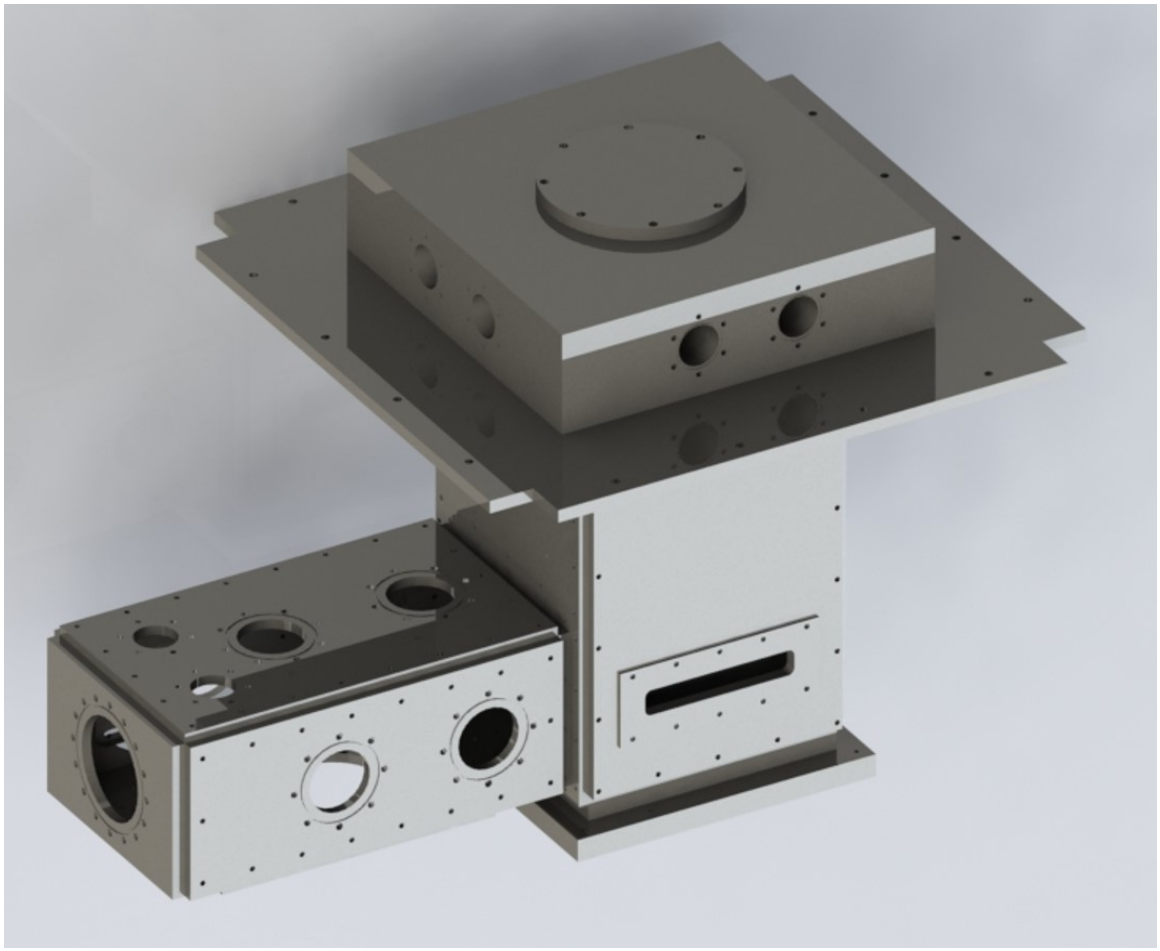

Figure 2-15: The 3D design picture of the buffer gas cooled molecular beam setup made, with Solidworks 2012.

made with Solidworks 2012. Figure 2-16 is a picture of the open source chamber. Figure 2-17 is a schematic diagram of the entire chamber from the top view. The detailed blueprints are in Appendix B. In this section, I have insufficient space to list all features of the design, but I describe the important ones, as following:

Cryomech pulsed tube refrigerator

To cool the cold plate to 4 K, I have two options: (1) liquid Helium; (2) a pulsed tube refrigerator. The setup for a liquid Helium cooling experiment is relatively simple. However, transferring the liquid Helium to a heat isolated reservoir and recycling the evaporated Helium gas are nontrivial and require a lot of routine student time to manage. In addition, the price of liquid Helium is currently increasing rapidly. The

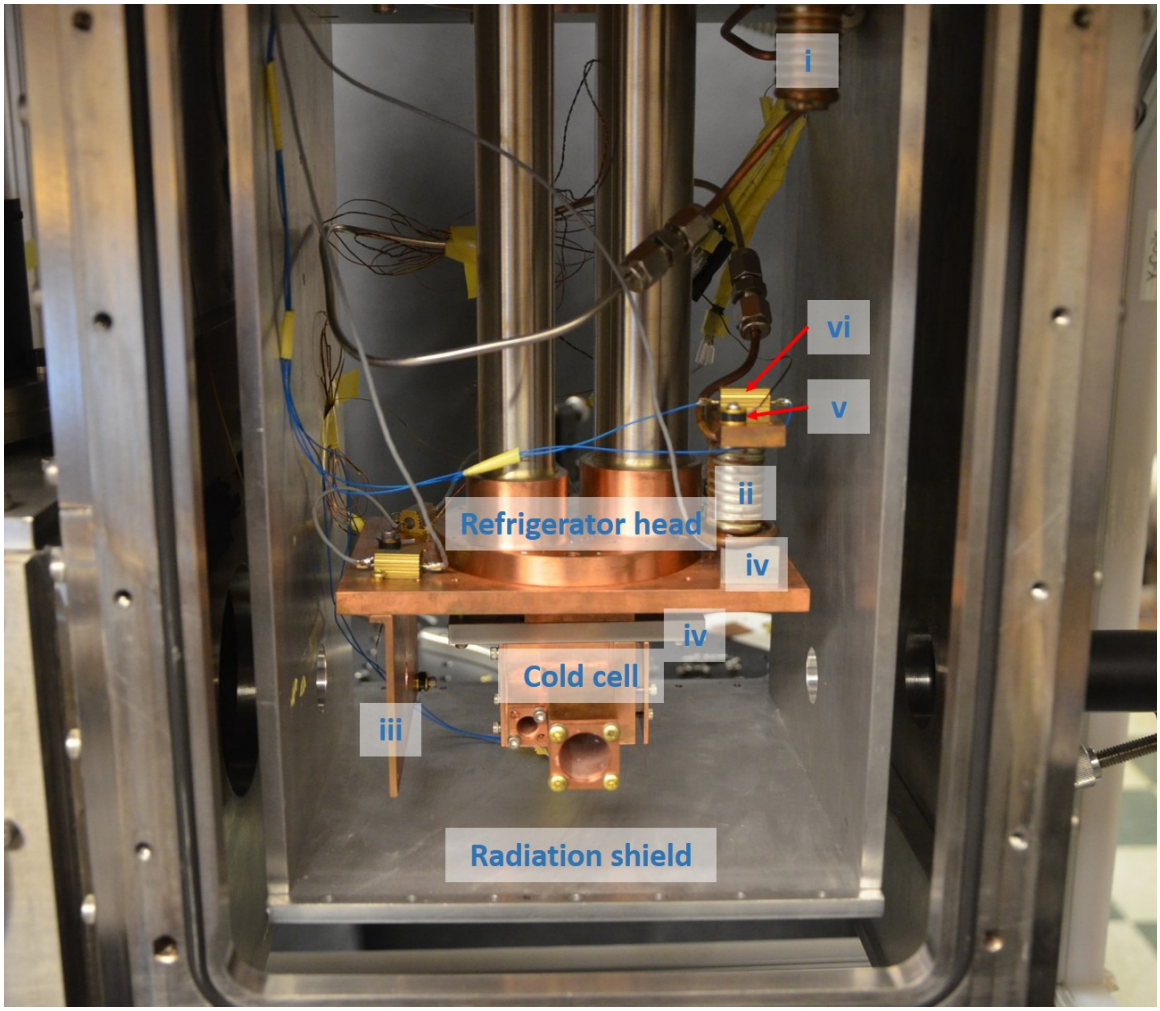

Figure 2-16: Inside photograph of the source chamber. The aluminum radiation shield is mounted on the first stage of the refrigerator, and the 4 K cold plate is mounted on the second stage. There are two stages of the gas cooling spiral units. One (i) is mounted on the radiation stage, and the other (ii) is mounted on the cold plate through a stainless steel adapter (iv). The cooling unit (ii) is heated by a resistive heater (vi), and its temperature is measured by a diode sensor (v). In typical experiments, the gas cooling unit (i) operates at 40 K and the gas cooling unit (ii) at 20 K. To minimize heat conduction, the gas tube between them is made of stainless steel which has poor heat conductance. The cold cell is mounted on the cold plate through a stainless steel adapter (iv). The heater and diode temperature sensor are mounted on the bottom surface of the cold cell, which are not visible in this photograph. (iii) is a flat cold plate, which has a 1 cm diameter hole at its center.

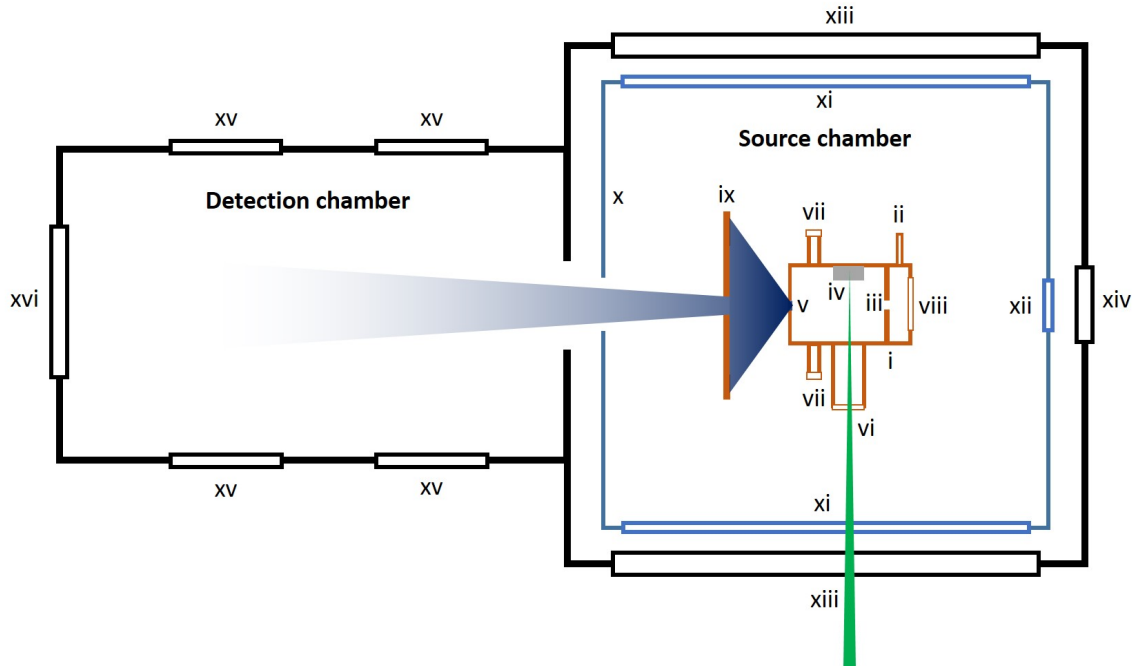

Figure 2-17: Schematic diagram of the buffer gas cooling chamber, top view. (i) The 20 K copper cold cell. (ii) Neon gas filling inlet of the 20 K buffer chamber of the cold cell. The ID=1/16" copper tube is soldered on the cold cell. (iii) Neon gas filling inlet to the main 20 K cold cell. The diameter of the inlet is 1/8". (iv) Round metal or salt precursor pellet with 0.7" diameter, such as BaF_2, CaF_2, Calcium or Barium. (v) Output aperture of the 20 K cold cell. The diameter and thickness of the aperture are 0.12" and 0.01", respectively. (vi) 0.8" diameter window for the ablation laser. It is hard Fused Silica with a high damage threshold, no AR coating. (vii) 0.4" diameter BK7 window for laser absorption and LIF experiments inside the cell. (viii) 1" diameter BK7 window for cell alignment laser and for transmitting fluorescence from inside the cell. (ix) Cold skimmer at 4 K with a 0.4" diameter hole at the center. (x) Aluminum radiation shield cooled by the first stage of the refrigerator at ~40 K. (xi) 0.7" × 6" × 1/8" customized rectangular quartz window mounted on the radiation shield. (xii) 1.6" diameter BK7 window for the alignment laser and for transmitting fluorescence, mounted on the radiation shield. (xiii) 1.8" × 7" × 1/2" customized rectangular fused silica window mounted on the side plate of the source chamber. (xiv) Window for the alignment laser and for transmitting fluorescence. (xv) 4.5" CF flange on the side plate of the detection chamber. (xvi) A 6" CF flange on the end of the detection chamber.

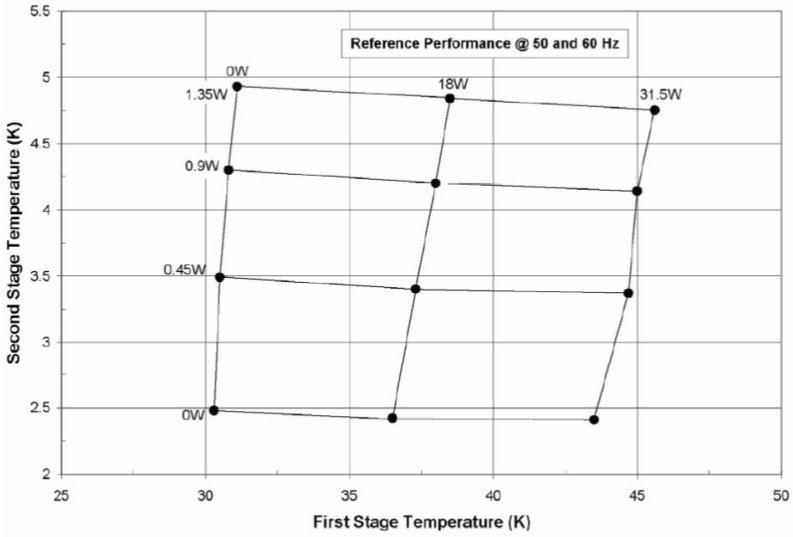

Figure 2-18: PT410-RM Cryorefrigerator Capacity Curve. The x axis and y axis represent the relationship between heating loads and temperatures of the first stage and second stage, respectively.[6]

time and expense are not practical for long-term use of liquid Helium. A pulsed tube refrigerator is a more advanced apparatus that uses a high power compressor and hundreds of capillaries to perform reversed Carnot cycles periodically with Helium gas. Due to the high compression ratio of the small capillaries and large gas reservoir, the lowest temperature of the new state of art refrigerator, PT410RM, is 2.8 K and its cooling capacitance is $\sim$1 W at 4 K, as shown in Figure 2-18. In addition, the compressor and reservoir of the PT410RM are not mounted on the cold head directly, but through a long flexible tube, which damps the vibration significantly. The operation of the pulsed tube refrigerator is quite easy. The $\sim$ 1.5 hour cool-down process does not require any human involvement. There is almost no daily maintenance required. Helium gas filling needs to be performed only once every year.

There are two minor issues of the PT410RM refrigerator that demand attention: (1) The cooling capacity is relatively low. To achieve fast cooling, the cold unit should be designed to be as small as possible. To obtain a temperature below 4 K, I need to minimize all unnecessary heat transfer processes (contact heat transfer or blackbody radiation). (2) The power consumption of the compressor for 1 W cooling capacity is 8.9 kW. Most of the electric power is converted to heat dissipation in the

power supply. I need low temperature (<20 °C) and large flow rate (2.3 Gallon per minute) of cooling water to carry away the excess heat. In addition, to make the compressor work stably and have a long lifetime, it is important for using clean and temperature stabilized cooling water. The lab chilled water is not qualified and the internal loop chiller usually does not have enough cooling capacity. My solution is to use a small chiller to directly cool the Cryomech compressor. However, before the hot water returns back to the chiller, it goes through a multi-plate heat exchanger that is cooled by the lab chilled water and carries away 95% of the heat. Thus, the cooling water in the compressor is always clean. The flow rate and temperature is controlled and stabilized by the chiller.

Vacuum pumps

Due to the high flow rate of continuous buffer gas input, a large vacuum pump is required to keep the pressure in the chamber low enough for the molecular beam experiment. The acceptable background gas pressure is no more than 30 μtorr at room temperature, in which the mean free path of the molecules is larger than 0.5 m. Thus, the molecular beam is not significantly attenuated during its transportation to the detection chamber. If the input flow rate is 10 SCCM, the minimum required pumping speed is 4000 L/s, which is calculated by:

$$S = \frac{Q}{p}, \tag{2.38}$$

where S is the pumping speed, Q is the input flow rate, and p is background gas pressure in the chamber. A conventional diffusion pump or turbo pump with 4000 L/s is very large and expensive. However, a cryogenic pump with similar pumping speed is relatively small and cheap. Even better, I do not need an external cryogenic pump. I can mount several 4 K cold plates around the molecular beam formation region. This is equivalent to locally implementing a large cryogenic pump. The

pumping speed of the cold surface for Neon buffer gas is:

$$S = cA\sqrt{\frac{k_B T}{2\pi m}}, \tag{2.39}$$

where c is the capture coefficient, which describes the probability of capturing a gas molecule with a single collision with the cold surface. The capture coefficient of Neon buffer gas on a 4 K cold surface is ∼1. A is the total area of the 4 K cold surface, k_B is the Boltzmann constant, m is the mass of the pumping gas, and T is the gas temperature, which is always referenced to room temperature to evaluate the pumping speed. In our apparatus, there is ∼500 cm^2 cold surface. Thus, the effective cryogenic pumping speed is ∼7000 L/s, which is sufficient to keep the pressure in the vacuum chamber below 30 μtorr. In addition to the cryogenic pump, I set up a 150 L/s turbo pump, which is used to pump the chamber, when the cryogenic pumping is not running. I always leave the small turbo pump on along with the cryogenic pump. However, after the cold head is cooled to 4 K, turning off the small turbo pump does not cause an increase in the background pressure in the chamber any more.

Cold cell

The cold cell is the central part of the buffer gas cooled molecular beam source, as shown in Figure 2-19. It is made of copper for good heat conductance. The internal diameter of the cell is 1.2", which is large enough to cool the hot plasma particles to the buffer gas equilibrium temperature before they hit the cell wall. The distance between the ablation spot and the output aperture is ∼ 1.2", which is sufficiently short to extract more than 10% of the target molecules out of the cell. There is another buffer cell connected at the backside of the main cell. The buffer gas is input to the buffer cell first, then turns 90 degrees and flows into the main cell. Such a design can reserves optical access through the back of the cell, which is useful for laser alignment of the cell or collecting fluorescence emission from inside the cell. The gas flow rates in all experiments are always far below the threshold of forming significant turbulence. Therefore, such a turn in the gas flow does not alter the gas dynamics

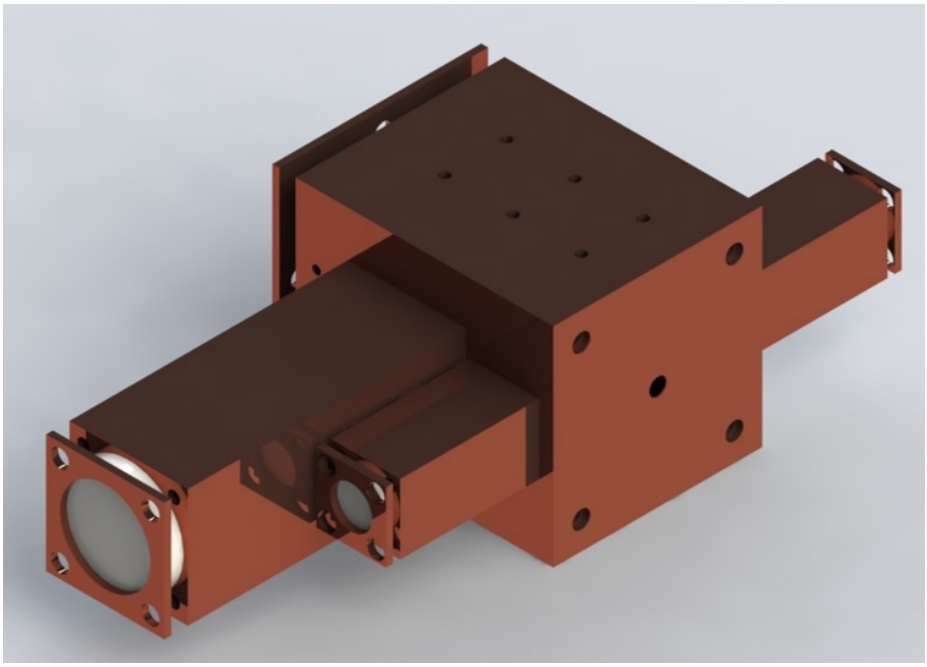

Figure 2-19: The 3D design picture of the cold cell, made with Solidworks 2012.

from laminar flow in the cell. The diameter of the output aperture is 3 mm, which is balanced by the extraction efficiency and molecular beam temperature.

Two optically accessible ports are mounted on the side of the cell. The larger one, with 0.65" diameter is for transmitting the ablation laser beam. Because the ablation laser needs to be spatially scanned to cover the maximum surface area of the pellet, the window should be large enough not to restrict access of the ablation laser beam. The two smaller optical ports, with 0.3" diameter, are for the excitation pulsed laser for LIF experiments or cw diode laser for absorption experiments. All ports extend far from the cell body with L=3d (L is the distance between the window and the cell, d is the diameter of the port). This design is to prevent the dust created in the cell from contaminating the window, especially the ablation laser window. The top of the cell is mounted on a stainless steel adapter, which is attached to the cold head of the refrigerator. The temperature sensor and the heater are mounted on the bottom of the cell.

Radiation shield

Based on the Stefan-Boltzmann law (Eq.(2.40)), the room temperature blackbody radiation is ∼500 mW/cm^{-2}, and ∼10% of the total power incident on the cell is absorbed by the 4 K cold surface (cold cell, cold plate, refrigerator head etc.) made of copper.

$$J = \sigma T^4 \tag{2.40}$$

where J is the total power radiated per unit area, T is the absolute temperature, and $\sigma = 5.67 \times 10^{-8}$ W m^{-2} K^{-4} is the Stefan-Boltzmann constant. The 4 K cold surface with ∼100 cm^2 area absorbs ∼5 W blackbody radiation power. Such high radiation power cannot be efficiently pumped by the second stage of the pulsed tube refrigerator. To decrease the blackbody radiation incident on the second stage of the refrigerator, it is necessary to surround the 4 K cold surface with a cool surface, the temperature of which is much lower than room temperature. I build an aluminum box, which is cooled by the first stage of the PT410 refrigerator, to surround the 4 K cold surface. The room temperature blackbody radiation is reflected and absorbed by the radiation shield. The heat dissipating power on the radiation shield is typically less than 15 W. The first stage of the refrigerator has enough capacity to pump such energy and maintain the radiation shield at ∼ 35 K. Due to the strong temperature dependence in Eq.(2.40), the blackbody radiation absorbed by the 4 K cold plate is decreased by a factor of 5000 and can be neglected. I choose aluminum, but not copper, to build the radiation shield, because it is light and relatively easily polished. A seriously oxidized surface on the radiation shield would increase the absorption of the blackbody radiation significantly, which increases the temperature of the radiation shield. Therefore, I must polish the surface of the radiation shield every few months, or cover the outside of the radiation shield with several layers of thin aluminum-coated Mylar super-insulation.

In addition to a ∼40 K radiation shield, the Doyle group also suggests building a 4 K radiation shield to further block radiation heating of the cold cell. The temperature in their Helium buffer gas cooling experiment must be as low as possible. In addition,

the 4 K radiation shield can also improve the performance of the cryogenic pump for Helium buffer gas. However, in our current Neon buffer gas cooling experiment, the required temperature is less than 8 K instead of less than 4 K. Therefore, we do not implement the second stage radiation shield, which should be added if we need to perform Helium buffer gas cooling experiments.

Temperature measurement and control

The cryogenic temperature measurement and control system are commercially available, but relatively expensive. I have decided to build our own system. In our system, I have two thermocouple sensors to measure the temperatures of the top and the bottom of the radiation shield, and four diode sensors to measure the temperatures of the components mounted on the second stage of the refrigerator (4 K cold head, 20 K cold cell, 20 K gas tube and 4 K cold skimmer). In principle, I can extend our current system up to 30 sensors without significantly increasing the cost. In addition to the low cost, using a Labview control program written by myself, I build a feedback loop to stabilize the temperature easily, and a more subtle automatic control program can be implemented in a few minutes.

There are two types of temperature sensors in our setup: (1) thermocouple sensor; (2) diode sensor. The Type K thermocouple sensor is very cheap and usually used for temperatures above 70 K. Below 70 K, the temperature response slope is very small, which decreases the measurement accuracy. With a high gain and low noise amplifier (AD 595), it is possible to measure the temperature to 1 K accuracy at T = 40 K, which is acceptable in my experiment. The AD 595 amplifiers used on my setup have been calibrated with liquid Nitrogen. The diode sensor is more expensive but has a large temperature response slope below 10 K. In addition, it is an active component driven by an external constant current source. The voltage across the diode is typically mV instead of μV of the thermocouple sensor, which can be read out directly by a voltage meter without an amplifier. In our experiment, I use a 10 μA, 8 V current source to drive four diodes in series, and use National Instrument DAQ card (NI 6031E) to read the voltage difference across the diode, which can be

converted to the temperature with a calibration curve. One diode is factory calibrated at 10 K to 20 mK accuracy. The other three are calibrated by myself to the calibrated one with a similar accuracy.

In the Neon buffer gas experiment, the cold gas tube and cold cell do not run at 4 K, but 20 K instead. First, I insert poor heat conductance materials, such as stainless steel, between the 20 K units and the 4 K cold head. Second, I attach small resistive heaters onto the 20 K units to maintain their temperatures around 20 K. To control the power of the heaters, I need an adjustable power supply with a programmable control, which can receive feedback from the real-time measured temperatures of the 20 K units. Figure 2-20 shows a schematic diagram of a home-built automatic temperature control system. The temperature reading and heating control both come from a computer based National Instrument DAQ card (NI 6031E). The adjustable power supply is home-built by a regular 10 V power supply and LM350 voltage regulator. The feedback is programmed in Labview with PID control. With optimized PID parameters, the temperature variations of the 20 K units are smaller than 0.05 K, as shown in Figure 2-21.

Laser ablation

In my buffer gas cooling experiment, the target molecules are introduced by laser ablating a solid pellet in the cold cell. Preparation of pellets and optimization of the ablation laser to maximize the yield of the target molecules are much more complicated than my expectation. The performance of a well optimized experiment can be more than 1000 times better than an unoptimized experiment. Due to its importance, I discuss these details separately in Section 2.4.

Beam collimation

Generally speaking, the requirements for collimation of the buffer gas cooled beam are less strict than the requirements for the supersonic beam, because the expansion is gentle, and reflections from the wall of the vacuum chamber is less destructive than in the supersonic beam. Therefore, in typical experiments, instead of using a

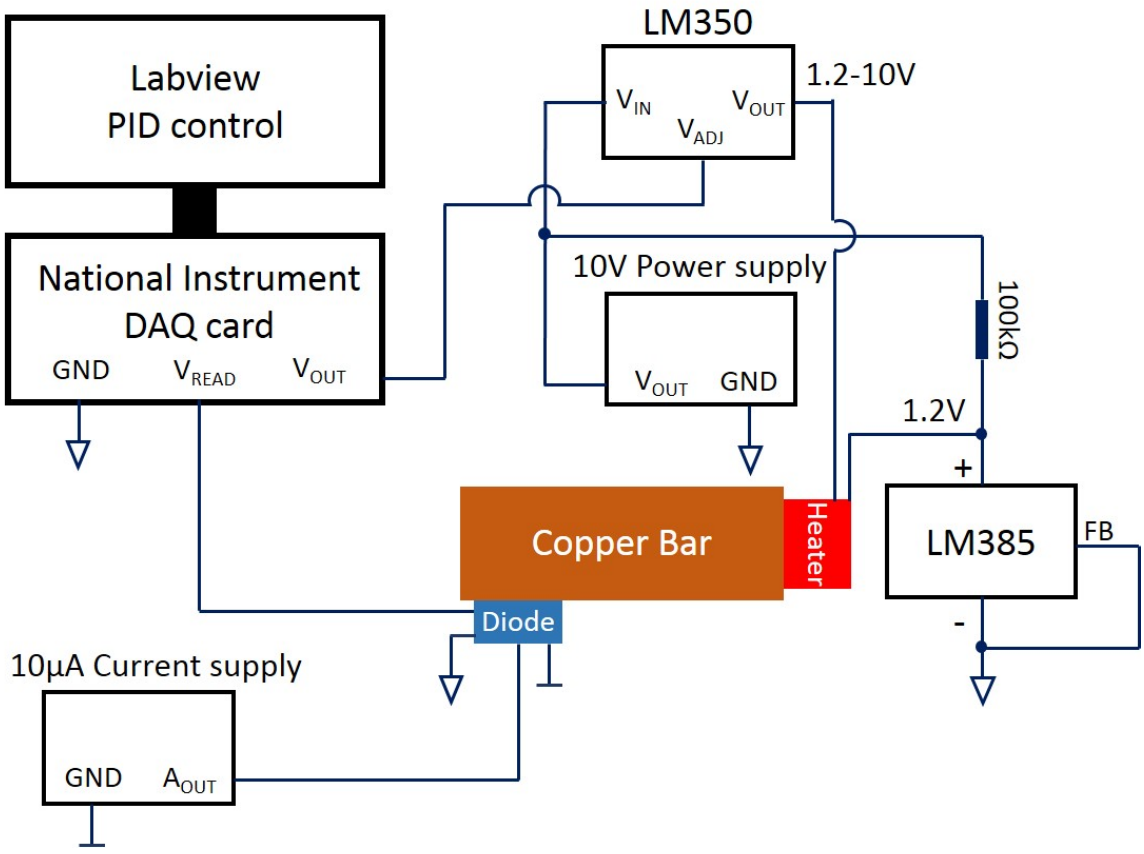

Figure 2-20: Schematic diagram of the temperature control system. The 10 μA current supply is used to drive the diode sensor. To decrease interference, the GND of the constant current supply is isolated. National Instrument DAQ card is used to read the voltage on the diode sensors and generate control voltage to control the power of the heater via LM350. LM385 is used to shift the output of LM350 by 1.2 V. Thus, the voltage on the heater is from 0 to 8.8 V. The PID control is implemented by the Labview program on the computer.

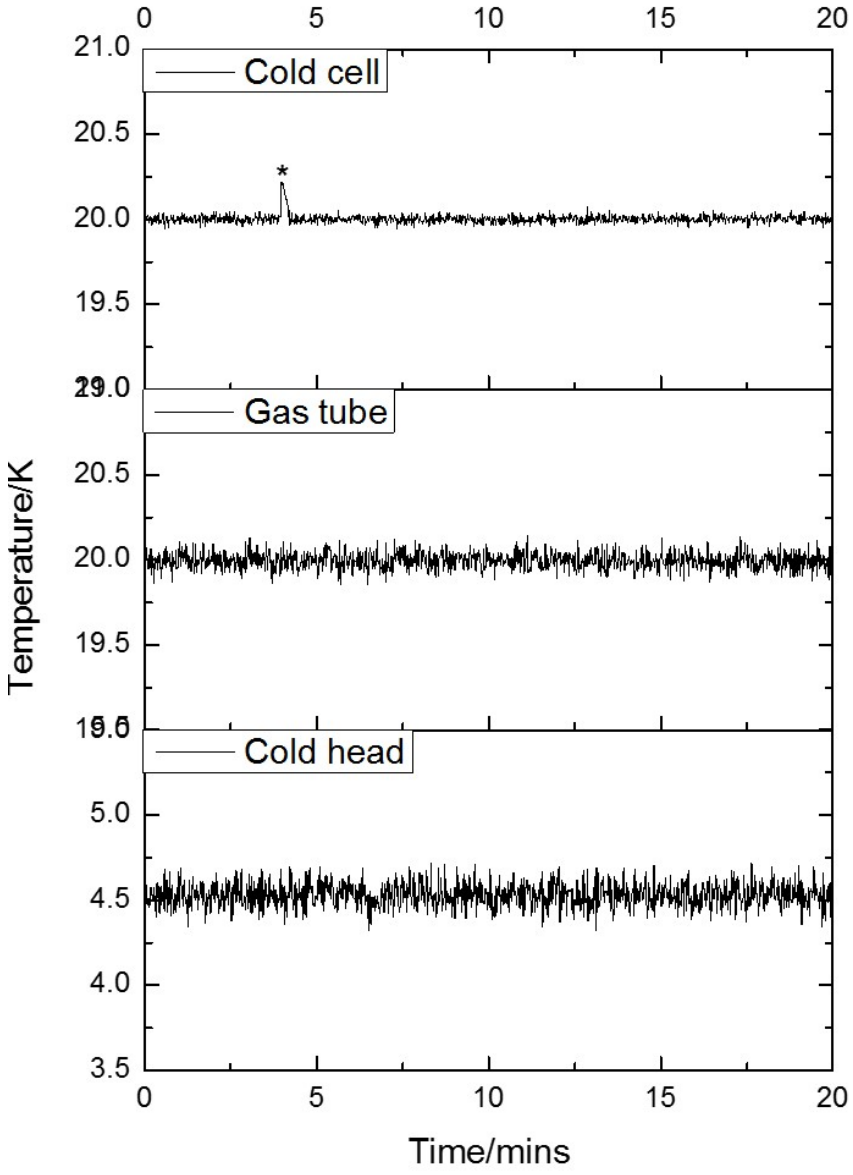

Figure 2-21: The stability of the temperatures with PID control. With the temperature control system, the temperatures of the cold cell, gas tube and cold head can be stabilized with 0.03 K, 0.05 K, 0.08 K short-term fluctuations and no long-term fluctuations. When the ablation laser is fired, there is a temperature jump (*) of the cold cell. The PID control can damp this heat impulse by adjusting the heating power for a few seconds.

conical skimmer, a plate with a hole is adequate to extract the center of the beam without destroying the beam. However, due to the continuous buffer gas flow, the local pressure just in front of the output aperture can be very high, and the pressure distribution in the vacuum chamber can be very inhomogeneous. A gas dynamics simulation shows that without any local cryogenic pumping (the nearest cryogenic pump is placed 10 cm away), the pressure at 1 cm away from the output aperture with 10 SCCM flow rate is ∼1 mtorr, which is three orders of magnitude higher than the average pressure in the source chamber ($\sim 1 \times 10^{-6}$ mtorr). Therefore, I need to add a local cryogenic pump in front of the output aperture to pump the large divergent buffer gas beam, while allow the center of the beam to pass through.

There are two usual ways to implement such a local cryogenic pump: (1) We can place a 4 K copper plate with a 1 cm diameter hole (called "cold skimmer") ∼5 cm away from the output aperture. In principle, most of the Neon gas is frozen on the surface of the cold skimmer and the effective pressure between the cold skimmer and output aperture should decrease significantly. However, the major disadvantage of this method is not all Neon gas will be captured with one collision on the cold skimmer (Helium gas would be worse). The pumping speed might not be as high as we expect. In addition, when a large amount of Neon gas is frozen on the surface (With 10 SCCM flow rate, there is ∼0.5 cm^3/hour Neon ice generated on the cold skimmer), the cryogenic pumping of the cold skimmer might be very unstable. (2) We can place a cool (∼40 K) conical skimmer with 5 mm diameter 3 cm away from the output aperture. The skimmer is not cold enough to cryogenically pump the Neon buffer gas, but can reflect the buffer gas with a large angle, preventing interference with the beam. The reflected gas can be cryogenically pumped by other cold plates that are mounted around the cold cell. There is no small-angle backward reflection with a conical skimmer. In addition, there is no ice on the skimmer and this setup can continuously run for a longer time. I have not performed a series of systematic experiments to compare these two methods carefully, and I know there is serious debate in the Doyle group and in our group. Based on my current experience, I prefer to use method (2) over method (1).

Table 2.4: Helmohltz coils

	x-coils	y-coils	z-coils
Current (A)	1.1	1.1	0.6
No. of Windings	30	30	150
Dimensions (inch)	24 × 24 × 42	24 × 24 × 42	24 × 24 × 42
x-nonflatness (%)	1	1	1
y-nonflatness (%)	<0.1	<0.1	<0.1
z-nonflatness (%)	<0.1	<0.1	<0.1

Helmholtz coils

I show in Section 3.3 that the highest resolution of the CPmmW spectrometer (∼100 GHz) combined with the designed buffer gas cooled molecular beam (hydrodynamic Neon buffer gas) is 50 kHz, which is limited by the room temperature blackbody radiation in the detection chamber. All other field-matter interactions, which can induce line shifts or broadening, should be minimized. Earth's magnetic field (∼0.5 Gauss) can cause $E_{Zeeman} = 2\ \mu_B\ \mathrm{B} m_j g_j$ ∼1.4 MHz splittings, which is much larger than our spectrometer resolution. Such stray magnetic field can be shielded or compensated carefully by μ metal or Helmholtz coils.

For considerations of guiding lasers, microwave, and molecular beams to the detection volume, I prefer to use three large rectangular pairs of Helmholtz coils that are placed around the entire vacuum setup. The dimensions and shape of the Helmholtz coils are based on several considerations: (1) Convenience for mounting on the T-slotting frame which supports the vacuum chamber. (2) Large enough to guarantee relatively homogeneous magnetic field in the detection volume (∼ 100 cm^3). (3) Coils with relatively low current (∼1 A) and few windings (<100) can completely compensate the earth's magnetic field in all directions. Table 2.4 lists the key parameters of the Helmholtz coils (details are in Appendix A). The compensated magnetic field has a parabolic spatial distribution. In the interaction volume, the upper limit of the field inhomogeneity is along the long axis of the detection volume (10 cm length). 1% non-flatness compensated magnetic field only causes <14 kHz line broadening, which is smaller than our spectrometer resolution and can be ignored.

The magnetic field generated by the Helmholtz coils can be fine tuned by tweaking

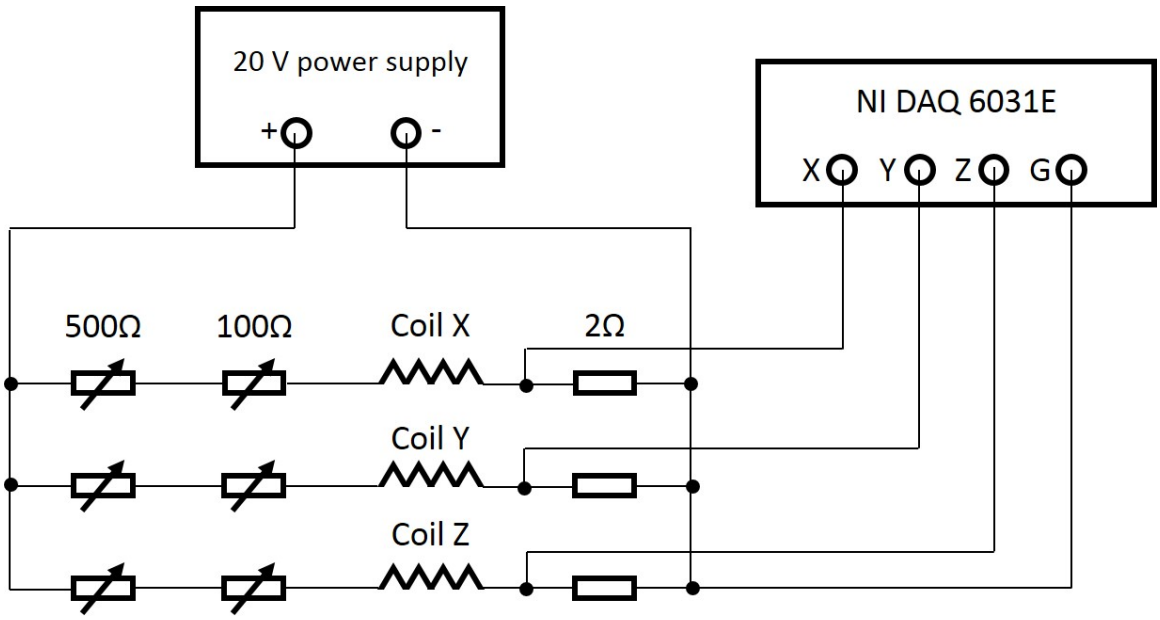

Figure 2-22: Control system for the Helmholtz coils. 2 Ω fixed resistor is for current readout, 500 Ω variable resistors are for rough tuning, and 100 Ω variable resistors are for fine tuning.

variable resistors, as shown in Figure 2-22. The current can be read out by National Instrument DAQ card (NI 6031E) and converted to the value of the magnetic field by a calibration curve.

2.2.4 Performance of the buffer gas cooling technique

Before transitting the CPmmW spectrometer from the supersonic beam system to the buffer gas cooling system, it is important to test the performance of the new apparatus. Most tests in this thesis employ LIF, which is well suited for measuring the number density and the rotational temperature of the target molecules. The diagram of the measurement system is shown in Figure 2-23. However, our pulsed dye laser resolution is not sufficient to measure the beam velocity precisely. The beam velocity information is obtained by the CPmmW experiment described in Section 3.3.1. My preliminary measurements show that the performance of our new apparatus is consistent with my expectations. David Grimes is currently working on using high resolution absorption spectroscopy with a cw diode laser to measure the performance more precisely.

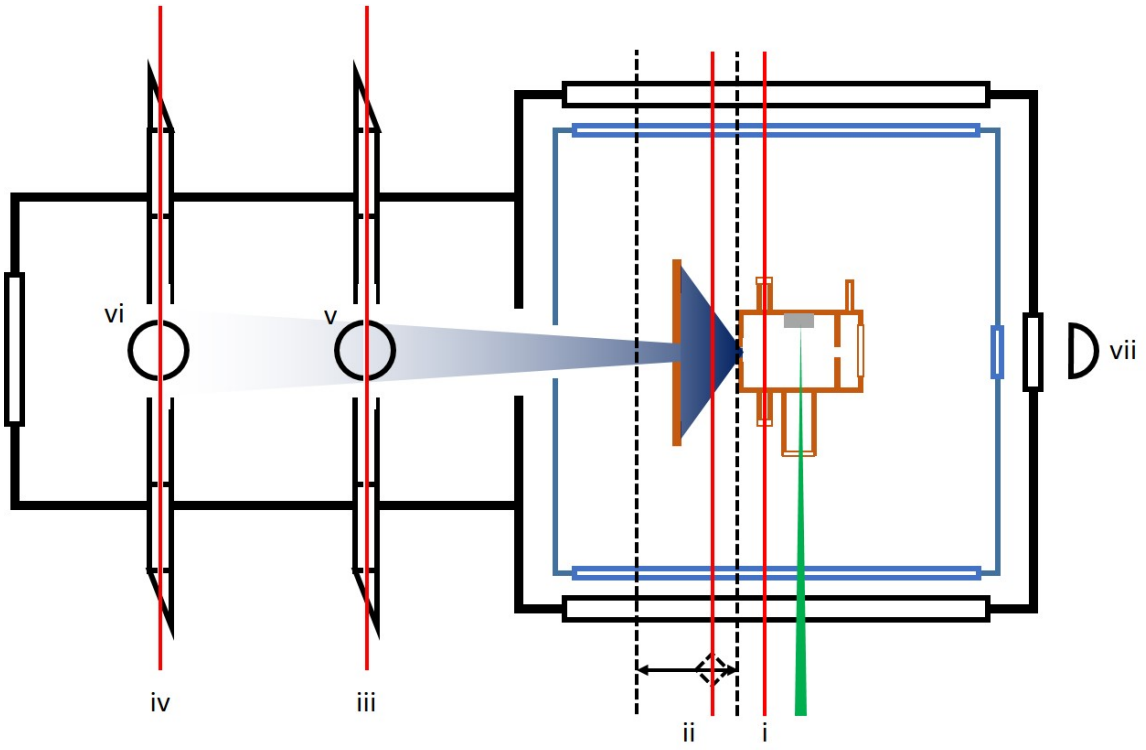

Figure 2-23: Diagram of LIF diagnostic experiments in the buffer gas cooled molecular beam system. (i) is the excitation Laser beam inside the cold cell. (ii) is the excitation Laser beam outside the cold cell. The laser beam can be translated from 1 cm to 8 cm downstream from the output aperture in the source chamber. (iii) is the excitation laser beam 20 cm downstream from the output aperture in the detection chamber. (iv) is the excitation laser beam 40 cm downstream from the output aperture in the detection chamber. (iii) and (iv) lasers go through a baffle to reduce scattered light. (v) and (vi) are PMTs that collect the fluorescence excited by (iii) and (iv) respectively. (vii) is a PMT that collects the fluorescence excited by (i) or (ii).

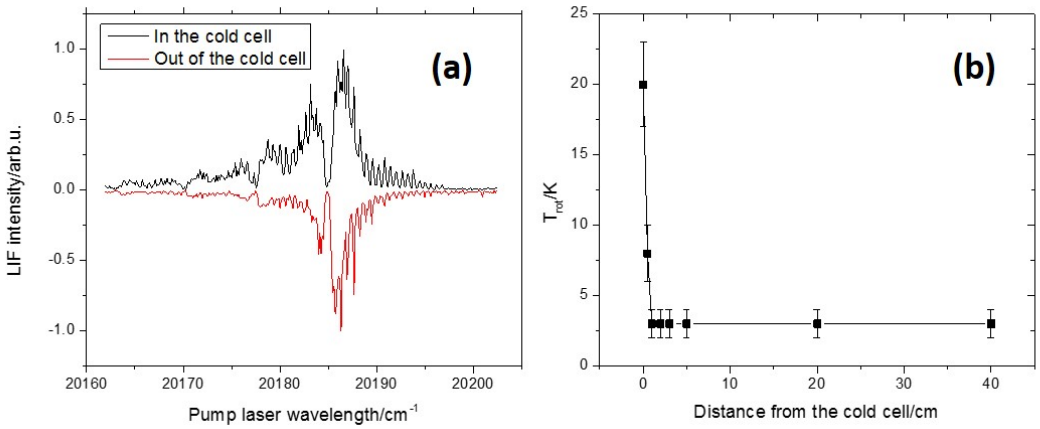

Figure 2-24: Rotational temperature measurement of the BaF molecules in the buffer gas cooled beam. Plot (a) shows the comparison of the LIF spectrum of 20 K BaF in the cold cell and 5 K BaF outside of the cold cell. Plot (b) shows the distance dependence of the rotational temperature.

Rotational temperature

The rotational temperature is sampled by a low resolution LIF spectrum, as shown in Figure 2-24, Plot (a). I fit the measured spectrum to the simulated spectrum, generated by Pgopher, to obtain the rotational temperature [98]. Figure 2-24, Plot (b) shows the rotational temperature of BaF molecules decreases rapidly via the hydrodynamic expansion, from 20 K to 3 K. This cooling process is completed ∼1 cm away from the output aperture, which is consistent with my expectation in Section 2.2.1.

Number density

The number density is measured by:

$$N = \frac{2S\tau}{50eG\eta_P\eta_S\eta_Y\eta_P} \tag{2.41a}$$

$$n = N/V, \tag{2.41b}$$

where N is the total number of the target molecules in the excitation region, V is the volume of the excitation region, n is the number density of the target molecules, S

Table 2.5: Typical values of the number densities of different species in the detection chamber for CPmmW experiments.

	Number density/cm^{-3}	Number density/states/cm^{-3}
Calcium	1×10^{10}	1×10^{10}
Barium	3×10^{9}	3×10^{9}
CaF	1×10^{8}	3×10^{7}
BaF	3×10^{8}	3×10^{7}
HfF	3×10^{7}	3×10^{6}

is the voltage amplitude on the oscilloscope, τ is the fluorescence lifetime, e is the charge of the electron, G is the gain of the PMT, η_P is the PMT detection efficiency, η_S is the detection solid angle, η_Y is the fluorescence quantum yield, and η_P is the rotational partition function. A factor of 2 in the numerator comes from the ratio of the total number of molecules to the number of excited molecules at saturated excitation, and a value of 50 in the denominator is the input impedance(Ω) of the oscilloscope. For example, in a typical BaF LIF experiment at 20 cm downstream from the output aperture in the detection chamber, S=200 mV, τ_{BaF}=20 ns, G=5×10^5, η_P=0.1, η_S=0.1, η_Y=1, η_Y=0.2, V=0.1 cm $\times$ 0.1 cm $\times$ 1 cm, and the measured number density is 3×10^8 cm^{-3}, which is three orders of magnitude larger than the number density in the supersonic beam. Table 2.5 lists typical values of the number densities of different species in the detection chamber for CPmmW experiments.

Figure 2-25, Plot (a) shows a shows a typical high resolution spectrum of BaF C-X transition using an intra-cavity etalon in the dye laser. The P, Q, and R branches are resolved. To measure the number density, I fix the laser wavelength on a single transition, which has a calculable lower state partition function with measured rotational temperature. Figure 2-25, Plot (b) shows the distance dependence of the number density in the buffer gas cooled beam. The measured data at different positions is consistent with the R^2-dependence, which means that our beam is not attenuated during propagation.

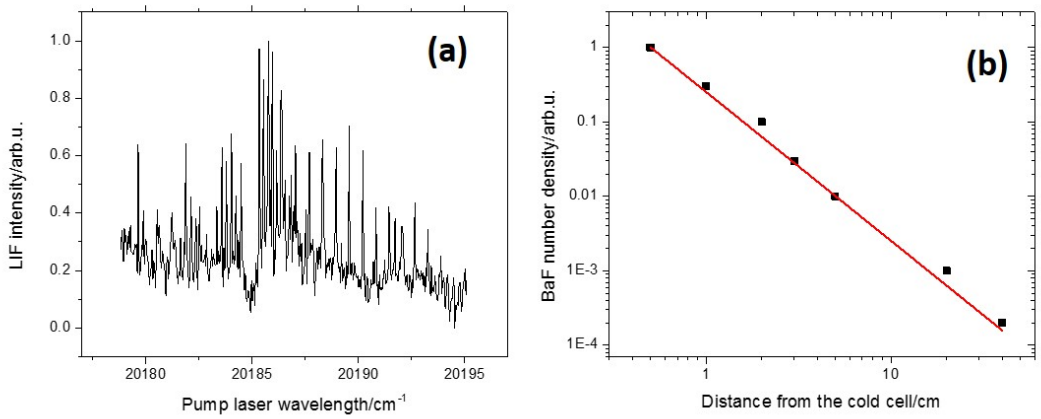

Figure 2-25: Plot (a) shows a typical high resolution LIF spectrum of the BaF C-X transition obtained using an intra-cavity etalon in the dye laser. Plot (b) shows the distance dependence of the number density in the buffer gas cooled beam. The red line represents the R^2-dependence.

Beam velocity

As mentioned in Section 2.2.1, the beam velocity-induced Doppler shift/broadening of ∼100 MHz cannot be measured precisely using a pulsed dye laser with 1 GHz linewidth. In Section 3.3.1, by measuring the Doppler shift/broadening with CP-mmW Rydberg spectroscopy, I find the forward velocity of the beam is 200 m/s. Measuring the Doppler broadening is more difficult with CPmmW Rydberg spectroscopy, because the blackbody radiation always induces larger frequency broadening than the Doppler broadening. To completely characterize the dynamics of the molecular beam, I still need to perform high resolution absorption spectroscopy.

Stability

Compared to the supersonic beam, the buffer gas cooled beam not only has much higher number density and lower forward velocity, but also has superior shot-to-shot stability. Figure 2-26 shows a comparison between the two beam sources obtained by recording LIF signals with a fixed excitation wavelength. I observe that the buffer gas cooled beam has a much smaller signal fluctuation (∼20%). Part of the fluctuations in Figure 2-26 might come from the excitation laser intensity fluctuation and mode-

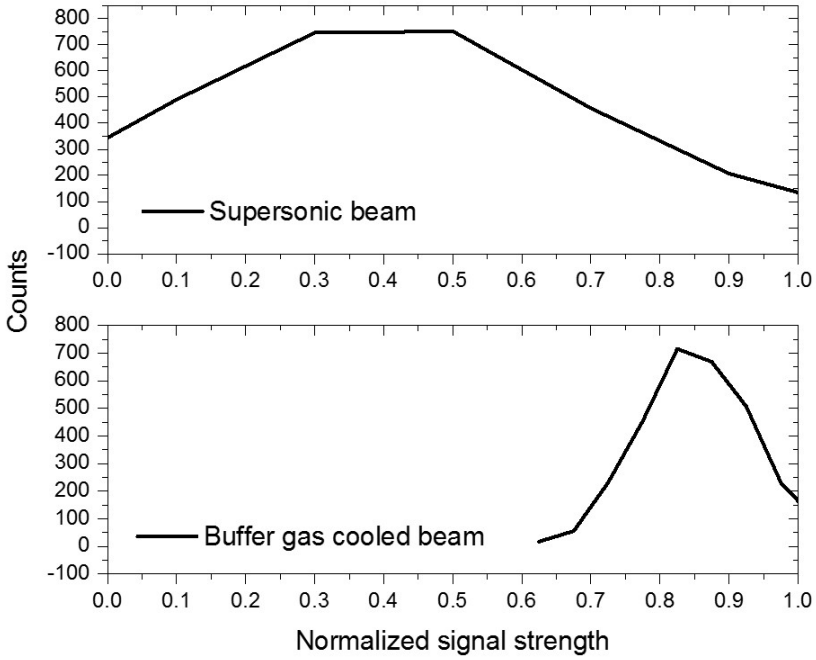

Figure 2-26: Comparison of the shot-to-shot stability in the supersonic beam and in the buffer gas beam. We take 3000 shots with fixed laser power and frequency to make the histogram. The width of the LIF signal distribution in the supersonic beam is >50%, while that in the buffer gas cooled beam is <20%.

hopping induced frequency jitter. Therefore, the actual fluctuation of the buffer gas cooled beam source might be as small as ∼10%. A more reliable stability test should come from the high resolution absorption spectrum.

2.2.5 Comparisons of the effusive beam, the supersonic beam and the buffer gas cooled beam

I briefly summarize the most important parameters of the effusive beam, the supersonic beam, and the buffer gas cooled beam in Table 2.6. The number density is evaluated at a position 20 cm away from the beam source. Translational temperature, shot-to-shot stability, and Doppler broadening should be remeasured by high resolution absorption spectroscopy. However, the improvement in the buffer gas cooled beam over the supersonic beam is clear and satisfactory.

Table 2.6: Comparisons of the effusive beam, the supersonic beam, and the buffer gas cooled beam.

	Effusive Oven	Supersonic jet	Buffer Gas
Beam Velocity	200-800 m/s	500-2000 m/s	150-200 m/s
Translational Temperature	500-2000 K	1-5 K	1-5 K
Rotational Temperature	500-2000 K	1-5 K	1-5 K
Particles/Pulse	CW	$\sim 10^{10}$	$> 10^{12}$
Number Density (cm^{-3})	$\sim 10^6$	$\sim 10^5$	$> 10^8$
Number Density/State (cm^{-3})	$\sim 10^3$	$\sim 10^4$	$\sim 10^7$
Shot-to-Shot Stability	$\sim 95\%$	$\sim 50\%$	$\sim 90\%$
Transient broadening	50 kHz	100 kHz	20 kHz
Doppler broadening	200 kHz	200 kHz	20 kHz

2.3 CPmmW spectrometer

Millimeter wave spectroscopy is a powerful tool for performing high precision measurements of atoms and molecules in the gas phase. Compared to laser spectroscopy, millimeter wave spectroscopy usually has much higher resolution and accompanying higher frequency accuracy [42, 43, 44, 7, 45, 46, 47]. However, for a conventional frequency-stepping millimeter-wave spectrometer, achieving high resolution and covering a broad bandwidth requires very long data collection times. For example, if a scanning spectrometer is used in conjunction with 10-20 Hz repetition rate Nd:YAG pumped lasers or pulsed molecular beams, to obtain a 20 GHz bandwidth spectrum with 20 kHz spectral resolution would require a month of data collection. In the early 1980s, the invention of cavity-enhanced Fourier-transform spectroscopy significantly increased the sensitivity and decreased the averaging time [56]. However, due to the mechanical tuning of the large cavity mirrors required for each frequency step, the data collection rate is still too slow for our experiments.

The recent invention of Chirped-Pulse Fourier-Transform Microwave (CP-FTMW) spectroscopy by Pate and co-workers shatters the limitation of the frequency stepping spectrometer, and obtains broadband spectra with high resolution in a very short data collection time [57, 58]. Barratt Park in our group has extended the CP-FTMW technique to the millimeter wave region, and designed a Chirped-Pulse millimeter-Wave (CPmmW) spectrometer in the region of 70-102 GHz [59, 60]. Based on Barratt's

work, I have built a similar CPmmW spectrometer with 76-98 GHz bandwidth. The details of the design and evaluation are included in Barratt's thesis (In preparation). In this section, I briefly introduce my design and emphasize the unique features for Rydberg experiments.

2.3.1 Spectrometer design

A schematic of the CPmmW spectrometer is shown in Figure 2-27. To generate a broadband millimeter-wave pulse at ∼85 GHz, a 4.2 GS/s arbitrary waveform generator (vi), clocked by a 4.2 GHz phase-locked oscillator (ii), creates a crafted RF pulse (user-defined pulse width, bandwidth, phase, and amplitude) at 0.2-2.0 GHz. A triply-balanced mixer (vii) mixes the RF pulse with a 6.2 GHz phase-locked oscillator (iii) to create a pulse with both sum and difference frequency components (6.4-8.2 GHz and 4.2-6.0 GHz). The upper frequency sideband (6.4-8.2 GHz) is chosen by a bandpass filter (ix) and delivered into an active frequency doubler (xiv) and an active frequency sextupler (xviii) sequentially. The output pulse retains the pulse width of the input pulse, but multiplies the frequencies ($12 \times f$ = 76.8-98.4 GHz), bandwidth ($12 \times \Delta f = 21.6$ GHz) and phase ($12 \times \delta\phi$). The millimeter-wave pulse is broadcast into free space by a standard rectangular gain horn (xx) and collimated into a molecular beam chamber by a Teflon (xxi) lens or a parabolic mirror (not shown in Figure 2-27). After the excitation pulse has polarized the sample, the FID is collected by another horn and down-converted by mixing with the output of another sextupler (xxvii) seeded by a frequency synthesizer (iv). The downconverted signal is amplified by a low-noise amplifier (xxix), digitized, and averaged by a 12.5 GHz oscilloscope (xxx). All frequency sources used in this spectrometer are phase locked to the same 10 MHz Rubidium frequency standard (i).

2.3.2 Part list

- i. 10 MHz Rubidium frequency standard (Stanford Research Systems FS725)
- ii. 4.2 GHz phase-locked dielectric resonator oscillator (Millitech, DLCRO-010-

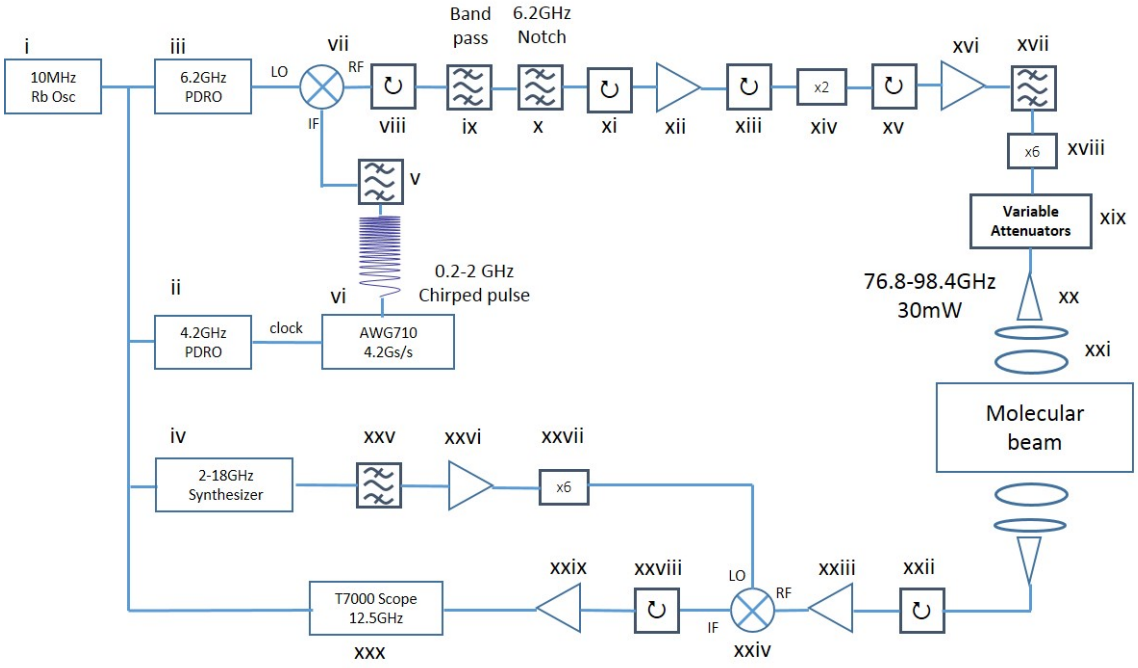

Figure 2-27: Detailed schematic diagram of the CPmmW Spectrometer. The part number of each component is in Section 2.3.2.

04200-4-15P)

- iii. 6.2 GHz phase-locked dielectric resonator oscillator (Millitech, DLCRO-010-06200-4-15P)
- iv. 2-18 GHz frequency synthesizer (HP,8673E)
- v. DC to 2.2 GHz Low pass filter, Mini-Circuits
- vi. 4.2Gs/s, Arbitrary Waveform Generator (AWG) (Tektronix, 710B)
- vii. Triple-Balanced mixer (Macom tech, M93)
- viii. Isolator (INNOWAVE, 4-12 GHz)
- ix. 6.3 GHz to 8.3 GHz, 20dB Bandpass filter (Spectrum Microwave)
- x. 300MHz bandwidth, 20dB, 6.2GHz notch filter, (K&L)
- xi. Isolator (INNOWAVE, 4-12 GHz)
- xii. Power amplifier (AVANTEK, 4-12 GHz, 20 dB, 10 dBm)
- xiii. Isolator (unknown, 8-16 GHz)

- xiv. Active frequency doubler (Marki, ADA-0512)
- xv. Isolator (unknown, 8-16 GHz)
- xvi. Power amplifier (CTT, 30 dB, 20 dBm)
- xvii. Bandpass filter (unknown, 12-18 GHz)
- xviii. Active Multiplier Chain ×6 (Millitech, AMC-10-RFHB0)
- xix. 0-60 dB Rotary attenuator (Flann Microwave Instrument) and voltage control fast attenuator (Millitech)
- xx. 24 dBi, W-band standard gain horn (TRG Control Data Co.)
- xxi. Teflon lens, f=10cm and f=50cm at 500GHz (Thorlabs)
- xxii. W-band Isolator (HP, 365A)
- xxiii. W-band Low Noise Amplifier (Millitech, LNA-10-02150)
- xxiv. Balanced Mixer (Millitech, MXP-10-RFSSL)
- xxv. Bandpass filter (K&L, FN366-1)
- xxvi. Low Noise Amplifier (AVANTEK, SF8-0770, 12-18 GHz, 43 dB, 14 dBm)
- xxvii. Active Multiplier Chain ×6 (Millitech, AMC-10-RFHB0)
- xxviii. 6-18 GHz 15dB Isolator (TRW Microwave, AMF 6483)
- xxix. 0.1 to 12.0 GHz, 43dB Low Noise Amplifier (MITEQ, AMF-5D-00101200-23-10P)
- xxx. 12.5GHz, 50Gs/s Oscilloscope (Tektronix, T7000)

2.3.3 Optimizations

To improve the performance of the CPmmW spectrometer, such as decreasing the noise frequency amplitude, increasing the phase stability, and better collimating the output beam, I have performed several careful optimizations as follows:

- The RF pulse generated by the AWG is cleaned by a DC to 2.2 GHz low pass filter (vi) to remove the Nyquist frequency ($f_{sample_rate} - f$).

- The triply-balanced RF mixer is designed for minimizing leakage (usually 20 dB suppression) of non-mixing IF and LO components. However, in our spectrometer, due to several stages of amplification and active multiplications, this small leaking noise might be amplified downstream. The leaking IF signal is broadband and cannot be filtered easily. However, the leaking LO signal is fixed and can be removed effectively by another high suppression notch filter. Therefore, I use high power LO input (5 dB more than typical) and low power IF (10 dB less than typical) for the RF mixer, from which the output RF signal can be kept at a typical level, but the non-filtered IF leaking signal is very low. The relatively strongly leaking LO signal is filtered by a customized 6.2 GHz notch filter (x). Thus, both noise signals of LO and IF can be reduced by at least 10 dB.

- To satisfy the 5 dBm input power threshold of the active multipliers (xiv, xviii), two low noise RF power amplifiers (xii, xvi) are inserted before each multiplier. The noise level of the multiplier output is determined by the gain of the amplifier. Gain and maximum/typical output are two key parameters of the power amplifier. For example, considering a power amplifier that has 20 dB gain and 10 dBm maximum output power. (1) If the input power is -10 dBm, the output power should be 10 dBm. The amplitudes of the noise and signal are both amplified by 20 dB, and the signal to noise ratio is unchanged. Therefore, the amplifier we use here is appropriate. (2) If the input power is 0 dBm, the output power is still no more than 10 dBm, which saturates the amplifier. The effective gain of the signal is only 10 dB, but that of the noise is still 20 dB, which decreases the signal to noise ratio by 10 dB. Therefore, it would be better to choose an amplifier with smaller gain. (3) If the input power is -30 dBm, the output power should be -10 dBm. To obtain 10 dBm power, I have to use two amplifiers in series. Usually, the signal to noise ratio of one high gain power amplifier is better than that of two sequential low gain amplifiers. In addition, most high quality amplifiers are optimized at the typical output power level. Therefore, it would be better to choose an amplifier with higher gain.

- RF/mmW reflection at boundaries can create a large number of noise frequencies and break down the phase stability. To minimize the impedance discontinuity at the boundaries: (1) For RF components with SMA connectors, I use 8 in-lbs torque wrench to carefully tighten the connectors. If the connectors are over tightened, it might cause irreversible damage. In addition, I balance the coaxial cable and minimize the transverse torque carefully, especially for the cables with a thick shielding shell. (2) I insert multiple isolators/circulators (viii, xi, xiii, xv, xxii, xxviii) in the RF/mmW circuits, especially after mixers and before active components (amplifier or multiplier).

- Modulate the output amplitude. Different from the passive frequency multiplier, the output power of the active multiplier is independent of the input power. If the input power is above a threshold, the output amplitude is constant. For example, a Gaussian shape RF pulse generated by the AWG with FWHM = 100 ns is converted to a 100ns rectangular mmW pulse. To shape the output pulse, I use a voltage-controlled fast attenuator (xix) with a user-defined pulse shape. In principle, I can create any pulse shape longer than 10 ns.

- Temperature and pressure stabilization. The stability of the phase in the millimeter-wave region is very sensitive to the temperature fluctuations and mechanical vibrations of the RF components and coaxial cables. To minimize such fluctuations, I mount most of the RF components on a water cooled plate, as shown in Figure 2-28. The temperature of the cooling water is controlled by a circulating cooler at 12 °C. A plastic case covers the components to minimize the effects of pressure fluctuations in the lab.

- The relationship of the actual millimeter-wave frequency and the downconverted RF frequency read by the oscilloscope is:

$$f_{mmW} = f_{LO} \pm f_{IF} = 6 \times f_{syn} \pm f_{IF} \tag{2.42}$$

f_{IF} is read by the oscilloscope, f_{syn} is generated by the HP synthesizer (iv). I cannot determine the sign in Eq.(2.42) with one downconverted spectrum. The ambiguity

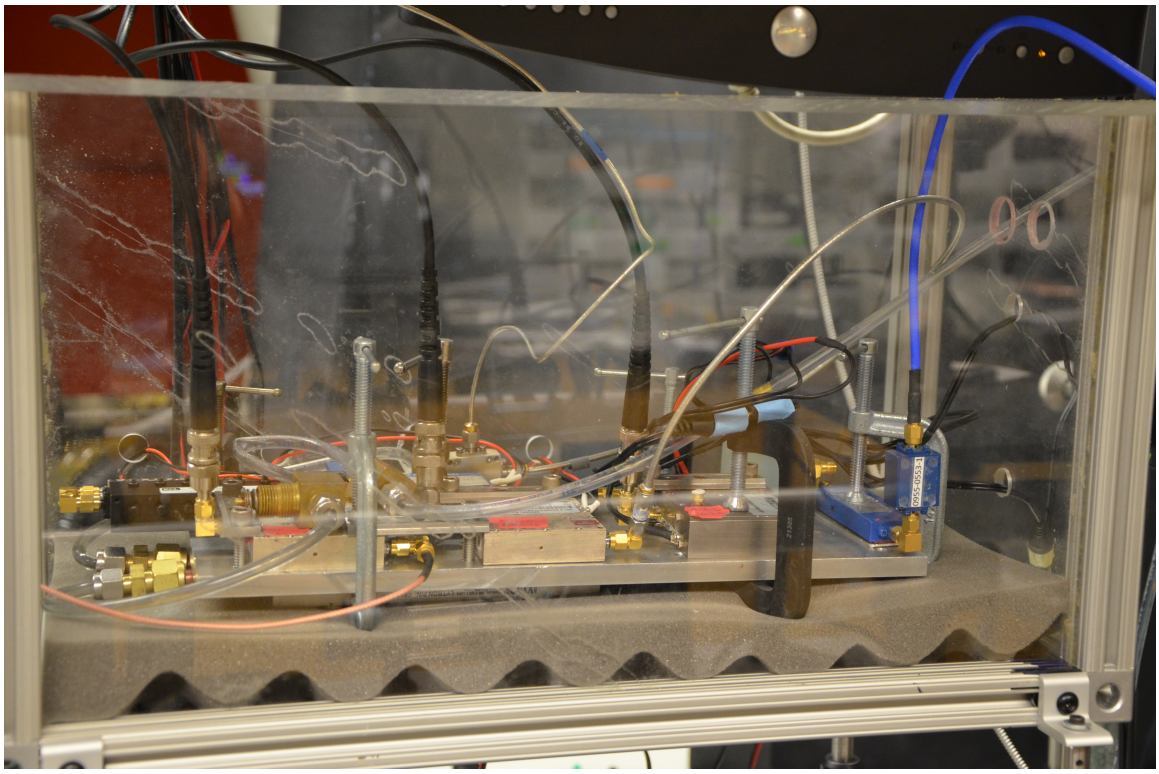

Figure 2-28: Mounting most RF components of the CPmmW spectrometer on a water cooled aluminum board in a plastic case reduces the effects of ambient for temperature and pressure stabilization.

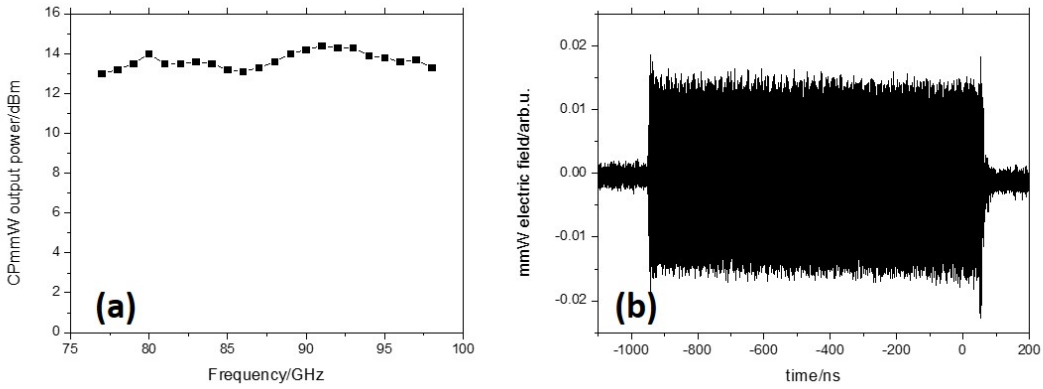

Figure 2-29: Performance of the CPmmW spectrometer. Plot (a) shows the output power of the CPmmW spectrometer at different frequencies. Plot (b) shows an example of a 500 ns, 84 GHz single frequency rectangular pulse.

is resolved by tuning the f_{syn} by 300 MHz and recording a second spectrum. There should be 1800 MHz shift of the downconverted frequency in the spectrum, and the shift direction is different according to the plus or minus sign in Eq.(2.42).

2.3.4 Performance of the CPmmW Spectrometer

To characterize our CPmmW spectrometer, I have performed several test experiments as follow:

- Output power: The output power is measured by a DET-10 power detector (Millitech), and shown in Figure 2-29, Plot (a).
- Single frequency generation: Figure 2-29, Plot (b) shows an example of a single frequency pulse with 500 ns, 84 GHz. The noise frequency level in the time-domain is <10 dB in the current setup.
- Phase noise: Phase noise is defined by:

$$E = \sin(2\pi f t + \phi(t) + \varphi(t)), \tag{2.43}$$

where $\phi(t)$ represents the short-term phase noise, which is a random function with similar time-scaled fluctuations as the carrier frequency. It is usually represented

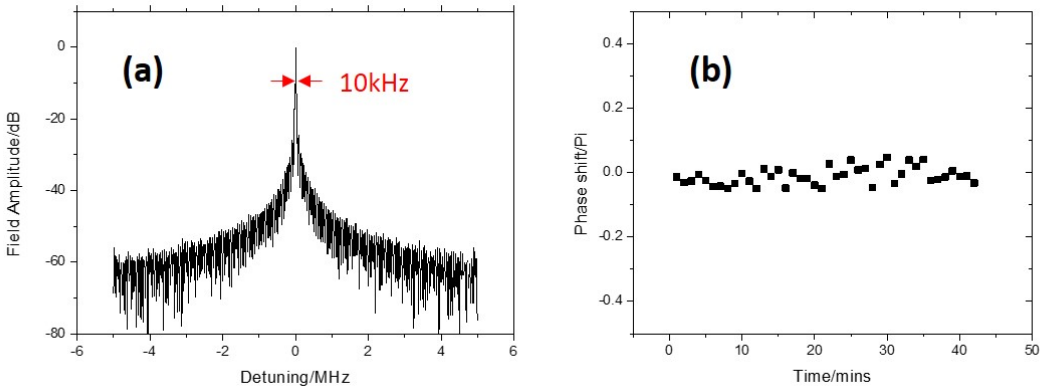

Figure 2-30: Performance of the CPmmW spectrometer. Plot (a) shows the short-term phase fluctuation of the CPmmW spectrometer. The frequency stability in 1 ms is 10 kHz. Plot (b) shows the long-term phase fluctuation of the CPmmW spectrometer. The phase does not drift more than 0.2π in one hour.

as a noise function:

$$L(f) = \frac{S(f)}{S_{total}}, \tag{2.44}$$

where S_{total} is the signal total power, and $S(f)$ is the signal power of 1 Hz of bandwidth at a frequency f away from the carrier frequency. Short-term phase noise would ruin the phase sensitive measurements and coherent control. The phase noise of our spectrometer is directly measured by the oscilloscope, as shown in Figure 2-30, Plot (a). $\varphi(t)$ represents long term phase noise (phase shift), which is slowly variating and causes unidirectional phase modulation. It would ruin the long term data average (π phase shift would completely cancel the signal). The phase shift of our spectrometer within an hour is no more than $\pi/5$, as shown in Figure 2-30, Plot (b). In addition, I also can correct the long-term phase shift automatically by data post-processing [59].

- Detection sensitivity: I define the detection sensitivity by S/N $>$ 3 with 5000 averages. It is frequency dependent, and also depends on the coupling efficiency between the emitting and receiving horn. The typical detection sensitivity for our experiments is <10 nW.

- Broadband pulse generation: Figure 2-31, Plot (a) shows an example of a 500 ns

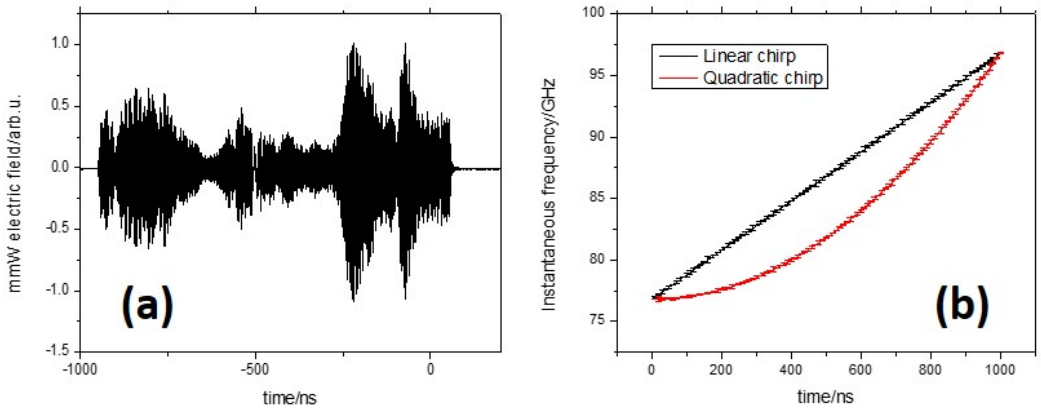

Figure 2-31: Performance of the CPmmW spectrometer. Plot (a) shows a 500 ns, broadband linear chirp (76.8 GHz to 98.4 GHz) in the time-domain. Plot (b) shows the linear frequency evolution in the linear chirp and the quadratic frequency evolution in the quadratic chirp.

linear chirp pulse over the full bandwidth of the CPmmW spectrometer (76.8 GHz to 98.4 GHz). The slow variation of the amplitude envelope in the time domain comes from the RF and millimeter-wave circuit frequency-dependent response. The fast variation comes from the accidental cavity modulations.

- Phase modulation: With the AWG, in principle, arbitrary phase modulation can be achieved quite easily. Therefore, the frequency can not only be linearly chirped, but can also be chirped quadratically or as some other nonlinear function of frequency, as shown in Figure 2-31, Plot (b).

- Pulse sequence generation: Our CPmmW spectrometer can generate a pulse sequence with any number of pulses, which have arbitrary frequencies and pulse lengths. With the help of the voltage-controlled fast attenuator (xix), the amplitude of each pulse can be user-defined arbitrarily. Figure 2-32 shows a pulse sequence with three segments. The first segment is a single frequency pulse with a triangle amplitude pulse envelope. The second segment is a single frequency rectangular pulse. And the last segment is a broadband chirped pulse.

- Intensity calibration: Since the data is recorded in the time-domain, the relative intensity in the frequency-domain of our spectrometer is not modulated by the

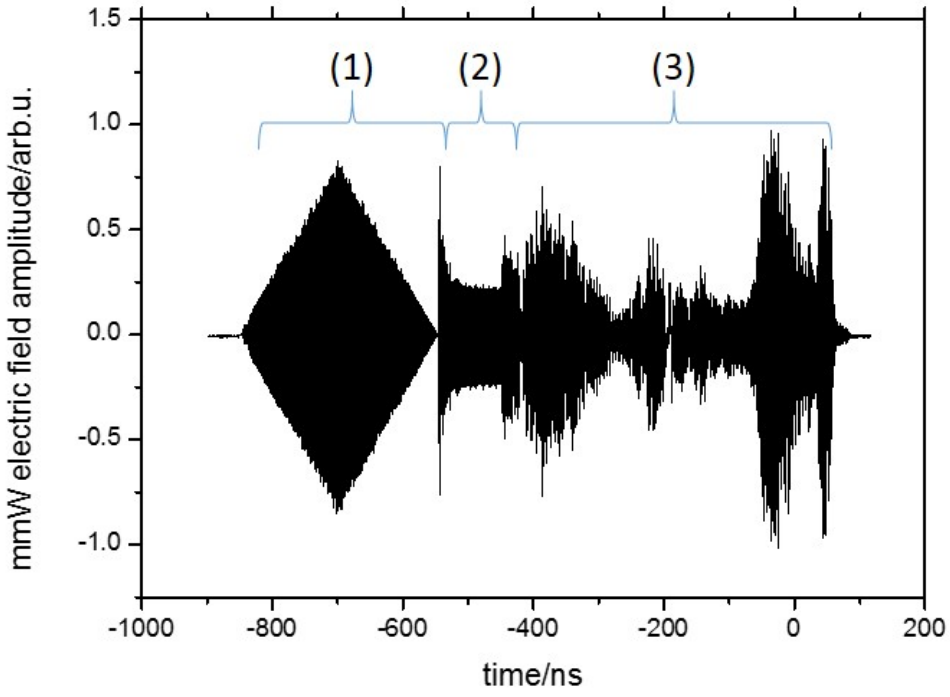

Figure 2-32: A pulse sequence with three segments generated by the CPmmW spectrometer. (1) 200ns, 80 GHz triangle pulse. (2) 100ns, 84 GHz rectangular pulse. (3) 500ns, 76.8 GHz to 98.4 GHz linearly chirped pulse.

fluctuations of the molecular beam source or lasers. However, millimeter-wave generation, propagation and detection of a broadband chirp are strongly frequency-dependent. The amplitude variations of the generation and detection arms are slow and fixed (modulation period in frequency domain ∼GHz). They can be calibrated with a power meter detector, which itself is well-calibrated by the manufacturer. The calibration of the propagation is more difficult, because the reflections from the horn, the Teflon windows, and the lens might form a low-Q millimeter-wave cavity, which would modulate the amplitude at different frequencies. The rate of this modulation depends on the cavity length and is usually very high (modulation frequency is ∼10 MHz). In addition, the envelope of the variation is very sensitive to alignment and can change day-to-day. Up to now, my best calibration has 10% uncertainty, which mainly is limited by the propagation modulation.

2.3.5 Implementation of the CPmmW Spectrometer in the supersonic cooled molecular beam apparatus (Gertrude)

Our first CPmmW spectrometer is setup on Gertrude, as shown in Figure 2-33. The millimeter-wave radiation from the emitting horn (i) is collimated by one or two Teflon lenses (iii), which are placed ∼30 cm away from the horn, and then turned 90 ° by a large aluminum mirror (v). The d ∼ 2" collimated millimeter wave beam enters the source chamber of Gertrude through a 4.5" fused silica window and crosses the molecular beam at 90 °. The transmitted millimeter wave and FID radiation are focused by a Teflon lens/window (iv) and collected by the receiving horn (ii). In this geometrical configuration, the power coupling efficiency of the millimeter wave between the horns is ∼ 15%. Most of the power loss comes from reflections from the window (vi) and using Teflon lenses with an inappropriate focal length. The laser beams are introduced through a small hole in the large aluminum mirror (v) and diverged by a lens (vii) placed behind it. The diameter of the laser beams is similar to the collimated millimeter-wave diameter. The overlap area of the molecular beam, laser beams and millimeter wave is ∼3 cm × 3 cm × 10cm = 90 cm^3 and ∼15 cm

away from the molecular beam source. With this configuration, the LIF experiment and TOF-MS experiment are compatible if the lasers can be guided through (viii) and (ix). These two experiments are used to tune the lasers onto resonance with the transitions, as in Section 3.1.

2.3.6 Implementation of the CPmmW Spectrometer in the buffer gas cooled molecular beam apparatus (Buffy)

To set up the CPmmW spectrometer in Buffy, I have two different configurations, transmission mode and reflection mode, which have unique features and are used for different experiments.

Transmission mode

The schematic diagram of the transmission mode is in Figure 2-34, which is similar to the setup in Gertrude. The millimeter wave radiation from the emitting horn (i) is collimated by a Teflon lens (iii) with short focal length, enters the detection chamber of Buffy through a Teflon window (iv), and intersects with the molecular beam perpendicularly. The transmitted millimeter wave and FID go through another Teflon window and Teflon lens and are focused into the receiving horn (ii). The emitting and receving arms are completely symmetric. The laser beams are introduced from a window on top of the chamber (not shown in Figure 2-34) and expanded to a cigar shape with a combination of a spherical mirror and a cylindrical mirror (not shown in Figure 2-34). The overlap area of the molecular beam, laser beams, and millimeter wave is $\sim$2 cm $\times$ 2 cm $\times$ 5 cm = 20 cm^3 and $\sim$20 cm away from the molecular beam source. Quartz glass windows (v) are used for LIF experiment, which are used to monitor the number density fluctuations of the sample during the CPmmW experiment.

Reflection mode

The schematic diagram of the reflection mode is in Figure 2-35, in which the laser beams and millimeter-wave beams are parallel with the molecular beam. 10% of the

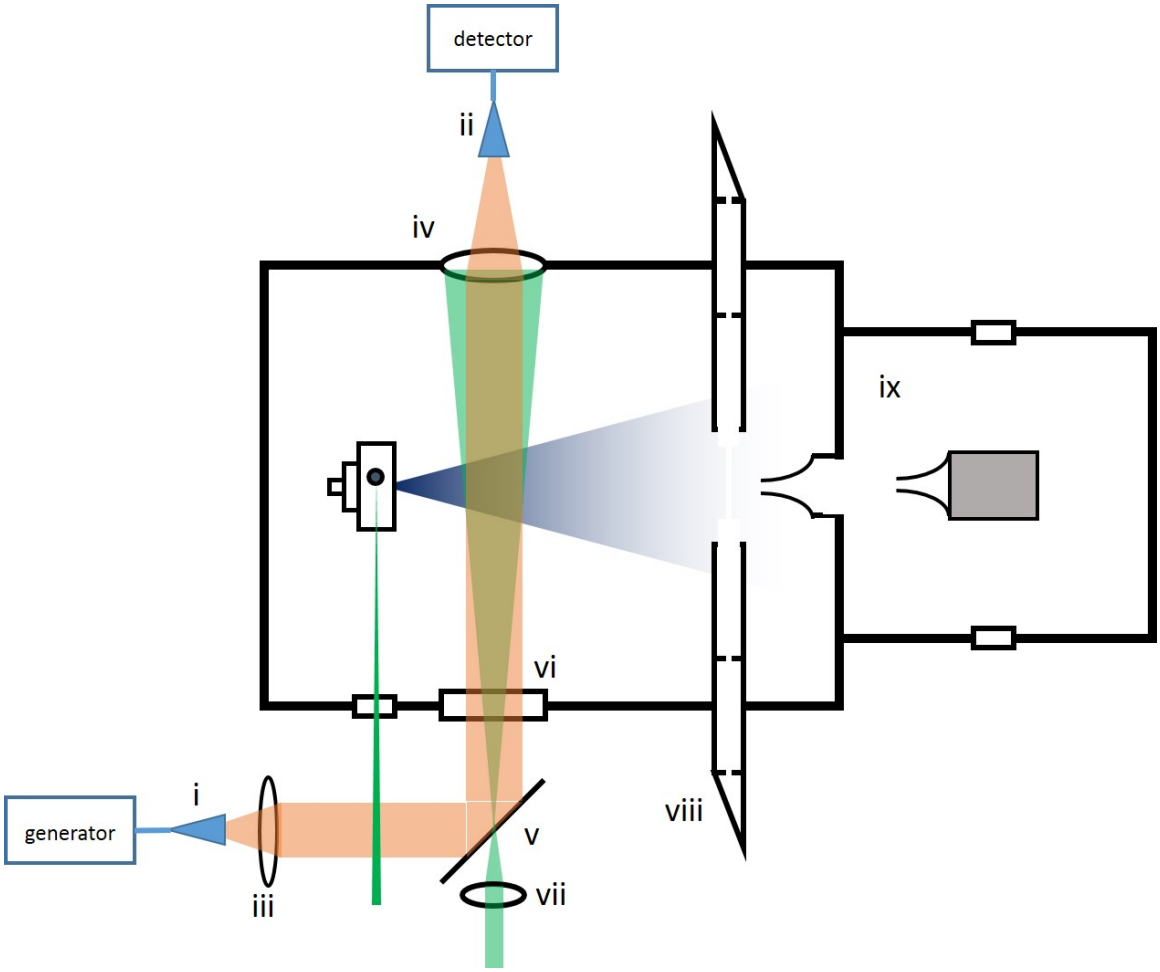

Figure 2-33: The transmission mode configuration of the CPmmW spectrometer in Gertrude. (i) Emitting horn. (ii) Receiving horn. (iii) 10" diameter Teflon lens, f = 30 cm. (iv) 5" diameter Plano-convex Teflon lens, f=20 cm. (v) 12" × 8" flat aluminum mirror with 1" × 0.5" rectangular hole. (vi) 4.5" Fused Silica window. (vii) Lens, f = 10 cm. (viii) LIF detection setup (collecting optics and PMT detector are not shown). (ix) TOF-mass spectrometer.

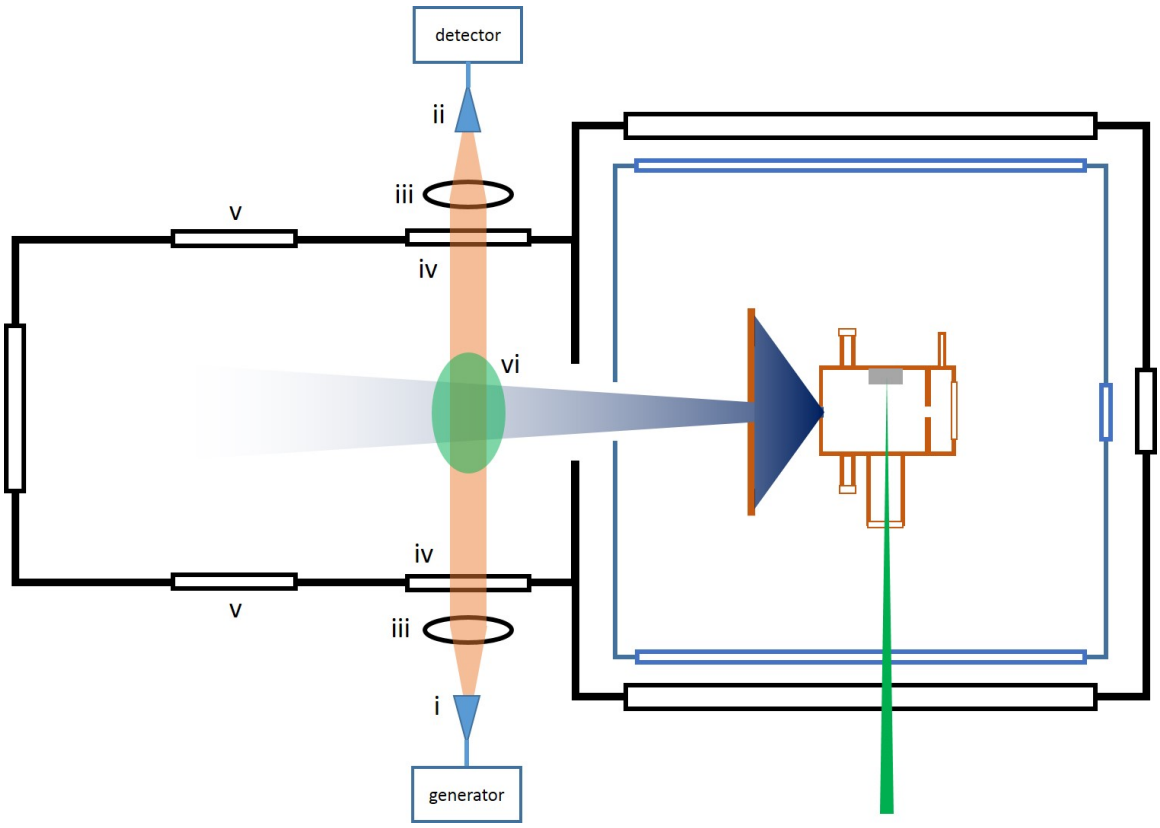

Figure 2-34: The transmission mode configuration of the CPmmW spectrometer in Buffy. (i) Emitting horn. (ii) Receiving horn. (iii) Teflon lens, f = 10 cm. (iv) 3" Teflon window. (v) 3" Quartz glass window. (vi) Cigar shape laser beams from above.

millimeter wave power generated by the emitting arm of the CPmmW spectrometer is sent into the standard gain horn (i) through a 10 dB directional coupler (ii). The millimeter-wave radiation goes through a flat teflon window (iii) into the end of the detection chamber. A parabolic mirror (iv) with 75 cm focal length collimates the millimeter wave and turns it 90 °. The millimeter wave with ∼3 cm diameter counter-propagates to the molecular beam and is reflected by a nickel plate (vii) with a 1 cm hole covered by highly transparent mesh, which is mounted on the cold skimmer in the source chamber. The reflected millimeter wave beam is refocused by the parabolic mirror into the standard gain horn (i), which is used as both the emitting antenna and receiving antenna. 90% of the received signal is delivered to the detection arm of the CPmmW spectrometer through the 10 dB directional coupler (ii). In the millimeter-wave propagation, 50% of the power is lost from the largely divergent part of the millimeter-wave beam, which cannot be collimated by the parabolic mirror. Therefore, the actual power in the interaction region is ∼ 5% of the power from the excitation arm, which is not a problem for a Rydberg experiment. However, the FID signal detection efficiency can be as large as 90%. The laser beams are focused by a lens (v) and introduced into the chamber by a fused quartz window (vi) and a tapered hole in the parabolic mirror (iv). The focal point is placed near the front surface of the parabolic mirror. The laser beams expand after the parabolic mirror overlap with the molecular beam and millimeter-wave beam in a volume ∼2 cm × 2 cm × 20 cm = 80 cm^3. Due to the double pass of the millimeter-wave beam, the effective interaction volume in this setup is ∼80 cm^3 × 2 = 160 cm^3. The laser and millimeter wave beams can interact with the molecular beam as near as 3 cm away from the source.

2.3.7 Future improvements

- Improving the purity of the frequency generation. In our CPmmW spectrometer, the noise frequencies mainly come from: (1) Reflecting waves in the coaxial cables or waveguides, which might re-enter the mixers or active components to generate new noise frequencies or amplify existing ones. (2) Leaking IF/LO/fundamental signals

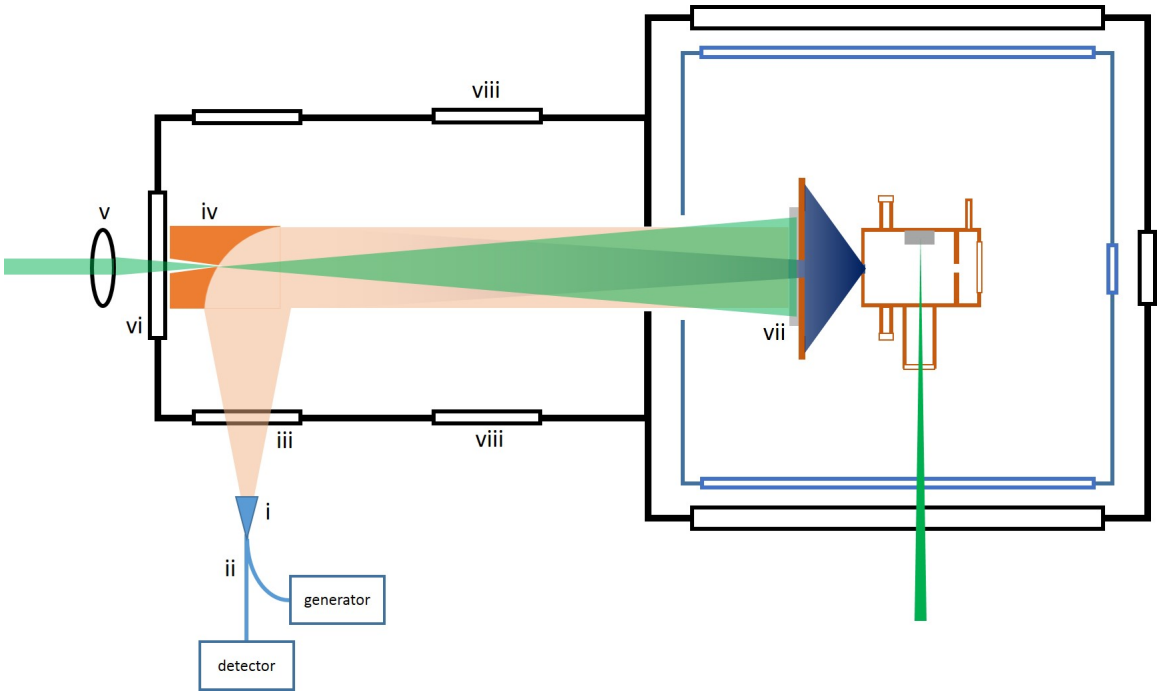

Figure 2-35: The reflection mode configuration of the CPmmW spectrometer in Buffy. (i) Standard gain horn. (ii) 10 dB directional coupler. (iii) 3" Teflon window. (iv) 3" parabolic mirror with a tapered hole (d = 2 mm at the front surface and 1 cm at the back surface), f = 75 cm. (v) Lens, f = 10 cm. (vi) 4.5" quartz glass window. (vii) 1.5" × 1.5" nickel plate with d = 1 cm mesh. 90% transparency. (viii) 3" Quartz glass window.

from mixers and multipliers, which can be mixed and amplified by the components downstream. (3) Reflecting or scattering waves from horns, Teflon windows, and walls of the vacuum chamber, which might generate noise as in (1), or form a pseudo-cavity to enhance some noise frequencies. In Section 2.3.3, I have employed several tricks to minimize such problems. However, some components cannot cover the full bandwidth of our spectrometer. Therefore, I find that near the lower and upper limits of our spectrometer, the noise frequencies increase significantly. Better filters, isolators, and amplifiers need to be explored and implemented to decrease such noise frequencies.

- Intensity calibration. The uncertainty of the relative intensities is 10%, which would be improved significantly if we could minimize the accidental reflections or calibrate the variation precisely. The intensity information might be very important for studying core-nonpenetrating Rydberg-Rydberg transitions.

- Waveguide feedthrough. The horns are placed outside of the chamber in the current setup. The millimeter wave radiation broadcast from the emission horn must transmit through the glass or Teflon window that is mounted on the vacuum chamber, and propagate a long distance to interact with the sample. The loss due to the transmission and propagation is significant. If we can build a low loss waveguide feedthrough, it will be possible to place the horns inside of the chamber. Mounting horns inside the chamber not only increases the coupling efficiency between the emitting and receiving horns, but also makes the alignment easier and more stable. I have built a waveguide feedthrough by drilling a 0.1" $\times$ 0.05" rectangular hole with sharp corners on a copper plate with 1/4" thickness, and inserting and gluing an acrylic bar into the hole to hold the vacuum. The tested loss is 3 dB, which is still larger than our requirement (<1dB). Using a thin plastic film instead of a thick acrylic bar might decrease the loss significantly.

- Quadrature phase detection. In our CPmmW spectrometer, I use mixers to down-convert millimeter-wave to RF frequency. In signal processing, this mixing process is called quadrature-sampling. Our down-conversion mixing is not a completely

coherent demodulation processes. The in-phase component still exists, but the quadrature component is lost. A direct ambiguity from this loss is that I cannot distinguish positive frequency and negative frequency after down-conversion. I can separate them by changing the down-conversion frequencies, as in Section 2.3.3. However, if the spectrum is very dense, it is possible to mislabel the down-conversion frequency shift. In addition, it requires recording every spectrum twice. With quadrature phase detection, according to the direction of the quadrature signal, we can know the sign of the demodulation signal directly.

- Dual-channel CPmmW. One limitation of our current CPmmW spectrometer is that I cannot generate two different frequencies at the same time, because: (1) Our AWG has one output channel; (2) The active multipliers do not work well for more than one frequency component at the same time. A two-channel AWG, two independent frequency up-conversion arms and a W-band coupler can generate an overlapped pulse pair, which can be used for coherent population trapping in a three-level Rydberg system and other coherent control experiments.
- Extending to sub-millimeter wave region. The main obstacle in extending from the millimeter wave region to the sub-millimeter wave region is the power loss significantly from >10 mW to less than 1 mW. However, this is not a problem for Rydberg states, which have extraordinarily large electric dipole transition moments. Therefore, two low-cost passive multipliers ($\times$ 6) and a sub-millimeter wave mixer can extend our 76-98 GHz CPmmW spectrometer into a 456-588 GHz CPsmmW spectrometer.

2.4 Laser ablation

In both apparatuses, Gertrude and Buffy, laser ablation is used to create the atoms or molecules entrained in the beams. Although this technique has been applied in many research fields for more than 30 years, there is still not a general theory or principle to guide experimentalists to systematically optimize the experimental conditions [99]. Each research group summarizes their own empirical rules for creating their target

Table 2.7: Comparisons between laser ablation of metal vs. salt experiments.

	Laser ablated metal	Laser ablated salt
Pulse energy	∼3 mJ	>20 mJ
Focused diameter	<1 mm	<100 μ m
Maximum repetition rate	>20 Hz	≤10 Hz

species. In my experiment, ablating metals (Ca/Ba) and salts (CaF_2/BaF_2) require significantly different experimental conditions, which is discussed in this section.

2.4.1 Comparison between laser ablation of metals and laser ablation of salts

Laser ablation processes involve very complicated energy transfer, gas dynamics and relaxation processes. Different materials usually behave quite differently. Most metals are easily ablated or vaporized, because they readily absorb photons due to the absence of a band-gap. However, typical ionic salts have a large band-gap (∼10 eV) and require simultaneous absorption of two or three photons. This nonlinear process requires a much higher local laser electric field. Therefore, a more tightly focused laser beam with higher pulse energy is used to achieve better ablation efficiency (more plasma and less dust). Based on my experiment, I summarize the generic optimized parameters between laser ablation of metals and laser ablation of salts in Table 2.7. Laser ablation of metals is usually much easier than the laser ablation of salts. Therefore, in this section, I focus on the optimization of the laser ablation of salts.

2.4.2 Laser focusing

From Table 2.7, I find that the laser ablation of salts requires a tightly focused laser. In my experiment, the ablation laser beam is expanded and collimated to 1.5 cm diameter, then focused with a f=50 cm best-form lens. A surprising difficulty is that the non-ideal optical components (HR mirrors and AR coating lens) could be deformed by the high intensity laser pulse. These deformations significantly change the focusing position, especially when the deformed optics are far from the focusing

spot. To avoid this problem, I apply several tricks: (1) Place the ablation laser and the optics near the vacuum chamber. (2) Use a concave-convex telescope instead of a convex-convex telescope to collimate the beam. (3) Before the laser beam enters the vacuum chamber, place a flip mirror to reflect the beam into a fixed pin hole to check the focal point every day.

2.4.3 Pellet preparation

A well prepared ablation pellet should have the following properties:

- The pellet is opaque at the ablation laser wavelength (532 nm) and can absorb laser energy efficiently.
- The pellet is non-fragile at relatively high ablation laser energy (∼20 mJ with 10 ns pulse length).
- The pellet has a high relative density (>90% of the crystal density).

Based on these criteria, I currently have a general procedure for pellet preparation as follows, which also might be improved in future.

(1) Barium fluoride, precipitated, 99.999% trace metals basis, is purchased from Sigma Aldrich (652458).

(2) Grind the rough BaF_2 granules into a fine powder in a mortar.

(3) Barium fluoride is very hygroscopic. Therefore, keep the powder in a desiccator all the time. If the BaF_2 powder is already hydrated, I put it in a glass tube vacuum furnace and evaporate the water at $\sim$ 400 °C for two hours. If the water is not removed completely, chemical reactions might occur when the pellet is heated to high temperature in step 6:

$$BaF_2 + H_2O \rightleftarrows BaO + 2HF$$

(4) Mix 50% BaF_2 powder (weight) with 50% CaF_2 powder. CaF_2 is used to improve the cohesiveness of the pellet.

(5) Load ∼3 g powder into a pellet die (made by MIT machine shop), and apply up to 35000 pounds of force over a 0.7 inch diameter area (650 MPa) on a benchtop

hydraulic press (Manley 147) to press into a pellet with ∼3 mm thickness. The pressure is gradually increased to 650 MPa in a minute and held for 20 minutes. Then, the hydraulic press is released slowly over 3 minutes. The density of the target in this step should be more than 80% of that of BaF_2 crystal.

(6) Transfer the targets into a vacuum furnace with < 50 mtorr pressure. Slowly increase the furnace temperature to 800 °C for two hours and then decrease to room temperature over an additional two hours. The density of the target should be more than 90% of that of BaF_2 crystal. The choice of 800 °C was made after careful empirical optimization. If the heating temperature is too high, the pellet becomes too hard to be ablated, and most of the ablation products from such hard pellets are Ba atoms instead of BaF molecules. If the temperature is too low, there is a large amount of dust generated during the ablation.

2.4.4 Minimize the generation of dust

Ablation is a pretty brutal process, which might create much more dust than homogeneous plasma. The dust has no contribution to our molecular beam, but brings several negative effects: (1) Decreasing the lifetime of the pellet; (2) Sticking on the window to attenuate the ablation laser; (3) Interfering with the gas dynamics in the cold cell. To decrease the dust generation, a tightly focused ablation laser and a dense target are two crucial points. Figure 2-36 shows the improvement of BaF experiment upon optimizing the ablation laser and pellet preparation.

2.4.5 Laser wavelength, repetition rate and focusing spot movement control

For the laser wavelength, I have tested the three usual outputs of Nd:YAG laser: 355 nm (THG), 532 nm (SHG) and 1064 nm (fundamental). Based on BaF/CaF yield, I have not found any significant difference among these three wavelengths. I choose 532 nm just because of the experimental convenience in our lab.

In principle, the laser ablation process is very fast (<10 μs). Therefore, <100 Hz

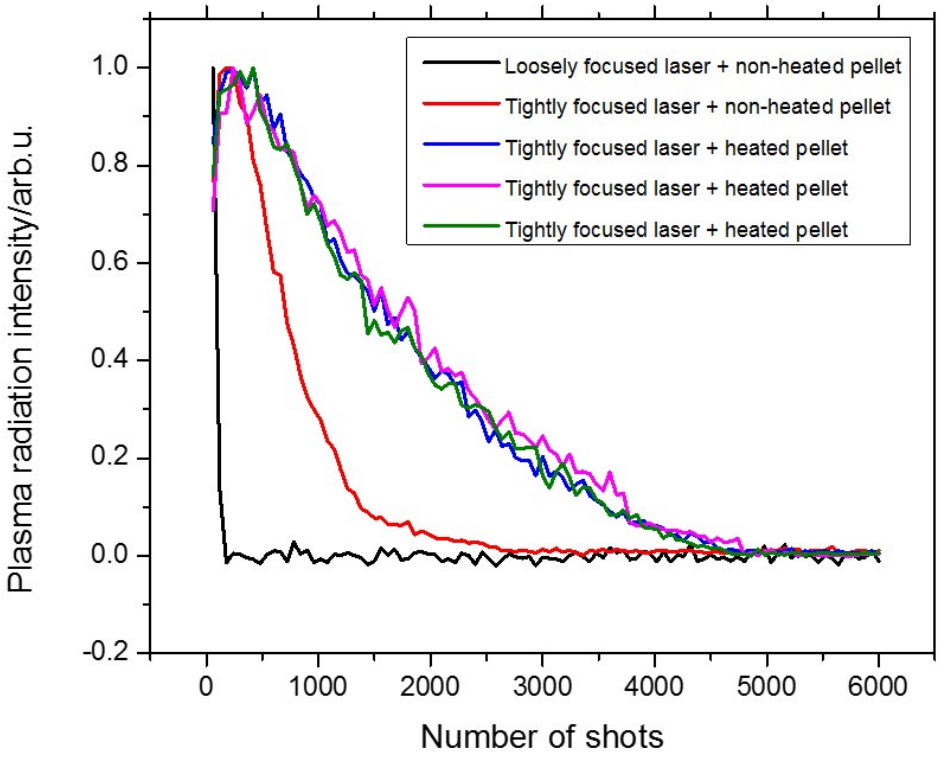

Figure 2-36: The ablation lifetime of the different BaF_2 pellets. This plot shows the normalized LIF signal of BaF with different ablation lasers and pellet conditions. The black curve shows a very short lifetime with a loosely focused ablation laser ($\sim$0.5 mm) and non-heated low-density pellet ($\sim$80%). The red curve shows an intermediate lifetime with a tightly focused ablation laser ($\sim$100 μm) and non-heated low-density pellet ($\sim$80%). The other three curves represent three measurements of very long and reproducible lifetimes with a tightly focused ablation laser and heat treated high-density pellet (>90%).

repetition rate is sufficiently low to be irrelevant to the ablation efficiency. This is true for ablating Barium or Calcium metals. However, the yield of BaF and CaF molecules decreases dramatically as the repetition rate of the laser is increased from 2 Hz to 20 Hz. The DeMille group also observes a similar phenomenon with the SrF molecule. There seems to be local effects, which do not relax quickly (>100 ms), that damage the structures or chemical compositions of the pellets. The degraded yield of molecules comes from repetitively ablating one spot. Therefore, if I can shift the focusing positions quickly, each shot would be on a new spot, even with a higher repetition rate. A Galvo mirror is perfect for this purpose, because: (1) its movement rate can be very high (>1 degree/100 ms). (2) The reproducibility is high (no backlash). In Figure 2-37, a 1.5" HR mirror on a Galvo mount is used to scan the beam quickly in the X direction. The Galvo mount is scanned at a 1 Hz rate. Therefore, in one second, there are 10 spots with ∼1 mm spacing in a line at a 10 Hz laser repetition rate. Another 1.5" HR mirror on a picomotor actuated mount is used to scan the beam slowly in the Y direction. The BaF/CaF yield of this 2D scanning mode with 10 Hz repetition rate is the same as that of the fixed position mode with 2 Hz repetition rate.

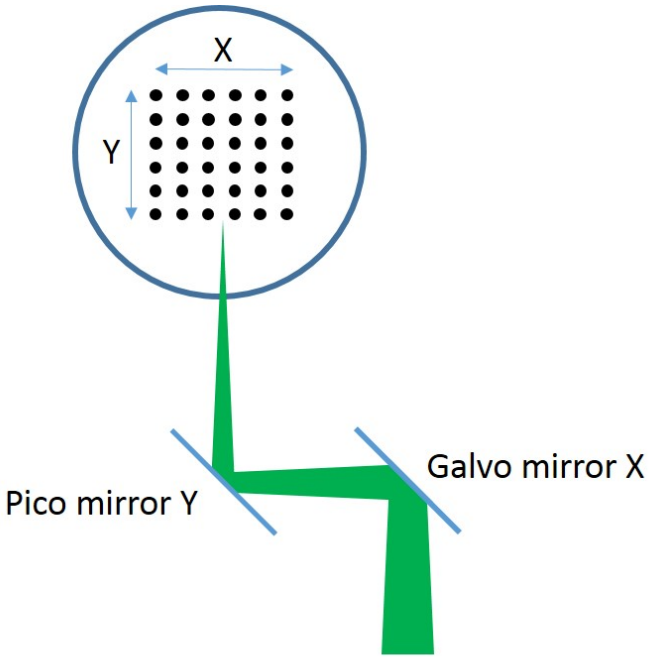

Figure 2-37: Diagram of the laser spot moving system. HR mirror on the Galvo mount vibrates with $\sim$ 1 Hz period and moves the laser spot on the target along a 1 cm line in the X direction. The HR mirror on the picomotor actuated mount moves the laser spot 0.5 mm every 5 seconds in the Y direction. If the laser spot is near the edge of the pellet, the direction of the movement is reversed.

Chapter 3

Atomic Rydberg-Rydberg transitions

In the first part of this chapter, I describe some efforts to obtain spectra of millimeter wave induced Rydberg-Rydberg transitions using Ramped Pulsed Field Ionization (Ramped-PFI) detection in an atomic Rydberg system. It is used for approximately locating the probe laser wavelength for two-color excitation of the molecular Rydberg states in Chapter 5. Then, I demonstrate the application of the CPmmW technique to induce atomic Rydberg-Rydberg transitions detected via FID radiation. Most of the experiments have been performed in the laser ablated supersonic atomic beam in the source chamber in Gertrude. Several techniques that facilitate data analysis, such as transient nutation measurement, interference between the electric field of the chirped pulse and FID, and extraction of phase information, are described in detail. Two classes of manipulation experiments with millimeter wave pulse sequences are introduced to demonstrate the ability to control population and coherence in the Rydberg system. In addition, some evidence of collective effects in my system inspire me to develop a new, more intense molecular beam source, namely a buffer gas cooled beam, to improve the observations. The last section of this chapter is an illustration of the improvement of the buffer gas cooled atomic beam, and presentation of an example of strong collective effects, superradiance. As a proof of principle experiment, I have not yet tried to perform a complete set of spectroscopic experiments to understand

all detailed spectroscopic features. Most of the techniques and information obtained in this chapter are used as a platform or guidance for further scientific research in cooperative radiation (Chapter 4) and molecular Rydberg spectroscopy (Chapter 5).

3.1 Pulsed Field Ionization (PFI) experiments in the supersonic beam setup

In this chapter, my purpose is not to study the structures of different atomic species, but to focus on the interactions between an abstract gigantic electric dipole transition moment and a millimeter wave field. Therefore, I treat on the same framework the atomic Rydberg states of different species (Calcium and Barium), which have similar transition frequencies and electric dipole transition moments at any specified principal quantum number, n$\sim$30 to 60. Calcium is used for early experiments, because the Calcium target is cheap and easily be machined. In the most recent experiments, a Barium target is used instead, because optical pumping to Barium Rydberg states requires only one UV photon, while excitation of Calcium Rydberg states requires one UV photon and one NIR photon. Schematic diagrams for optical excitation of Rydberg states of Calcium and Barium atoms and millimeter wave induced Rydberg-Rydberg transitions are depicted in Figure 3-1.

3.1.1 Experimental implementations

For Calcium atoms, two pulsed dye lasers (Laser 1: Sirah Precision Scan, Laser 2: Lambda Physik Scanmate 2E) are used to optically pump to d series or s series Rydberg states. Laser 1, with Coumarin 540A dye, is pumped by an injection-seeded Spectra-Physics Nd:YAG laser (GCR-290, Third Harmonic Generation (THG), 7 ns, 150mJ, 20 Hz repetition rate). A $\sim$20 mJ, $\sim$544 nm pulse is generated. This pulse is frequency doubled by a β-BBO crystal to $\sim$272 nm, $\sim$2 mJ (maximum power, typical $<$200 μJ is used), and used to pump the first transition from the ground $4s^2\ ^1S_0$ state to the $4s5p\ ^1P_1$ state. Laser 2, with LDS 798 dye, is pumped by the

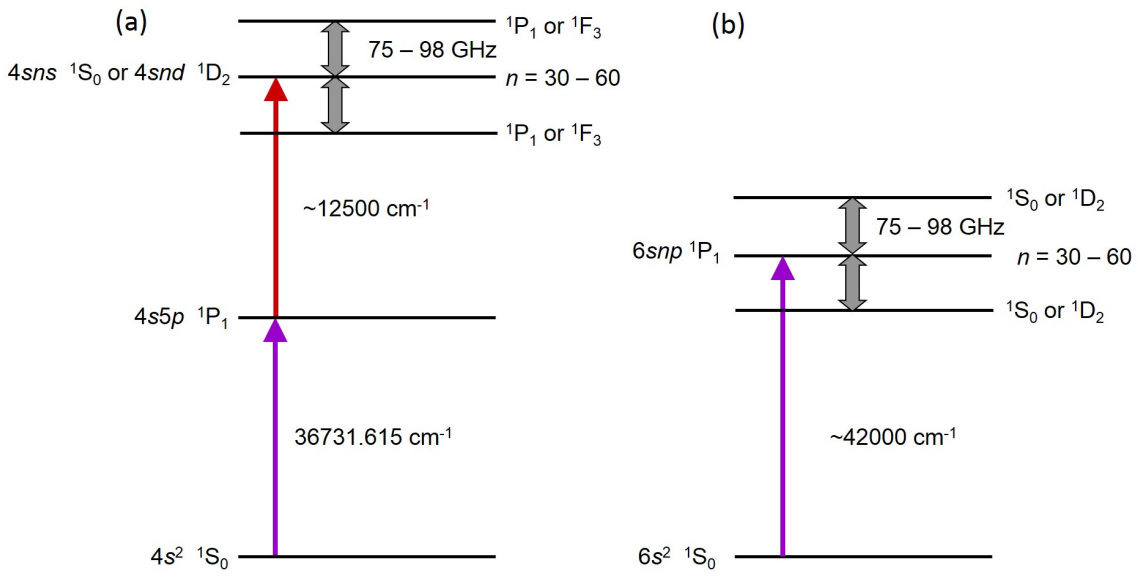

Figure 3-1: Schematic diagram of energy levels of Calcium (a) and Barium (b) atoms. The level spacings are not to scale. Calcium Rydberg states with n=30 to 60 are pumped via the $5p$ intermediate state by a UV photon (∼272 nm) and a NIR photon (∼800 nm). Barium Rydberg states with n=30 to 60 are pumped directly by a UV photon (∼238 nm) only. The millimeter-wave spectra of Calcium contain three series of Rydberg-Rydberg transitions (p-d, f-d, p-s), and the ones of Barium consist of two series of Rydberg-Rydberg transitions (s-p, d-p).

same injection-seeded Spectra-Physics Nd:YAG laser (GCR-290, Second Harmonic Generation (SHG), 7 ns, 150 mJ, 20 Hz repetition rate), and creates a ∼800 nm, ∼30 mJ (maximum power, typical <1 mJ is used) pulse, which is used to pump the second transition to either a $4sns\ ^1S_0$ or a $4snd\ ^1D_2$ state of n=30 to 60.

For Barium atoms, only one pulsed dye laser is used to optically pump Barium atoms to p series of Rydberg states. A dye laser with Coumarin 480 dye is pumped by the same injection-seeded Spectra-Physics Nd:YAG laser (GCR-290, Third Harmonic Generation (THG), 7 ns 150mJ, 20 Hz repetition rate), and creates a ∼476 nm, ∼15 mJ pulse, which is doubled by a β-BBO crystal to ∼238 nm, ∼1.5 mJ and used to pump transitions from the ground $6s^2\ ^1S_0$ state to the $6snp\ ^1P_1$ states with n=30 to 60.

3.1.2 Location of the Rydberg series using Ramped Pulsed Field Ionization detection (Ramped-PFI)

To locate transitions into atomic Rydberg states, I apply a 2 μs ramped DC electric field up to ∼250 V/cm, which sequentially ionizes Rydberg states ranging from high principal quantum numbers down to low principal quantum numbers (n=35), and the ions are collected by an MCP detector. Figure 3-2 shows the schematic diagram of the Ramped-PFI experiment. With the ramped pulse, I can not only gate to select the Rydberg states with different principal quantum number n, but can also exclude the background of ions that from the non-resonant multi-photon ionization, as shown in Figure 3-3, which increases the signal to noise ratio by a factor of three, compared to conventional PFI experiments with a rectangular DC field pulse for ionization.

Figure 3-4 shows optimized Calcium Rydberg (Plot (a)) and Barium Rydberg spectra (Plot (b)), with Ramped-PFI detection. Based on our current laser resolution (3 GHz without intracavity etalon) and stray electric field level (200 mV/cm), we can resolve the s and d series of Calcium Rydberg states up to n=40 (and resolve the series of s-d complexes up to n=70) and p series of Barium Rydberg states up to n=74. Assignment is straightforward using the Rydberg formula (3.1) and does not

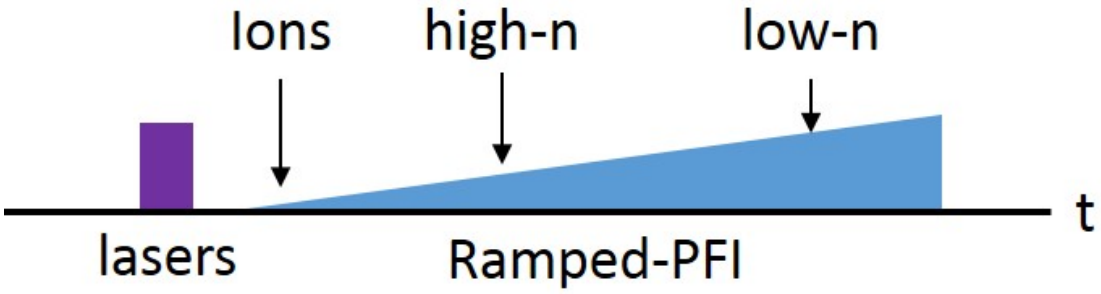

Figure 3-2: Schematic time-sequence diagram of the Ramped-PFI experiment. Typically, the delay between the lasers and the start of the ramped pulse is set to ∼50 ns. The maximum amplitude of the ramped pulse is 250 V/cm, which is limited by the current settings of our TOF focusing ion optics. The ramped pulse length can be varied from 50 ns to 10 μs. The prompt ions created by the lasers are extracted first, and the Rydberg states with high n^* to low n^* are ionized and extracted sequentially. The state resolution is determined by the length of the ramped pulse and the settings of the focusing ion optics. Based on typical settings, neighboring Rydberg states (Δn=1) at n∼40 can be completely resolved.

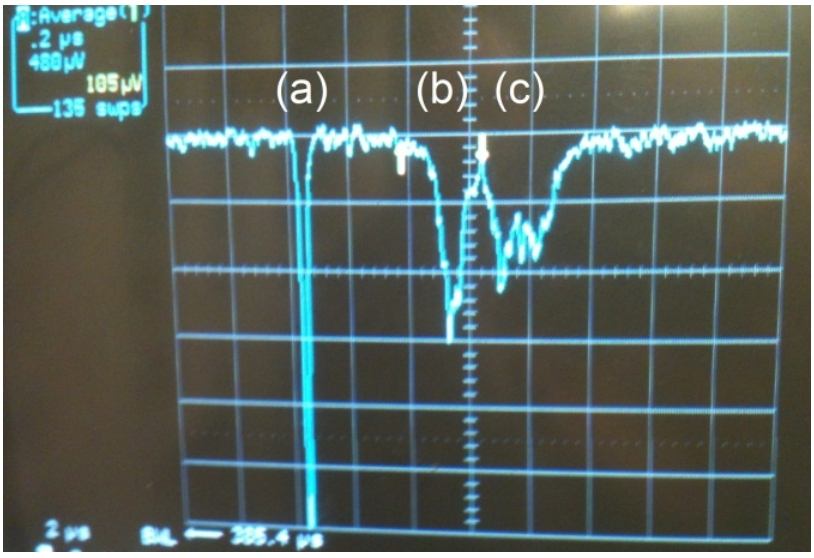

Figure 3-3: Raw data on the oscilloscope showing the Calcium 36p-36s transition. The three peaks in the time-domain represent the ion signals created by: (a) 1+1 REMPI or nonresonant multi-photon ionization; (b) field ionized 36p states; (c) field ionized 36s state.

require absolute calibration of the laser wavelength or an accurate ionization potential.

$$\Delta E = \frac{2\Re(n_2^* - n_1^*)}{\bar{n}^{*3}}. \tag{3.1a}$$

$$\bar{n}^* = \frac{n_1^* + n_2^*}{2}, \tag{3.1b}$$

n_1^* and n_2^* are the principal quantum numbers of neighboring Rydberg states in a series (with the same orbital angular momentum quantum number l), and $\Re$ is the Rydberg constant.

3.1.3 Minimization of the stray electric field

To obtain a clean Rydberg spectrum, I must minimize the stray electric field in the interaction volume, which destroys the parity, induces significant Stark ℓ-mixing, and causes frequency shifts and broadening [13]. Due to their gigantic electric dipole transition moment for $|\Delta n^*| \sim 1$ transitions, Rydberg states are extremely sensitive to very weak stray electric fields. In Section 2.1.5, I describe the stable and finely adjustable high voltage power supply. Here, I describe the use of atomic Rydberg states as a probe to measure the stray electric field locally [55], and the use of a fine tunable power supply to minimize this field. The atomic Rydberg stray electric field "probe" has two modes: low sensitivity mode and high sensitivity mode.

The low sensitivity mode is used to minimize the forbidden transitions of Barium atoms(*s*-*s* or *d*-*s*) in the laser spectrum, as shown in Figure 3-5. With a stray electric field, the dark s and d states can borrow intensity from the bright p states and be directly pumped by a single laser photon, as shown in Plot (b) in Figure 3-5. This intensity borrowing is weak for low Rydberg states due to the large energy gaps between bright and dark states, and the relatively small electric dipole transition moments. At large principal quantum number, the strong mixing of bright and dark states can completely destroy the periodic Rydberg patterns, as shown in Plot(a) in Figure 3-5. Therefore, I always start from the low Rydberg states to minimize the stray electric field, and then move step by step toward high Rydberg states. The

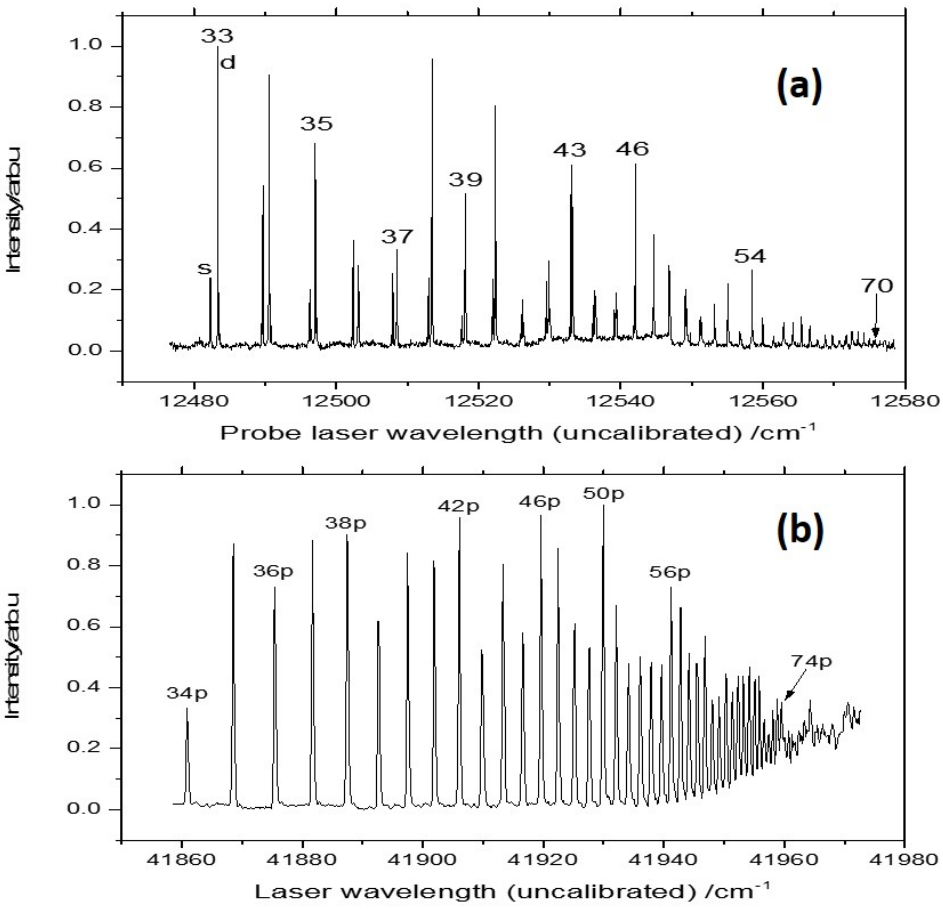

Figure 3-4: Ramped-PFI detected atomic Rydberg spectrum. Plot (a) shows s and d series of Calcium Rydberg spectrum for n from 33 to 70. The neighboring s and d states cannot be resolved by our current laser above n=40. The series of s-d complexes can be resolved up to n=70. The principal quantum numbers of the s series are marked in the plot, and that of the d series are (n-1). Plot(b) shows p series of Barium Rydberg spectrum with n from 34 to 74.

sensitivity of this method is limited by the signal to noise ratio of the laser spectrum and can be estimated by:

$$I_{s/d} = \left(\frac{\Delta - \sqrt{4d^2 + \Delta^2}}{2d} \right)^2 \tag{3.2a}$$

$$d = \mu E/\hbar, \tag{3.2b}$$

where Δ is the energy difference of the bright states (p) and dark states (s or d), $\sim$3 GHz for n $\sim$60, which can be resolved by our pulsed laser. μ is the electric dipole transition moment of the neighboring bright and dark states, $\sim$ 5000 Debye. Based on the current signal to noise ratio for a typical bright state (S/N $\sim$30 with 40 averages), I can detect transitions into dark states, the intensity of which is 5% that of the bright states (S/N$\sim$2). Therefore, the expected sensitivity to the stray electric field E from Eq. (3.2) is $\sim$1 V/cm. My experimental result, Plot (c) in Figure 3-5, confirms this estimate.

The stray electric field not only mixes the bright state characters into the dark states, but also shifts the states by:

$$\Delta f_p = \frac{1}{2}\left(\Delta - \sqrt{4d^2 + \Delta^2}\right). \tag{3.3}$$

I substitute the parameters above into Eq. (3.3) and obtain the frequency shift $\sim$100 MHz with 1 V/cm stray electric field. It is difficult to precisely measure the 100 MHz frequency shift using 1 GHz linewidth pulsed laser. However, cw millimeter-wave radiation can be used to measure the frequency shift at $\sim$MHz resolution. Therefore, I can minimize the stray electric field by minimizing the millimeter wave frequency shift with a much higher sensitivity.

To measure the millimeter-wave frequency shift induced by the stray electric field, I perform an optical-optical-millimeter-wave triple resonance experiment on Calcium atoms. Millimeter-wave radiation is used to pump the low Rydberg states (n*) to higher Rydberg states (n*+1 or n*+2), which are detected as described earlier by ramped PFI. The raw data obtained in the time-domain on the oscilloscope is shown

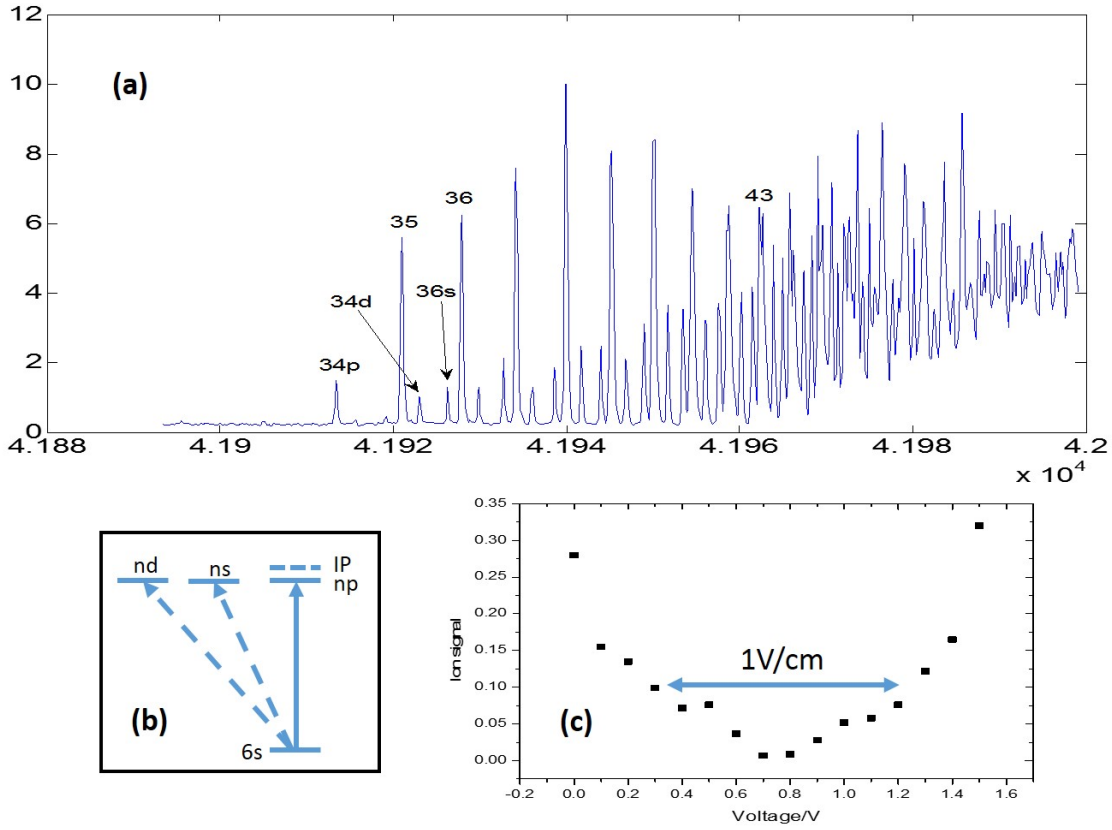

Figure 3-5: Minimization of the stray electric field by minimizing the intensities of the "dark" states in the laser spectrum of Barium Rydberg states. Plot (a) shows the pre-optimized spectrum in the presence of significant stray electric field. In addition to p Rydberg series, s and d series show up in the spectrum. Plot (b) illustrates the schematic diagram of optical pumping to the "bright" p series and "dark" s and d states. Plot (c) displays the minimization of intensity for transitions into a high Rydberg dark states ($n > 60$) by carefully tuning the finely adjustable power supply to compensate for the stray electric field.

in Figure 3-3. Three peaks can be clearly distinguished. From left to right, the peaks represent: (a) ions generated from multi-photon ionization; (2) ions generated from pulsed field ionization of the $36p$ state (n*=34.13), which is excited by lasers and millimeter-wave; (3) ions generated by pulsed field ionization of the $36s$ state (n*=33.67), which is pumped by lasers only. I scan the cw millimeter-wave frequency across the $36p$-$36s$ resonant frequency, and record the ion signal of $36p$ only. To demonstrate the nearly linear Stark shift, I intentionally add stray electric field from -4V/cm to 3V/cm at the interaction volume and record the millimeter-wave spectrum with Stark frequency shift and broadening (inhomogeneous Stark shift), as shown in Figure 3-6. From the measured frequency shift and Eq. (3.3), I obtain the electric dipole transition moment (3.6±0.6 kDebye observed vs 3.8 kDebye calculated), and the non-flatness of the inhomogeneous stray electric field ($> 80\%$).

After carefully tuning the fine adjustment of the electric field, I can minimize the stray electric field to 200 mV/cm, in which the linewidth of the millimeter wave transition is ∼5 MHz, as shown in Figure 3-7. To reduce the linewidth to 100 kHz, I must minimize the stray electric field to below 30 mV/cm. To reduce the stray electric field to this level, I not only need to compensate for the non-balanced voltage on the Stark plates, but also must shield the external electric field produced by the high voltage ion optics, which is difficult.

In addition to the poor millimeter-wave resolution in the presence of the current stray electric field, to obtain a relatively smooth spectrum, as shown in Figure 3-7, I must record the same spectrum more than 10 times and average them to eliminate short-term and long-term fluctuations. Therefore, the data collection rate is very low. Thus, to obtain a broadband spectrum of molecular Rydberg states, as in Chapter 5 with 20 GHz bandwidth, I would have to spend more than 100 hours, which is unacceptable. Even worse, if I want to perform millimeter-wave multiple resonance experiments, the signal searching and recording time increase geometrically. Therefore, I must give up performing millimeter wave spectroscopy using Ramped-PFI detection, but retain use of this technique only for minimizing the stray electric field in the ion detection setup. Several survey experiments are performed in the ion

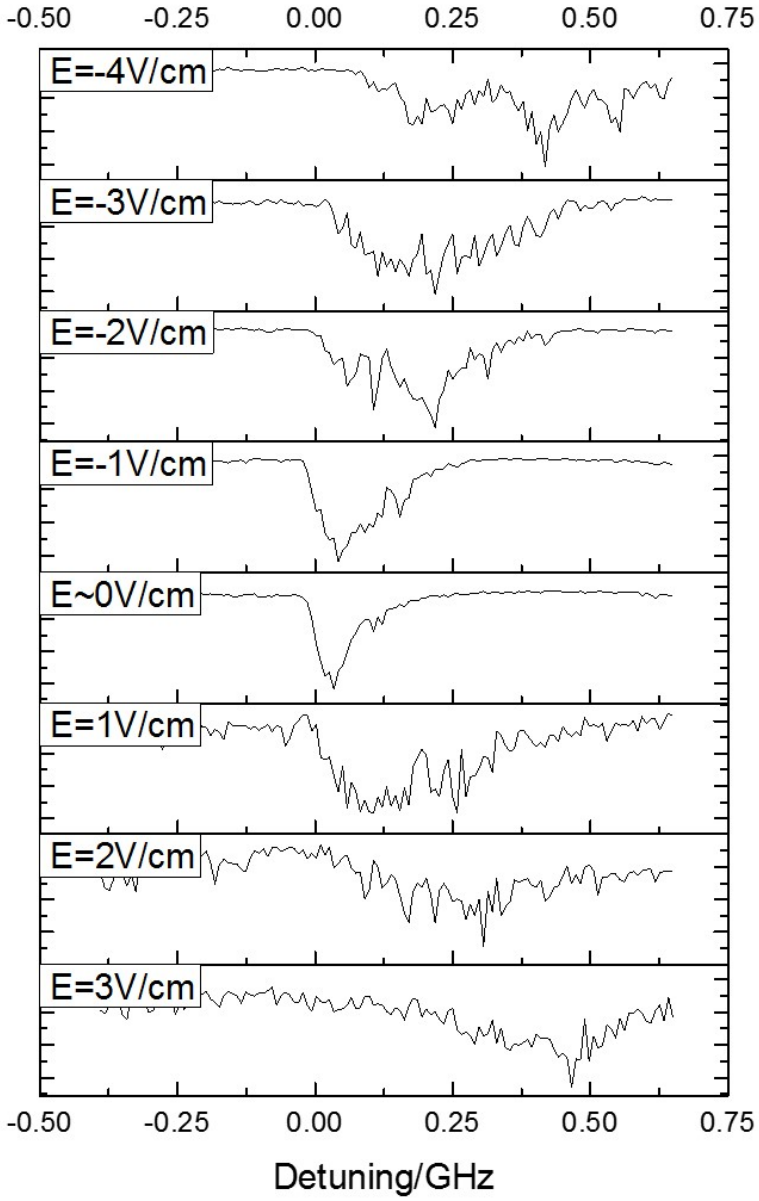

Figure 3-6: Stark frequency shift and broadening of the Calcium 36p-36s transition, as measured by millimeter wave spectroscopy. The frequency axis is plotted relative to a high precision measurement by Kleppner [7]. The frequency shift is due to the linear Stark effect, and the broadening comes from the inhomogeneous electric field in the interaction volume.

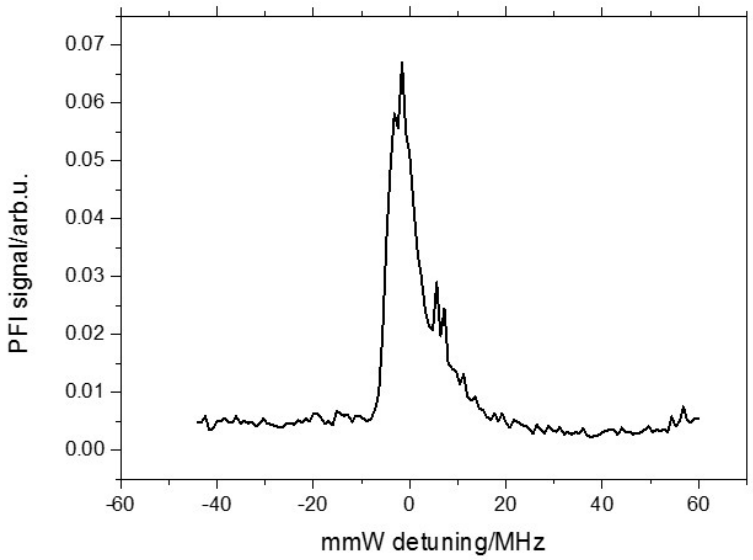

Figure 3-7: The best Ramped-PFI spectrum of millimeter wave spectrum of Calcium $36p$-$36s$ transition with 5 MHz linewidth. The asymmetric lineshape might come from the asymmetric stray electric field. To achieve a acceptable signal to noise level, this spectrum is the average of the 10 spectra with the same bandwidth. The total data collection spends ~ 30 minutes.

detection setup with minimized stray electric field, such as approximately locating the laser wavelength in the region of interest in molecular Rydberg experiments, as in Chapter 5.

3.2 Free Induction Decay (FID) experiments in the supersonic beam setup

Because of disadvantages of millimeter-wave spectroscopy with ion detection, as discussed above, I must explore a new technique with high data recording efficiency, high resolution, and low noise level. Chirped Pulse Fourier Transform MicroWave (CP-FTMW) and Chirped Pulse millimeter Wave (CPmmW) techniques have been demonstrated by the Pate and Field groups, respectively [57, 58, 59, 60]. Different from the traditional sequential stepping of the frequency through individual resolution elements, chirped pulse techniques can record the entire broadband spectrum (>20 GHz) in a single shot and retain the high spectroscopic resolution (∼100 kHz) that is limited only by the coherence lifetime. This improvement increases the data collection efficiency by a factor of ten thousand and has revolutionized the field of rotational spectroscopy. In this section, I show that the CPmmW technique also perfectly fits the study of Rydberg-Rydberg transitions. Even better, due to the gigantic electric dipole transition moments, the current limitation of the millimeter-wave power in rotation spectroscopy is not relevant and the improvement over the traditional sequential stepped millimeter-wave spectroscopy can be more than a factor of a hundred thousand.

3.2.1 Direct observation of atomic Rydberg-Rydberg transitions by recording FID radiation

Similar to the Ramped-PFI experiment, I use one or two tunable pulsed lasers to populate selected initial Rydberg states, as shown in Figure 3-1. Then a short duration chirped millimeter wave pulse (<100 ns, >500 MHz) instead of cw single frequency

millimeter wave radiation is applied to polarize the Rydberg-Rydberg transitions and the resultant FID radiation is detected in the time-domain. The new CPmmW technique has several advantages: (1) The broadband excitation can simultaneously polarize all transitions within the bandwidth of the spectrometer, and the fast digitizer can digitize a broadband signal without losing or distorting any frequency elements. (2) Recording the data in the time-domain automatically eliminates both short-term and long-term fluctuations that distort the relative intensities in the frequency-domain. (3) Due to the gigantic electric dipole transition moments, the degree of polarization of Rydberg-Rydberg transitions is not limited by the millimeter wave power, even for a 20 GHz broadband chirp.

$$P \propto \frac{\mu E_0 N}{\alpha^{1/2}} \tag{3.4}$$

As in Eq. (3.4), we can always compensate for the loss of the polarization P from a chirped pulse with large bandwidth α by increasing the excitation pulse amplitude E_0 (μ is electric dipole transition moment. Due to the large μ of Rydberg transitions, the optimal E_0 here is usually far below the spectrometer power limit). Therefore, the figure of merit of CPmmW Rydberg spectroscopy has an extra $\sqrt{\alpha}$ improvement compared to rotational spectroscopy. (4) There are no high voltage electric circuits in this system. Therefore, the stray electric field is always negligible.

However, compared to the most CPmmW rotational spectroscopy experiments with permanent gas, the CPmmW Rydberg spectroscopy has its own challenges. The major one is the number density of the laser ablated alkali/alkali earth atoms, such as Calcium and Barium, or diatomic radicals, such as BaF and CaF, entrained in the beam is relatively low. In the supersonic beam, the total number of laser ablated particles is usually n$<10^7$cm^{-3}. However, the 1% permanent gas seeded in the supersonic beam is usually n$>10^{11}$cm^{-3}. In addition, the excitation efficiency of multi-color optical pumping to Rydberg states is usually less than 10%. Even worse, most of the laser accessible Rydberg states of diatomic molecules have short lifetime due to the fast predissociation [25, 100, 101, 102, 103, 104, 105, 106, 107, 108]. Therefore, the number density of the initial Rydberg states for CPmmW spectroscopy is usually as low

as n<10^5cm^{-3} in the supersonic beam, which is almost six order magnitudes smaller than the number density in CPmmW rotation spectroscopy. An obvious solution to overcome this difficulty is to design a new beam source with higher beam density, such as buffer gas cooled beam (n>10^9cm^{-3}), or use a dense Rydberg gas prepared from a permanent gas, such as Nitric Oxide. However, higher number density of Rydberg states brings in another problem, the coherence time of the Rydberg states is shortened by fast cooperative and collisional dephasing. Both of these effects are proportional to the electric dipole transition moment, number density and polarization degree($\tau_{cooperative/collision} \propto n\mu P$). P represents the polarization degree. For rotation spectroscopy, P is usually smaller than 0.1, because the current millimeter wave radiation source is not strong enough to saturate the transitions with small μ. For Rydberg spectroscopy, P is easy to be 1. Therefore, for rotational spectroscopy, the cooperative and collisional dephasing mechanisms do not play an important role with n=10^{11}cm^{-3}. However, for Rydberg spectroscopy with gigantic μ_{Ryd}=1000μ_{rot}, cooperative [109, 110, 111, 112] and collisional dephasing mechanisms [91, 90, 89, 92] can significantly modify the radiative behavior with n=10^7cm^{-3}. There are a lot of interesting cooperative and collisional phenomena in a dense Rydberg gas, as in Section4. However, these two dephasing mechanisms degrade the spectroscopic resolution and should be avoided in the regular high resolution spectroscopic experiments.

To avoid accelerating the cooperative and collisional dephasing, but still collecting enough emitting power from the sample, I must increase the interaction volume and decrease the number density. If the total number of Rydberg states is fixed, enlarging the interaction volume by a factor of M (decreasing the number density by a factor of M) can keep the total emitting power, but decrease the cooperative dephasing by a factor of $\sim \sqrt{M}$ and the collisional dephasing by a factor of M. In addition, the geometry of the sample also determines how much forward radiation power can be collected by the detection horn, as $P \propto \sqrt{S}L$, where S is the cross section of the sample perpendicular to the millimeter wave propagation direction, and L is the length of the sample along the millimeter wave propagation direction. Therefore, to maximize the forward emission, a cylindrical shape of the interaction volume is

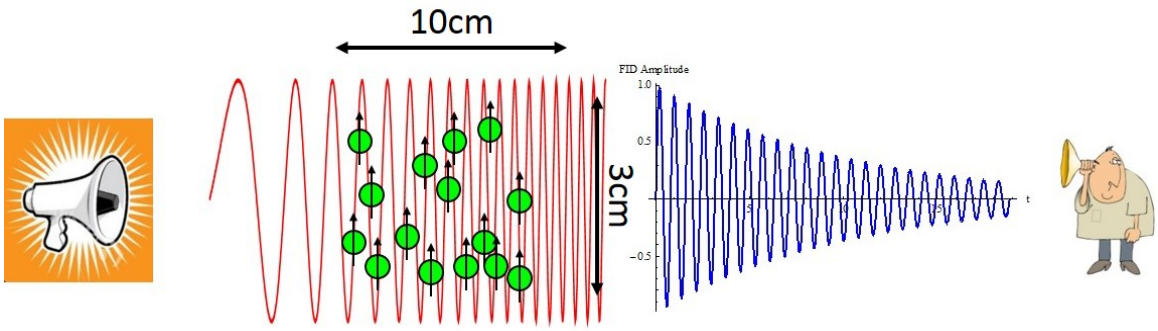

Figure 3-8: Schematic diagram of polarizing Rydberg atoms by CPmmW and detecting FID radiation in the time-domain. The length of the sample is 10 cm and the diameter of the active, irradiated region is 3 cm.

preferred to a disk shape. However, the diameter of the cross section must not be too small to avoid diffraction losses, as $d \sim \lambda$, where d is the diameter of the millimeter wave beam, and λ is the millimeter wave wavelength. Near this limit, diffraction causes the forward propagating wave to expand significantly, which prevents efficient coupling into the detection horn. Based on these two considerations, I shape the typical interaction volume to a cylinder shape with S ~10 cm^2 and L ~10 cm by overlapping the expanded lasers, the collimated millimeter wave beam, and the non-skimmed molecular beam, as shown in Figure 2-33. In a typical laser ablation Calcium atomic supersonic beam, the maximum number density of Calcium Rydberg states in the interaction volume, which is ~ 15 cm away from the nozzle, is ~10^5 cm^{-3}. Therefore, if fully polarized, the total number of the Rydberg emitters is $\sim 5 \times 10^6$.

Figure 3-9 shows the time-sequence of the CPmmW-FID experiment. In a typical experiment, the delay between lasers and chirped pulse is <10 ns and the FID FT-window is placed ~ 30 ns after the chirped pulse. The length of the chirped pulse can be varied from 3 ns to 1 μs, and the bandwidth can be arbitrarily set from FT-limited bandwidth to 20 GHz. The length of the FID FT-window is chosen to match the coherence lifetime (~ 50 ns to 20 μs). The saturation laser power is measured in the Ramped-PFI experiment and scaled to the larger beam size in CPmmW experiment. In the Calcium experiment with d=3 cm, the saturation power of the pump laser is ~100 μJ, and that of the probe laser is ~1 mJ. It is better not to over saturate

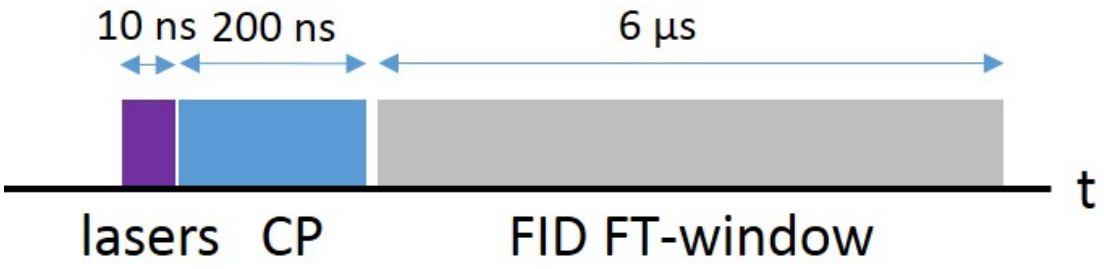

Figure 3-9: Schematic diagram of time-sequence in CPmmW-FID experiment. The timing values in this figure are for typical experiments. The gap of lasers and chirped pulse is ∼10 ns, and the gap of the chirped pulse and FID FFT window is ∼30 ns.

the transition, which might create a large amount of ions by multi-photon ionization. Ions not only destroy the coherence by collisions, but also create a stray electric field, which shifts the resonant frequency, as discussed previously. The power of the chirped pulse can be estimated using Eq.(3.5), with the calculated electric dipole transition moment.

$$E = \frac{\pi\hbar\sqrt{\alpha T}}{\mu T} \tag{3.5a}$$

$$P = \frac{1}{2} c\varepsilon_0 E^2 S, \tag{3.5b}$$

where α is the bandwidth of the chirped pulse, T is the pulse duration, μ is the electric dipole transition moment, and S is the cross section area of the millimeter wave. I substitute typical values into this equation (α = 500 MHz, T = 10 ns, μ = 3500 Debye, S = 10 cm^2) and obtain the power required for full polarization to be 0.2 mW. Therefore, I need to set the variable attenuator to ∼20 dB attenuation (Full output power of CPmmW spectrometer is 30 mW).

Figure 3-10 is the first FID spectrum of Calcium 36p-36s transition recorded in the supersonic beam apparatus. I apply a 10 ns, 500 MHz, 0.3 mW chirped pulse to polarize 36p-36s transition and record the resultant FID radiation. The raw data in the time-domain (Plot(a) in Fig.3-10) is after 5000 averages in 5 minutes (the experimental repetition rate is 20 Hz, but the data collection rate is a little bit smaller than 20 Hz due to the limit of the oscilloscope computer speed). A frequency-domain

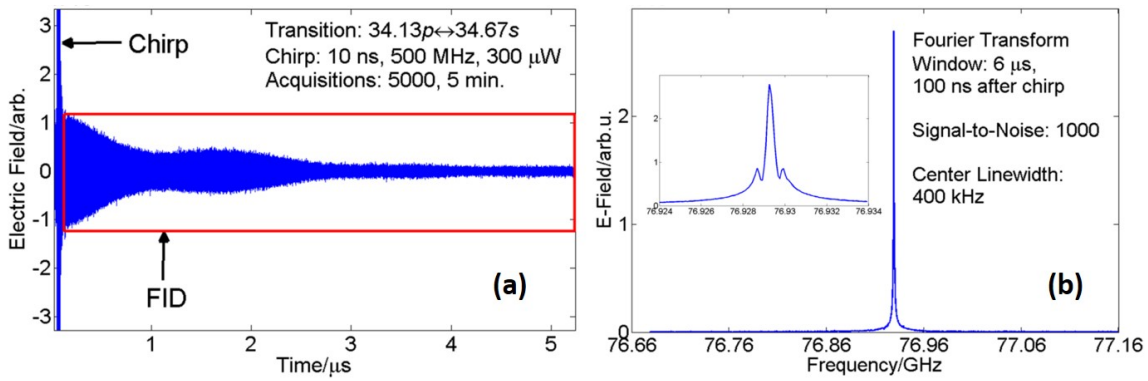

Figure 3-10: The first FID spectrum of Ca Rydberg-Rydberg transition in the supersonic beam apparatus. The left figure is the raw data recorded in the time domain. The right figure is the amplitude of the Fourier transformation of the time-domain data in the red box. The data with 1000 signal to noise ratio is obtained with 5000 averages in 5 minutes. The center linewidth is 400kHz, which is limited by transverse Doppler broadening. The side peaks comes from the Zeeman splittings induced by the earth's magnetic field.

spectrum (Plot(b) in Fig.3-10) is obtained by applying a FFT with a 6 μs rectangular window 30 ns after the chirped pulse. The center linewidth is $\sim$450 kHz, which is dominated by the transverse Doppler broadening. From the Doppler broadening, we can calculate the transverse velocity distribution of the unskimmed He supersonic beam to be $v = \frac{\Delta f}{f} c = 1500$ m/s, which is near the forward velocity of He supersonic beam (1800 m/s). The side peaks (700 kHz detuning from the center) come from the Zeeman splittings induced by the earth's magnetic field ($\Delta f_{Zeeman} = \mu_B B = 1.4 \times 10^4$ MHz/Tesla$\times$0.5 Gauss = 700kHz). I built a rectangular cage of Helmholtz coils to compensate the earth magnetic field, as described in Appendix A.

In addition to $36p$-$36s$ transition, I have recorded another three transitions, $32p$-$31d$, $39p$-$39d$ and $41f$-$43d$, as shown in Figure 3-11. Although the optimized powers of lasers and millimeter wave are slightly different, the lineshape and linewidth are almost identical. Among these four transitions, the directions of the first two transitions are upward in energy, and the directions of the last two transitions are downward. I cannot extract information about the transition directions from the amplitude spectra in the frequency-domain. However, I show how to extract such information from the nutation curve in the time-domain or from the relative phase of the excitation

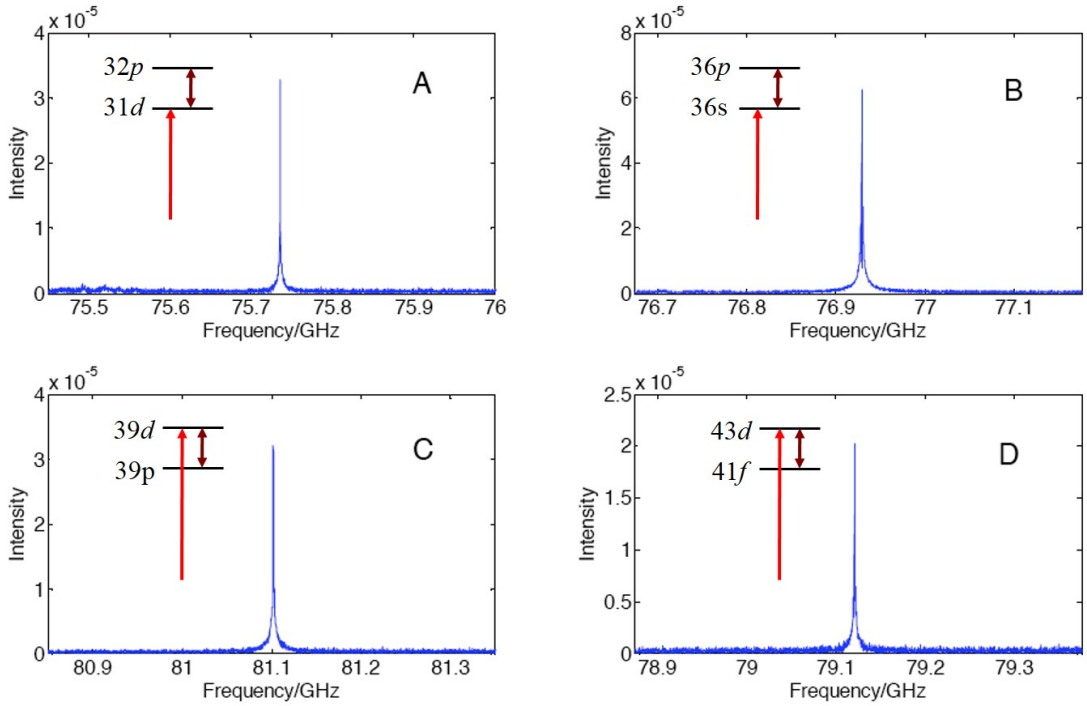

Figure 3-11: Four FID spectra of Calcium Rydberg-Rydberg transitions in the supersonic beam apparatus. Figure (A) and Figure (B) are up transitions. Figure (C) and Figure (D) are down transitions. The inset plots show the schematic diagram of laser and millimeter-wave transitions.

pulse and FID radiation, in Section 3.2.5.

3.2.2 Measurement of the total number of molecules in one Rydberg state by transient absorption/emission

To evaluate the sensitivity of the CPmmW spectrometer, I need to measure the total number of the emitters in our interaction volume. One method is using Laser Induced Fluorescence (LIF) first to measure the total number of atoms in the ground state within a small interaction volume first, and then scale that value to a larger volume. To convert to the total number of atomic Rydberg states, I must multiply by the laser pumping efficiency (At saturation power, each laser pumping step has 50% efficiency). For a typical Calcium experiment, the measured number density of Calcium Rydberg states in the supersonic beam at 15 cm downstream from the nozzle is 5×10^4 cm^{-3}. However, the disadvantages of this method are: (1) LIF cannot be used to measure

the absolute number reliably, because there are many experimental parameters, which are not easy to evaluate, especially the fluorescence quantum yield. (2) LIF measures the ground states instead of the Rydberg states directly. (3) If the number density distribution in the beam is not uniform, scaling the total number from small a LIF interaction volume to a large CPmmW interaction volume could result in a large error. In the following, I describe a direct measurement by transient absorption/emission of millimeter wave radiation instead of LIF.

A conventional cw millimeter-wave absorption/emission experiment described by Beer's law requires the linear absorption approximation, which is difficult to satisfy in the highly polarized Rydberg system. (In principle, we can apply extremely weak cw millimeter-wave radiation. However, the sensitivity of the detector is not sufficient in such an extreme situation.) I replace the requirement of cw linear absorption/emission to pulsed transient absorption/emission to avoid this difficulty. This method can measure the total number of Rydberg atoms in a single quantum state directly in a single measurement. The basic theory of this measurement is illustrated in Figure 3-12. I apply a 500 ns single frequency pulse to fully polarize the $36p$-$36s$ transition, by maximizing the amplitude of FID to find an exactly $\pi/2$ pulse. An absorption area is observed superimposed on the rectangular excitation pulse. I integrate the total area of the original rectangular excitation pulse and the absorption/emission area (if the transition direction is downward, there is an emission area instead of absorption area), and calculate the power ratio r of the total excitation power to the absorption/emission power (area $\propto$ field amplitude, area^2 $\propto$ power amplitude), which is also the ratio of the total number of millimeter-wave photons to the number of absorbed millimeter-wave photons. With a $\pi/2$ pulse, the $N_{Rydberg} = 2 \times N_{abs}$. There is a factor of 2, because half of the Rydberg atoms are polarized. Therefore, if I know the total number of original input millimeter-wave photons (N_{total}), I can calculate the total number of the Rydberg atoms by $N_{Rydberg} = 2 \times N_{total}/r$.

The total number of millimeter wave photons can be obtained from the input millimeter-wave power, using the geometrical configuration parameters. I also can use the optimized $\pi/2$ pulse with precisely calculated electric dipole transition mo-

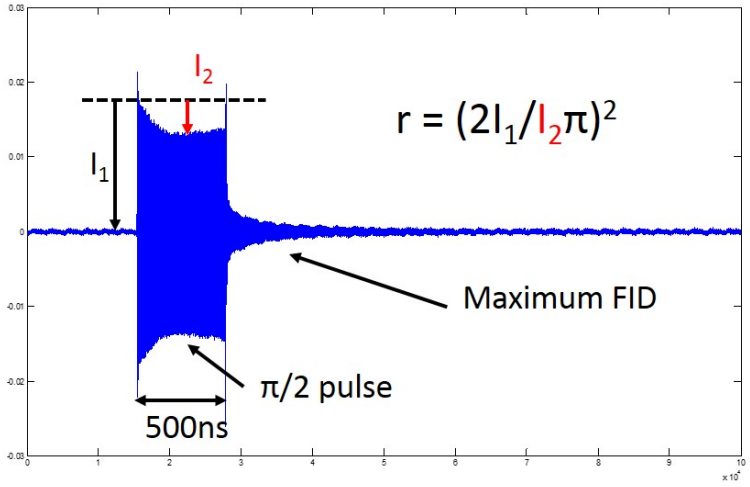

Figure 3-12: Determination of the total number of atoms in a single Rydberg state by millimeter wave transient absorption experiment. The FID amplitude is maximized by tuning the power of the millimeter wave to find an exact $\pi/2$ pulse. I_1 is the amplitude of the original millimeter wave, and I_2 is the maximum absorbed amplitude. The power ratio equation is derived using the assumption of a sinusoidal absorption envelope.

ment to calculate the millimeter-wave photon number, as in Eq.(3.6). This method directly measures the local millimeter-wave power, which is not disturbed by large frequency dependence of power or reflection/diffraction along the wave propagation. The measured number density of Calcium Rydberg atoms in Figure 3-12 is 5×10^4 cm^{-3}, which is consistent with the LIF measurement.

$$E = \frac{\pi\hbar}{2\mu T} \tag{3.6a}$$

$$Energy_{mmW} = \frac{1}{2}c\varepsilon_0 E^2 ST \tag{3.6b}$$

$$N = \frac{Energy_{mmW}}{r \times \hbar\omega} \tag{3.6c}$$

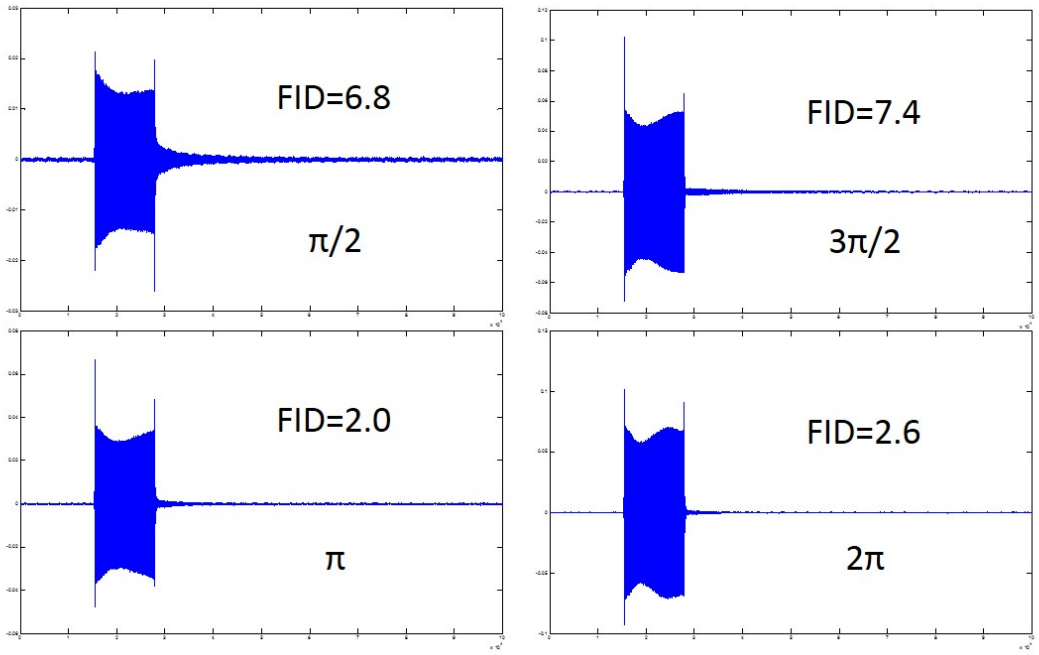

Figure 3-13: Transient nutation with a fixed pulse duration but different amplitudes in the Calcium $36p$-$36s$ transition.

3.2.3 Transient nutation of the excitation millimeter wave pulse

Previously, I introduced a method of using $\pi/2$ transient nutation (absorption/emission) to measure the number density of atoms in a single Rydberg state [113]. In this section, I discuss more generic properties of transient nutation, not only for a single frequency excitation pulse, but also for a chirped pulse. Figure 3-13 shows four different transient nutation signals with different excitation pulse areas ($\pi/2$,π,$3\pi/2$,2π) but the same pulse duration for the Calcium $36p$-$36s$ transition. Figure 3-14 shows two different transient nutation signals with different excitation pulse area ($\pi/2$,π) but the same pulse amplitude. Rabi flopping envelopes are clearly observed superimposed on the excitation pulses. The excitation pulse area can be measured by Rabi flopping angle, or by the amplitude and the phase of the FID. The expected relationships of the excitation pulse and FID are summarized in Table 3.1.

[1]Assume an upward transition here
[2]Population difference, $N_{final} - N_{initial}$

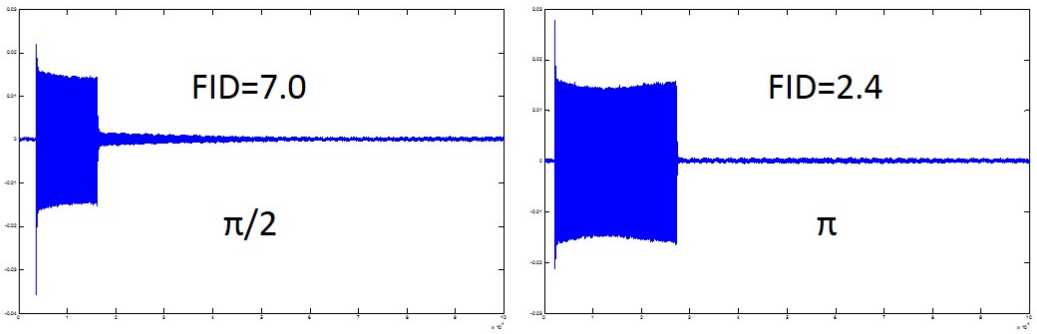

Figure 3-14: Transient nutations with fixed pulse amplitude but different durations for the Calcium $36p$-$36s$ transition.

Table 3.1: Correlations between excitation pulse and FID

	Rabi flopping angle	FID amplitude	$\phi_{ex} - \phi_{FID}$ [1]	ΔN [2]
$\pi/2$	90	maximum	π	0
π	180	minimum	—	1
$3\pi/2$	270	maximum	0	0
2π	360	minimum	—	-1

In Figures 3-13 and 3-14, the envelopes of the excitation pulses and the amplitudes of FIDs qualitatively agree with the predictions in Table 3.1. Non-zero FID at nominal π or 2π pulse associates with the inhomogeneous millimeter wave intensity, which deviates the pulse area. The phase measurement of the excitation pulse and FID are discussed in Section 3.2.5, which also agrees with Table 3.1. I have performed a semi-classical calculation (See Chapter 4) to predict variation of FID amplitudes and population differences with continuous adjustment of the excitation pulse amplitude and pulse duration. To confirm the agreement between the calculations and experiments, I have performed a series of systematic measurements. The FID amplitude measurements are straightforward. To measure the population difference, I apply a second excitation pulse after the main pulse, which polarizes another transition between the final Rydberg state and a third Rydberg state. By monitoring the FID between the second state and the third state, I can measure the population variations of the second state, which is populated by the initial millimeter wave pulse. The calculation and experimental results are plotted in Figures 3-15 and 3-16.

Their agreement is evident. I have not performed experiments to check the calculations in Figure 3-16, which I do not believe would be qualitatively different from the calculations.

In addition to applying a single frequency excitation pulse, I also apply a broadband chirped pulse to polarize the Rydberg-Rydberg transition. McGurk and coworkers [114] point out that if the chirp rate and pulse amplitude obey the Landau-Zener approximation [115, 54], Eq. (3.7), a chirped pulse excitation of a two level system can be treated as adiabatically tuning through an avoided crossing, which is unidirectional and cannot behave as Rabi flopping. My calculations and measurements confirm McGurk's theory. In addition, I find that, compared to a single frequency excitation pulse, the chirped pulse exhibits much larger tolerance for the inhomogeneity of the millimeter wave field, especially for obtaining a π pulse in the population transfer experiment. From Figures 3-15 and 3-16, it is obvious that a too intense single frequency excitation pulse significantly depopulates the final state. However, a too intense chirped pulse does not. Therefore, in population transfer experiments, I always choose a narrow bandwidth chirped pulse ($\sim$100 MHz) with $\sim$3 times more power to induce $\sim$ 100% population transfer, even with an inhomogeneous millimeter wave field.

$$P = \exp\left[-2\pi \frac{|\mu E|^2}{\hbar\,(dE/dt)}\right] \approx 0 \tag{3.7}$$

3.2.4 Interference of the chirped excitation pulse and FID radiation

Due to the gigantic electric dipole transition moment, for a moderately high number density of the atoms in a single Rydberg state, the amplitude of the induced macroscopic polarization is comparable to the amplitude of the excitation pulse. Therefore, I can not only detect the relatively intense FID radiation after the excitation pulse, but can also detect their interference during the excitation pulse. Because the interference amplitude is still $<$ 20% of the excitation amplitude, I can still assume that the excitation and radiation processes are decoupled. The radiation during the

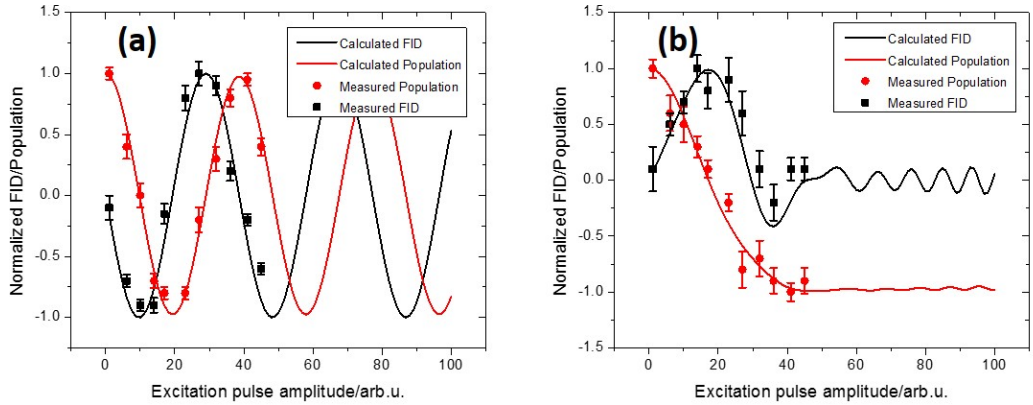

Figure 3-15: Comparison of calculations and experiments with a single frequency excitation pulse (a) and a chirped excitation pulse (b). The pulse duration of the single frequency pulse and chirped pulse are both 500 ns, and the bandwidth of the chirped pulse is 1 GHz. The black curves and dots are the normalized calculated and measured FID amplitudes, and the red curves and dots are the normalized calculated and measured population difference.

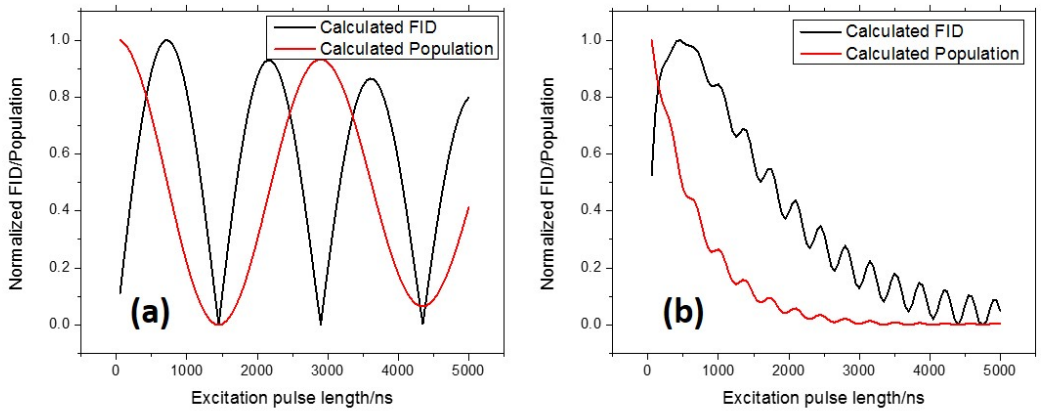

Figure 3-16: The calculated results of a single frequency excitation pulse (a) and a chirped excitation pulse (b). The amplitudes of the single frequency pulse and the chirped pulse are both fixed, and the bandwidth of the chirped pulse is 1 GHz. The black curves are the normalized calculated FID amplitudes, and the red curves are the normalized calculated population difference.

chirp is not strictly Free Induction Decay. However, this radiation still comes from the macroscopic polarization induced by the excitation pulse and is almost decoupled from the excitation pulse in an optically thin medium. If the number density of the atoms in a single Rydberg state is still larger, this assumption would be invalid, which is discussed in Chapter 4. In Figure 3-17, the black curve is a normalized chirped pulse with 500 ns pulse duration and 500 MHz bandwidth. The center frequency of the chirped pulse is resonant with the $36p$-$36s$ transition. An obvious absorption dip at the center of the red curve is observed, and a series of interference beating nodes follows. The frequency of the beating nodes increases linearly because the radiation from the polarization has a single carrier frequency but the excitation pulse is linearly chirped. To extract the resonance frequency, we have two methods: (1) Simply pointing out the position of the absorption dip. The accuracy is limited by the chirp rate and absorption depth, and is typically $\sim$ 10 MHz. (2) Linearly scaling the time axis with the chirp rate and Fourier transforming the scaled beating nodes. The accuracy is limited by the coherence lifetime, and is typically <1 MHz. For transitions with a short lifetime (<100 ns), I can extract high resolution information by measuring the interference pattern instead of FID.

3.2.5 Extraction of Information from the radiation phase shifts

In Figure 3-11, the first two plots correspond to upward transitions and the last two plots correspond to downward transition. This sort of information cannot be obtained from the signal amplitude in the frequency-domain spectrum. In the time-domain, I have two methods to determine the transition direction: (1) Transient nutation. As in Figure 3-18, absorption nutation on the excitation pulse of plot (a) represents an upward transition, and emission nutation on the excitation pulse of plot (b) represents a downward transition. This method is quite simple and straightforward, but requires a single frequency or slowly chirped excitation pulse and relatively strong absorption/emission. If I apply a short, broadband chirped pulse to induce multiple

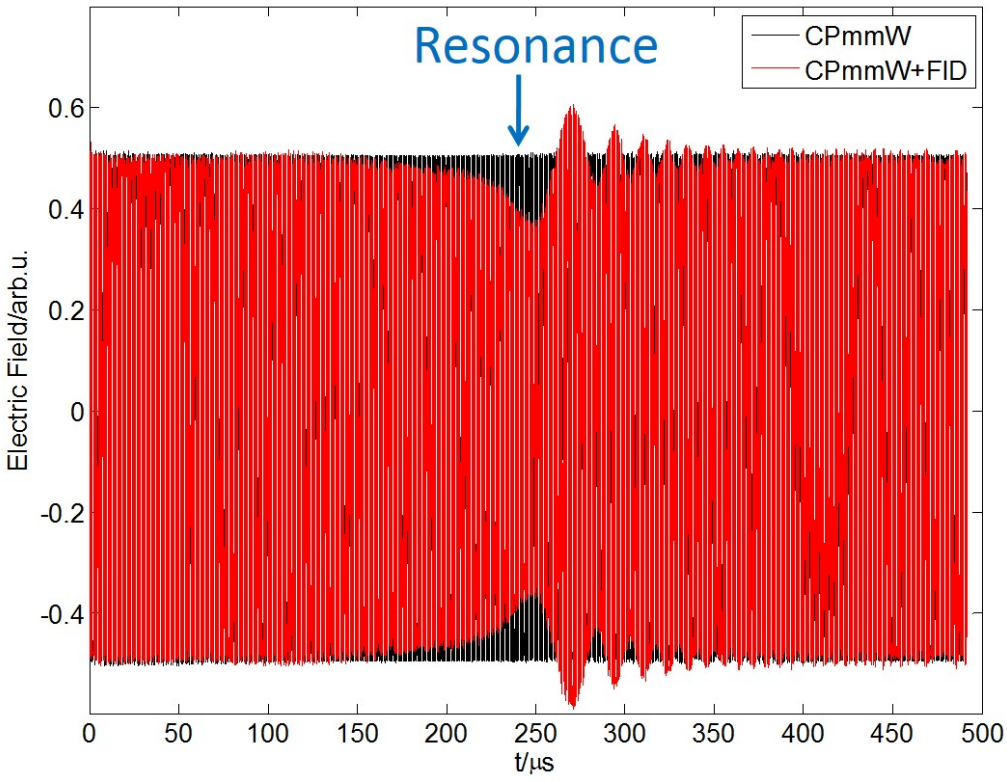

Figure 3-17: Interference of the chirped excitation pulse and the FID radiation. The black curve is a normalized 500 ns length, 500MHz bandwidth chirped pulse. The red curve represents the interference of the chirped pulse and the FID radiation.

transitions simultaneously, this method does not work well. (2) Phase difference of the excitation pulse and the FID. We zoom into the boundary area of the excitation pulse and the FID, and find that for an upward transition, there is a phase discontinuity with a π shift. However, for a downward transition, there is no such phase shift. This method does not have the limitations discussed above. However, the phase shifts are usually not very obvious due to the broadband background noise in the time-domain. Dr. Colombo [116, 52] in our group has developed a technique that first filters the time-domain noise, and then fits and extracts the phase of the excitation pulse and the FID separately in the time-domain. I have developed a complementary technique that applies FFT to extract the phase of the excitation pulse and FID respectively in the frequency-domain. These two methods are essentially the same and have similar accuracy. My method might have advantages for a broadband chirped pulse exciting more than one transition. The Fourier Transform method is more easily understood for a single transition polarized by an excitation pulse with a single frequency, which I discuss first. Then this method is extended to generic situations with multiple transitions that are polarized by a chirped pulse.

The single frequency pump pulse can be Fourier transformed as in Eq.(3.8), in which f_0 is the resonance frequency. The FID has the same resonance frequency, f_0, and can be Fourier transformed as in Eq.(3.9). Different from the excitation pulse, the FID has a t_P shift in the time-domain, which corresponds to an extra $2\pi f_0 t_P$ phase shift in the frequency-domain. t_P is the time interval between the leading edges of the FT-windows of the excitation pulse and the FID, which is approximately the same as the length of the excitation pulse. Since the envelope modulations of the excitation pulse and the FID are much slower than the oscillations of the carrier frequency, they can assumed to be constant. The individual phase of the excitation pulse and the FID can be extracted from the FFT easily and the phase difference can be calculated using Eq.(3.10). If mod($\Delta\Phi/2\pi$)=0, the transition is downward. And if mod($\Delta\Phi/2\pi$)=1, the transition is upward.

$$Pulse(t) = A_P e^{-i(2\pi f_0 t + \phi_P)} \rightarrow Pulse(\omega) = A_P e^{i\phi_P}\delta(\omega - 2\pi f_0) \tag{3.8}$$

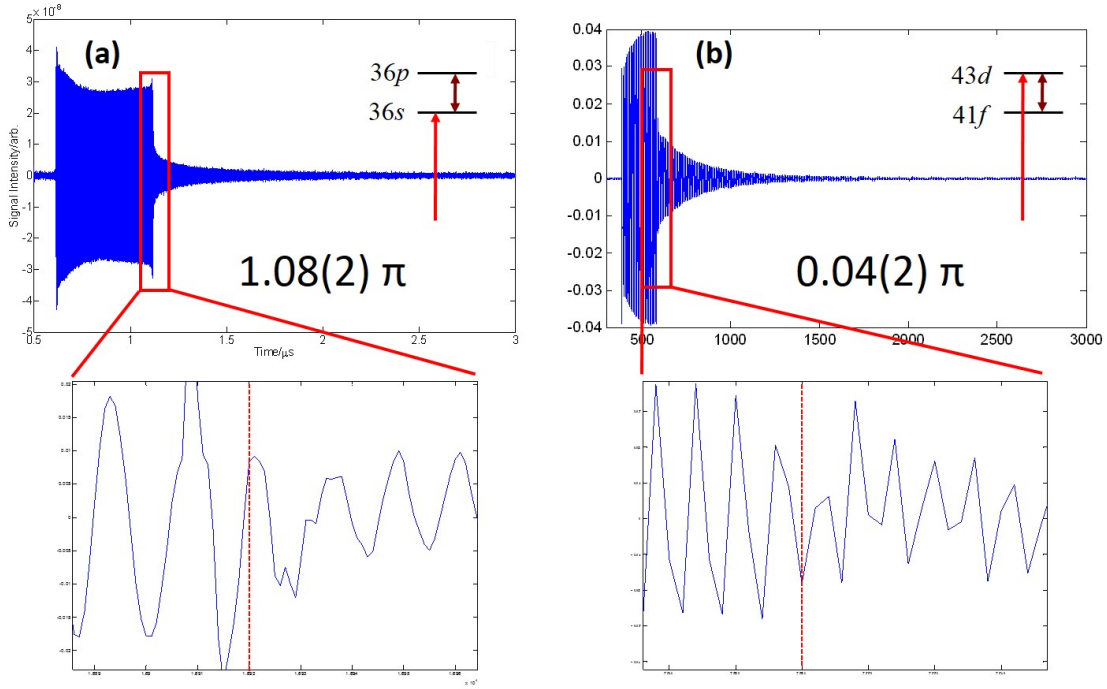

Figure 3-18: Determine the upward or downward direction of the transition based on transient nutation and the phase difference of the excitation pulse and the FID. Plot (a) is $36p$-$36s$ upward transition with absorption nutation and π phase shift. Plot(b) is $41f$-$43d$ downward transition with emission nutation and 0 phase shift. The lower plots expand the boundary area between the excitation pulse and the FID to display the phase continuity/discontinuity. These two transitions are both polarized by single frequency pulses.

$$FID(t-t_P) = A_F e^{-i(2\pi f_0(t-t_P)+\phi_F)} \rightarrow FID(\omega) = A_F e^{i(2\pi f_0 t_P+\phi_F)}\delta(\omega - 2\pi f_0) \quad (3.9)$$

$$\Delta\phi = 2\pi f_0 t_P + \phi_F - \phi_P \quad (3.10)$$

The precise measurement of phase is determined by the precise measurement of resonance frequency, f_0. The errors of ϕ_F and ϕ_P are determined by:

$$\delta\phi_{F/P} = \frac{\delta f_{F/P}}{\Delta f_{F/P}}\pi. \quad (3.11)$$

where Δf is the resonance linewidth and δf is the precision of the center frequency f_0. δf and f_0 are related by, $\delta f = \Delta f/SNR$, where SNR is the signal to noise ratio. Usually, SNR>10 and the errors of ϕ_F and ϕ_P are both less than 0.1π. These errors cannot be directly reduced by reducing the linewidth, because both δf and Δf decrease at the same rate. However, increasing the SNR can linearly increase the accuracy of ϕ_F and ϕ_P. In addition, the errors of ϕ_F and ϕ_P always have the same sign, which can therefore be partially canceled. To make this cancellation better balanced, we choose the same size Fourier transformation window for the excitation pulse, Figure 3-19 Plot (b) and early FID, Figure 3-19 Plot (c). A simulation shows that choosing early FID only instead of total FID can decrease the resultant static phase error ($\phi_F - \phi_P$) by a factor of three. The error of $2\pi f_0 t_P$ comes from the absolute value of δf, but not from the ratio of δf to Δf. For a typical spectrum, δf can be as small as 50 kHz. If the excitation pulse duration t_P=500 ns, the error of $2\pi f_0 t_P$ is only 0.05π. In addition, in the buffer gas cooled beam, the linewidth is one order of magnitude smaller ($\sim$50 kHz), and the absolute value of δf also decreases by a factor of ten ($\sim$5 kHz). Therefore, the phase error of $2\pi f_0 t_P$ can usually be ignored relative to ϕ_F and ϕ_P. The basic procedure of the FFT phase extraction method is summarized in Figure 3-20. The typical total phase error should be no larger than 0.08π.

I have shown the FFT phase extraction method works well for a single frequency excitation of a single transition. To extend this analysis to chirped pulse excitation of

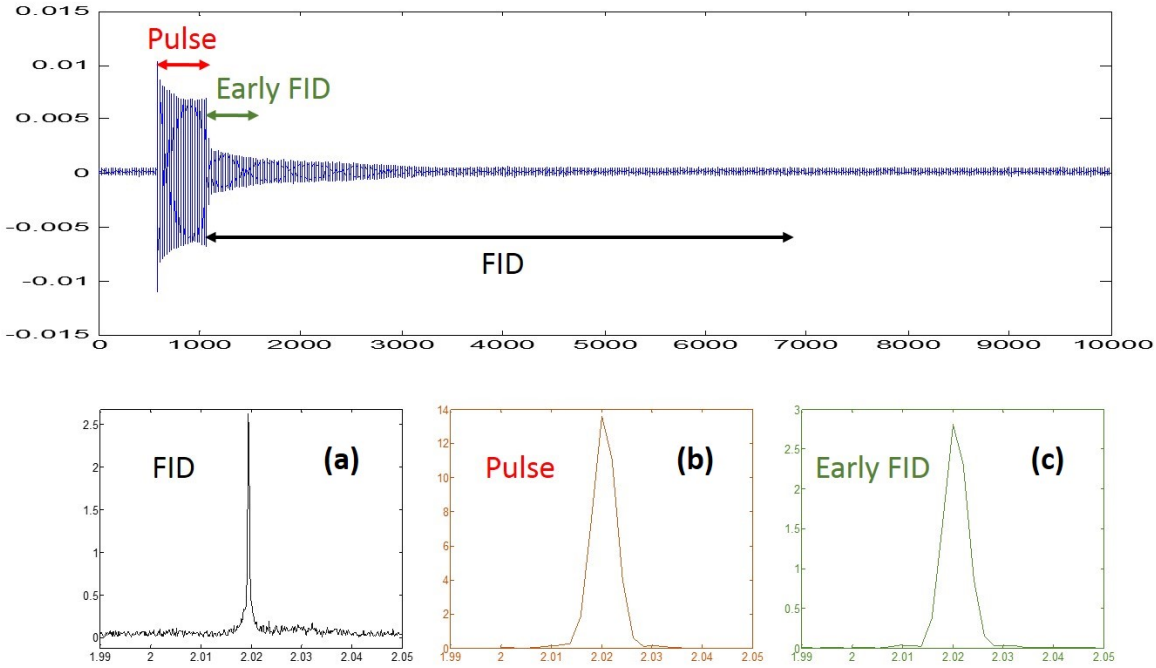

Figure 3-19: Fourier transform of different parts of a spectrum for phase extraction. The top plot shows a single frequency excited FID spectrum of the Calcium $36p$-$36s$ transition. The bottom three plots show the Fourier transformations with different windows. The typical window sizes of the excitation and early FID are 200-500 ns, and the typical window size of the total FID is larger than 5μs.

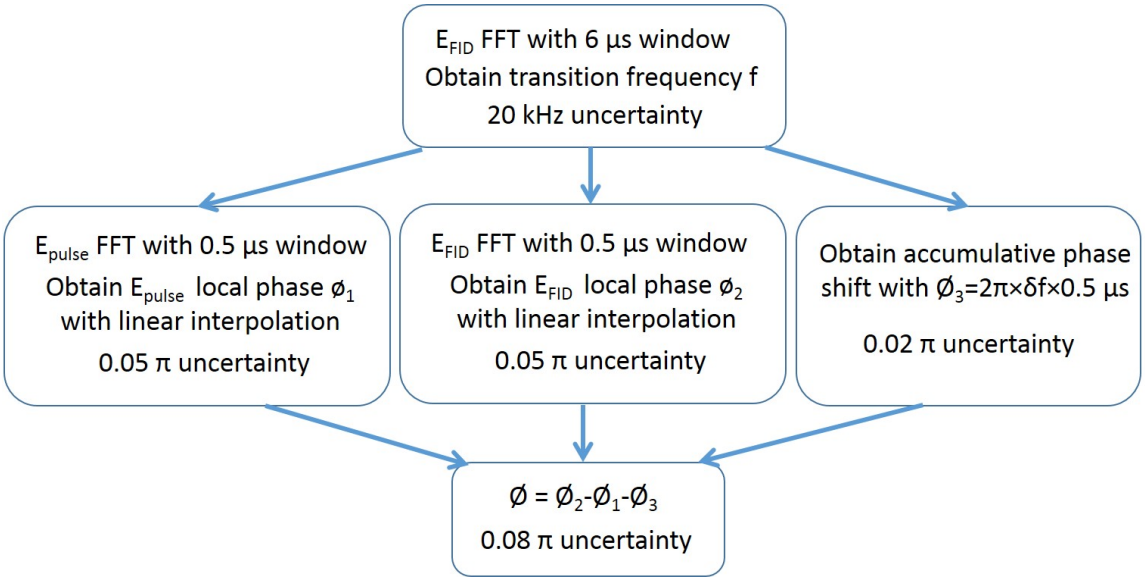

Figure 3-20: Procedure for the phase information extraction and the uncertainties, which are estimated based on supersonic beam experiments. The total uncertainty is the quadratic mean of the three uncertainties. If I consider the cancellation of ϕ_F and ϕ_P, the total uncertainty is reduced to 0.02π. The uncertainties listed in this figure can be reduced by an additional factor of 3 with the data from buffer gas cooled beam experiments.

multiple transitions, I first decompose the FID into multiple single frequency signals:

$$FID(t) = \sum_m A_{Fm} e^{-i(2\pi f_m t + \phi_{Fm})} \rightarrow \sum_m A_{Fm} e^{i\phi_{Fm}} \delta(\omega_m - 2\pi f_m) \rightarrow A_F e^{i\phi_F} \delta(\omega - 2\pi f_0) \tag{3.12}$$

I can assume that all transitions are completely isolated from each other, and the analysis of the FID part reduces to the single frequency case. This assumption is valid for most of our experiments (except for a system that exhibits strong collective effects, discussed in Chapter 4), because typical neighboring transitions in our Rydberg system have >10 MHz spacing, therefore the resonant interaction is 10 MHz/400 kHz = 25 times stronger than the non-resonant interactions (400 kHz is the typical linewidth in the supersonic beam experiment). Thus, the non-resonant component in the FID part can be ignored. However, due to the continuous frequency elements in a linearly chirped pulse, when I can ignore the non-resonant excitation is non-trivial. I evaluate the systematic error of the phase shift from the non-resonant excitation in

a linearly chirped pulse as following:

$$CP(t) = A_{CP}e^{-i(2\pi(f_0+\frac{1}{2}\alpha t)t+\phi_P)} \rightarrow \frac{A_{CP}}{\sqrt{2\pi\alpha}}e^{-i\frac{\pi}{4}}e^{-i\phi_P}e^{i\frac{(\omega-2\pi f_0)^2}{4\alpha\pi}} \tag{3.13}$$

A linearly chirped pulse with chirp rate α can be represented by Eq.(3.13). The Fourier transformation of the linearly chirped pulse has a regular phase shift ϕ_P, a constant phase shift $\pi/4$, and a quadratic frequency dependent phase shift term, which have contributions from non-resonant excitation. For a two-level system, it is easy to show that the non-resonant excitation contribution to the population transfer is $|a_1|^2 = \frac{\omega_R^2}{\omega_R^2+\Delta^2}$. Therefore, if the detuning frequency is larger than 3 times the Rabi frequency (ω_R), non-resonant excitation can be ignored. I substitute $\Delta = \omega_R - 2\pi f_0 = 3\omega_R$ into the last phase term of Eq.(3.13) and find that the systematic phase error ($\delta\phi$) should be proportional to E^2/α ($\omega_R = \mu E/\hbar$, E is the amplitude of the excitation pulse), as in Eq.(3.14). However, E and α are not independent, as in Eq.(3.15). P is the macroscopic polarization, μ is the electric dipole transition moment, and N is the total number of atoms. To keep a fixed excited macroscopic polarization, E must be proportional to the square root of the chirp rate α. Therefore, the systematic phase error is independent of the chirp rate, but depends on the Rabi flopping angle of the excitation, $\delta\phi \propto P^2$. For the maximum Rabi flopping angle ($\pi/2$ excitation), I substitute typical experimental parameters into Eqs.(3.14), (3.15), and show that the systematic phase error is $\sim \pi/2$. To decrease this error below $\pi/20$, I must reduce the excitation from $\pi/2$ to $\pi/6$, which significantly reduces the contribution of the non-resonant excitation.

$$\delta\phi = \frac{9\omega_R^2}{4\alpha\pi} \propto \frac{\omega_R^2}{\alpha} \propto \frac{E^2}{\alpha} \tag{3.14}$$

$$P \propto \frac{\mu E N}{\alpha^{1/2}} \rightarrow E \propto \alpha^{1/2}. \tag{3.15}$$

In addition to reducing the Rabi flopping angle of the excitation, I can also apply two chirped pulses with opposite chirp directions. The systematic phase errors due to the non-resonant excitation coming from above and below the resonance cancels symmetrically. A simulation shows that based on the current signal to noise ratio and

frequency-dependent E-modulations, this cancellation can reduce the phase error by a factor of 10.

3.2.6 millimeter wave photon-echo

The CPmmW technique has not only advantages in recording broadband spectra with high efficiency, but it also is convenient for control of the coherence and population of quantum states. In this section, I show a millimeter wave photon-echo experiment, which demonstrates that I have the ability to perform NMR type spin-echo experiments [117, 118] in the millimeter wave region [119, 120, 121] for Rydberg systems.

As usual, I apply a 10 ns, single frequency pulse (excitation pulse) with $\pi/2$ pulse area to polarize $36p$-$36s$ transition, and the resultant FID lifetime is dominated by inhomogeneous Doppler dephasing (T_2^*). After a $\sim$2 μs waiting time ($\Delta t > T_2^*$), another pulse with the same frequency but π pulse area (rephasing pulse) is applied. The rephasing pulse reverses the phase evolution of all inhomogeneous components. The FID revives (incompletely) after Δt, and then dephases again, as shown in Figure 3-21.

The lifetimes of the initial dephasing FID and the subsequent rephasing echo are both determined by the inhomogeneous T_2^*. The difference is that the former one is T_2^* and the latter one is $2T_2^*$. To bypass the inhomogeneous lifetime T_2^* and measure the homogeneous lifetime T_2 ($T_2 > T_2^*$ here), I record a series of photon echo spectra with different waiting times, as shown in Figure 3-22. The amplitudes of the echo are determined by homogeneous decay over the $2\Delta t$ interval. The homogeneous lifetime, T_2, can be extracted using Eq.(3.16). Normalizing the echo amplitude to the initial FID amplitude cancels the number density fluctuations of the Rydberg populations in different measurements.

$$\frac{A_{echo}}{A_{FID}} = e^{-t/T_2} \tag{3.16}$$

The fitted homogeneous T_2 in Figure 3-23 is 1.3(2) μs, which corresponds to a 230 kHz homogeneous linewidth. This linewidth is smaller than the 450 kHz inho-

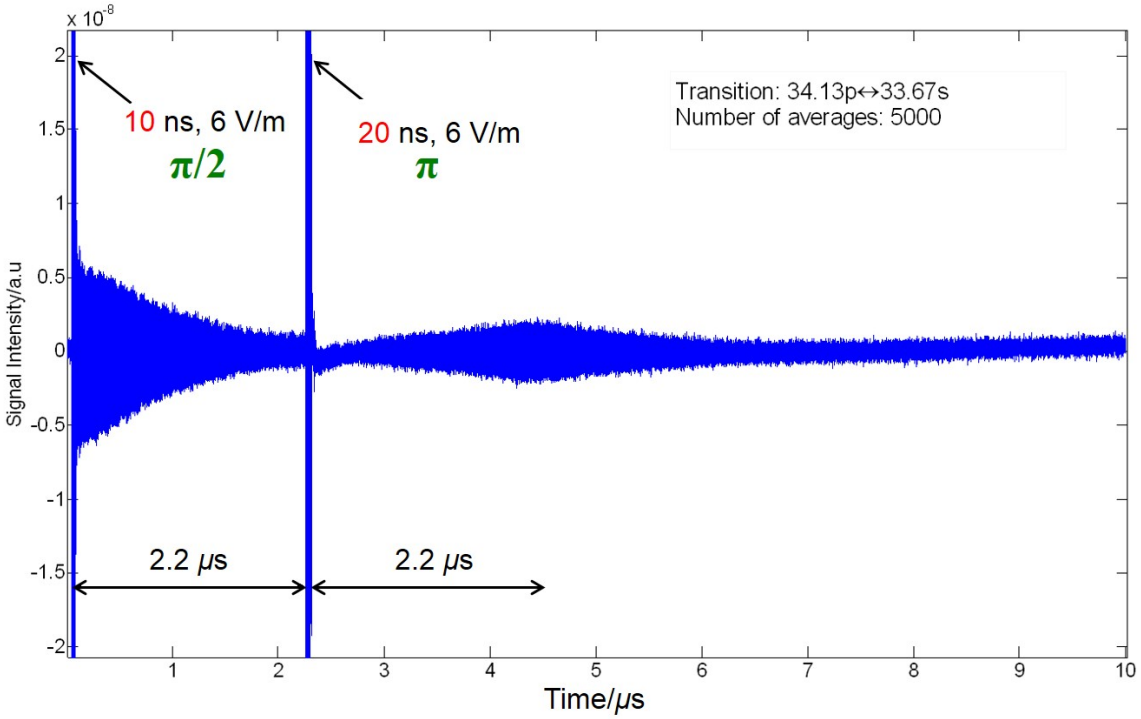

Figure 3-21: A typical millimeter wave $\pi/2 - \pi$ photon-echo spectrum. Excitation pulse ($\pi/2$) is a 10 ns, 6V/m single frequency pulse and the rephasing pulse (π) is a 20 ns, 6V/cm single frequency pulse. The duration of both pulses is far shorter than the dephasing and rephasing times.

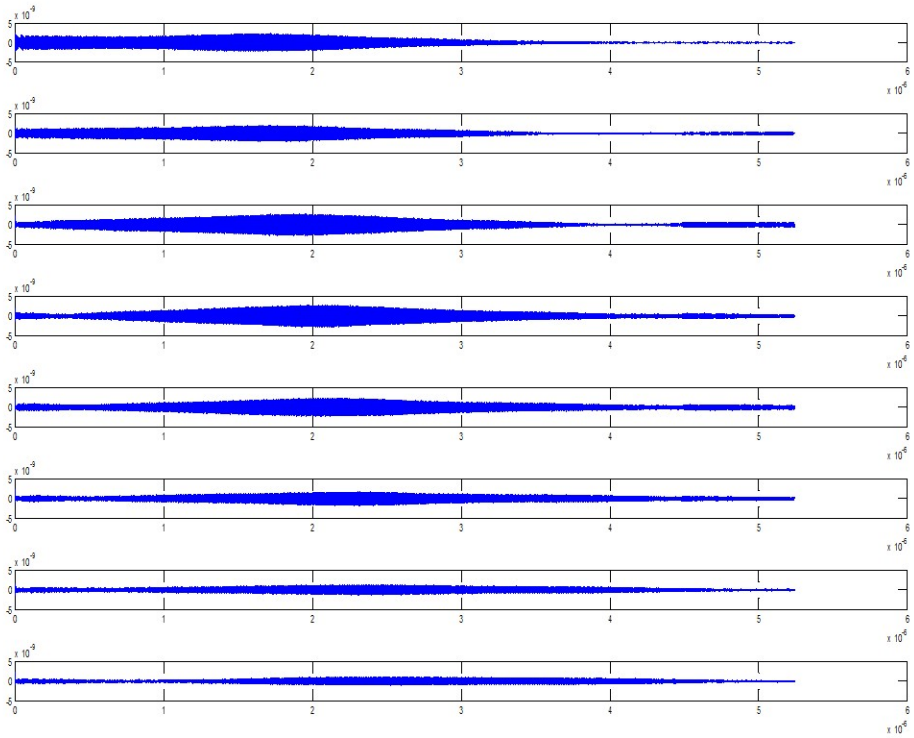

Figure 3-22: Echo signals with different waiting times of excitation-rephasing pulses. The center positions of the rephasing nodes are shifted linearly with the waiting time. The amplitudes of the rephasing nodes are not normalized in this figure. After normalizing to the initial FIDs, the echo amplitudes decay exponentially with increasing the waiting time, as shown in Figure 3-23.

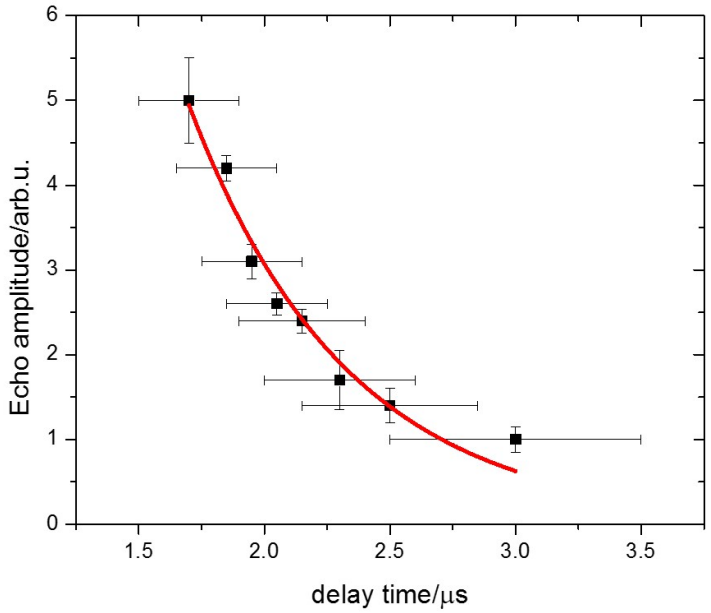

Figure 3-23: Fitting the Homogeneous lifetime from the data of photon-echo experiments. The normalized echo amplitudes are fitted by a single exponential decay to different waiting times. The error bars of the delay time come from the fitting errors of the rephasing node positions. Because the time interval between the initial excitation pulse and the echo is 2×waiting time, the fitted exponential decay lifetime should be $T_2/2$.

mogeneous Doppler linewidth. This measurement suggests that if I could decrease the transverse Doppler broadening, we would improve the spectroscopic resolution up to 230 kHz. I have achieved this in the Argon supersonic beam instead of the Helium supersonic beam, and in the Neon buffer gas cooled beam. How the 230 kHz limitation is overcome is discussed briefly at the end of this chapter.

3.2.7 Populating high-ℓ states using a crafted pulse sequence

I show a proof of principle experiment in which a millimeter-wave pulse sequence is applied to transfer population from low-ℓ to high-ℓ Rydberg states. I apply two laser pulses to initially prepare $57d$ state, and then apply three 10 ns pulses with different frequencies to sequentially excite the $54f$-$57d$, $56g$-$54f$, and $54h$-$56g$ transitions. All three pulses are not exact π pulses. Therefore, in addition to the population

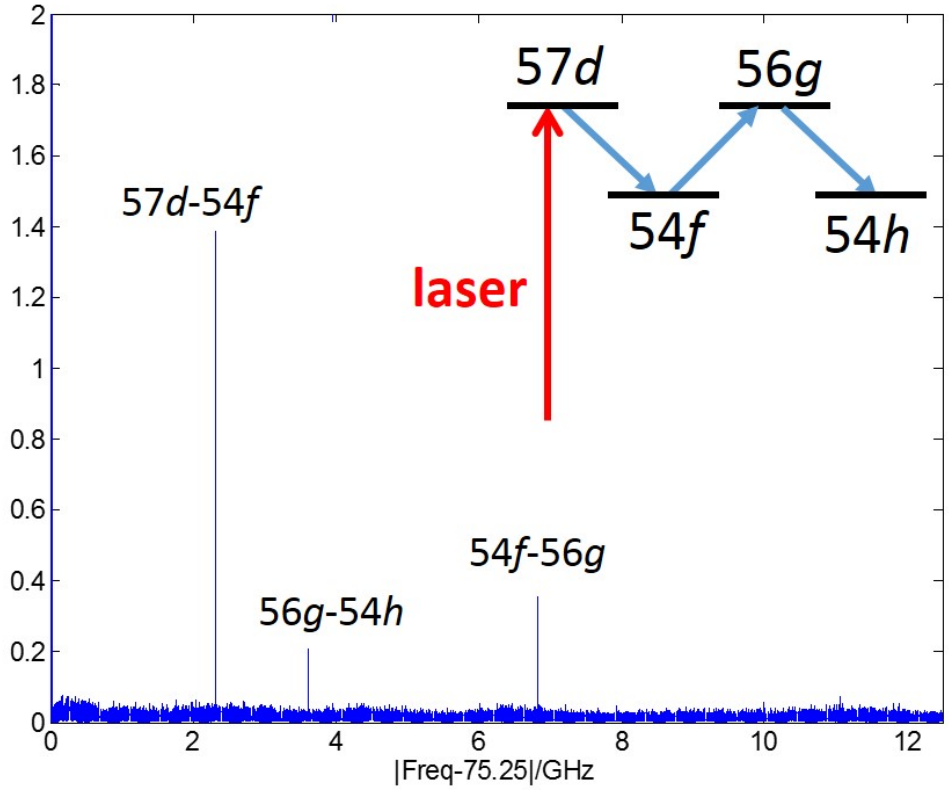

Figure 3-24: Populating high-ℓ states with a crafted pulse sequence. The inset plot shows a schematic diagram of the four energy levels and three transitions that contribute to the spectrum. The 57d state is initially pumped by the laser. Three 10 ns single frequency resonant millimeter-wave pulses sequentially move a part of population from ℓ=2 to ℓ=5. Since no pulse area is chosen to be exact π, each transition undergoes FID and therefore appears in the frequency spectrum.

transfer, strong FID radiation is observed, as shown in Figure 3-24. In principle, I can replace the single frequency pulses by chirped pulses to achieve nearly 100% population transfer efficiency for each step, and to climb up to higher-ℓ states beyond ℓ=5. This technique is applied in molecular Rydberg experiments to prepare core-nonpenetrating states, as discussed in Chapter 5 and Chapter 6.

3.2.8 Evidence for collective effects

Until now, all details of the spectra I have recorded, such as nutation curvature, lifetime, phase shift, and FID amplitude can be explained and simulated by McGurk's

FID formalism [114], in which all atoms are treated as isolated and interacting linearly with the field. However, in a few spectra, some new features appear, which cannot be explained by the usual FID picture. All of these new features occur at relatively high density in the Rydberg gas. In this section, I discuss two examples observed in the supersonic beam apparatus. Such unconventional spectra are observed in most experiments in the buffer gas cooling apparatus, in which the number density of Rydberg atoms is usually much larger. More details of the theoretical calculations are presented in Chapter 4.

Figure 3-25 shows that in a spectrum with N $\sim 3\times10^5 \mathrm{cm}^{-3}$ (the highest number density I can obtain in the supersonic apparatus) of Calcium atoms in a single Rydberg state, early FID and late FID have profoundly different linewidth and lineshape. After a 500 ns single frequency excitation pulse, there is an intense but short-lived early FID, followed by a weak but long-lived late FID. In the frequency domain (Inset plots in Figure 3-25), the early FID has a Lorentzian lineshape (a dominantly homogeneous lineshape is Lorentzian) with $\sim$ 800 kHz linewidth, and the late FID has a Gaussian lineshape (dominantly inhomogeneous dephasing lineshape is Gaussian) with $\sim$ 300 kHz linewidth. To confirm that this effect arises from the optical density of the sample, I decrease the power of the two pumping lasers, which results in a decrease of the number density by a factor of 3. I observe that the amplitude of the early FID decreases by a factor of $\sim$10, and the linewidth is $\sim$ 500 kHz. However, the amplitude of the late FID only decreases by a factor of $\sim$ 3, and the linewidth is unchanged.

In addition to the deviation of lineshape and linewidth of the early FID from McGurk's formalism [114], the curvature of the nutation is also inconsistent with the expectation summarized in Table 3.1. The maximized FID intensity is not created by an excitation pulse with $\pi/2$ nutation curvature. I tune the pulse area by changing the pulse duration in order to measure the dependence of the FID amplitude and the degree of the nutation curvature, as shown in Figure 3-26. Such dependence in dense and dilute Rydberg systems is completely different. At low number density, there is the expected Rabi flopping as the pulse area is measured. However, at high

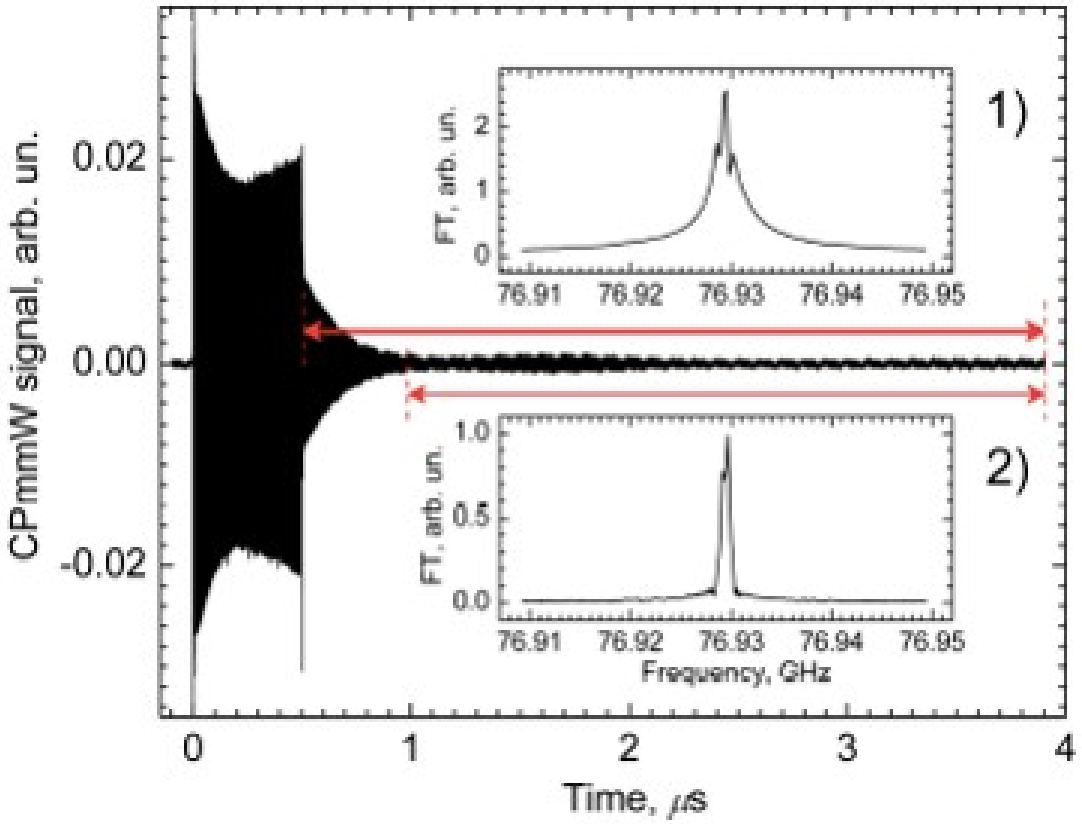

Figure 3-25: Different lineshapes and linewidths of the early FID and the late FID in a spectrum of the Calcium $36p$-$36s$ transition. The FID amplitude is maximized by optimizing the excitation pulse area. However, the nutation curvature deviates from $\pi/2$ significantly. Inset Plot (1) is the magnitude Fourier transform of the entire FID (early FID is dominant, time window indicated by the upper, red double-arrow). Inset Plot (2) is the magnitude Fourier transform of the late FID only (time window indicated by the lower, red double arrow).

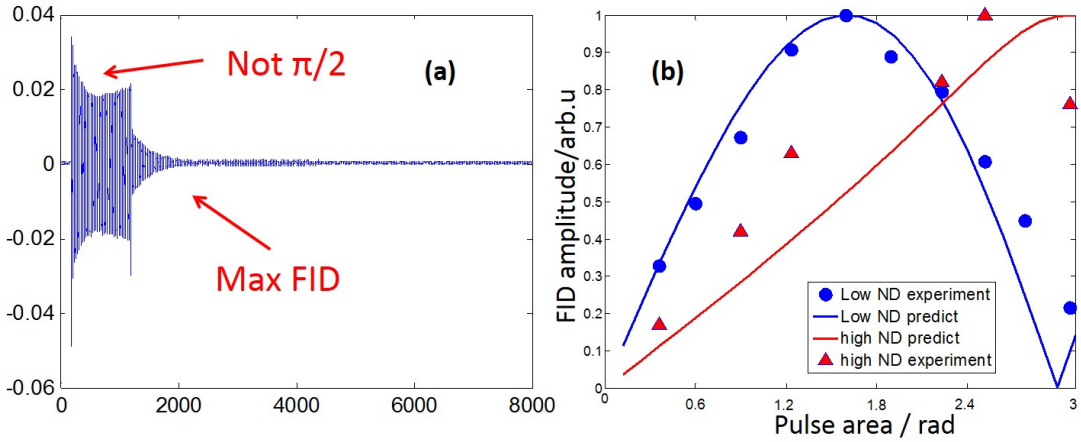

Figure 3-26: Relationship of the FID amplitude modulation and nutation curvature modulation in dense and dilute Rydberg gas. Plot (a) shows deviation from $\pi/2$ nutation curvature at maximized FID amplitude. Plot (b) shows systematic measurements of the relationship of the FID amplitude modulation and nutation curvature modulation to a chamge in the excitation pulse area. The blue circles are measurements at low number density (N $\sim 3\times 10^4 \mathrm{cm}^{-3}$). The red triangles are measurements at high number density (N $\sim 3\times 10^5 \mathrm{cm}^{-3}$). The blue and red lines are the results of the calculation, which agree with the experimental measurements, and is discussed in Chapter 4.

number density, there seems to be saturation. In Chapter 4, I present a semi-classical calculation to model this phenomenon. I find that my model is completely consistent with my current experimental measurements.

3.3 Experiments in the buffer gas cooled beam setup

In Section 2.2, I have shown that the buffer gas cooled beam can increase the beam brightness by a factor of 1000 and decrease the beam velocity by a factor of 10 compared to the supersonic beam. In the present section, I describe the implementation of this setup in the atomic Rydberg system and demonstrate that signal strength and spectroscopic resolution can be significantly improved. In addition, I have a large parameter space in which to study the strong collective effects in the buffer gas cooled beam. The goal of this section is not to describe a repeat of all experiments

in the supersonic beam setup, but to show a few examples that demonstrate the improvement. More new experiments that can be performed on this new setup are proposed in Chapter 4. Such improvement is more significant and important for our experiments on molecules, which is discussed in Chapter 5.

3.3.1 Atomic Rydberg-Rydberg transitions by recording FID radiation

Figure 3-27 shows a typical single-shot FID spectrum of the Barium $40p$-$41s$ transition, obtained without averaging multiple chirps in the buffer gas cooled beam. The current configuration of the interaction volume is shown in Figure 2-34. The interaction volume is 3 cm $\times$ 3 cm $\times$ 20 cm $\sim$200 cm^3, in which the number density distribution is not uniform. To avoid significant superradiant broadening (see Chapter 4), I attenuate the pump laser power to reduce the average number density as low as 1×10^4 cm^{-3}. The total strength of the FID also decreases as the number density is reduced, but I can still observe a single-shot FID signal without averaging. The linewidth in Figure 3-27 is still dominated by the homogeneous superradiant decay. When I decrease the number density by a factor of 10 (1×10^3 cm^{-3}) and average 1000 times, we obtain $\sim$40 kHz spectroscopic resolution. I cannot push this resolution further because: (1) The signal to noise rato decreases rapidly with decreasing number density; (2) Blackbody radiation dephasing limits the coherence time ($\sim$10 μs) at n $\sim$ 40, which corresponds to $\sim$30 kHz linewidth; (3) Although the Doppler broadening of 3 K gas (thermal Doppler) is only $\sim$3 kHz, the Doppler broadening from the unavoidable divergence of the beam (geometric Doppler) can be $\sim$40 kHz. The double peaks in Figure 3-27 are two Doppler components, which are from co-propagation and counter-propagation of the millimeter-wave radiation relative to the atomic beam. By measuring this Doppler splitting, I obtain the buffer gas cooled beam forward velocity, $\sim$ 200 m/s.

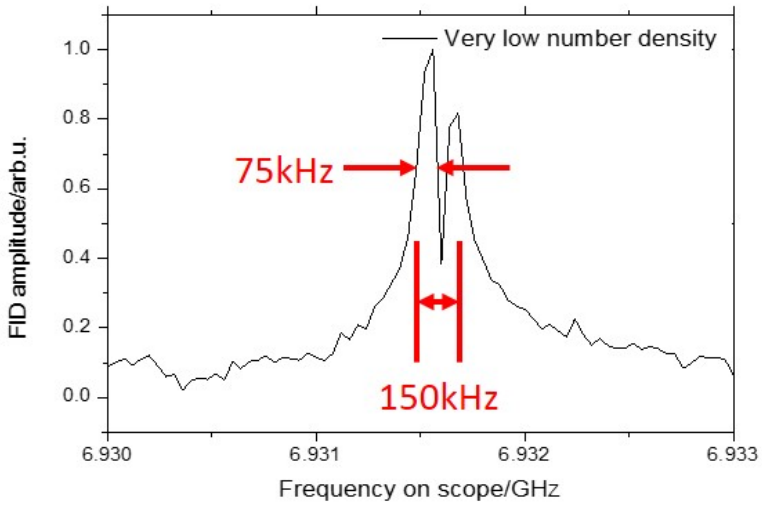

Figure 3-27: An observed single-shot FID spectrum of the Barium $40p$-$41s$ transition in the buffer gas cooled beam at low average number density (1×10^4 cm^{-3}). The splitting, at a 150 kHz separation, is Doppler doublet of the co-propagation and counter-propagation of the millimeter wave relative to the atomic beam. The linewidth of each Doppler component is $\sim$ 75 kHz.

3.3.2 Experimental demonstration of the collective effects

In section 3.2.8, I list several pieces of evidence for collective effects. The limitations of the supersonic beam setup prevent observation of strong collective effects: (1) relatively low number density; (2) relatively large Doppler broadening. These two obstacles are overcome by the buffer gas cooled beam setup. Therefore, much stronger collective effects are expected to be observed. Figure 3-28 shows the envelopes of the radiation field of the Barium $40p$-$41s$ transition (the transition direction is downward). At low number density, the coherence can only be established by the excitation pulse, and the amplitude is maximum at t=0, then decays as a single exponential. However, at high number density, the coherence initiated by the excitation pulse can be amplified in dense Rydberg gas. During this amplification process, the internal energy of a population inverted system is dumping. When the population difference is zero, the amplification terminates, and the coherence is maximal. Then the coherence decays exponentially. Different from the conventional FID picture, the coherence here is not only created by the external excitation pulse, but also contains a significant contri-

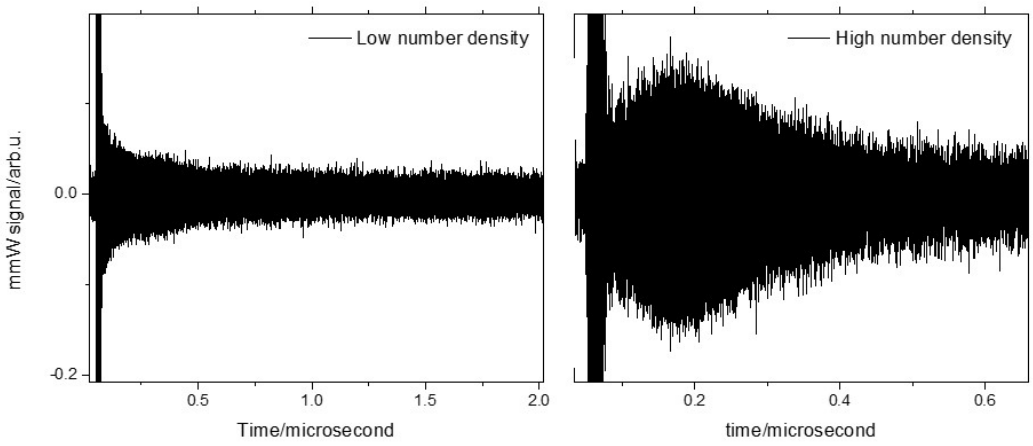

Figure 3-28: A comparison of the radiation field envelope of the Barium $40p$-$41s$ transition in the time-domain in the buffer gas cooled atomic beam. Plot (a) shows the expected single exponential decay at low number density. Plot (b) shows the unexpected fast amplification initially followed by decay. The rates of amplification and decay in Plot (b) are both much faster than the rate of decay in Plot (a). The time scales of these two plots are different.

bution from the population inversion. In addition, the maximum of the coherence amplitude, the rate of amplification, and the decay are time-dependent and strongly depend on the number density of the Rydberg sample. This is discussed in detail in Chapter 4.

Figure 3-29 shows the lineshape and linewidth of the Barium $40p$-$41s$ transition in the frequency-domain, which is obtained by Fourier transformation and is shown in the two plots in Figure 3-28. The linewdith at high number density is much broader than the linewidth at low number density, because of the fast amplification and decay of the coherence. In addition, the center frequency is shifted by 1 MHz. If I examine at Figure 3-29 more carefully, I find that there are two resonant peaks in the spectrum at high number density. One has an $\sim$1 MHz shift and the other does not. If I choose two Fourier transformation windows, as in Figure 3-25, I find that the first peak comes from the early radiation and the second peak comes from the late radiation, which is consistent with my observations from the supersonic beam. Why does the late radiation exhibit relatively weak collective effects? There are two

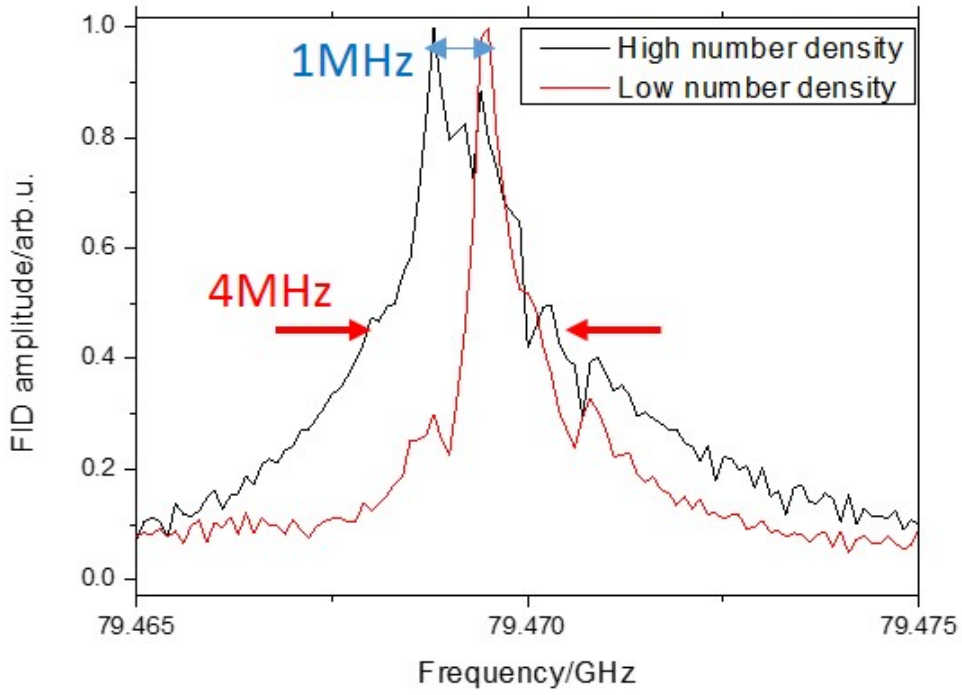

Figure 3-29: A comparison of the lineshape and linewidth of the Barium $40p$-$41s$ transition observed at moderately low and high number density. The line shape in a dense Rydberg gas has 4 MHz linewidth and 1 MHz frequency shift, as the black curve. The line shape in a dilute Rydberg gas has 1 MHz linewidth and almost zero frequency shift relative to the average frequency of the two Doppler doublet in Figure 3-27.

possible contributions: (1) The number density of the Rydberg gas is inhomogeneous. The early strong collective radiation comes from the dense part of the sample, but the late weak collective radiation comes from the dilute part. (2) According to Dicke's formalism [110], the early radiation comes from large ℓ Dicke states, and the late FID comes from small ℓ Dicke states. I believe both contributions exist and how they may be separated is discussed in Chapter 4. In addition, the explanation for the 1 MHz shift is also discussed in Chapter 4.

Chapter 4

Superradiance in a dense Rydberg gas

Superradiance is one example of a collective effect, in which a coherence is created between several atoms contained in a small volume and propagates throughout the entire system by radiative coupling [122, 111, 110, 109, 123, 112]. The details of the initial coherence (initial conditions) and its subsequent propagation (boundary conditions) represent a complete description of the system. This chapter discusses the possibility of using a dense Rydberg gas to observe and study detailed features of superradiance in the millimeter-wave regime. Compared to a millimeter-wave induced rotational transition, Rydberg-Rydberg transitions have enormous electric dipole transition moments and polarizabilities, which are sensitive to external and self-induced electromagnetic fields. In a dense Rydberg gas, a large group of atoms can share an electric field, and absorb and radiate collectively. With carefully designed initial and boundary conditions and the capability for angularly and temporally resolved radiation measurements, subtle light-matter interactions beyond the standard assumptions of isolated emitters and semi-classical approximations can be observed and microscopically characterized. Highly nonlinear coherent control mechanisms such as Self Induced Transparency (SIT) [124, 125, 126], Electromagnetically Induced Transparency (EIT) [88, 87, 86], and Autler-Townes effects [127, 128] can also be studied.

In this chapter, I use a classical picture and a quantum picture with the simplest two-atom model to discuss the essence of superradiance. Second, I briefly discuss the two standard quantum mechanics calculation methods: the Schrödinger picture and the Heisenberg picture. I show that the Schrödinger picture is better for explaining the inter-atomic coupling explicitly in a small area ($L << \lambda$), and the Heisenberg picture is better for calculating the radiation in a large area ($L >> \lambda$). Then, based on my experimental system and combined advantages of the Schrödinger and Heisenberg pictures, I perform a semi-classical calculation to compare the experimental data in Chapter 3 and Chapter 5. In the last section, I propose several new experiments that are planed in the near future.

4.1 What is superradiance?

In this section, I attempt to answer two questions: (1) What is the essence of superradiance? Is it a quantum phenomenon or a statistical phenomenon? (2) When is field quantization necessary and when is it not? For simplicity, I examine two abstract systems consisting of two particles. The classical system consists of two classical dipole oscillators, and the quantum system consists of two two-level dipole polarizable atoms. I calculate the differences in the radiative lifetime and frequency of a collective system and of an isolated system. The calculation methods in this section are not easily extended to a real system with many particles. However, it is easy to capture the fundamental mechanism of the light-matter interaction.

4.1.1 Classical picture

In the classical system, there are two dipole oscillators with the same radiative lifetime and resonant frequency, as shown in Figure 4-1 [8]. For simplicity, I assume the initial phases of the excited oscillators are the same, but this assumption is not generally required. If I assume that these two oscillators are oscillating and radiating

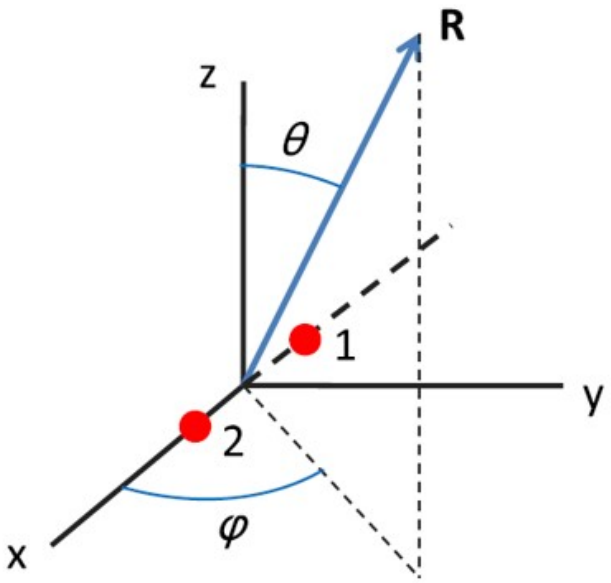

Figure 4-1: Geometry for radiation by two dipole oscillators. Reprinted from [8]

independently, the equation of motion can be described as damped oscillators:

$$\ddot{x}_i + 2\gamma\dot{x}_i + \omega^2 x_i = 0 \tag{4.1a}$$

$$x_i(0) = 0, \dot{x}_i(0) = v_i, \tag{4.1b}$$

where γ is the radiative decay rate of an isolated oscillator, ω is the resonant frequency, and v_i is the initial velocity of the oscillator. The initial total energy of these two oscillators is $W_0 = \frac{1}{2}m(v_1^2 + v_2^2)$. The envelope variation of the oscillator can be obtained by considering the excited state decay rate, γ,

$$x_i = A_i e^{-i\omega t} \rightarrow \dot{A}_i = -\gamma A_i \rightarrow A_i(t) = \frac{iv_i}{2\omega} e^{-\gamma t}. \tag{4.2}$$

It is easy to obtain the radiative electromagnetic field in the far field and the total radiative energy by integrating over time and all angular coordinates,

$$W_r = \int dt \int R^2 d\Omega \left\langle \vec{S} \right\rangle \cdot \hat{R} = W_0 \left(1 + \frac{3\beta \sin\xi}{2\xi}\right) \tag{4.3}$$

where $\left\langle \vec{S} \right\rangle$ is the Poynting vector, R is defined graphically in Figure 4-1, β is $\frac{2v_1v_2}{v_1^2+v_2^2}$, and ξ is the dimensionless distance between the two dipole oscillators, which is defined as $\xi = \frac{2\pi d_0}{\lambda}$ (d_0 is the distance between the two oscillators, λ is the wavelength of the radiation, $\lambda = 2\pi c/\omega$).

Typically, $\frac{3\beta \sin\xi}{2\xi} \neq 0$ and the radiative energy is thus not equal to the initial energy. This violation of energy conservation is not acceptable. It might come from the failure of the initial assumption that the two oscillators are independent. Therefore, I include radiation coupling between two oscillators,

$$\dot{A}_1 = -\gamma A_1 - \gamma_{12}(\xi) A_2 \tag{4.4a}$$

$$\dot{A}_2 = -\gamma A_2 - \gamma_{12}(\xi) A_1 \tag{4.4b}$$

$$\gamma_{12}(\xi) = \gamma \frac{3e^{i\xi}}{2i\xi}\left[1 + \frac{i}{\xi} - \frac{1}{\xi^2}\right], \tag{4.4c}$$

where $\gamma_{12}(\xi)$ is the distance dependent radiative coupling term, which can be derived from classical electromagnetic theory. The solution of Eq.(4.4) is:

$$A_1(t) = e^{-\gamma t}\left[\frac{iv_1}{2\omega} - \frac{iv_2\gamma_{12}(\xi)t}{2\omega}\right] \tag{4.5a}$$

$$A_2(t) = e^{-\gamma t}\left[\frac{iv_2}{2\omega} - \frac{iv_1\gamma_{12}(\xi)t}{2\omega}\right]. \tag{4.5b}$$

The first term inside the bracket is the time-independent initial amplitude, which is the same as Eq.(4.2). The second term is time-dependent and modifies the decay rate (real part) and the radiation frequency (imaginary part). Figure 4-2 shows the distance dependence of the decay rate and frequency shift. If the two oscillators are placed very near to each other, the additional decay rate is similar to the natural decay rate. The frequency shift is divergent at small separation distances, but can be corrected by quantum renormalization theory [129]. That calculation is beyond the scope of this thesis. With increasing distance between the two oscillators, the coupling strength decreases and oscillates about zero. Positive coupling increases the decay rate (superradiance), and negative coupling decreases the decay rate (subradiance). Similar to Eq.(4.3), I can integrate the Poynting vector to obtain the total radiated

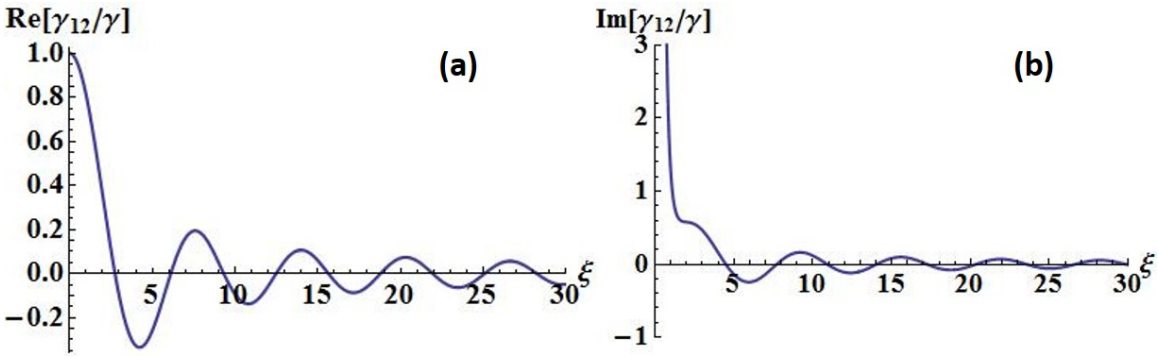

Figure 4-2: Real part (Plot (a)) and imaginary part (Plot (b)) of the extra time-dependent dynamical properties of the two classical dipole oscillators with collective effects.

power,

$$W_r = \int dt \int R^2 d\Omega \left\langle \vec{S} \right\rangle \cdot \hat{R} = W_0. \tag{4.6}$$

The radiated power and initial power are now equal. And the radiation decay rate can be evaluated by,

$$\frac{dW_r}{dt} = 2\gamma e^{-2\gamma t} \left(1 - 2\gamma t\right), \tag{4.7}$$

in which I assume that the two oscillators are placed at the same position. The effective radiation power decay rate is approximately 4γ instead of 2γ. For an N-oscillator system, the rate is expected to be $2N\gamma$. Through the example of two classical dipole oscillators, we find that: (1) Superradiance can happen in a purely classical system; (2) The radiative lifetime is proportional to the number of dipole oscillators in a small volume.

4.1.2 Quantum picture

Although superradiant radiation does not require any quantum mechanism, we are often concerned with the emission of photons from microscopic particles, which must be described by quantum mechanics. In this section, I replace the two classical dipole oscillators with two two-level quantum dipole oscillators, as shown in Figure 4-3. The two atoms are exactly the same, and all other interactions between them except for the radiative coupling can be ignored. Their populations, coherence and electric

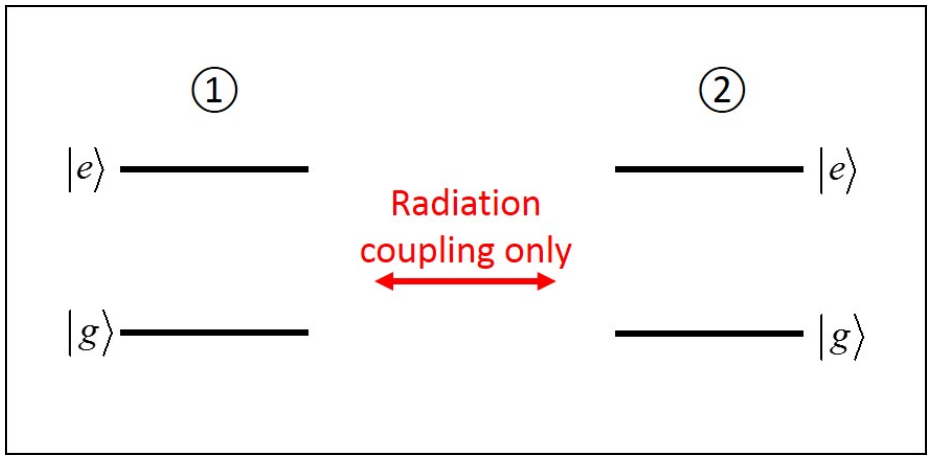

Figure 4-3: The energy diagram of collective two-level quantum dipole oscillators.

dipole transition moments can be described by a density matrix and a dipole matrix,

$$\rho_i = \begin{pmatrix} \rho_{ee,i} & \rho_{eg,i} \\ \rho^*_{eg,i} & \rho_{gg,i} \end{pmatrix}, \mu_i = \begin{pmatrix} 0 & \mu_{eg,i} \\ \mu_{eg,i} & 0 \end{pmatrix} \tag{4.8}$$

where i=1,2 is the index of the two dipole oscillators, e represents the excited state, and g represents the ground state. The polarization of each dipole oscillator, which directly induces the radiation, is

$$P_i = Tr\left(\rho_i \mu_i\right) = 2\mathrm{Re}(\rho_{eg,i})\mu_{eg,i} \tag{4.9a}$$

$$P = P_1 + P_2 = 2\mathrm{Re}(\rho_{eg,1})\mu_{eg,1} + 2\mathrm{Re}(\rho_{eg,2})\mu_{eg,2}. \tag{4.9b}$$

The total polarization is the sum of the two individual polarizations. Coupling the two atoms with the radiation electromagnetic field, I calculate the dynamics of the atoms and radiation field similarly to the classical picture. However, the collective two-level model does not include dipole correlations in the atomic part, but in the radiation field part instead. This physical picture of the dipole-dipole coupling is hidden in the iterations of the atom-field coupling, which is opaque. Dicke proposed to use a stacked multi-level system to replace the two-level system, which will be shown to incorporate the dipole correlations in the atomic part [110].

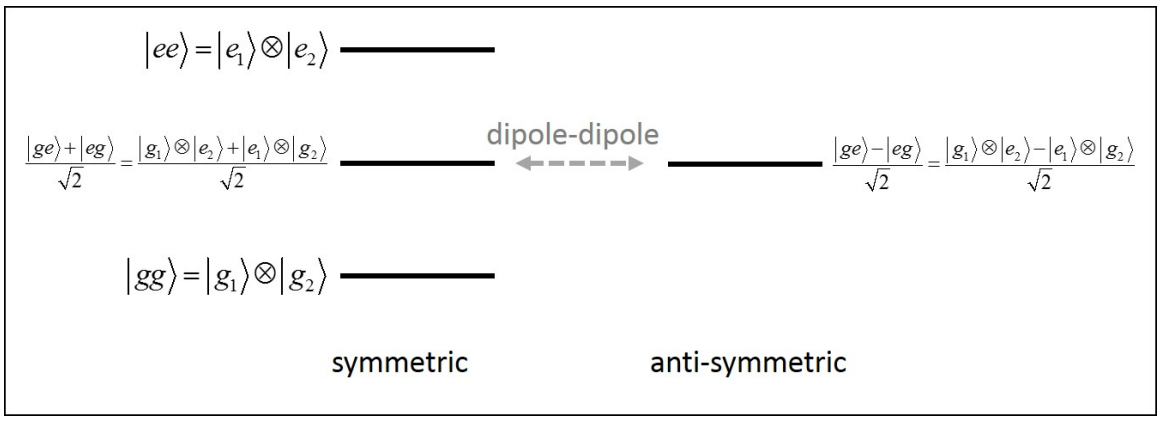

Figure 4-4: Dicke states of a system with two quantum dipole oscillators.

Dicke states are direct products of the atomic states, as in Figure 4-4. The state with the highest energy consists of two excited atoms $|ee\rangle$, and the state with the lowest energy consists of two ground state atoms $|gg\rangle$. The state with intermediate energy can be a symmetric or anti-symmetric superposition of $|ge\rangle$ and $|eg\rangle$. The symmetric state is a "bright" state, which can be polarized by the radiation field and contribute to the superadiant emission. The anti-symmetric state is a "dark" state that is almost isolated and has no contribution to the superradiant emission. To prove the equivalence of the collective two-level model and the symmetric Dicke states, I write the density matrix and dipole matrix of the symmetric Dicke states as Eqs.(4.10) and (4.11).

$$\rho = \begin{pmatrix} \rho_{ee,1}\rho_{ee,2} & \frac{\rho_{eg,1}\rho_{ee,2}+\rho_{ee,1}\rho_{eg,2}}{\sqrt{2}} & \rho_{eg,1}\rho_{eg,2} \\ \frac{\rho^*_{eg,1}\rho^*_{ee,2}+\rho^*_{ee,1}\rho^*_{eg,2}}{\sqrt{2}} & \frac{\rho_{gg,1}\rho_{ee,2}+\rho_{ee,1}\rho_{gg,2}+\rho_{ge,1}\rho_{eg,2}+\rho_{eg,1}\rho_{ge,2}}{2} & \frac{\rho_{eg,1}\rho_{gg,2}+\rho_{gg,1}\rho_{eg,2}}{\sqrt{2}} \\ \rho^*_{eg,1}\rho^*_{eg,2} & \frac{\rho^*_{eg,1}\rho^*_{gg,2}+\rho^*_{gg,1}\rho^*_{eg,2}}{\sqrt{2}} & \rho_{gg,1}\rho_{gg,2} \end{pmatrix} \tag{4.10}$$

$$\mu = \begin{pmatrix} 0 & (\mu_{eg,1}+\mu_{eg,2})/\sqrt{2} & 0 \\ (\mu_{eg,1}+\mu_{eg,2})/\sqrt{2} & 0 & (\mu_{eg,1}+\mu_{eg,2})/\sqrt{2} \\ 0 & (\mu_{eg,1}+\mu_{eg,2})/\sqrt{2} & 0 \end{pmatrix} \tag{4.11}$$

The total polarization evaluated by the density matrix and dipole matrix of the Dicke

states, Eq.(4.12), is the same as Eq.(4.9).

$$P = Tr\left(\rho\mu\right) = 2\mathrm{Re}(\rho_{eg,1})\mu_{eg,1} + 2\mathrm{Re}(\rho_{eg,2})\mu_{eg,2} \tag{4.12}$$

The collective two-level model includes the symmetry information in the Hamiltonian of the light-matter interaction term, which is analogous to the Bloch theory and better suited for numerical calculations. The Dicke model includes this information in the Hamiltonian of the matter term, which gives a more transparent physical picture for describing the collective correlations in a many body system.

Similar to Section 4.1.1, I derive the radiation decay rate of the two-atom system. This derivation is much easier with Dicke states [130]. In the symmetric three level Dicke states, the initial conditions are $\Pi_1(0) = 1, \Pi_0(0) = \Pi_{-1}(0) = 0$ (Π_i, i=1,0,-1, represent the populations of Dicke states). Based on the standard kinetic equation, the decay process of the upper state $|1\rangle$ can be described as in Eq.(4.13a). And in Eq.(4.13b), the left side represents the photon emission rate, and the right side represents the population decay rates of state $|1\rangle$ and $|2\rangle$. Due to energy conservation, the left hand side and right hand side in Eq.(4.13b) must be the same.

$$\frac{d\Pi_1}{dt} = -2\gamma\Pi_1 \tag{4.13a}$$

$$\frac{d\left(2\Pi_1 + \Pi_0\right)}{dt} = 2\gamma\left(\Pi_1 + \Pi_0\right), \tag{4.13b}$$

where γ is the spontaneous decay rate of the excited state of an isolated atom, and Π_1, Π_0, and Π_{-1} are the populations of the upper, intermediate, and lower Dicke states, respectively. The solution to Eq.(4.13) is

$$\Pi_1(t) = e^{-2\gamma t} \tag{4.14a}$$

$$\Pi_0(t) = 2\gamma t e^{-2\gamma t} \approx e^{-4\gamma t}. \tag{4.14b}$$

The decay rate of the upper Dicke state is the same as the regular spontaneous

decay rate, but that of the intermediate Dicke state is approximately twice as large. The radiation decay rate can be obtained easily as in Eq.(4.15), which is the same as Eq.(4.7) derived from the classical theory,

$$\frac{dW_r}{dt} = 2\gamma e^{-2\gamma t}\left(1 + 2\gamma t\right). \tag{4.15}$$

To review the quantum picture: (1) The quantum picture and classical picture give the same radiation decay rate. The superradiant decay rate does not come from any quantum effect; (2) Compared to the collective two-level system, the Dicke states do not involve any new interactions, but they incorporate the symmetry information into the atomic Hamiltonian; (3) The derivation of the superradiant decay rate in Eq.(4.15) does not require any information about the electromagnetic field. Therefore, it is clear that the symmetry, instead of the quantum effects of the matter and the electromagnetic field, is the essence of superradiance. In other words, superradiant emission is directly related to the indistinguishability of the atoms, which is a classical statistical effect. Any interactions that break this symmetry suppress the superradiant emission. In Figure 4-4, the dipole-dipole interaction, which is discussed in Section 4.2.1, couples the bright symmetric states to the dark anti-symmetric states, which reduces the superradiant emission significantly.

4.2 Calculation methods

In the previous section, I used a two-particle model system to discuss the essence of superadiance. However, in most practical experiments, the number of atoms is much larger than two. In this section, I briefly review two conventional fully quantum mechanical calculation methods first, and then describe a simplified semi-classical calculation method, which is much easier to implement and fits the requirements of the Rydberg system. The next two sections follows the discussion of Gross and Haroche [130].

Extending the physical picture of the collective two-level system and Dicke states

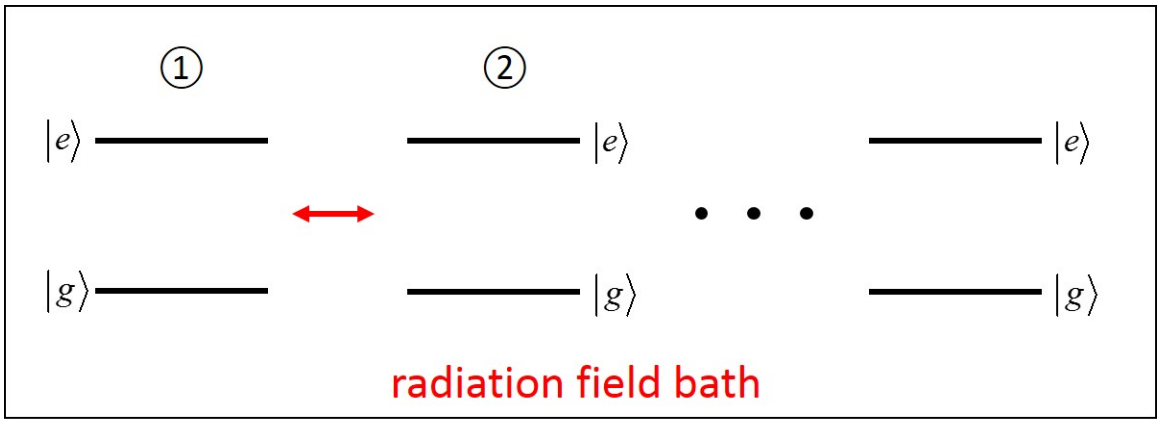

Figure 4-5: Collective two-level model of an N-atom system. The red arrow represents the radiation coupling between two atoms. All atoms are placed in a large radiation field bath. Any radiation fluctuation induce a global response of the entire system.

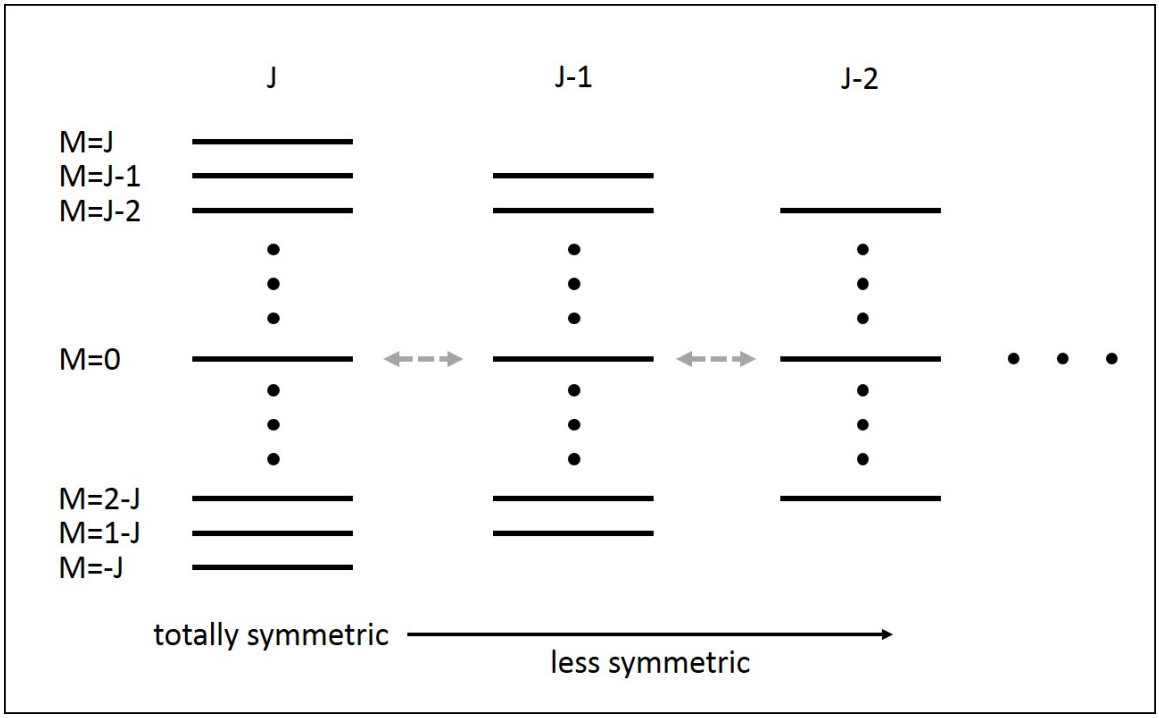

Figure 4-6: Dicke states of an N-atom system. Similar to a collective spin system, J and M are used to label each eigenstate. The left column (max(M)=J) is totally symmetric. The symmetry of the states decreases to the right (max(M)<J). The dashed arrows represent the possible couplings between the columns, such as dipole-dipole interactions. The radiation coupling can couple the neighboring states in each column, but cannot couple the states in different columns.

from two atoms to N-atom does not require new physics, as shown in Figures 4-5 and 4-6. The Hamiltonians of the N-atom system, the electromagnetic field, and the light-matter dipole interaction are

$$H = H_{at} + H_{rad} + V \tag{4.16a}$$

$$H_{at} = \hbar\omega_0 \sum_i D_i^3 \tag{4.16b}$$

$$H_{rad} = \sum_{k\varepsilon} \hbar\omega_k \left(a_{k\varepsilon}^\dagger a_{k\varepsilon} + \frac{1}{2} \right) \tag{4.16c}$$

$$V = -\sum_i \left(E^+(r_i) + E^-(r_i) \right) \cdot D_{ai} \tag{4.16d}$$

$$E^+(r) = -i \sum_{k,\varepsilon} \mathcal{E}_{k\varepsilon} a_{k\varepsilon} e^{ik\cdot r} \tag{4.16e}$$

$$E^-(r) = i \sum_{k,\varepsilon} \mathcal{E}_{k\varepsilon} a_{k\varepsilon}^\dagger e^{-ik\cdot r} \tag{4.16f}$$

$$\mathcal{E}_{k\varepsilon} = \sqrt{\frac{\hbar ck}{2\varepsilon_0 V}} \varepsilon, \tag{4.16g}$$

where ω_0 is the resonant frequency of the atom, D_i^3 represents the population difference of each atom ($\sum_i D_i^3 = M$), k and ϵ label the mode and the polarization of the radiation field, $a^\dagger$ and a are the creation and annihilation operators of the radiation field, D_α is the electric dipole transition moment, and V is an arbitrary quantization volume, which is much larger than the sample dimension.

4.2.1 Schrödinger picture

In the Schrödinger picture, the wavefunction obeys the Schrödinger equation. To focus on the light-matter interaction Hamiltonian, which governs the dynamics of the system, I perform two transformations: (1) Transforming from the Schrödinger representation into the interaction representation, as in Eq.(4.17); (2) Computing the

tracing of the wavefunction over the field variables, as in Eq.(**??**).

$$i\hbar\frac{d\tilde{\Phi}}{dt} = \left[\tilde{V}, \tilde{\Phi}\right] \tag{4.17a}$$

$$\tilde{\Phi} = \exp\left[i\left(H_{at}+H_{rad}\right)t/\hbar\right]\Phi\exp\left[-i\left(H_{at}+H_{rad}\right)t/\hbar\right] \tag{4.17b}$$

$$\tilde{V} = \exp\left[i\left(H_{at}+H_{rad}\right)t/\hbar\right]V\exp\left[-i\left(H_{at}+H_{rad}\right)t/\hbar\right] \tag{4.17c}$$

where $\tilde{\Phi}$ and $\tilde{V}$ are the wavefunctions and light-matter interaction term transformed into the interaction representation with the zeroth-order Hamiltonian $H_{at}+H_{rad}$. With straightforward integration and iteration, I obtain an integro-differential equation to describe the state evolution of the atoms,

$$\frac{d\tilde{\rho}}{dt} = -\frac{1}{\hbar^2}Tr_{rad}\int_0^t d\tau\left[\tilde{V}(t),\left[\tilde{V}(t-\tau),\tilde{\Phi}(t-\tau)\right]\right] \tag{4.18a}$$

$$\tilde{\rho}(t) = Tr_{rad}\tilde{\Phi}(t). \tag{4.18b}$$

To solve Eq.(4.18), I apply two approximations, the Born and Markov approximations, to cut off the past time integration over the atoms and all field modes. The Born approximation neglects the build-up of correlation between the atoms and the field ($\tilde{\Phi}(t-\tau)\rightarrow\tilde{\rho}(t-\tau)\otimes|0\rangle_{radrad}\langle 0|$). The Markov approximation neglects the atom-field correlation time relative to the evolution time of the atomic system ($\tilde{\rho}(t-\tau)\rightarrow\tilde{\rho}(t)$). These two approximations are always correct if there is no cavity to suppress the decay of the field coherence. The evolution of the atomic quantum state can be described by the superradiance master equation in the Schrödinger picture:

$$\begin{aligned}\frac{d\rho}{dt} &= \frac{1}{i\hbar}\left[\sum_i H_j,\rho\right] - \frac{cd^2}{16\varepsilon_0\pi^3\hbar}\int_0^\infty d\tau\int_0^\infty k^3dk\int\Omega(\varepsilon\cdot\varepsilon_a)^2\sum_{ij}\exp\left[ik\cdot(r_i-r_j)-ick\tau\right]\\ &\times\left[D_i^+\exp\left(-\frac{iH_j\tau}{\hbar}\right)D_j^-\exp\left(\frac{iH_j\tau}{\hbar}\right)\rho-\exp\left(-\frac{iH_j\tau}{\hbar}\right)D_j^+\exp\left(\frac{iH_j\tau}{\hbar}\right)\rho D_i^-\right]+h.c.\end{aligned} \tag{4.19}$$

To explicitly solve Eq.(4.19), it is necessary to know precise information about the atomic spatial distribution. When all atoms are confined in a small volume, it is pos-

sible to make an approximation that all atoms are placed at the same position. This assumption automatically guarantees that the system is fixed in the completely symmetric Dicke state, which induces a perfect case of superradiance. The superradiant master equation can be simplified significantly. This approximation is questionable and discussed later. With this approximation, the real part of the master equation is

$$\left(\frac{d\rho}{dt}\right)_{real} = -\frac{\Gamma}{2}\left[D^+D^-,\rho\right]_+ + \Gamma D^-\rho D^+ \tag{4.20}$$

where $\Gamma = k_0^3 d^2/(3\pi\varepsilon_0\hbar)$ is the single atom spontaneous emission rate. To evaluate the matrix elements, I project the operators in Eq.(4.20) onto the Dicke states, shown in Figure (4-6),

$$\frac{d\rho_M}{dt} = -\Gamma(J+M)(J-M+1)\rho_M + \Gamma(J+M+1)(J-M)\rho_{M+1}. \tag{4.21}$$

Equation.(4.21) describes the decay rate of the M-state. It is easy to find that the M=J state has the same decay rate as the atomic spontaneous emission, and the M=0 state has the largest decay rate (enhanced by a factor of J^2). The imaginary part of the master equation is

$$\left(\frac{d\rho}{dt}\right)_{imag} = \frac{1}{i\hbar}\left[\sum_i D_i^- D_i^+,\rho\right]_- . \tag{4.22}$$

Equation.(4.22) gives the collective Lamb shift. If there is only one atom, this shift converges to the ordinary Lamb shift. However, if the approximation that all atoms are placed at the same position is relaxed, which is not a good description for typical experiments, there is a pre-factor on the right hand side of Eq.(4.20) to reduce the superradiant emission rate. In the classical picture, this pre-factor is the real part of Eq.(4.4c). In the quantum picture, it has a similar format

$$F_{ij}(r_{ij}) = \left[1-(\varepsilon_a\cdot\hat{r}_{ij})^2\right]\frac{\sin kr_{ij}}{kr_{ij}} + \left[1-3(\varepsilon_a\cdot\hat{r}_{ij})^2\right]\left[\frac{\cos kr_{ij}}{(kr_{ij})^2} - \frac{\sin kr_{ij}}{(kr_{ij})^3}\right]. \tag{4.23}$$

Both Eqs.(4.4c) and (4.23) have a similar distance dependence, as shown in Figure

4-2. In addition, the small displacement of each atom not only decreases the superradiant emission rate, but also induces a frequency shift. In the classical picture, the frequency shift comes from the imaginary part of Eq.(4.4c). In the quantum picture, it comes from the imaginary part of Eq.(4.19),

$$\left(\frac{d\rho}{dt}\right)_{imag} = \frac{1}{i\hbar}\left[\sum_{i>j}\Omega_{ij}D_iD_j,\rho\right]_- \tag{4.24a}$$

$$\hbar\Omega_{ij} = \frac{d^2}{4\pi\varepsilon_0 r_{ij}^3}\left[1-3(\varepsilon_a\cdot\hat{r}_{ij})^2\right]. \tag{4.24b}$$

It is clear that Eq.(4.24) is just the electrostatic Van der Waals dipole-dipole interactions between the atoms. From the above discussion, I know that: (1) If all atoms are placed at the same position, the superadiant emission rate is fastest, and the frequency shift is a collective Lamb shift; (2) If the atomic gas is completely homogeneous (neighboring atoms are placed with the same distance, δr), the superradiant emission rate is suppressed by a factor of F(δr), and there is an extra dipole-dipole frequency shift $\Omega(\delta r)$; (3) If the atomic gas is inhomogeneous (the distances between the neighboring atoms are not the same), the pre-factor of the superradiant emission rate is the average of $F(r_{ij})$, and the dipole-dipole interaction not only induces a frequency shift, $\langle\Omega_{ij}\rangle$, but also broadens the linewidth, $\sqrt{\langle\Delta\Omega_{ij}^2\rangle}$.

4.2.2 Heisenberg picture

The Schrödinger picture is good for describing problems in a small symmetrical subspace of the full Hilbert space. However, if the sample dimension is larger than the wavelength, not all atoms can participate in the collectivity and be described by Dicke states. Therefore, the Schrödinger picture is applicable, but inconvenient. The Heisenberg picture does not require Dicke states and is straightforward to extend it from a small volume to a large volume. In addition, the formalism of the Heisenberg picture is much closer to the semi-classical light-matter interaction.

In the Heisenberg picture, two new physical observables, which are equivalent to

the wavefunction in the Schrödinger equation, are population difference and polarization, defined as

$$N(r) = \sum_i \delta(r - r_i) D_i^3 \tag{4.25a}$$

$$P^{\pm}(r) = d\varepsilon_a \sum_i \delta(r - r_i) D_i^{\pm}. \tag{4.25b}$$

The physical observables, such as population difference, N, electric field, E, and polarization, P, evolve according to the Heisenberg equation of motion,

$$\frac{dX}{dt} = \frac{1}{i\hbar}[X, H]. \tag{4.26}$$

I insert these three physical observables into the Heisenberg equation and obtain the equations of motion,

$$\frac{\partial N}{\partial t} = \frac{i}{\hbar} E^- \cdot \left(P^+ - P^-\right) + \frac{i}{\hbar}\left(P^+ - P^-\right) \cdot E^+ \tag{4.27a}$$

$$\frac{\partial P^+}{\partial t} = i\omega_0 P^+ + 2i\frac{d^2}{\hbar}(\varepsilon \cdot \varepsilon_a)\left(E^- N + N E^+\right) \tag{4.27b}$$

$$\frac{\partial^2 E^+}{\partial t^2} - c^2 \nabla \times \nabla E^+ = \frac{1}{\varepsilon_0}\frac{\partial^2 P^-}{\partial t^2}, \tag{4.27c}$$

where Eq.(4.27a) describes the evolution of the atoms, Eq.(4.27b) describes the evolution of the light-matter interaction, and Eq.(4.27c) describes the propagation of the field. These equations are known as the Bloch-Maxwell equations. Similar to the transformation from the Schrödinger picture into the interaction picture, I can apply

$$\mathbf{E}^{\pm} = \mathcal{E}^{\pm}(z,t) \exp\left[\mp i(\omega_0 t - k_0 z)\right] \varepsilon_a \tag{4.28a}$$

$$\mathbf{P}^{\pm} = \wp^{\pm}(z,t) \exp\left[\pm i(\omega_0 t - k_0 z)\right] \varepsilon_a. \tag{4.28b}$$

Equations.(4.28) separate the slow envelope variation of the electric field and polarization from the fast carrier frequency. More profoundly, this factorization also

includes the Born-Markov approximation in the Schrödinger picture.

$$\frac{\partial N}{\partial \tau} = \frac{i}{\hbar}\left(\wp^{+}\mathcal{E}^{+} - \mathcal{E}^{-}\wp^{-}\right) \tag{4.29a}$$

$$\frac{\partial \wp^{+}}{\partial \tau} = \frac{2id^{2}}{\hbar}\mathcal{E}^{-}N \tag{4.29b}$$

$$\frac{\partial \mathcal{E}^{+}}{\partial z} = \frac{i\omega_{0}}{2\varepsilon_{0}c}\wp^{-}, \tag{4.29c}$$

where $\tau = t - z/c$ is the time in the retarded frame. The Heisenberg picture has thus been demonstrated to be equivalent to the Schrödinger picture. From Eqs.(4.29), it is not easy to extract information about the emission rate and frequency shift, which are obvious in Eq.(4.19). However, the Heisenberg picture is convenient to obtain a numerical solution and does not require the assumption of a small volume. Therefore, to calculate the superradiant emission in a large volume with significant propagation effects, the Heisenberg picture is more advantageous. In addition, it is necessary to notice that, due to field quantization, N and P on one side and E^{+} and E^{-} on the other side are non-commuting. This non-commutation is necessary for initializing spontaneous radiation, but is unnecessary for typical propagation calculations. In addition, if the initial coherence is not established by spontaneous emission, as in our Rydberg experiments where initial coherence is created by an external field, field quantization is not necessary. The Heisenberg method can be simplified into the semi-classical theory directly, which is the subject of the next subsection.

4.2.3 Simplified semi-classical calculation

The semi-classical calculation method uses a similar Bloch-Maxwell equation, Eq.(4.27), but without the non-commuting properties of the electric field and polarization operators [131, 132, 133, 134, 135, 136, 137, 138]. The Bloch equation can be extended from a two-level system to a multi-level system directly. And the Maxwell equation includes the propagation effects of the radiated electromagnetic field in a large volume. Another advantage of using the Bloch equation is the convenience of including phenomenological longitudinal decays in the diagonal matrix elements and transverse

decays in the off-diagonal matrix elements. Such phenomenological decay rates can either be measured in the experiments or calculated by the Schrödinger method, such as in Eq.(4.23), which is demonstrated in Section 4.3. To simplify further, the classical description of the radiation electromagnetic field does not need to be included in the Hamiltonian. To ensure energy conservation, the electric field E in Eq.(4.30) is treated as the local electric field, $E_{input} + E_{radiation}$, which must be evaluated iteratively until self-consistency is achieved. Therefore, the Hamiltonian of N atoms interacting with an electric field via an electric dipole transition moment is:

$$H = H_0 + V(t) = H_0 + \hbar \sum_{j \neq 1} (|j\rangle \, \Delta\omega_{1j} \, \langle j| + |1\rangle \, \mu_{1j} E(t) \, \langle j|), \tag{4.30}$$

where H_0 is the Hamiltonian of the N non-interacting atoms, $\Delta\omega_{1j} = \omega_{1j} - \omega$ is the detuning of the millimeter wave frequency, μ_{1j} is the transition dipole moment between the initial state and the jth state. In this Hamiltonian, I assume that all atoms are placed at the same position. The effect of deviation from this assumption is included in the phenomenological longitudinal decays and transverse decays.

Numerical solution of the Bloch-Maxwell equations is achieved by transformation to a frame rotating at the electric field carrier frequency. Following the rotating wave approximation (RWA), the far off-resonant components are discarded. For a two-level system, the transformed equations are the conventional Bloch equations. For a multi-level system, a group of coupled first-order partial differential equations is obtained, which has n-1 diagonal and 2(2n-3) density matrix elements. For the Maxwell equation, the rotating frame transformation also removes fast oscillations, which have no significant effect here. The transformation from the local time frame to a retarded time frame further simplifies the description to a first order ordinary

differential equation:

$$i\hbar\frac{\partial\sigma}{\partial t} = [V_r, \sigma] \tag{4.31a}$$

$$V_r = U^\dagger V U \tag{4.31b}$$

$$\rho = U\sigma U^\dagger, \tag{4.31c}$$

where ρ, V and μ are the density matrix, electric dipole interaction operator, and electric dipole transition moment in the non-rotating frame, σ and V_r are the corresponding operators in the frame rotating at the electric field carrier frequency, and U is the unitary transformation matrix between these two frames. The polarization is described by:

$$P = 2\left[P_r\cos\left(\omega t - kz\right) - P_i\sin\left(\omega t - kz\right)\right] = NTr\left(\rho\mu\right), \tag{4.32}$$

where P_r and P_i are the real and imaginary parts of the macroscopic polarization, which are induced by the real and imaginary parts of the electric field. N is the number density of molecules in a specific quantum state. The spatial dependence of the electric field is

$$\frac{d\varepsilon_{i,r}}{dz} = \frac{2\pi\omega}{c}P_{i,r}. \tag{4.33}$$

The computer program described in Section 4.3 can numerically solve the coupled differential equations, (4.31), (4.32) and (4.33) to obtain the dynamics of superradiance[109]. The details of the calculation are discussed in the next section.

4.3 Semi-classical calculations of a dense Rydberg gas

In this section, I apply the semi-classical method to calculate the quantum state evolution of the Rydberg atoms and the dynamics of the superradiant millimeter-wave emission in a dense Rydberg gas [133]. The initial polarization can be induced by

spontaneous photons, blackbody radiation photons, or external excitation photons. However, the number of blackbody photons (the number of 100 GHz millimeter-wave photons in one mode of room temperature blackbody radiation is about 80) and external excitation photons (the number of photons in a weak chirped pulse (2nW, 50ns), is more than 10^6) is typically much larger than the number of vacuum fluctuation photons. Therefore, only the initial polarization induced by the blackbody radiation and the external chirped pulse are considered in our typical experiments. Due to the initial photon number being much larger than 1 in a mode, the semi-classical approximation is always valid. The millimeter-wave radiation can be treated as a classical electromagnetic field without a need for field quantization. I do not attempt to show all possible results of these calculations in thre present section. I only highlight the most interesting and unexpected results.

4.3.1 Two-level System

The coherence and population dynamics in an inverted two-level system are discussed here. The population in the upper state of the inverted two-level system can be prepared by optical or infrared pumping from an energetically remote non-Rydberg state. The lower state of the inverted two-level system is a neighboring Rydberg state with $|\Delta n| = 1$ or 2, and $|\Delta l| = 1$ without any initial population. The initial condition of the millimeter-wave transition is that the population starts in the upper state and both states are nondegenerate and energetically distant from any perturbing states. In a typical rotational spectrum with a small electric dipole transition moment, each molecule usually radiates independently without coupling to other molecules. However, in a dense Rydberg gas with large electric dipole transition moments, many molecules are coupled together via a shared radiation field, and are therefore excited and radiate cooperatively.

I define the input pulse as a rapidly oscillating carrier frequency ω, and a slowly oscillating envelope $\mathcal{E}(t)$, where $\mathcal{E}_r$ and $\mathcal{E}_i$ are the real and imaginary parts of the

complex electric field:

$$E(z,t) = 2\left[\mathcal{E}_i(t)\cos\left(\omega t - kz\right) + \mathcal{E}_r(t)\sin\left(\omega t - kz\right)\right]. \tag{4.34}$$

For a single-frequency pulse:

$$\mathcal{E}_i(t) = \frac{1}{2}E_0 \tag{4.35a}$$

$$\mathcal{E}_r(t) = 0. \tag{4.35b}$$

For a linearly-in-time chirped pulse:

$$\mathcal{E}_i(t) = \frac{1}{2}E_0\cos\left(\frac{1}{2}\alpha t^2\right) \tag{4.36a}$$

$$\mathcal{E}_r(t) = -\frac{1}{2}E_0\sin\left(\frac{1}{2}\alpha t^2\right), \tag{4.36b}$$

where α is the chirp rate.

The Hamiltonian of the semi-classical system is:

$$H = H_0 - 2\mu\left[\mathcal{E}_i\cos\left(\omega t - kz\right) + \mathcal{E}_r\sin\left(\omega t - kz\right)\right], \tag{4.37}$$

where H_0 is the atomic Hamiltonian and μ is the electric dipole transition moment. Considering the atomic two-level basis, the matrix form of the Hamiltonian can be written as Eq.(4.38). There are two ways to separate the zeroth-order Hamiltonian and interaction terms. The first form is in Eq.(4.38a), which treats the atomic Hamiltonian as zeroth-order. Therefore, the interaction term includes only the off-diagonal dipole interaction. The second form is in Eq.(4.38b), which treats the dressed atomic Hamiltonian as zeroth-order. Therefore, the interaction term not only includes the off-diagonal dipole interaction, but also a diagonal frequency detuning term. ω_0 is the frequency difference between the ground state and excited state of the atom. ω is the frequency of the external millimeter-wave field. The detuning is defined as

$\Delta\omega = \omega_0 - \omega$. The second form is advantageous to transform into the rotating frame, which is shown in the following:

$$H = H_0 + V = \begin{pmatrix} E_g & 0 \\ 0 & E_g + \hbar\omega_0 \end{pmatrix} + \begin{pmatrix} 0 & V_{12} \\ V_1 & 0 \end{pmatrix} \tag{4.38a}$$

$$H = S + V_I = \begin{pmatrix} E_g & 0 \\ 0 & E_g + \hbar\omega \end{pmatrix} + \begin{pmatrix} 0 & V_{12} \\ V_1 & \hbar\Delta\omega \end{pmatrix}. \tag{4.38b}$$

The evolution of the density matrix is transformed into the interaction picture using a dressed-atom zeroth-order Hamiltonian S, as in Eq.(4.39).

$$i\hbar\frac{\partial\sigma}{\partial t} = [H, \sigma] \rightarrow i\hbar\frac{\partial\rho}{\partial t} = [V_S, \rho] = [H_0 - S - (\mathcal{E}_i \pm i\mathcal{E}_r)\,\mu, \rho] \tag{4.39a}$$

$$V_S = \exp\left[\frac{iS}{\hbar}\left(t - \frac{z}{c}\right)\right] V_I \exp\left[-\frac{iS}{\hbar}\left(t - \frac{z}{c}\right)\right] \tag{4.39b}$$

$$\rho = \exp\left[\frac{iS}{\hbar}\left(t - \frac{z}{c}\right)\right] \sigma \exp\left[-\frac{iS}{\hbar}\left(t - \frac{z}{c}\right)\right], \tag{4.39c}$$

where σ is the density matrix operator in the Schrödinger picture, V_s and ρ are the interaction term and density matrix operator in the interaction picture, and t-z/c is the retarded time. In the two-level atomic basis, the matrix elements of the density operator and converted operator Eq.(4.39) can be evaluated into three regular differential Eqns.(4.40).

$$i\hbar\left\langle g\right|\frac{\partial\rho}{\partial t}\left|e\right\rangle = -\hbar\Delta\omega\left\langle g\right|\rho\left|e\right\rangle + (\mathcal{E}_i - i\mathcal{E}_r)\left\langle g\right|\mu\left|e\right\rangle(\left\langle g\right|\rho\left|g\right\rangle - \left\langle e\right|\rho\left|e\right\rangle) \tag{4.40a}$$

$$i\hbar\left\langle g\right|\frac{\partial\rho}{\partial t}\left|g\right\rangle = -(\mathcal{E}_i - i\mathcal{E}_r)\left\langle g\right|\mu\left|e\right\rangle\left\langle e\right|\rho\left|g\right\rangle + (\mathcal{E}_i + i\mathcal{E}_r)\left\langle e\right|\mu\left|g\right\rangle\left\langle g\right|\rho\left|e\right\rangle \tag{4.40b}$$

$$i\hbar\left\langle e\right|\frac{\partial\rho}{\partial t}\left|e\right\rangle = -(\mathcal{E}_i + i\mathcal{E}_r)\left\langle e\right|\mu\left|g\right\rangle\left\langle g\right|\rho\left|e\right\rangle + (\mathcal{E}_i - i\mathcal{E}_r)\left\langle g\right|\mu\left|e\right\rangle\left\langle e\right|\rho\left|g\right\rangle. \tag{4.40c}$$

For the conventional phase choice, the plus sign in Eq.(4.39) is for $\langle e|\,\mu\,|g\rangle$, and the minus sign is for $\langle g|\,\mu\,|e\rangle$. The diagonal matrix elements represent the populations of the two states and must be real. The off-diagonal matrix elements represent the

coherences and are complex. I define:

$$\Delta\aleph = \langle g|\,\rho\,|g\rangle - \langle e|\,\rho\,|e\rangle \tag{4.41a}$$

$$\wp_r + i\wp_i = N\,\langle e|\,\mu\,|g\rangle\,\langle g|\,\rho\,|e\rangle\,, \tag{4.41b}$$

where $\Delta\aleph$ is the population difference between the ground and excited states, $\wp_r$ and $\wp_i$ are the real and imaginary parts of the macroscopic coherence, respectively. I use $\Delta\aleph$, $\wp_r$, and $\wp_i$ with clear physical meanings to replace the density matrix elements in Eq.(4.40), and obtain equations to describe the time-dependence of the real and imaginary parts of the macroscopic polarization and population difference.

$$\frac{\partial}{\partial t}\wp_r = -\mathcal{E}_r\frac{\mu_{eg}^2}{\hbar}\Delta\aleph - \Delta\omega\wp_i \tag{4.42a}$$

$$\frac{\partial}{\partial t}\wp_i = -\mathcal{E}_i\frac{\mu_{eg}^2}{\hbar}\Delta\aleph + \Delta\omega\wp_r \tag{4.42b}$$

$$\frac{\partial}{\partial t}\Delta\aleph = \frac{4}{\hbar}\left(\mathcal{E}_r\wp_r + \mathcal{E}_i\wp_i\right). \tag{4.42c}$$

Equation.(4.42) does not include any depopulation or decoherence processes, which are unavoidable in typical experiments. Therefore, two phenomenological parameters are added into Eq.(4.42),

$$\frac{\partial}{\partial t}\wp_r + \Delta\omega\wp_i + \kappa^2\mathcal{E}_r\left(\frac{\hbar\Delta\aleph}{4}\right) - \frac{\wp_r}{T_2} = 0 \tag{4.43a}$$

$$\frac{\partial}{\partial t}\wp_i - \Delta\omega\wp_i + \kappa^2\mathcal{E}_i\left(\frac{\hbar\Delta\aleph}{4}\right) - \frac{\wp_i}{T_2} = 0 \tag{4.43b}$$

$$\frac{\partial}{\partial t}\left(\frac{\hbar\Delta\aleph}{4}\right) - \left(\mathcal{E}_r\wp_r + \mathcal{E}_i\wp_i\right) - \frac{\hbar\left(\Delta\aleph - \Delta\aleph_0\right)}{4T_1} = 0, \tag{4.43c}$$

where T_1 is the depopulation (longitudinal) decay lifetime, T_2 is the homogeneous decoherence (transverse) decay lifetime, $\kappa = 2\mu_{eg}/\hbar$, and $\Delta\aleph_0$ is the population difference at equilibrium. A Mathematica program is written to numerically solve

Eq.(4.43). With $\wp_r$ and $\wp_i$, the macroscopic polarization can be calculated:

$$\begin{aligned} P &= NTr\left(\mu\sigma\right) = NTr\left\{\mu \exp\left[-\tfrac{iS}{\hbar}\left(t-\tfrac{z}{c}\right)\right]\rho \exp\left[\tfrac{iS}{\hbar}\left(t-\tfrac{z}{c}\right)\right]\right\} \\ &= N\left[\langle e|\,\mu\,|g\rangle\,\langle g|\,\rho\,|e\rangle\, e^{i(\omega t-kz)} + \langle g|\,\mu\,|e\rangle\,\langle e|\,\rho\,|g\rangle\, e^{-i(\omega t-kz)}\right] \\ &= (\wp_r + i\wp_i)e^{i(\omega t-kz)} + (\wp_r - i\wp_i)e^{-i(\omega t-kz)}, \end{aligned} \tag{4.44}$$

where ω and k are the frequency and wavevector of the millimeter-wave field. The radiative electric field can be calculated by the Maxwell equation:

$$\frac{\partial^2 E}{\partial z^2} = \frac{1}{c^2}\frac{\partial^2 E}{\partial t^2} + \frac{4\pi}{c^2}\frac{\partial^2 P}{\partial t^2}, \tag{4.45}$$

where c is the speed of light, and z is the one-dimensional propagation distance. With a slow variation approximation of the electric field envelope as in Eq.(4.34), Eq.(4.45) can be simplified into:

$$\frac{\partial \mathcal{E}_i}{\partial z} + \frac{1}{c}\frac{\partial \mathcal{E}_i}{\partial t} = \frac{2\pi\omega}{c}\wp_i \rightarrow \frac{d\mathcal{E}_i}{dz} = \frac{2\pi\omega}{c}\wp_i \tag{4.46a}$$

$$\frac{\partial \mathcal{E}_r}{\partial z} + \frac{1}{c}\frac{\partial \mathcal{E}_r}{\partial t} = \frac{2\pi\omega}{c}\wp_r \rightarrow \frac{d\mathcal{E}_r}{dz} = \frac{2\pi\omega}{c}\wp_r. \tag{4.46b}$$

Thus, a complex second-order partial differential equation is simplified into two real first-order partial differential equations. In addition, the time-dependent term can be contracted into the spatial-dependent part in a retarded frame. Therefore, the fully simplified Maxwell equations are two real ordinary first-order differential equations, which can be integrated directly.

Figure 4-7 shows the flow diagram of the semi-classical calculation. Most of the procedures have been discussed except for the summation step for macroscopic polarization [132]. In Eq.(4.44), I multiply the number of atoms by the microscopic polarization. This operation is based on the assumption that all atoms are placed at the same position. As discussed in Section 4.2.1, relaxing this assumption to an arbitrary spatial distribution leads to: (1) a prefactor which reduces the macroscopic polarization; (2) a line broadening due to the dipole-dipole collisions. These two processes,

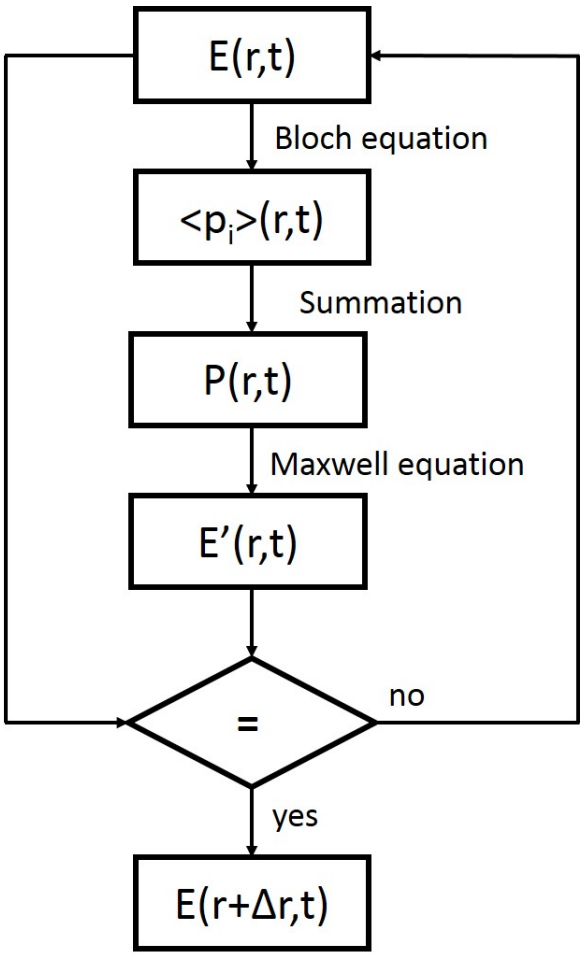

Figure 4-7: Flow diagram of the semi-classical calculation.

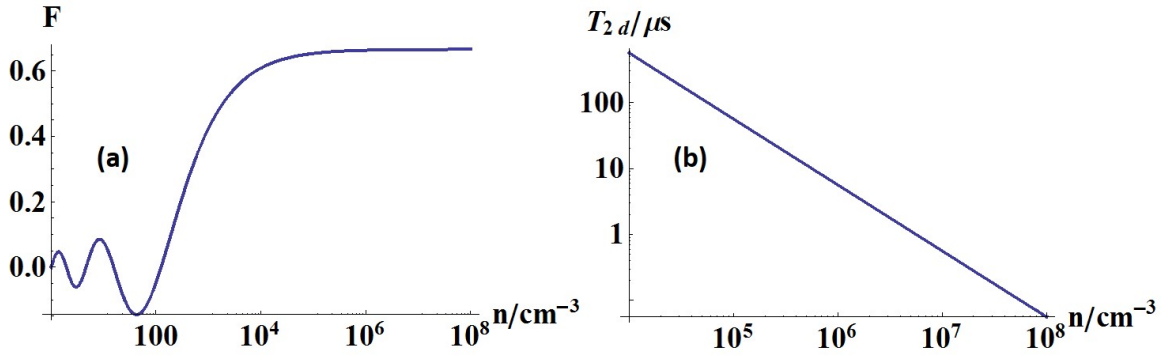

Figure 4-8: Number density dependent polarization summation prefactor (Plot (a)) and dipole-dipole dephasing lifetime (Plot (b)).

which are not included in the regular semi-classical calculation, can be obtained by the Schrödinger picture. The prefactor F can be calculated by Eq.(4.23). Plot (a) in Figure 4-8 shows a number density dependent F factor. Therefore, Eq.(4.44) is modified from P=Np to P=NFp. Similar, the line broadening can also be obtained from the Schrödinger picture and calculated by Eq.(4.24) with an assumed number density distribution. Plot (b) in Figure 4-8 shows the dipole-dipole dephasing lifetime with a Gaussian shaped number density distribution (σ=n/2, σ is the FWHM of the Gaussian distribution, and n is the average number density). This dipole-dipole T_{2d} can be incorporated into the other phenomenological homogeneous dephasing processes by,

$$\frac{1}{T_2} = \frac{1}{T_{2d}} + \frac{1}{T_{other}}. \tag{4.47}$$

In the following, based on practical experimental parameters, I compare the dynamical behaviors and the information encoded in a millimeter-wave spectra for a 1 Debye rotational system vs. a 5 kDebye Rydberg system. Typical parameters used in this calculation are summarized in Table 4.1. The number densities of molecules in Rydberg states and non-Rydberg molecules in rotation-vibration levels listed in Table 4.1 come from typical experimental considerations. The pulse amplitude, 10 V/m, is the maximum millimeter-wave electric field created by our CPmmW spectrometer, which is used to polarize the rotation-vibration transitions with small electric transition dipole moments. A much weaker pulse, 5 mV/m, is chosen to polarize the

Table 4.1: Typical calculation parameters

	Electric Dipole	Number Density	Pulse Amplitude	Pulse Width	T_1	T_2
Rotation	1 Debye	$10^{10} cm^{-3}$	$10 V/m$	25ns	100 ms	10 μs
Rydberg	5k Debye	$10^{6} cm^{-3}$	$5 mV/m$	10ns	100 μs	$\sim$3 μs

Rydberg-Rydberg transitions via their large electric transition dipole moments. The choice of such parameters is based on two reasons: (1) I want to make the two types of transitions, which have significantly different electric transition dipole moments, have the same initial polarization (0.5% of the maximum polarization); (2) The initial polarization is large enough to induce collective effects, but small enough not to interfere with the collective radiative pattern. T_1 is the longitudinal population decay lifetime, which is determined by the natural lifetime and blackbody radiation, and T_2 is the collisional transverse decay lifetime, which is number density dependent for Rydberg states, as shown in Figure 4-8. I ignore the Doppler effect, because typical experiments in the buffer gas cooled molecular beam have much smaller Doppler broadening than the collisional broadening.

Point source sample

The sample is treated as a point source, which is much smaller than the 4 mm radiation wavelength. Propagation effects, such as emission and reabsorption can be neglected. I use a short (25 or 10 ns) and weak (10 V/m for 1 D, 5 mV/m for 5 kD) millimeter-wave pulse to polarize the sample. The radiation is detected in a 70 μs window following the excitation pulse. In a gas with a small electric dipole transition moment, the macroscopic polarization generated by the millimeter-wave pulse induces Free Induction Decay (FID), radiated with a $1/T_2$ single-exponential decay. Due to the weak polarization and much slower spontaneous emission rate, after the FID dies away most of the unpolarized population remains in the upper state for a long time, as shown in Figure 4-9.

In a Rydberg gas with a large electric dipole transition moment, the initially prepared polarization does not directly produce FID radiation with a single exponential

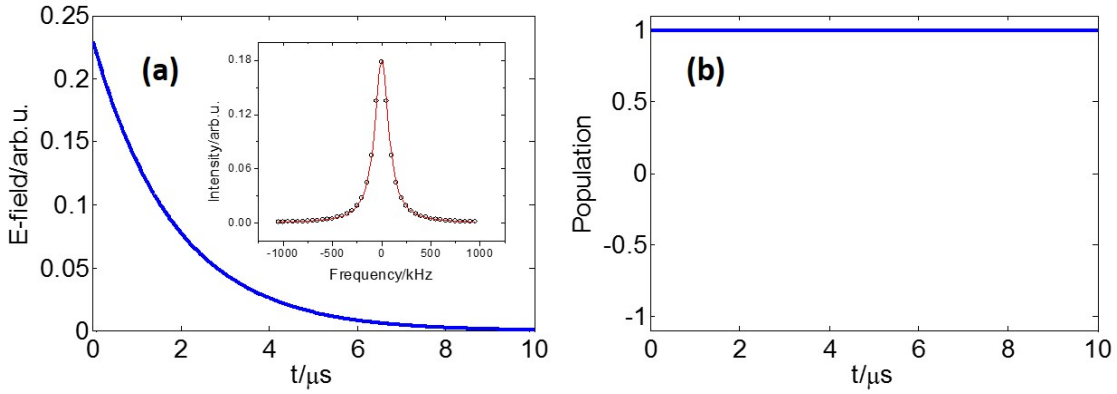

Figure 4-9: Free induction decay radiation in a nearly isolated system. Plot (a) shows the electric field of the coherent radiation after a 10 ns excitation pulse at moderately high number density of molecules with 1 D electric dipole transition moment. The inset shows the Lorentzian lineshape and the linewdith is π/T_2. Plot (b) shows the population evolution. Due to the relatively large T_1, the population decay on this time scale is not obvious.

decay. Instead, the FID amplifies itself through coupling to other unpolarized excited molecules. Such amplification becomes stronger with time until a maximum is reached when half of the polarized molecules are in the upper state. After this polarization maximum, the system is no longer inverted, thus the amplification must terminate and the macroscopic polarization must decrease. The radiative lifetime can be approximated as $T_R = T_{sp}\,(8\pi/n\lambda^2 L)$ [109]. Different from the FID emitted via rotational transitions, in which radiated energy only comes from the initial population transfer induced by a short excitation pulse, the energy radiated from a Rydberg gas is continuously extracted from the inverted molecular system. To satisfy energy conservation, population in the upper states decreases.

From Figure 4-10, at low number density, the radiation decay curve is a single exponential, the lineshape is Lorentzian, the lifetime is T_2, and the population distribution is constant after excitation. At intermediate number density, the radiation decay curve has a broad maximum peak in the time-domain, and the linewidth is smaller than $1/T_2$. In addition, the population evolves as the radiation is emitted. At high number density, the radiation curve has a sharp maximum in the time-domain, the lineshape is distorted, and the linewidth is broadened. More than 50% of the

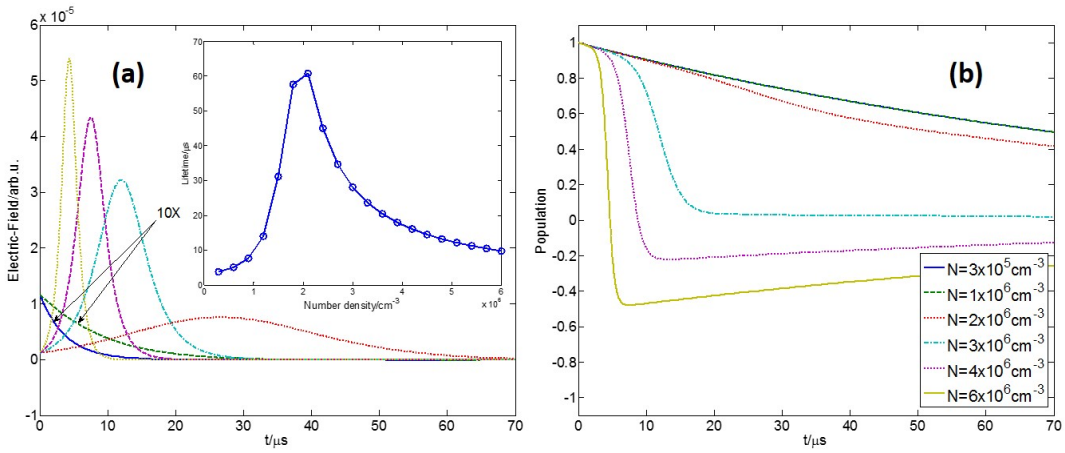

Figure 4-10: Coherent radiation in a cooperative system. Plot (a) shows the electric field of the coherent radiation after a 10 ns excitation pulse observed at different number densities. The inset shows the dependence of the coherence lifetime on number density. The coherence lifetime here is defined as the time at which the evolving polarization is 1/e times the initial polarization. Plot (b) shows how the population evolution depends on the inital population density.

population decays to the lower state in a short time as the system radiates. Such contrasting behavior is due to the difference between the strengths of the molecular radiation field and the input electric field. When the radiation field is weak compared with the input field, its contribution to the local electric field can be neglected. Thus, each molecule may be treated as interacting independently with a constant external electric field, and the final result is just the sum of each individual molecule's field. But when the radiation is strong or the molecular response to the radiation is sensitive, I cannot ignore the effect that such radiation has on the emitters themselves. This radiation field is shared by many molecules, therefore it couples them together and forces them to behave cooperatively.

The most unexpected feature in this calculation is, at intermediate number density, the radiation can be kept at a relatively low amplitude, but can last for a very long time ($> T_2$). This can be explained by the following physical picture. If there is only one atom in a system, and decoherence of the radiation occurs by some sort of dephasing mechanism (such as collisions, inhomogeneous field, etc.) in a time T_2, the system would lose coherence completely. However, if there are several atoms, and a

weak excitation pulse only polarizes one or a few of them, before the excited atoms undergo decoherence in time T_2, they could transfer their coherence to neighboring atoms. Due to this transfer mechanism, a complete loss of coherence in the entire system takes a much longer time. However, coherence transfer needs to be driven by the internal energy of the system. Therefore, when the number density is very high, although coherence transfer can occur frequently (effective $1/\mathrm{T}_2$ is increasing), the internal energy of the system will be depleted quickly at the same time (effective $1/\mathrm{T}_1$ is decreasing). The net effect would decrease the lifetime of the coherence significantly at high number density. In the calculation shown in Figure 4-10, there is an optimized number density, at which the radiation persists for more than $20 \times T_2$.

Extended sample source

In our typical millimeter-wave experiments, the sample is designed to have a cylindrical shape with Fresnel number $2\mathrm{A}/\lambda\mathrm{L}>>1$ (A and L are the cross-sectional area and length of the cylindrical sample source) in order to obtain more intense and directional output radiation. In the calculation, I assume the number density distribution along the millimeter-wave propagating axis is a cut-tail Gaussian distribution, (see the inset Figure of 4-11b). The calculation shows that if the dimension of the sample is longer than the wavelength of millimeter-wave radiation, the FID radiation from the initially polarized molecules polarizes additional molecules downstream, especially if they have a large electric dipole transition moment. The π phase shift of emission followed by reabsorption changes the sign of the electric field envelope, thus forming a ringing pattern at the tail of the coherent radiation in the time-domain, as shown in Figure 4-11a. A time-domain ringing pattern with several nodes results in peak splittings in the frequency-domain spectrum. Similar to the Mollow triplet[139, 140], the splittings here are produced by modulation from Rabi cycling ($\Omega(t) = \mu E(t)/\hbar$). However, Rabi cycling here is not induced by an external electric field, rather by the radiation from upstream emitters. The resultant time-varying radiation amplitude induces broadband Rabi cycling, which may either distort or even smooth out the splittings that result from the ringing pattern. Such frequency triplet structure has

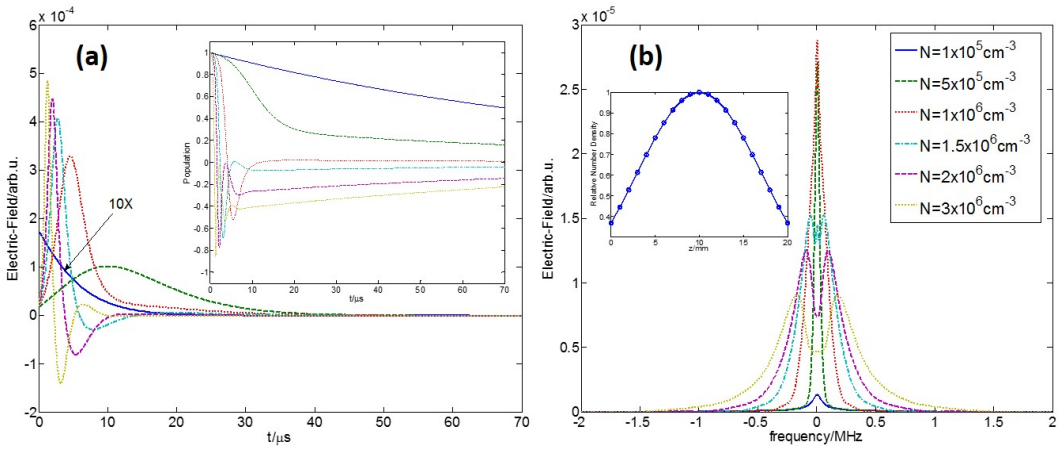

Figure 4-11: Coherent radiation in an extended sample. Plot (a) shows the coherent radiation emitted from a 1 cm long sample at different number densities. At large number density (dashed curve), a ringing tail is observed. The inset figure shows that the population dynamics are synchronized by radiation. Plot (b) shows the Fourier transformation into the frequency domain. This illustrates the qualitative differences between lineshapes that arise from large and small number densities. The inset figure shows the normalized number density distribution along the millimeter-wave propagating axis, and the number density listed in Plot (b) represents the peak number density.

always been difficult to observe, *except in a dense Rydberg gas*.

In addition to calculating the propagation of the radiation in an extended sample, it is also easy to calculate the behavior of a long excitation pulse propagating in the sample. Different from previous calculations, a non-inverted two level system is used here with a $\pi/2$ pulse to maximally polarize the transition. Figure 4-12 shows how a 500 ns $\pi/2$ excitation pulse propagates in a long and dense Rydberg gas. Plot (a) shows a 3D plot of the pulse electric field, and Plot (b) shows a 3D plot of the polarization field. At the front of the sample, because the accumulated response radiation is small compared to the excitation pulse, the nutation exhibits $\pi/2$ curvature as I expect. However, at the back of the sample, because of the strong absorption and emission from the front, the radiation is comparable or even larger than the excitation pulse. The nutation deviates far from nominal $\pi/2$ curvature and has several nodes. I use such an effective local electric field to calculate the induced polarization, in Plot (b) and find that at the front of the sample, there is a

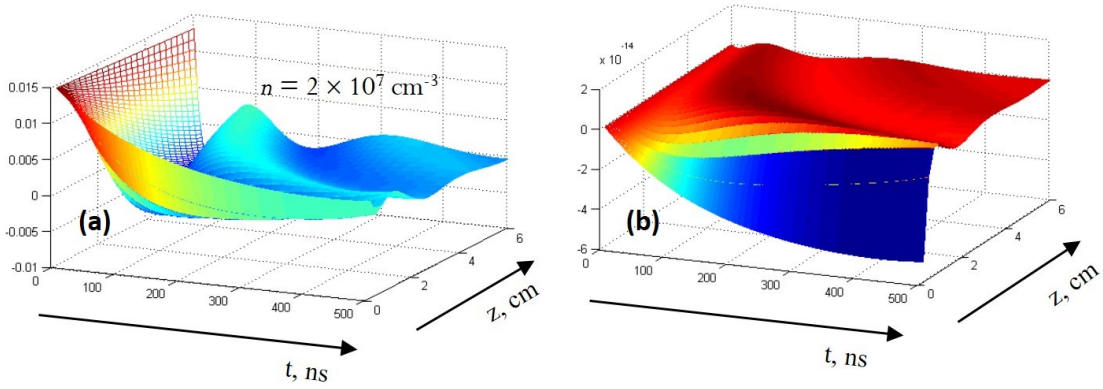

Figure 4-12: A $\pi/2$ excitation pulse propagates in an extended sample. Plot (a) shows the time-dependence and position-dependence of the pulsed electric field, and Plot (b) shows that of the polarization created by the electric field in Plot (a).

large macroscopic polarization. However, at the back, no macroscopic polarization is created, because the excitation pulse cannot penetrate the sample deeply. This shallow excitation suggests a possibility that a reflection wave might be strong. This is discussed in Section 4.4.

4.3.2 Three-level System

In principle, the semi-classical calculations of the three-level system are not different from those for the two-level system. The Maxwell equations are the same, and the number of Bloch equations increases quadratically with the number of states involved. In this section, I derive the Bloch equation for an inverted Λ-type three-level system first, and demonstrate the existence of unique collective effects in this system by numerical calculation. Figure 4-13 is a diagram of the inverted Λ-type three-level system. The laser populates state $|1\rangle$, and a weak, short, chirped millimeter-wave pulse polarizes the transitions $|2\rangle \leftarrow |1\rangle$ and $|3\rangle \leftarrow |1\rangle$ at almost the same time. The difference in the transition frequencies ω_1 and ω_2 is small, $(\omega_1 - \omega_2) << \omega_1$ or ω_2.

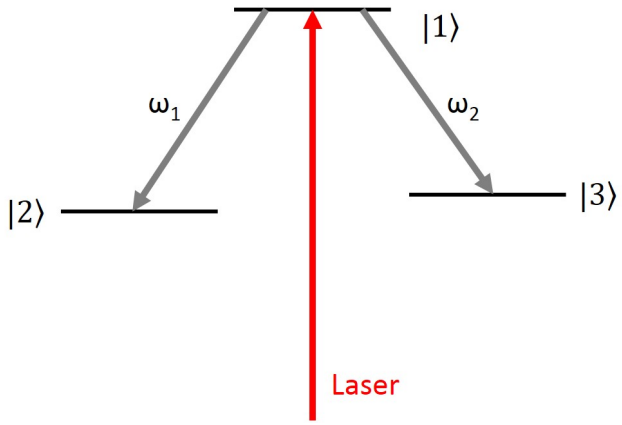

Figure 4-13: Diagram of an inverted Λ-type three-level system.

Similar to Eq.(4.38), the Hamiltonian of an inverted three-level system is,

$$H = H_0 + V = \begin{pmatrix} E_a & 0 & 0 \\ 0 & E_a + \hbar\omega_1 & 0 \\ 0 & 0 & E_a + \hbar\omega_2 \end{pmatrix} + \begin{pmatrix} 0 & \mu_1 E & \mu_2 E \\ \mu_1 E & 0 & 0 \\ \mu_2 E & 0 & 0 \end{pmatrix} \quad (4.48a)$$

$$H = S + V_I = \begin{pmatrix} E_a & 0 & 0 \\ 0 & E_a + \hbar\omega & 0 \\ 0 & 0 & E_a + \hbar\omega \end{pmatrix} + \begin{pmatrix} 0 & \mu_1 E & \mu_2 E \\ \mu_1 E & \hbar\Delta\omega_1 & 0 \\ \mu_2 E & 0 & \hbar\Delta\omega_2 \end{pmatrix}, \quad (4.48b)$$

where ω is the millimeter-wave carrier frequency, ω_1 and ω_2 are the transition frequencies, the detunings are $\Delta\omega_1 = \omega_1 - \omega$ and $\Delta\omega_2 = \omega_2 - \omega$, μ_1 and μ_2 are the electric dipole transition moments of $|2\rangle \leftarrow |1\rangle$ and $|3\rangle \leftarrow |1\rangle$, and E is the electric field amplitude of the chirped pulse millimeter-wave. Similar to Eq.(4.39), I transform the evolution of the density matrix into the interaction picture with a dressed-atom zeroth-order Hamiltonian S,

$$i\hbar\frac{\partial\sigma}{\partial t} = [H, \sigma] \rightarrow i\hbar\frac{\partial\rho}{\partial t} = [V_S, \rho] \quad (4.49a)$$

$$V_S = H_0 - S - 2\mu_S \left[\mathcal{E}_i \cos(\omega t - kz) + \mathcal{E}_r \sin(\omega t - kz)\right] \quad (4.49b)$$

The matrix form of V_S is

$$V_S = \begin{pmatrix} 0 & \mu_1 E e^{-i\omega\tau} & \mu_2 E e^{-i\omega\tau} \\ \mu_1 E e^{i\omega\tau} & \hbar\Delta\omega_1 & 0 \\ \mu_2 E e^{i\omega\tau} & 0 & \hbar\Delta\omega_2 \end{pmatrix} \rightarrow \begin{pmatrix} 0 & \mu_1 (\mathcal{E}_i - i\mathcal{E}_r) & \mu_2 (\mathcal{E}_i - i\mathcal{E}_r) \\ \mu_1 (\mathcal{E}_i + i\mathcal{E}_r) & \hbar\Delta\omega_1 & 0 \\ \mu_2 (\mathcal{E}_i - i\mathcal{E}_r) & 0 & \hbar\Delta\omega_2 \end{pmatrix}. \tag{4.50}$$

The matrix form of Eq.(4.49) is,

$$i\hbar \begin{pmatrix} \frac{\partial\rho_{11}}{\partial t} & \frac{\partial\rho_{12}}{\partial t} & \frac{\partial\rho_{13}}{\partial t} \\ \frac{\partial\rho_{12}^*}{\partial t} & \frac{\partial\rho_{22}}{\partial t} & 0 \\ \frac{\partial\rho_{13}^*}{\partial t} & 0 & \frac{\partial\rho_{33}}{\partial t} \end{pmatrix} = \left[\begin{pmatrix} 0 & \mu_1 (\mathcal{E}_i - i\mathcal{E}_r) & \mu_2 (\mathcal{E}_i - i\mathcal{E}_r) \\ \mu_1 (\mathcal{E}_i + i\mathcal{E}_r) & \hbar\Delta\omega_1 & 0 \\ \mu_2 (\mathcal{E}_i - i\mathcal{E}_r) & 0 & \hbar\Delta\omega_2 \end{pmatrix}, \begin{pmatrix} \rho_{11} & \rho_{12} & \rho_{13} \\ \rho_{12}^* & \rho_{22} & 0 \\ \rho_{13}^* & 0 & \rho_{33} \end{pmatrix} \right]. \tag{4.51}$$

In Eq.(4.51), I ignore the coherence between states $|2\rangle$ and $|3\rangle$, because there is no direct dipole coupling between them and the coherence must be created by multi-quantum excitation, which can be ignored in my typical experiments. This assumption might fail in a extremely dense Rydberg gas or with a strong external driving field, but such systems are beyond the scope of this thesis. As I discussed above, the diagonal terms of the density matrix represent the population and are real, and the off-diagonal terms represent the coherence and are complex. Therefore, The following matrix elements are relevent:

$$\rho_{11}=\rho_{r11} \tag{4.52a}$$

$$\rho_{22}=\rho_{r22} \tag{4.52b}$$

$$\rho_{33}=\rho_{r33} \tag{4.52c}$$

$$\rho_{12}=\rho_{r12} + i\rho_{i12} \tag{4.52d}$$

$$\rho_{13}=\rho_{r13} + i\rho_{i13} \tag{4.52e}$$

$$\rho_{12}^*=\rho_{r12} - i\rho_{i12} \tag{4.52f}$$

$$\rho_{13}^*=\rho_{r13} - i\rho_{i13}. \tag{4.52g}$$

The result is seven coupled real differential equations,

$$\frac{\partial \rho_{r11}}{\partial t}+\frac{2\mu_1}{\hbar}\left(\mathcal{E}_r\rho_{r12}+\mathcal{E}_i\rho_{i12}\right)+\frac{2\mu_2}{\hbar}\left(\mathcal{E}_r\rho_{r13}+\mathcal{E}_i\rho_{i13}\right)+\frac{\rho_{r11}}{T_{11}}=0 \tag{4.53a}$$

$$\frac{\partial \rho_{r22}}{\partial t}-\frac{2\mu_1}{\hbar}\left(\mathcal{E}_r\rho_{r12}+\mathcal{E}_i\rho_{i12}\right)+\frac{\rho_{r22}}{T_{12}}=0 \tag{4.53b}$$

$$\frac{\partial \rho_{r33}}{\partial t}-\frac{2\mu_2}{\hbar}\left(\mathcal{E}_r\rho_{r13}+\mathcal{E}_i\rho_{i13}\right)+\frac{\rho_{r33}}{T_{13}}=0 \tag{4.53c}$$

$$\frac{\partial \rho_{i12}}{\partial t}+\frac{\mu_1}{\hbar}\mathcal{E}_i\left(\rho_{r22}-\rho_{r11}\right)-\Delta\omega_1\rho_{r12}+\frac{\rho_{i12}}{T_{21}}=0 \tag{4.53d}$$

$$\frac{\partial \rho_{r12}}{\partial t}+\frac{\mu_1}{\hbar}\mathcal{E}_r\left(\rho_{r22}-\rho_{r11}\right)+\Delta\omega_1\rho_{i12}+\frac{\rho_{r12}}{T_{21}}=0 \tag{4.53e}$$

$$\frac{\partial \rho_{i13}}{\partial t}+\frac{\mu_1}{\hbar}\mathcal{E}_i\left(\rho_{r33}-\rho_{r11}\right)-\Delta\omega_2\rho_{r13}+\frac{\rho_{i13}}{T_{22}}=0 \tag{4.53f}$$

$$\frac{\partial \rho_{r13}}{\partial t}+\frac{\mu_2}{\hbar}\mathcal{E}_r\left(\rho_{r33}-\rho_{r11}\right)+\Delta\omega_2\rho_{i13}+\frac{\rho_{r13}}{T_{22}}=0, \tag{4.53g}$$

where T_{11}, T_{12} and T_{13} are the phenomenological longitudinal lifetimes of states $|1\rangle$, $|2\rangle$, and $|3\rangle$, and T_{21} and T_{22} are the phenomenological transverse lifetimes of transitions $|2\rangle \leftarrow |1\rangle$ and $|3\rangle \leftarrow |1\rangle$. The part of T_2 due to dipole-dipole collisions can be calculated in the same way for the two-level system. Similar to Eq.(4.44), the macroscopic polarization can be calculated by,

$$\begin{aligned} P &= NTr\left(\mu\sigma\right)=NTr\left\{\mu\exp\left[-\tfrac{iS}{\hbar}\left(t-\tfrac{z}{c}\right)\right]\rho\exp\left[\tfrac{iS}{\hbar}\left(t-\tfrac{z}{c}\right)\right]\right\} \\ &= 2\mathrm{Re}\left(\mu_{12}\rho_{12}e^{i\omega\tau}\right)+2\mathrm{Re}\left(\mu_{13}\rho_{13}e^{i\omega\tau}\right). \end{aligned} \tag{4.54}$$

Equation.(4.54) is also based on the assumption that all atoms are placed at the same position. To include the spatial distribution, the multiplicative prefactor F is employed in the same way as in the two-level system. In principle, the same method can be used to extend this semi-classical calculation method to multi-level system. However, the computation time increases quadratically with the number of levels.

Branching ratio of the radiation in an inverted Λ-type three-level system

Consider a Λ-type, inverted three-level system, as shown in the inset of Figure 4-14, Plot (a). All of the population starts in the upper state, and a fast, broadband chirp

(10 ns pulse, 5 mV/m, 200 MHz bandwidth) induces tiny polarizations ($<\pi/1000$) of both transitions (100 MHz frequency difference). Similar to the two-level system, both polarizations can amplify themselves cooperatively and reach a maximum amplitude with a μs delay time. In conventional fluorescence or FID measurements with small electric dipole transition moments, the observed radiative intensities of the two transitions should be proportional to the ratio of their oscillator strengths, which are each proportional to μ^2. But in a cooperative amplification system, I find that more energy flows into the transition that has the larger electric dipole transition moment.

Figure 4-14, Plot(a) describes the evolution of the time-integrated intensity ratio of the two transitions. Initially, most of the polarization is induced by the external broadband electric field, which has similar amplitudes at the two transition frequencies. In addition, at early times, the amplification is less important, thus the intensity ratio is close to the oscillator strength ratio. However, at later times, the amplified polarization is completely dominated by the cooperatively radiated electric field from the coherently coupled molecules. This causes most of the radiated energy to be steered into the more polarizable channel. The intensity ratio is far from the independent-transition prediction based on the oscillator strength ratio.

In Figure 4-14, Plot (b), the integrated intensity ratio of the two transitions is plotted vs. the electric dipole transition moment ratio μ_1/μ_2. At low number density, the energy steering is weak. However, at higher number density, when the cooperative effect dominates, such energy steering is increased significantly. For example, at $3\times\ 10^7$ cm^{-3} number density, when the ratio of the two electric dipole transition moments is 1.5, the intensity ratio is larger than a factor of 500. Unlike in a dispersed spontaneous-fluorescence spectrum, a cooperative system with a relatively high number density effectively has only one open radiation channel and only one feature in the frequency-domain. The calculation shows that early self-induced amplification is the dominant cause of the energy steering. If we use a moderate initial excitation pulse ($\sim\pi/100$) instead of weak pulse ($<\pi/1000$), the early self-induced amplification is supressed by the external driving field. In such a situation, the intensity ratio of the two transitions decreases and approaches the oscillator strength ratio (a factor of

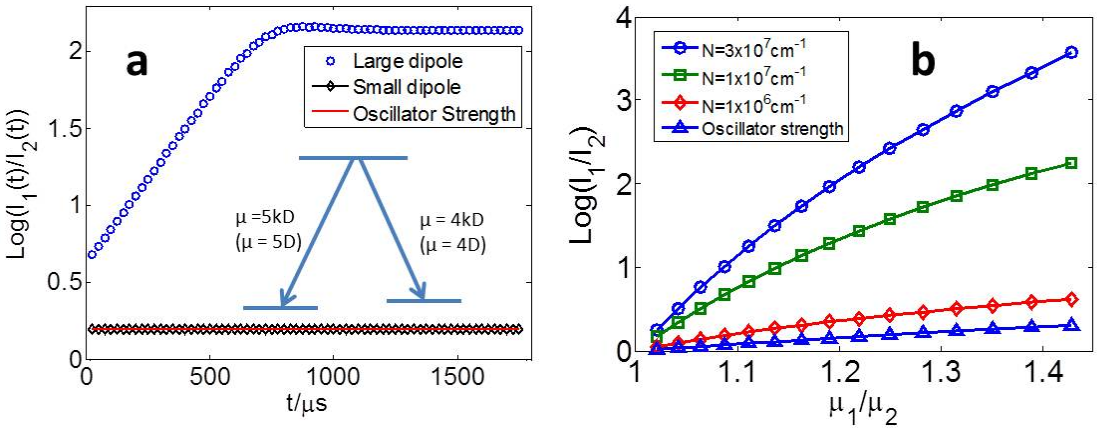

Figure 4-14: Coherence radiation in a Λ-type three-level system. The inset figure of Plot (a) presents the level diagram of the three-level system. The vertical axis of Plot (a) is the time-integrated intensity ratio of the two transitions. The oscillator strength predicts that this ratio is constant and equal to μ^2_{ratio} plotted as a red line. Diamonds represent the intensity ratio of a rotational spectrum, and the circles represent the intensity ratio of a dense Rydberg gas. Plot (b) presents the total intensity ratio vs. electric dipole transition moment ratio at different number densities of the Rydberg gas, all of which deviated from the oscillator strength prediction, shown as triangular dots.

5 instead of 500).

4.4 New experiments

The major challenges of experiments dealing with collective effects are [141]: (1) preparing a dense, homogeneous, and strongly interacting medium by optically thin optical pumping at short wavelength that can radiate at long wavelength in an optically thick manner; (2) creating an initial coherence in a precisely controllable manner; and (3) creating an arbitrarily shaped, sharply defined boundary of the initially interacting volume, the shape of which governs the propagation of the coherence. The combination of the recent upgrade of our molecular beam source (buffer gas cooled ablation source), optimization of our CPmmW spectrometer, and our achievement of an efficient scheme for preparing core-nonpenetrating Rydberg states, which is discussed in Section 6, enable a series of systematic experiments that observe the coherence generation, propagation, and response to external manipulations. Based

on the preliminary experiments in Section 3.3 and the calculation results in this chapter, I believe that our dense Rydberg gas is unique for two reasons: (1) the initial Rydberg state is prepared by optical pumping from a valence state. Such a transition is optically thin, thus the sample is uniform; (2) the Rydberg-Rydberg transition is initialized and probed by millimeter-wave excitation and the induced FID radiation. This transition is optically thick and exhibits strong collective effects. For fundamental photonics research, the existence of uncoupled preparation and probing processes enables unprecedented control over the initial and boundary conditions of samples that exhibit cooperative effects. Qualitatively distinct from ultracold many-body collisional experiments performed at high density but small volume, our setup have a large, homogeneous, and geometrically well-defined interaction volume along with a precisely known total number of molecules. These conditions are essential for fundamental studies of radiation-induced collective inter-particle interactions.

4.4.1 Superradiance lineshape

The buffer gas cooled photoablation technique creates an intense molecular beam at a density of 1×10^9 cm^{-3}. Two or three crossed tunable laser beams, with carefully designed beam geometries, pump the molecules into a single Rydberg state in either a tube-like or disk-like volume. The maximum transition dipole moment of normally-used laser optical pumping schemes in the UV region is $\sim$1 Debye, which is in the optically thin limit (<5% laser beam attenuation occurs through L=2 cm and $N_{density}$ ~1 $\times10^9$ cm^{-3} Rydberg gas). However, for $|\Delta n| \leq 1$ Rydberg-Rydberg electronic transitions, the large electric dipole transition moments ($\sim$5 kDebye) result in a system in the extreme optically thick limit (>99.9% millimeter-wave beam attenuation occurs through L=2 cm and $N_{density}$ ~1 $\times10^6$ cm^{-3} Rydberg gas). A medium with such an enormous optical thickness will be an ideal test platform for the study of nonlinear phenomena, especially collective effects. In Section 3.3, I have presented the observations of the linewidth broadening and the near Gaussian and near Lorentzian lineshapes, which are in qualitative agreement with the semi-classical calculations in this chapter. The quantitative comparison will require one to com-

pletely characterize the properties of the Rydberg samples, such as: (1) Precisely measuring the average number density and inhomogeneity of the Rydberg sample (number density distribution); (2) Minimizing or monitoring the shot-to-shot fluctuations of the Rydberg sample, because the collective effects are strongly number density dependent; (3) Improving and characterizing the geometry of the excitation laser beams, which define the boundary of the Rydberg sample. In addition to the experimental improvements, several data analysis techniques that are under investigation might be used to complement the lineshape observations, such as observing the phase evolution of the superradiant emission, or applying a crafted pulse sequence to detect the coherence and population during or after the superradiant emission.

4.4.2 Superradiance anisotropy

In my experiments, the Rydberg system is prepared by incoherent laser excitations, and the initial coherence is established by a weak millimeter-wave pulse. Such coherence propagates along the pulse propagation direction. Therefore, I expect to detect forward radiation. In addition to the coherence initialized by the millimeter-wave pulse, additional coherence can be established by the self-amplified superradiant emission. Such coherence prefers to propagate along the z axis of the sample (Here, I consider a cylindrically shaped sample in a cylinder shape, where z is the length of the cylinder). Therefore, I expect to detect radiation in the z direction. In my typical experiments, the excitation millimeter-wave pulse also propagates along the z axis. However, what happen if the direction preferences are different? More deeply, this question is equivalent to the discussion of the initial phase symmetry and evolution, as shown in Figure 4-15. Theorists have performed detailed calculations to predict the radiation dynamics of the timed atomic state and symmetric atomic state [142, 9, 143, 144]. However, very few experiments successfully demonstrate the predictions. Here, I propose a new class of experiment in the Rydberg system. Figure 4-16 shows an experimental diagram for detecting the radiation anistropy. The initial coherence is generated by a millimeter-wave pulse from horn 1 or 3. Horn 2 is used to detect the radiation. Based on this geometry, a millimeter-wave excitation pulse

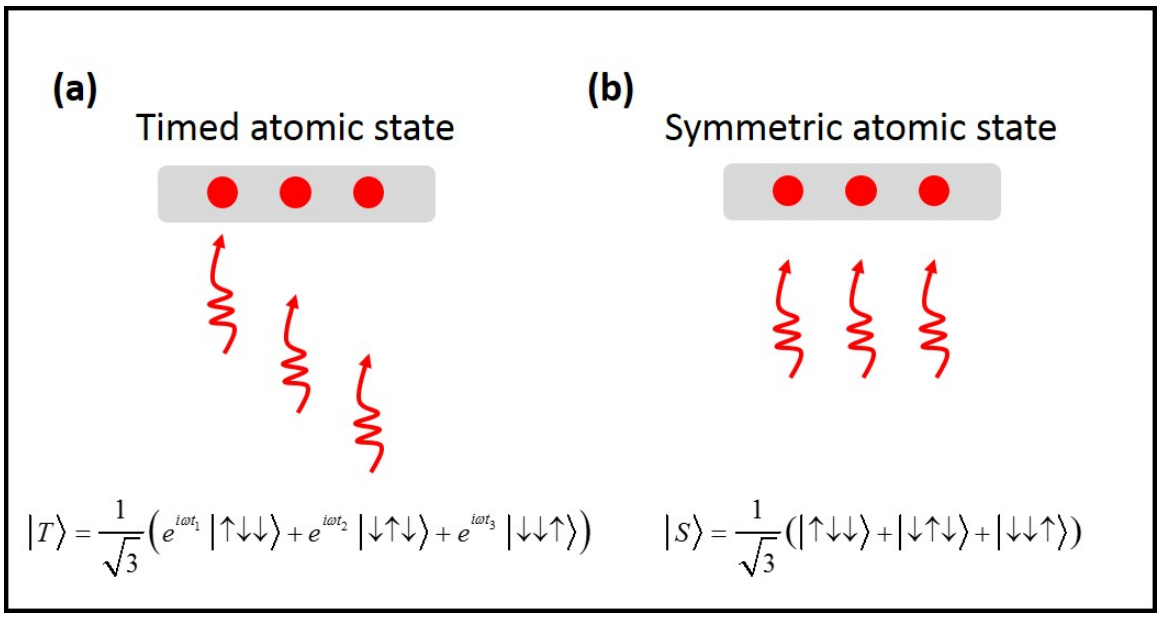

Figure 4-15: Plots (A) and (B) show different initial phase relationships between neighboring molecules. Different time evolution behaviors induce anisotropic propagation effects. Reprinted from [9]

from horn 1 prepares the timed atomic state, and that from horn 3 prepares the symmetric atomic state. To make the amplitudes of the initial coherences the same, it is possible to apply a slightly off-resonant excitation pulse, which is not attenuated significantly by the Rydberg atoms. The anisotropy of the radiation can be measured by the relative intensities $I_\perp$ and $I_\parallel$. In addition to the amplitudes of the radiation, the radiation frequency might be different in different directions, which is discussed in the following.

4.4.3 Superradiance frequency shift

An atom interacting with the electromagnetic field by an electric dipole transition moment exhibits frequency shifts. For example, Weisskopf and Bethe predict that a radiation field can induce a small frequency shift in radiation from the $2s_{1/2}$ state of Hydrogen atom [145, 146]. The interaction between the electron and the virtual photon leads to the familiar Lamb shift. Scully has shown that this frequency shift can be amplified by a collective interaction in an ensemble, giving rise to a collective Lamb shift [142, 9]. The collective Lamb shift has a similar mechanism to the ordinary Lamb

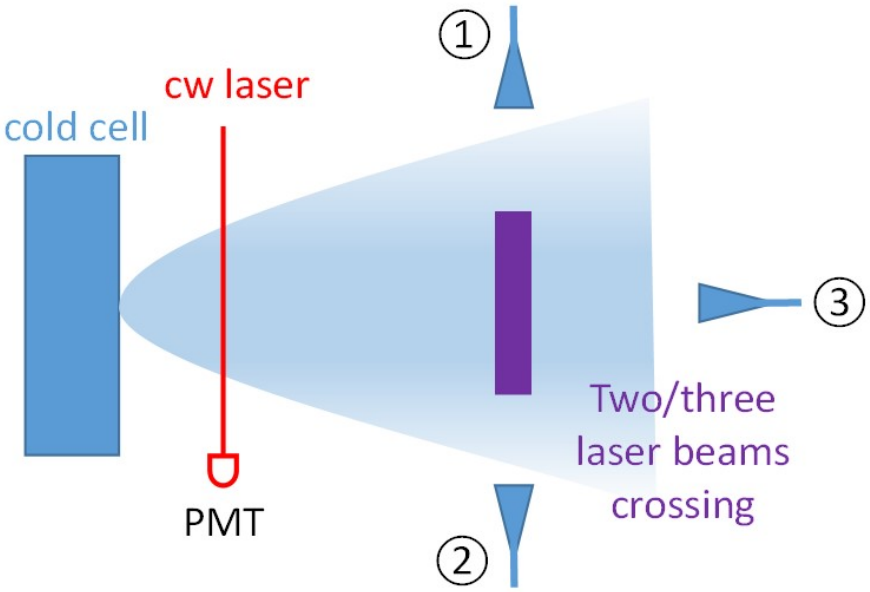

Figure 4-16: A schematic diagram for detecting the radiation anistropy. cw laser absorption is used to calibrate the pulse-to-pulse number density fluctuations of the molecular beam source. The rectangular box represents the initially prepared Rydberg sample using two or three crossed tunable lasers (not shown). Three identical millimeter-wave horns are used to broadcast the excitation pulse or receive the radiation.

shift except that the virtual photon emitted by one atom can be absorbed by another. The collective Lamb shift had not been observed until 2010 by Rohlsberger [147]. The usual difficulty of preparing a system with optically thin pumping and optically thick radiation is overcome in our system. However, due to the gigantic electric dipole transition moment of Rydberg-Rydberg transitions, other frequency shift mechanisms exist in our system, such as the Coulomb shift, the resonant collision shift, and the dipole-dipole shift, each of which must be characterized carefully. Fortunately, theorists find that the different frequency shift mechanisms have different dependence on the geometry of the sample [148, 149, 144]. We have the ability to systematically change the sample geometry by shaping the excitation laser beams, to isolate the collective Lamb shift. In addition to experimental difficulties, a precise measurement of the center frequency of the radiation is non-trivial. For example, in Figure 3-29, at high number density, due to the 4 MHz linewidth of the superradiant broadening, accurately measurement of the center frequency is difficult. It is only possible to extract the information from the tail of the radiation. Alternatively, it would be possible to develop a Ramsey-type pulse sequence experiment in order to gate the information extraction only from long lifetime components.

4.4.4 Rydberg mirror

In Figure 4-12, I show that a sufficiently weak excitation pulse ($\Omega_{Rabi} \times \tau_{\text{pulse}} \sim 1$) cannot penetrate deeply into the dense Rydberg sample. Is the non-penetrating excitation wave reflected by the boundary of the vacuum and the dense Rydberg gas? In a classical system, this question can be answered easily, as in Figure 4-17.

According to the Fresnel equation, it is easy to compute the transmitted electric field and the reflected electric field,

$$E_1 = \frac{\sqrt{\varepsilon_1} - \sqrt{\varepsilon_2}}{\sqrt{\varepsilon_1} + \sqrt{\varepsilon_2}} E_0 \tag{4.55a}$$

$$E_2 = \frac{2\sqrt{\varepsilon_1}}{\sqrt{\varepsilon_1} + \sqrt{\varepsilon_2}} E_0, \tag{4.55b}$$

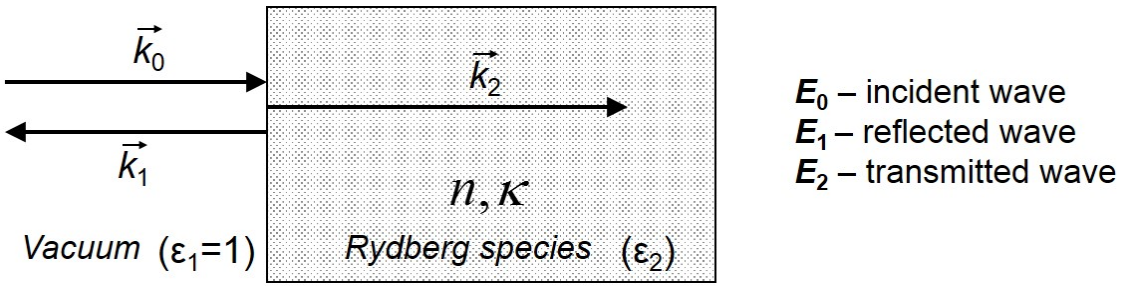

Figure 4-17: A schematic diagram of a transmission wave and a reflection wave at the boundary of the vacuum and the dense Rydberg sample.

where E_0 is the incident electric field, E_1 and E_2 are the reflected and transmitted electric fields respectively, and ε_1 and ε_2 are the permittivity of the vacuum and the Rydberg species respectively. The permittivity of the vacuum is real and of unit magnitude, and that of the Rydberg species is complex and can be divided into dispersion and absorption terms, $\sqrt{\varepsilon_2} = n_2 + i\kappa_1$. I substitute this into Eq.(4.55),

$$E_1 = \frac{1 - n_2 - i\kappa_2}{1 + n_2 + i\kappa_2} E_0 \tag{4.56a}$$

$$E_2 = \frac{2}{1 + n + i\kappa} E_0. \tag{4.56b}$$

Therefore, the relationship between the transmitted wave and reflected wave is

$$E_1 = \frac{E_2}{2}(1 - n_2 - i\kappa_2) \rightarrow E_1 = -i\kappa_2 \frac{E_2}{2} \tag{4.57}$$

On resonance, n_2=1, the ratio of the electric fields of the reflected wave to the transmitted wave is proportional to the absorption coefficient. For a dense Rydberg gas with a large absorption coefficient, the reflected wave is significant. In the quantum mechanical picture, the phase relationships of the three waves (incident, reflected and transmitted) are more complicated and discussed in detail by Yelin [150].

If a dense Rydberg gas can resonantly reflect the millimeter-wave pulse, this would enable use to detect the resonant signal at the back side of the sample, which is totally separate from the excitation pulse. It is similar to a transient absorption experiment, but the background is zero. With such a resonant Rydberg mirror, we would be able

to separate excitation and radiation spatially. This spatial separation can not only increase the sensitivity to detect weak signals, but also can enable detection of fast decay process during the excitation. In addition, in this geometrical configuration, the Doppler shift instead of Doppler broadening limits the spectroscopic resolution.

Chapter 5

CPmmW spectroscopy of BaF Rydberg-Rydberg transitions

I choose BaF as the first candidate on which to perform molecular Rydberg-Rydberg transition experiments, because:

- The dissociation threshold of BaF lies higher in energy than the ionization limit ($v^+ = 0$ and 1) [151]. This unique feature eliminates nonradiative decay via predissociation for $v^+ < 2$. Therefore, all states belonging to $v^+ = 0$ Rydberg series are stable and have lifetimes similar to Calcium or Barium Rydberg states. Thus, I have sufficient time to populate high-ℓ states by stepwise laser and millimeter-wave pulsed excitation.

- The states belonging to $v^+ = 1$ Rydberg series have similar spectroscopic structures to $v^+ = 0$ Rydberg series, but with much shorter lifetimes due to autoionization dynamics. Therefore, the detailed analysis of the $v^+ = 0$ Rydberg series can help to assign the spectra of $v^+ = 1$ Rydberg series. By comparing $v^+ = 0$ and $v^+ = 1$ Rydberg spectra, I can systematically study vibrational autoionization dynamics, which directly connects to the R-dependence quantum defects.

- $v^+ = 1$ Rydberg series with controllable and predictable non-radiative lifetimes

provide us with a good test system for new quantum control techniques for lossless access to core non-penetrating states, see Section 6.

- Considering experimental convenience, our lab possesses a large amount of data from low-lying Rydberg states of BaF ($4.4 \leq n^* \leq 14.3$) that simplifies our exploration and accelerate our assignment of the higher-n^* Rydberg states, especially the core-nonpenetrating Rydberg states [152, 153, 154, 155, 151].

Similar to Chapter 3, BaF experiments are performed in two different apparatuses (Gertrude chamber and Buffy chamber) in parallel. The experiments in the Gertrude chamber are done to approximately locate the molecular Rydberg states and provide laser frequency information for the initial Rydberg state preparation. The experiments on millimeter-wave excited molecular Rydberg-Rydberg transitions are performed exclusively in the Buffy chamber. In this chapter, I describe the standard experimental procedures for obtaining a high quality FID spectrum. Then, I discuss several non-standard experimental and data analysis techniques, to access more fruitful information efficiently, as well as to simplify and organize the data automatically. Although the proof of principle experiments are successful, there are several technical problems preventing systematic collection of the data for analysis. I discuss such problems and propose several possible solutions.

5.1 BaF experiment in the supersonic beam apparatus

Although the most important BaF FID spectra cannot be recorded on the supersonic beam apparatus, a high quality Optical-Optical Double Resonance (OODR) spectrum of BaF Rydberg states at $n^* \sim 40$ is still fairly necessary for the following FID experiments in the buffer gas cooled beam apparatus. Such OODR spectra were far more difficult to collect than I expected.

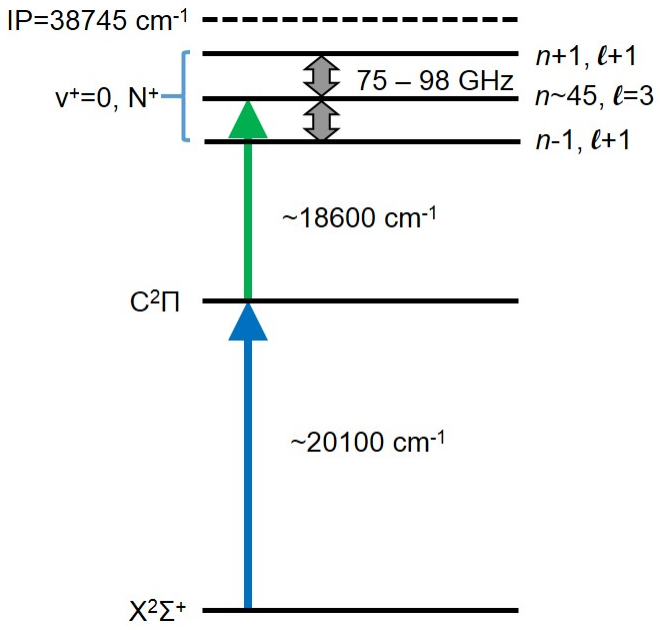

Figure 5-1: A schematic diagram of the energy levels of the BaF molecule.

5.1.1 Experimental implementations

BaF molecules are prepared by laser ablating Ba metal to form a plasma, which reacts with 0.2% SF_6 gas in Argon carrier gas. A Spectra-Physics Nd:YAG laser (BigSky CRF200, 7 ns, 8 mJ 532nm pulse, 20 Hz repetition rate) is focused to ∼1 mm diameter by a biconvex lens with f = 1 m and ablates Barium from a rotating and translating Barium rod (0.245" diameter). The ablated Barium plasma is entrained in the carrier gas and reacts in a 180 μs long pulse of 30 PSI 0.2% SF_6 and Argon gas mixture, which is generated by a General Valve (Parker Hannafin Corporation) Series 9 1 mm nozzle with an IOTA One driver. The nozzle configurations are described in Section 2.1.2.

A schematic diagram of the energy levels of the BaF molecule involved in this section is depicted in Figure 5-1. Two pulsed dye lasers (Pump laser: Lambda Physik Scanmate 2E, with intracavity etalon, 0.05 cm^{-1} resolution, LD 490, Probe laser: Sirah Precision Scan, double gratings, 0.03 cm^{-1} resolution, Coumarin 540A) are used to stepwise excite BaF molecules from the ground state X $^2\Sigma^+$ via a C $^2\Pi_{3/2}$ intermediate state to a Rydberg state $^2\Sigma^+$, $^2\Pi$, $^2\Delta$ or $^2\Phi$. The C $^2\Pi_{3/2}$ state was

Table 5.1: Optimized parameters of the BaF molecular beam.

Items	Best option	Tested candidates
Chemical reactant	SF_6	SF_6, CHF_3
SF_6 concentration*	0.1%	0.005% - 10%
Buffer gas	Ar	He, Ne, Ar
Backing pressure	30 PSI	10 - 100 PSI
Ablation laser power*	8 mJ	2 - 15 mJ
Diameter of ablating spot	1 mm	0.1 - 2 mm
Gas pulse duration	180 μs	150-250 μs
Delay between gas pulse and ablation laser pulse*	The optimized time window is only 20 μs wide	

chosen as the intermediate state due to the laser wavelength convenience. Both dye lasers are pumped by an injection-seeded Spectra-Physics Nd:YAG laser (GCR-290, 7 ns 100mJ 355nm pulse, 20 Hz repetition rate). The pump laser (495.5-496.5 nm) is calibrated by the Te_2 absorption spectroscopy, and the probe laser (539-542 nm) is calibrated by I_2 LIF spectroscopy.

5.1.2 Optimization of the BaF molecule generation

To obtain a stable and bright BaF molecular beam, I optimize several parameters of the beam source by detecting the LIF signal, which will be described in Section 5.1.3. The optimized parameters are listed in Table 5.1. The items with asterisk are the most sensitive and need to be optimized carefully. Figure 5-2 shows systematic measurements of BaF yield and temperature with different ablation laser power and SF_6 concentrations. In addition, I find that the delay between the gas pulse and ablation laser pulse is very sensitive. A larger than 20 μs deviation from the optimized value would decrease the signal by a factor of 5.

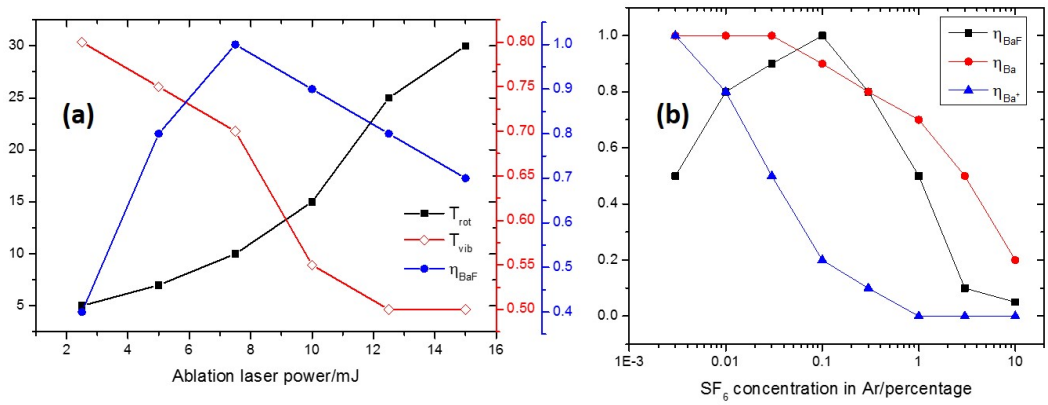

Figure 5-2: Optimization of the BaF beam source. In Plot (a), the blue curve shows the ablation laser power dependence of BaF yield. The black curve shows that the rotational temperature of BaF increases with higher ablation laser power, and the red curve shows the decrease of the number density of BaF molecules in the vibrational ground state with higher ablation laser power. Plot (b) shows titration curves of Ba with different concentrations of SF_6. The BaF yield is maximum at 0.1% SF_6. With high concentration of SF_6, most of the Barium appears to react with SF_6 to create BaF_2, which cannot be optically detected here.

5.1.3 Laser Induced Fluorescence (LIF) and Resonance Enhanced Muli-Photon Ionization(REMPI) spectra of BaF C $^2\Pi_{3/2}$ - X $^2\Sigma^+$ transitions

The transition C $^2\Pi_{3/2}$ - X $^2\Sigma^+$ has already been measured precisely. In this chapter, my purpose is not to refine the spectroscopic data. The LIF experiment is used to roughly measure the BaF number density per single rotational state, which is used for optimization of both the supersonic cooled beam source and the buffer gas cooled beam source. The REMPI experiment is used for optimizing the TOF-MS to achieve a better OODR spectra, as discussed in the next section.

In the LIF experiment, the supersonic molecular beam is skimmed by a 3 mm diameter conical skimmer, which is placed 3 cm downstream from the supersonic nozzle, and then crossed with the pump laser (6 cm downstream), which is collimated with 3 mm diameter. Because the fluorescence wavelength is almost the same as the excitation wavelength, which cannot be separated by a regular interference filter, I

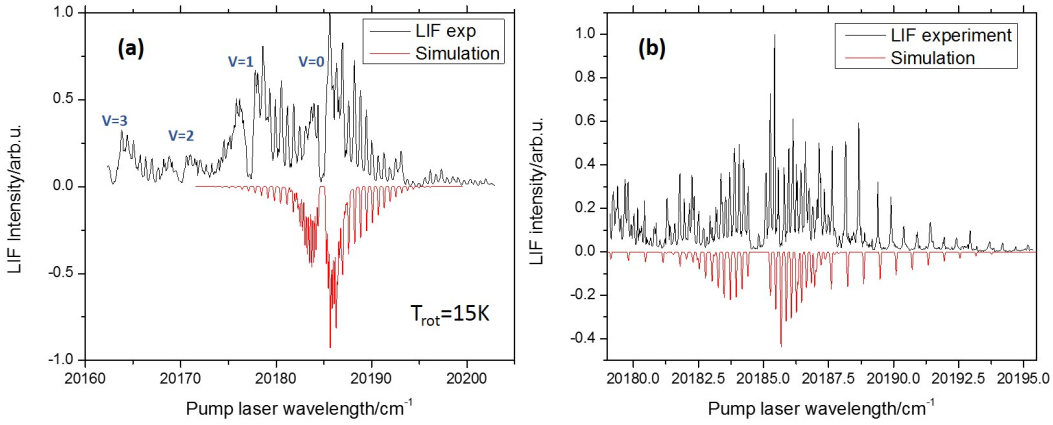

Figure 5-3: LIF spectrum of BaF C $^2\Pi_{3/2}$ - X $^2\Sigma^+$ transitions in the supersonic beam apparatus. In Plot (a), the top spectrum is a typical low resolution (0.15 cm^{-1} without intracavity etalon) LIF spectrum. Several transitions branches from different vibration states are observed. The bottom spectrum is a simulated BaF spectrum from ground vibration state at 15 K rotational temperature. Plot (b) shows a typical high resolution (0.05 cm^{-1} with intracavity etalon) LIF spectrum and a simulated spectrum.

must carefully construct a baffle to minimize the scattered photons arriving at the PMT detector. The fluorescence is collected by a f=5 cm lens above and a f=5 cm parabolic mirror below. The collected photons are focused through a d=3 mm iris and detected by a PMT. Figure 5-3 is a typical LIF spectrum of BaF C $^2\Pi_{3/2}$ - X $^2\Sigma^+$ transitions. The assigned $^2\Pi_{3/2}$ - $^2\Sigma^+$ spectrum recorded by LIF is used not only to characterize the pump laser wavelength, but also to measure the saturation power of the pump transitions, which is useful for the FID experiments. For typical transitions, the saturation power (defined by the laser power generating ~80% of the maximum LIF signal) is 100 $\mu J/cm^2$.

In addition to recording LIF spectra, I also record REMPI spectra by ion detection for several reasons: (1) Ion detection has much higher sensitivity (100% detection efficiency); (2) With a TOF-MS, I can separate the five different isotopologues of BaF by their different arrival times; (3) Optimizing REMPI spectra is helpful for the OODR with Ramped-PFI experiment, to be discussed in the next section. The details of the TOF-MS have been described in Jason Clevenger's thesis [93]. Here I

only list several matters that require attention. The notation below can be found in Jason Clevenger's thesis.

- The amplitude of the extraction pulse on A1 should be below 250 V/cm. Otherwise, the ions with the same e/m cannot be focused in the time-domain. The detailed discussions and calculations are in Christopher Gittins' thesis [156].

- Although focusing the excitation laser can also increase the mass resolution of the TOF-MS, it reduces the total number of ions. With a 1 mm^2 loosely focused laser spot, I must tweak the ion optics carefully to focus the ions temporally and spatially. The resolution of our spectrometer is high enough to resolve all five isotopologues of BaF.

- For BaF C $^2\Pi_{3/2}$ - X $^2\Sigma^+$ transitions, I cannot use 1+1 REMPI (two photons with the same frequency). The transition dipole moment of the C $^2\Pi_{3/2}$ - X $^2\Sigma^+$ transition is >20 times larger than the transition dipole moment of the ion state - C $^2\Pi_{3/2}$ transition. When the laser power is strong enough to create BaF ions, it has already power broadened the C $^2\Pi_{3/2}$ - X $^2\Sigma^+$ transition. To avoid power broadening, I use 1+1' REMPI instead. A loosely focused weak pulse (1 μJ) is used to excite C $^2\Pi_{3/2}$ - X $^2\Sigma^+$ transitions, and a loosely focused strong pulse (1 mJ, <530 nm) is used to ionize C $^2\Pi_{3/2}$ states.

Figure 5-4 shows the raw data of a BaF REMPI spectrum. It is easy to gate different isotopologues of BaF and obtain their REMPI spectra individually, as in Figure 5-5. In my experiment, I am only interested in ^{138}BaF. I can obtain the following information from the spectroscopic assignment of the ^{138}BaF REMPI spectrum: J (total angular momentum), N (total angular momentum without spin), ΔN, ΔJ, F_n (spin component), which will be used in the analysis of OODR spectra and in service of FID experiments. The spectroscopic assignment of the BaF molecule has been done by Effantin et al. [98], and is not repeated here.

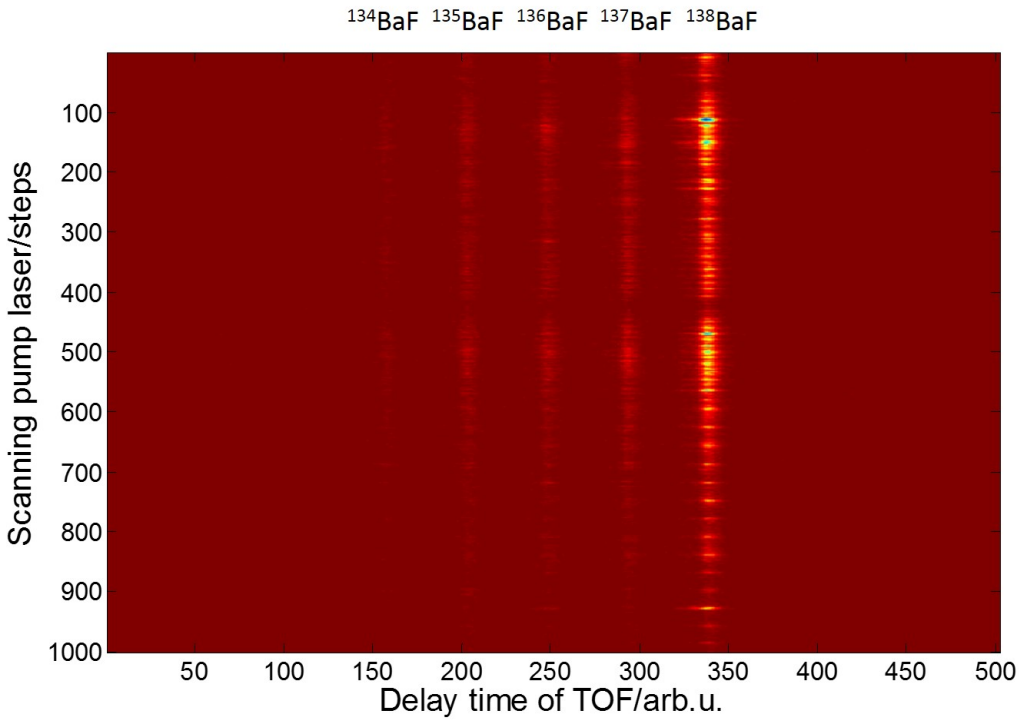

Figure 5-4: Raw data of BaF REMPI spectrum. The x axis is the arrival time of the detected ions. The y axis is the frequency scan of the pump laser. Each vertical line represents an isotopologue of BaF, which are labeled at the top of the figure.

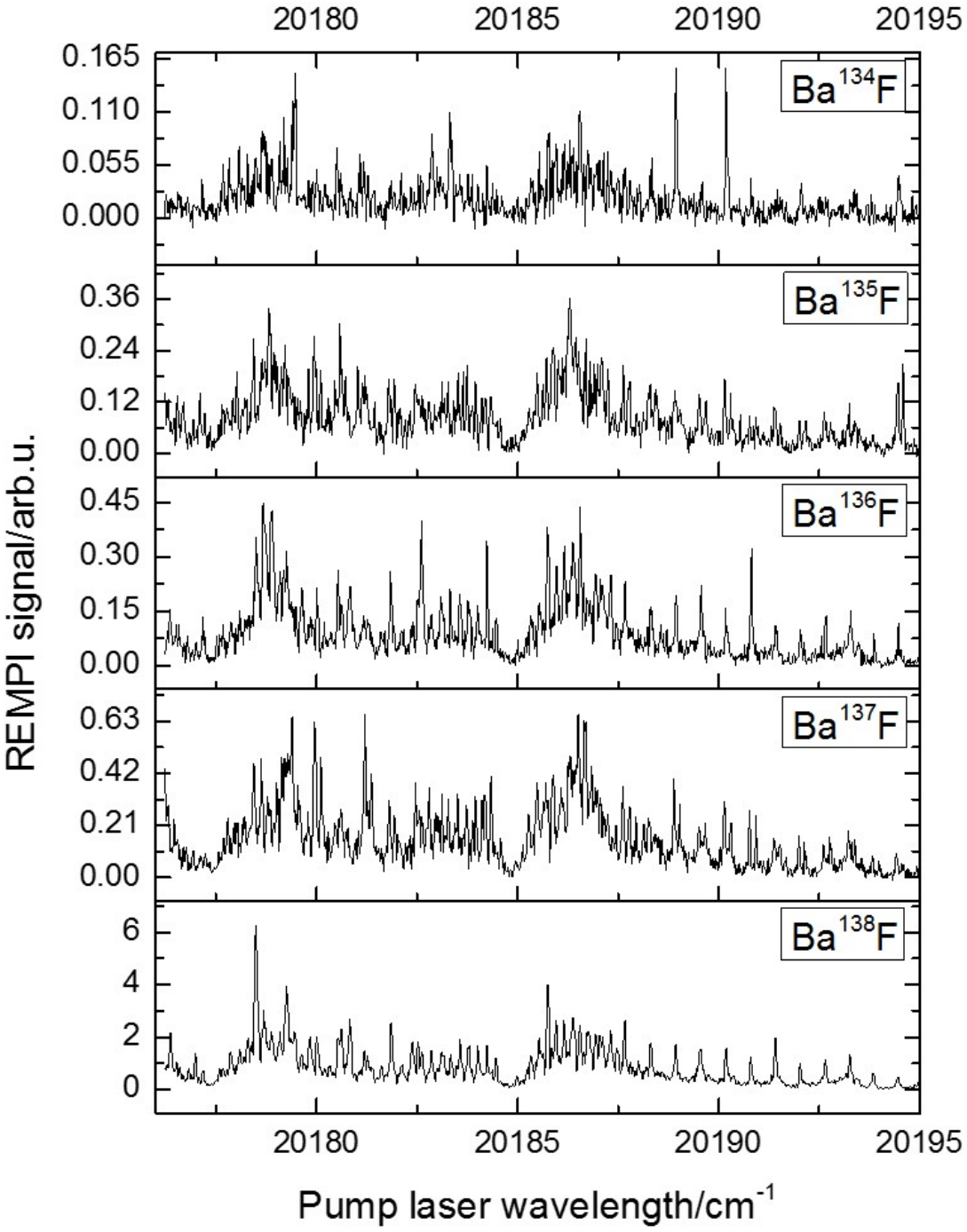

Figure 5-5: REMPI spectra of five BaF isotopologues. x axis is the uncalibrated pump laser wavelength. Due to non-zero nuclear spin of ^{135}Ba and ^{137}Ba, we can observe nuclear spin induced splittings in ^{135}BaF and ^{137}BaF spectra.

5.1.4 Optical-Optical Double Resonance (OODR) with Ramped Pulsed Field Ionization detection (Ramped-PFI)

With the spectroscopic information on the intermediate C $^2\Pi_{3/2}$ state of BaF, I use another pulsed dye laser (Probe laser) to populate Rydberg states with n*∼40 and v=0. The ionization potential (IP) of BaF has been measured by Jakubek et al [151]. Using the Rydberg formula, I can approximately estimate the probe laser wavelength. Because the Rydberg states with v=0 are bound states, I must apply a pulsed electric field to ionize them. As discussed in Section 3.1.2, I apply a ramped pulsed field, which provides additional information about n*. The threshold of the pulsed field ionization for a Rydberg state with n* is

$$E = \frac{1}{16n^{*4}}. \tag{5.1}$$

In Eq.(5.1), E is the threshold of PFI electric field in atomic units. The energy spacing between n* and n*+1 is ∼3 cm^{-1} for n*∼40. However, the number of electronic-rotational transitions can be as large as 100. Therefore, a tiny stray electric field might couple multiple neighboring levels thereby washing out the periodic structure of the Rydberg series. Therefore, before I record the OODR data, I must minimize the electric field with the methods discussed in Section 3.1.3. Figure 5-6 shows the raw data of the OODR spectrum with Ramped-PFI detection. The pump laser is fixed and populates the N=2 C $^2\Pi_{3/2}$ intermediate state of BaF. The probe laser is scanned across a ∼50 cm^{-1} range, which covers from n*=37 to the IP. In Figure 5-6, I can identify vertical lines corresponding to the multi-photon ionized isotopologues of BaF. Multi-photon ionization is an unwanted process and is independent of probe laser wavelength, which is discussed in Section 5.3. The curved line shows the Ramped-PFI of BaF Rydberg states. Rydberg states with different n* are ionized at different electric fields. Therefore, the signals appear at different delay times. The Ramped-PFI signals are probe laser wavelength dependent. I apply integration windows with different widths and delays for different n^* to integrate the ion signals at each probe laser wavelength to obtain the spectra shown in Figure 5-7. Although the spectroscopic transition density is very high and most of the structures

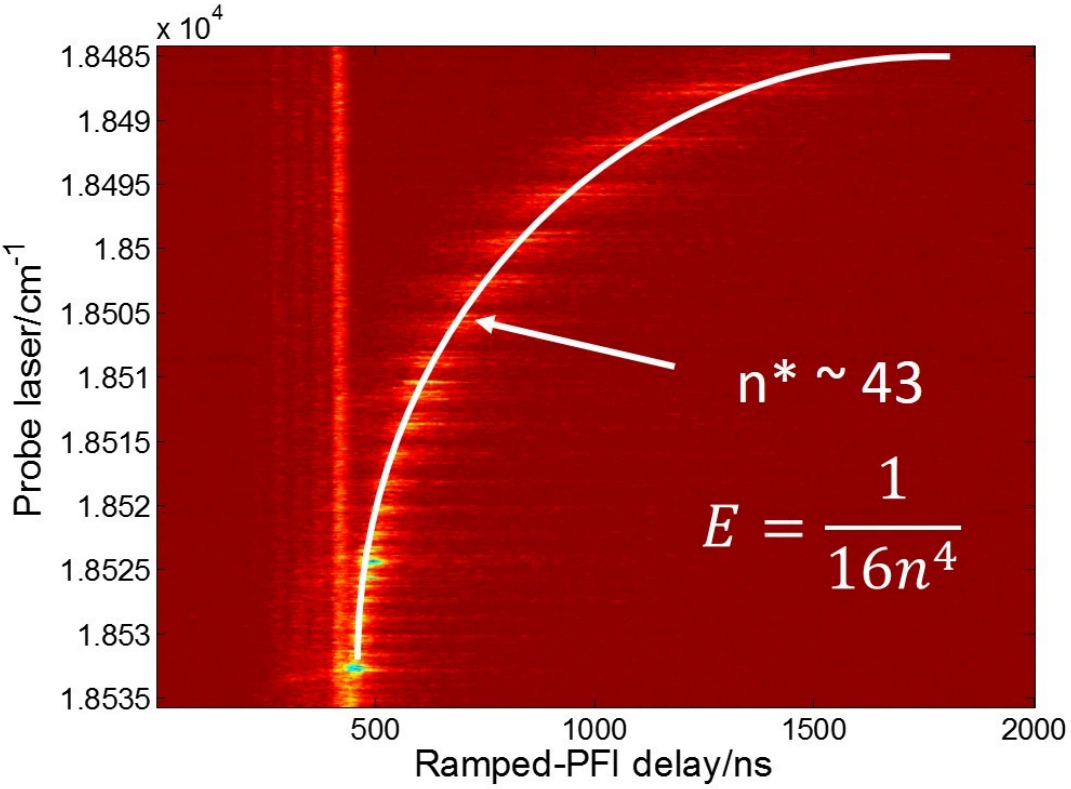

Figure 5-6: Raw data of BaF OODR Ramped-PFI spectrum. The x axis is the arrival time of the detected ions. The y axis is the wavelength of the probe laser. The vertical lines represent the multi-photon ionized isotopolgoues of BaF. The curved line represents the Ramped-PFI of BaF Rydberg states. Different isotopolgoues of BaF Rydberg states cannot be resolved in the time-domain.

cannot be resolved, I still obtain a periodic structure of Rydberg series. With the Rydberg formula, I can assign the n^* for each group of Rydberg states. This assigned n^* is consistent with the calculated n^* based on the known IP of BaF.

The ramped pulse in this experiment is used to isolate the Rydberg states from the ions created by multi-photon ionization. This method decreases the background to zero and increases the signal to noise by a factor of 3 compared to conventional PFI with a rectangular pulse. A disadvantage is that I cannot separate the signals of different isotopologues. As mentioned, to obtain a spectrum as shown in Figure 5-7, I must minimize the stray electric field carefully, which is non-trivial. However, when the OODR experiment is used only for obtaining n^* for the subsequent millimeter-wave experiments, we use a much less demanding method. From Eq.(5.1) [13] and

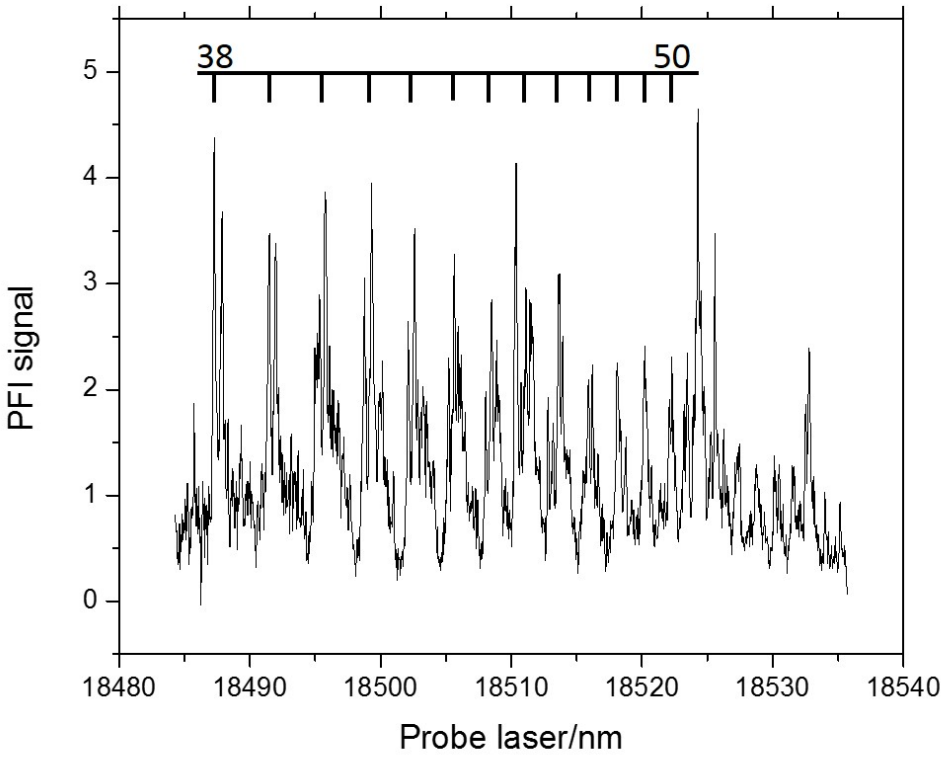

Figure 5-7: OODR spectrum of BaF Rydberg states. The assignment of n^* is labeled on the top of the spectrum.

the characterized ramped pulsed electric field, as shown in Figure 2-6, I can connect the n^* to the delay time of the ion signal, which appears the solid curve in Figure 5-6. I can fit the delay time vs. wavelength of the probe laser to determine n^* approximately. Due to the broad distribution of ions in the time-domain, and the deviation of Eq.(5.1) for a non-hydrogenic system, this method might result in an error of ± 1 in n^*, which is acceptable for my present purpose.

As in the REMPI experiment, I also measure the saturation power of the probe transitions. The typical saturation power is $\sim$10 mJ/cm^2, which is much higher than that of the pump transitions.

5.2 BaF CPmmW experiment in the buffer gas cooling setup

The BaF CPmmW experiment is the central experiment in my thesis. Most of the experiments discussed previously have been in preparation for this. The experiments, analysis, and theoretical calculations that follow this section are all extensions and applications based on the BaF CPmmW experiment.

5.2.1 Experimental implementations

There are no new experimental implementations for the BaF CPmmW experiment. All necessary preparations have been discussed in previous sections. Here, I will outline the necessary steps as follows:

- Molecular beam source: optimized buffer gas cooled molecular beam, as described in Section 2.2.
- Pump and probe lasers: two tunable pulsed dye lasers pumped by an injection seeded Nd:YAG laser. Their wavelength and powers can be set according to the LIF spectrum and OODR spectrum, which have been described in Section 5.1. Due to the high saturation power (100 mJ/pulse) of the probe transition, I cannot saturate this transition with a d=10 cm^2 expanded laser beam. A typical value of the pulse energy of the probe laser used in the BaF CPmmW experiment is 20 mJ, which is the maximum output of our pulsed dye laser.
- CPmmW spectrometer: 76-98 GHz, 15 dBm maximum power, as described in Section 2.3.
- Implementation of the CPmmW spectrometer with the buffer gas cooling apparatus: reflection mode for maximizing the interaction volume, as described in Section 2.3.6.
- Typical time-sequence: Regular Lasers-CPmmW-FID pulse sequence, as described in Section 3.2.

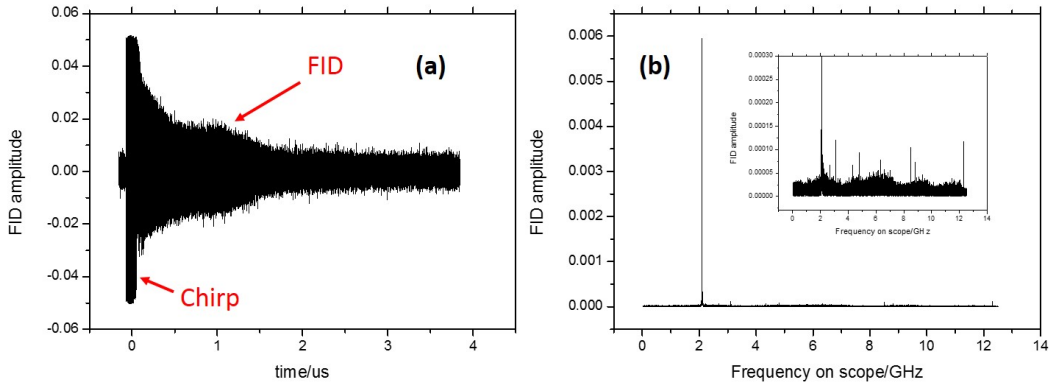

Figure 5-8: First CPmmW spectrum of BaF Rydberg-Rydberg transitions. Plot (a) shows BaF Rydberg-Rydberg transitions polarized by a 100 ns, 0 dBm, 76-98 GHz broadband chirped pulse in the time-domain. Plot (b) is the Fourier transform power spectrum of the FID in Plot (a). The inset plot shows several weak transitions.

5.2.2 Millimeter wave induced Rydberg-Rydberg transitions with Free Induction Decay detection (FID)

Figure 5-8 shows my first CPmmW spectrum of BaF. All transitions are induced by a 100 ns, 0 dBm, 76-98 GHz broadband chirped pulse. I observe a strong FID after the excitation in the time-domain, as shown in Figure 5-8, Plot (a). Plot (b) is the Fourier transform power spectrum of the FID in Plot (a). This spectrum is averaged 100 times in 10 s.

As far as I know, this is the first spectrum of FID-detected molecular Rydberg-Rydberg transitions in the world. However, I find two suspicious problems after carefully studying this spectrum: (1) One transition is much stronger than the others. As we know, there should be several transitions, ΔN=0, $\pm$1, $\Delta\ell$=$\pm$1, from the same initial Rydberg state. Their electric dipole transition moments should not be different by a factor of 10. (2) The linewidth of the strong transition is $\sim$400 kHz, which is larger than the resolution of the FT-window. However, the linewidth of the weak transitions are $\sim$150 kHz, which is limited by the FT-window. This is also unexpected, because I do not think that the lifetime of one Rydberg state is significantly shorter than that of the others.

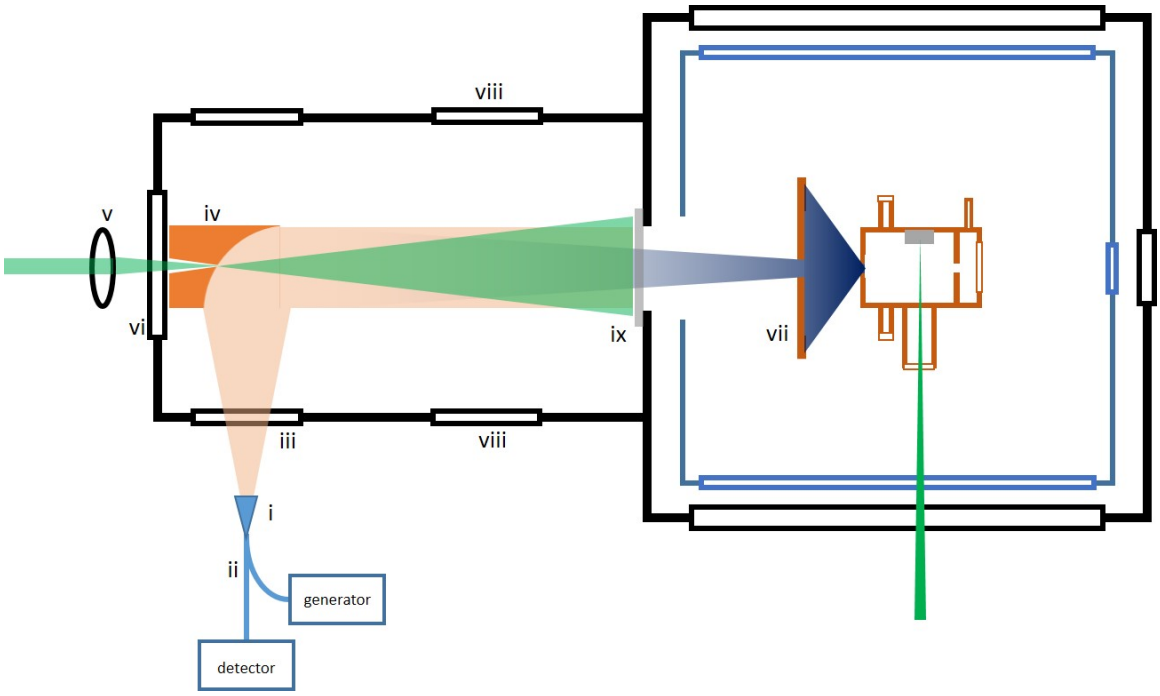

Figure 5-9: Modification of the interaction volume to avoid superradiant decay in the BaF experiment. Different from Figure 2-35, I move the nickel mesh (ix) from the cold skimmer (vii) to the wall of the detection chamber.

One possible explanation of these unexpected phenomena is superradiance. As I discuss in Section 4, in a system with multiple transitions, strong collective effects can focus intensity to one transition that has a relatively larger transition dipole moment. The same as shown in Figure 4-14, although the strongest transition in Figure 5-8 has slightly larger transition dipole moment, almost all radiation goes through this channel. At the same time, the strong collective effect increases the decay rate of the strongest transition, thus inducing much broader linewidth. To confirm this hypothesis, I decrease the number density of the Rydberg molecules interacting with the millimeter-wave radiation by two different methods: (1) Decrease the pump or probe laser power. (2) Move the reflection nickel mesh from the cold skimmer to the wall of the detection chamber, as shown in Figure 5-9. This prevents the millimeter-waves from interacting with the most dense region of Rydberg molecules.

As shown in Figure 5-10, I find that both modifications decrease the intensity ratio of the strong and weak peaks. In addition, all peaks have similar linewidth, $\sim$

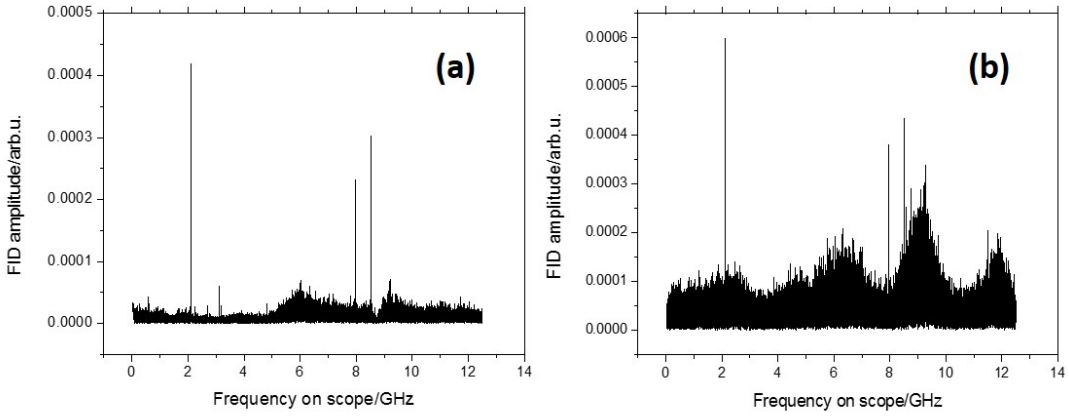

Figure 5-10: Spectra of BaF Rydberg-Rydberg transitions without significant superradiant decay. Plot (a) is the spectrum, which is taken after we move the reflection nickel mesh. Plot (b) is the spectrum with much lower pump and probe laser power.

150 kHz, which is limited by the FT-window.

Another important issue for obtaining intense FID is laser power. Figure 5-11 shows the dependence of the FID on the power of the pump and the probe lasers. Plot (a) shows a maximum FID with 0.7 mJ pulse energy, which is consistent with the saturation power measured by LIF. However, a surprisingly steep decrease instead of a flat saturation curve follows. Based on my experience with the REMPI experiment, I know that a high energy pump laser creates many ions by 1+1 REMPI. The collisions between ions and Rydberg molecules are likely to reduce the FID radiation significantly. This argument seems to be reasonable, but has not been studied quantitatively. In typical experiments, I must tune the pump laser power carefully to maximize the FID amplitude. Plot (b) shows a standard saturation curve. However, the saturation power (15 mJ/10 cm^2) in this figure is far smaller than that measured by OODR. This inconsistency might come from the balance between populating the target Rydberg state (increased FID amplitude) and generating ions (decreased FID amplitude). In a typical experiment, I always use the maximum power of the probe laser (15-20 mJ). The problem of the laser power is revisited in Section 5.3.

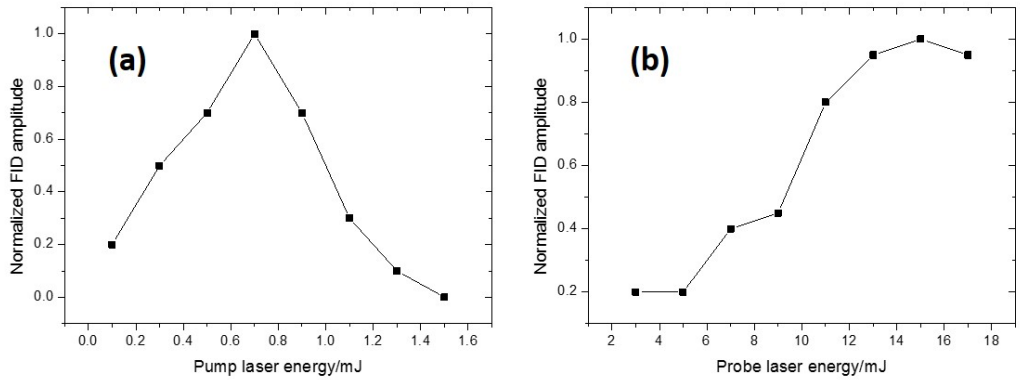

Figure 5-11: Power dependence of the FID on the pump laser, Plot (a), and the probe laser, Plot (b).

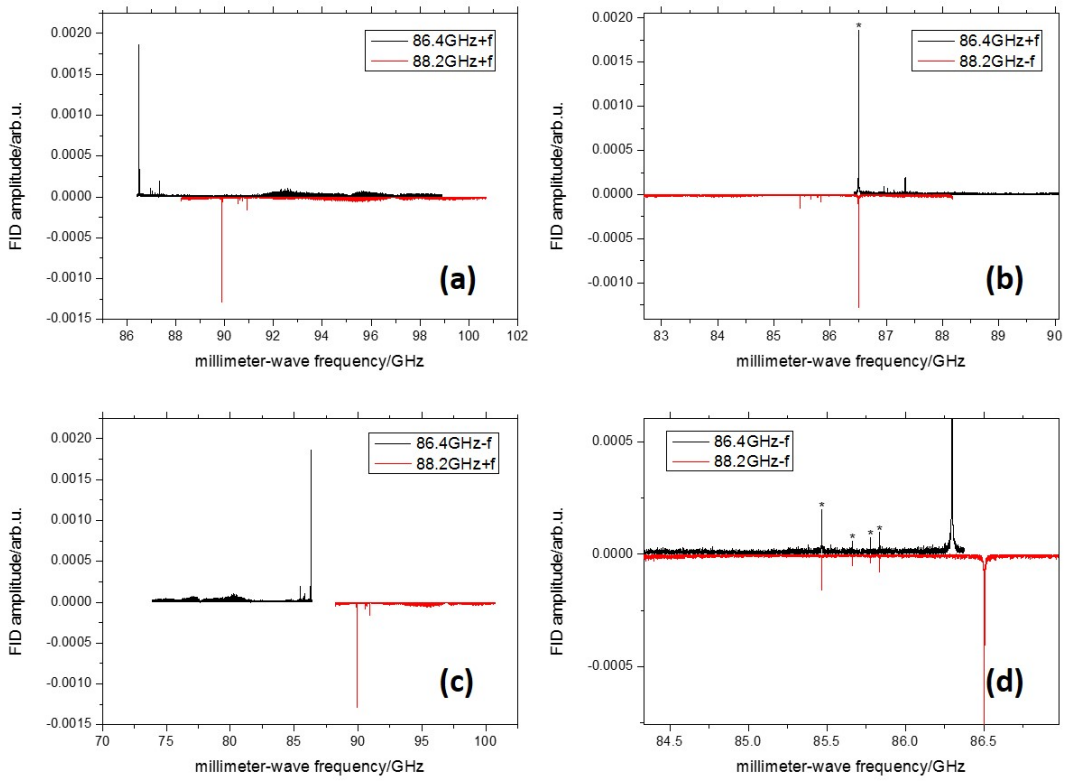

Figure 5-12: Recovering the millimeter-wave frequency. Plots (a) to (d) show four combinations of the two spectra with different intermediate down-conversion frequencies. The stars mark the transitions for which the millimeter-wave frequency is recovered.

5.2.3 Recovering the millimeter-wave frequency

The frequencies measured by the fast oscilloscope are down-converted by mixing the FID radiation with an intermediate frequency. Due to the absence of quadrature phase detection, I cannot recover the millimeter-wave frequency unambiguously using only one intermediate frequency. An easy solution is to record the same spectrum twice with different intermediate frequencies. In my experiment, I set f_{I1}=86.4 GHz and f_{I2}=88.2 GHz to record two spectra. The possible real frequencies of spectrum 1 are f_s+f_{I1} and f_s-f_{I1}. (f_s is the frequency measured by the scope), and that of spectrum 2 are f_s+f_{I2} and f_s-f_{I2}. As shown in Figure 5-12, a Matlab program automatically matches the overlapped peaks from the two spectra. This method requires doubling the data collection time. However, the spectrum with f_{I2} does not need to be averaged as many times as the spectrum with f_{I1}. In addition, based on the spectrum with f_{I1}, I can judge whether I need to record the spectrum with f_{I2} (If there is no FID in spectrum with f_{I1}, I do not need to record another one with f_{I2}). Therefore, this method only increases the data collection time by 5% in typical experiments.

5.2.4 Applying weighted averaging to reduce noise in the millimeter wave spectrum

Weighted averaging is a technique inherited from extended cross correlation (XCC) [10, 11], a method for spectroscopic pattern recognition, developed by Jacobson et al. in our group. The details of XCC are included in Jacobson's thesis and not repeated here [157]. The essence of XCC is to record two spectra which contain a linear combination of several patterns, as shown in Figure (5-13), Plot (a). Then I plot the intensity of the spectrum 1 vs. the intensity of the spectrum 2, to produce a recursion map, as shown in Figure (5-13), Plot (b). In the recursion map, it is easy to find two linear clusters of points, which represent the two patterns in the original spectra. To extract such pattern information by reducing the noise, XCC employs a

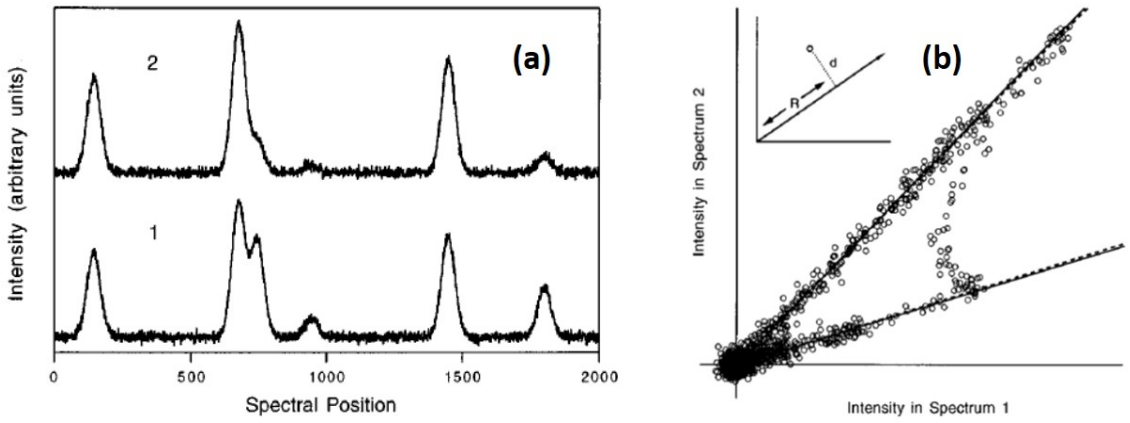

Figure 5-13: An illustration of the XCC method. Plot (a) shows a synthetic spectrum which contains a linear combination of two patterns. Plot (b) is a recursion map of the spectra in Plot (a). The x axis of the recursion map is the intensity of spectrum 1, and the y axis is the intensity of spectrum 2. The inset shows the (R,d) coordinates that are in Eq.(5.2). Reprinted from [10, 11].

re-descending robust estimator:

$$G(\alpha) = \sum_i g_i(\alpha) = \sum_i R_i \times \exp\left(-d_i^2/2V_d\right) \tag{5.2}$$

where i labels each data point, R and d are defined in Figure (5-13), Plot (b), V_d is an estimated noise level, α is the angle between the pattern line and x axis. The XCC pattern recognition process is simply to minimize G. The procedure of separating the recognized patterns in XCC technique is not relevant in this thesis.

What I need in the FID experiment is not pattern recognition, but noise reduction. However, I can modify the XCC method to achieve our goal. Similar to the XCC method, I record the FID spectrum twice (spectrum 1 and spectrum 2) with the same experimental conditions. The standard method to reduce the noise is just to average them. My method is to apply a weighted average. The weight factor is in Eq.(5.2). Different from XCC, the typical noise level in my spectrum is very large, especially for a weak signal. Therefore, it is not easy to obtain α. A wrong α could accumulate noise in a weighted average to create a fake signal. An easy solution is to replace the positive variable R in Eq.(5.2) by R-$R_{baseline}$, which can be positive or negative, and $\langle R - R_{baseline} \rangle = 0$. Thus, the accumulation occurs only for "asymmetric" signal, but

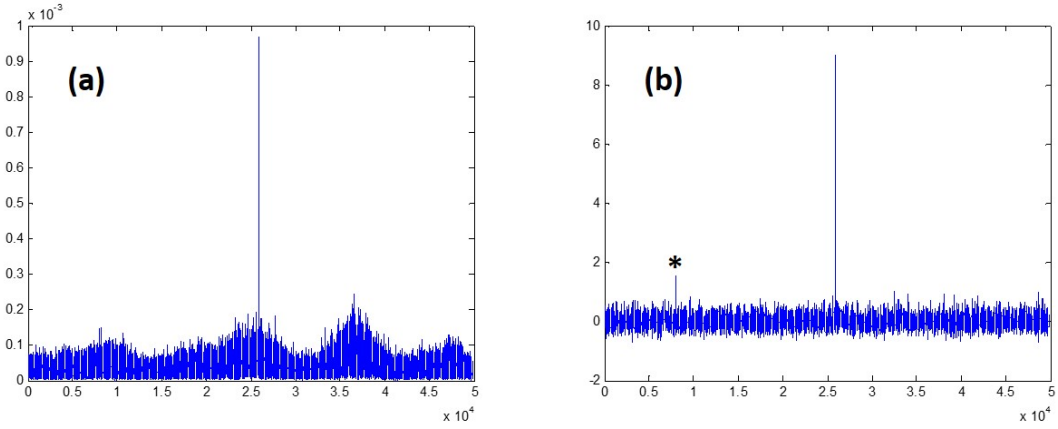

Figure 5-14: Applying weighted averaging to reduce the noise. Plot (a) is produced by simple average of two spectra, and Plot (b) is produced by weighted averaging the same two spectra.

not for "symmetric" noise. A method to obtain $R_{baseline}$ has also been develpoed by Jacobson et al., in our group [158]. Figure 5-14 shows an example comparing the standard average and weighted average. Plot (a) is produced by simply averaging two spectra, and Plot (b) is produced by weighted averaging the same two spectra. The line marked by a star barely seen in Plot (a), can be picked up easily in Plot (b). In addition, if I perform weighted averaging for many averages, the noise reduction rate can be much faster (determined by the setting of the weight parameter).

5.2.5 Laser-millimeter-wave 2D Spectrum

For spectroscopic purposes, I am interested in millimeter-wave transitions from not only a specific initial Rydberg state pumped by the probe laser. Therefore, to systematically obtain all millimeter-wave transitions from a wide range of initial Rydberg states, I must scan the probe laser. Figure 5-15 displays the raw data of a laser-millimeter-wave 2D spectrum. This 2D spectrum is produced by arranging several hundred FID spectra with different probe laser wavelengths together. Each FID spectrum is recorded for 10 seconds with 100 averages. The entire 2D spectrum with ∼200 millimeter-wave transitions is recorded in ∼1 hour.

It is easy to extract a millimeter-wave spectrum with a specific probe laser transition, as shown in Figure 5-16. Figure 5-17 shows two zoomed-in transitions from

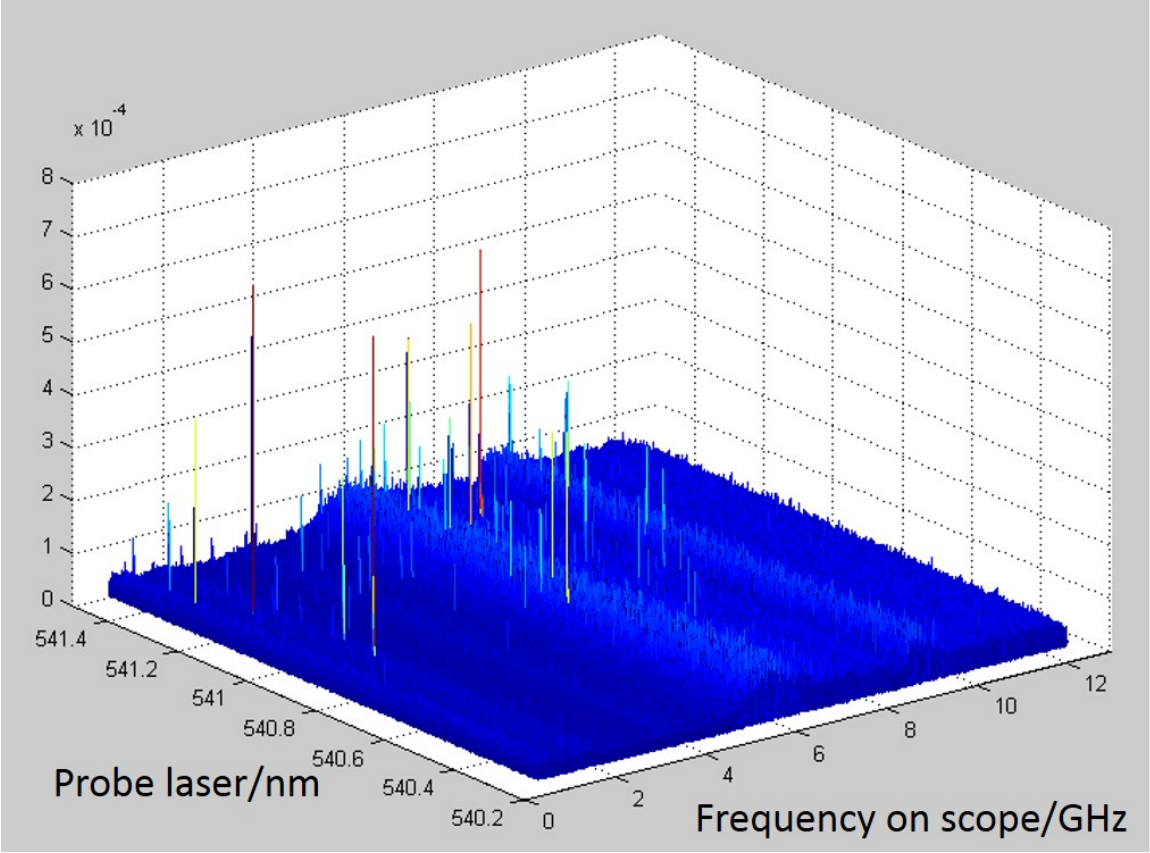

Figure 5-15: Raw data of a laser-millimeter-wave 2D spectrum. The pump laser is used to selectively populate N=2, e/f of the C $^2\Pi_{3/2}$ state. The probe laser covers n^*=33 to 38. The CPmmW spectrum covers 76-98 GHz.

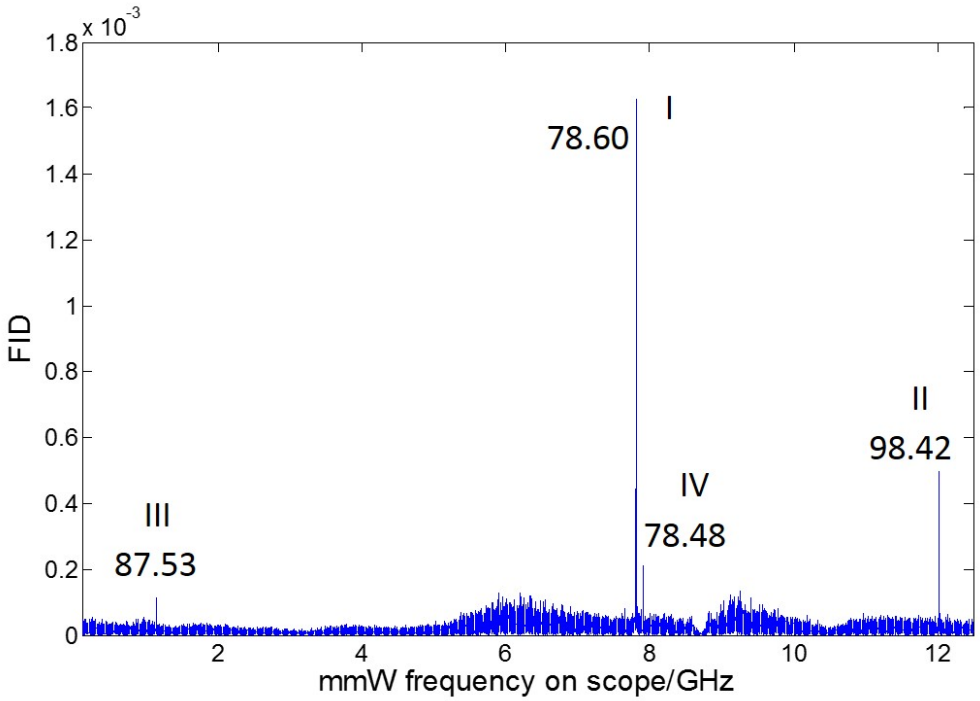

Figure 5-16: An example of a millimeter-wave spectrum with $\nu_{probe} = 18482.85$ cm^{-1}. The recovered millimeter-wave transition frequencies (in GHz) are labeled in the figure.

Figure 5-16. The lineshapes are quite different for the two transitions. The highest achieved resolution is 50 kHz, which is obtained by recording a 20 μs FID in the time-domain. However, recording a large data set decreases the data collection rate. Therefore, for typical survey spectra, I only record 4 μs FID and achieve moderately high resolution (150 kHz).

Figure 5-18 is a laser spectrum of initial Rydberg states obtained by integrating over the millimeter-wave FID radiation. Its spectroscopic resolution is $\sim$0.08 cm^{-1}, which is limited by power broadening discussed in Section 5.3. In Figure 5-18, I observe clear $1/n^3$ Rydberg periodicity and intense transitions, labeled by their approximate principal quantum numbers.

In a typical FID spectrum, there are many more than one millimeter-wave transition. If I integrate the four transitions in Figure 5-16 individually, I can produce four FID action laser spectra, as shown in Figure 5-19. I find that I and IV have similar lineshapes and the same center frequency, both of which are slightly differ-

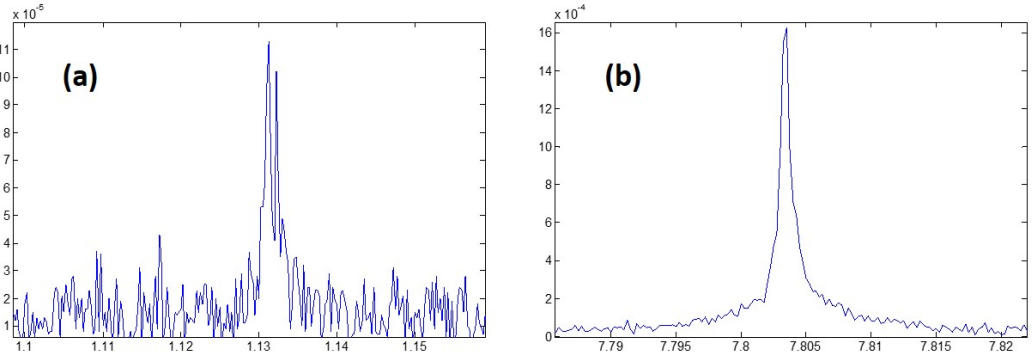

Figure 5-17: Different millimeter-wave transitions have different lineshapes. Plot (a) shows the 87.53 GHz transition in Figure 5-16, and Plot (b) shows 78.6 GHz transition in Figure 5-16.

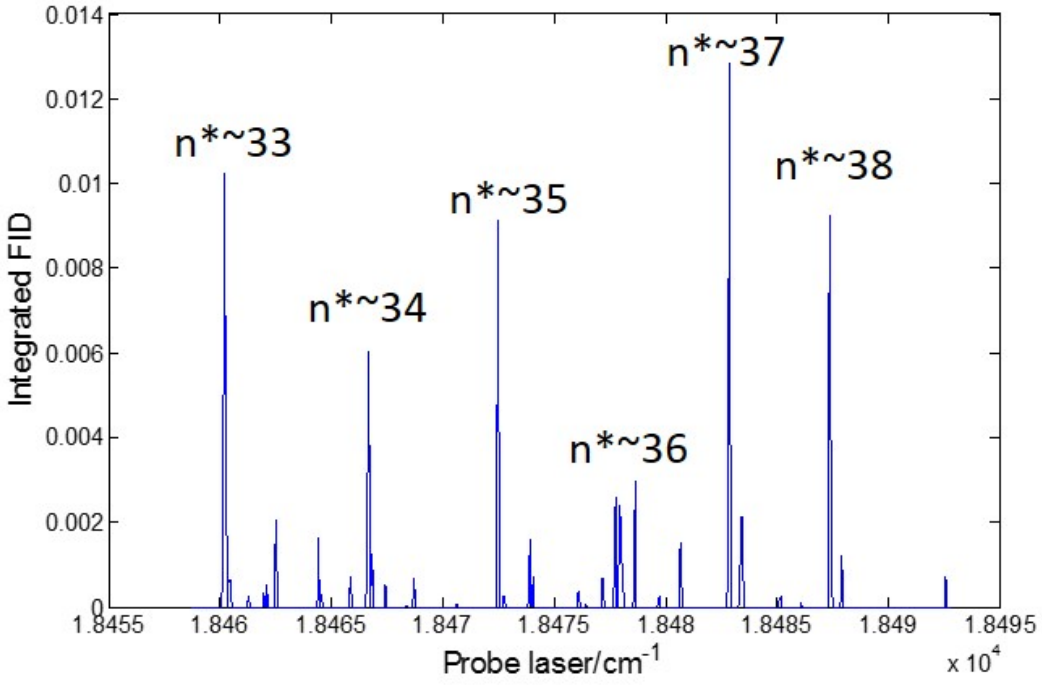

Figure 5-18: Laser spectrum of initial Rydberg states by integrating over all of the millimeter-wave FID transitions.

ent from spectra II and III. Through fitting four transition peaks, I measure their shift to be 0.03 cm^{-1}, which is smaller than the linewidth and cannot be resolved by Ramped-PFI detected laser spectroscopy. From the FID action spectrum, I know that transitions II and III start from different Rydberg states. The difference in the linewidth is discussed in Section 5.3. With FID action spectroscopy, I obtain a 0.01 cm^{-1} precision for the laser transition.

After reducing noise, recovering the millimeter-wave frequency, and precisely measuring the laser transition wavelength, I can create a refined laser-millimeter-wave 2D spectrum, as shown in Figure 5-20. The sizes of the dots represent the intensity of the FID amplitude signal. For visual clarity, the relationship between the dot size and FID amplitude is chosen to be not linear. In addition, the resolution of the millimeter-wave spectrum is much higher than it appears in this 2D plot (vertical scale: $\sim$20 GHz, resolution: $<$150 kHz, $>10^5$ pixels along the vertical axis).

5.2.6 Connecting laser wavelengths to millimeter-wave transitions

There are many observed transitions in Figure 5-20. They are not isolated transitions and can be connected into a global energy level diagram by the laser wavelength and millimeter-wave frequency. Figure 5-21 shows two types of connections. Figure 5-21, Plot (a) shows the first type of connection with one millimeter-wave photon:

$$f_{laser1} + f_{mmW} = f_{laser2} \rightarrow \Delta f_{laser} = f_{mmW}. \tag{5.3}$$

In the 2D spectrum, this means I can find two transitions with the same millimeter-wave frequency y_0, and the difference of the laser wavelength coordinates Δx is equal to y_0. In addition, the direction of the millimeter-wave transition with lower laser frequency should be up, and that with higher laser frequency should be down. Alternatively, the direction of the millimeter-wave transition can be extracted by the phase measurement discussed in Section 3.2.5. Strictly speaking, the parity selection rule is incompatible with such an assignment. However, if any state, such as a Π

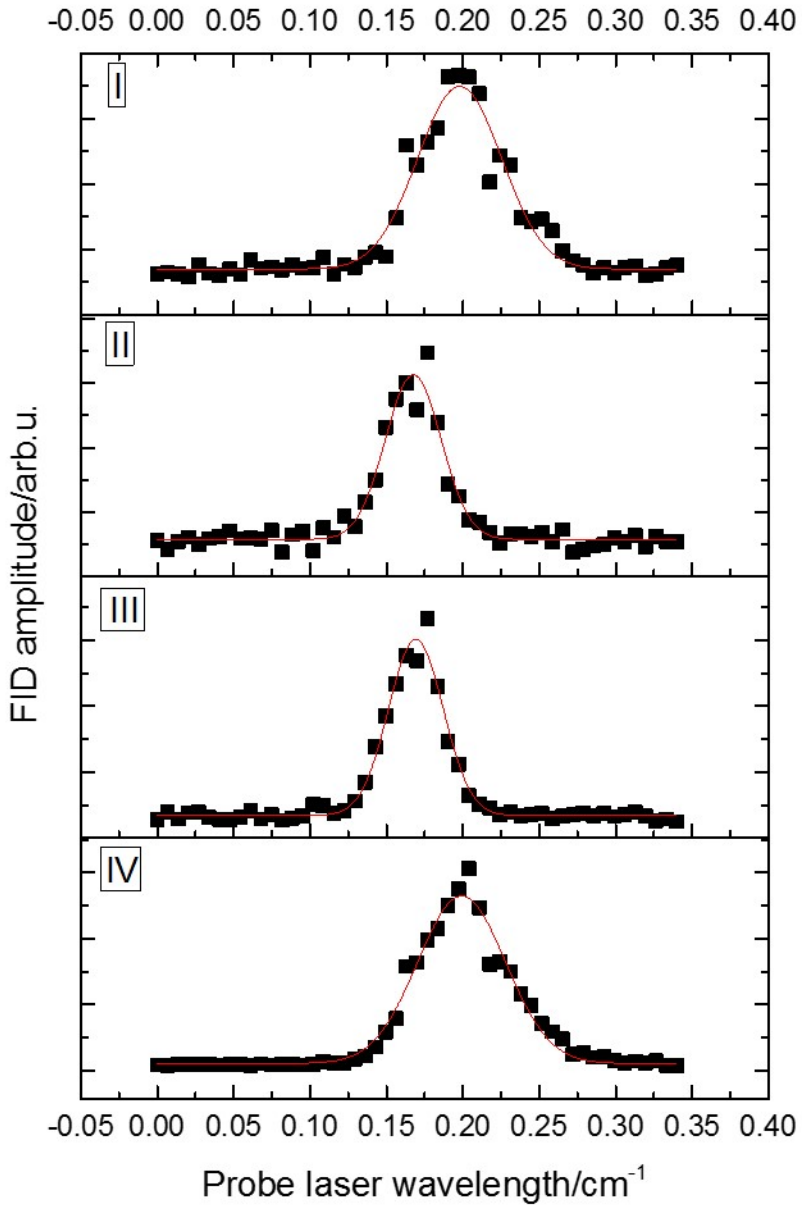

Figure 5-19: FID action spectroscopy. The fully resolved millimeter-wave spectra of these four FID-integrated transitions are shown in Figure 5-16.

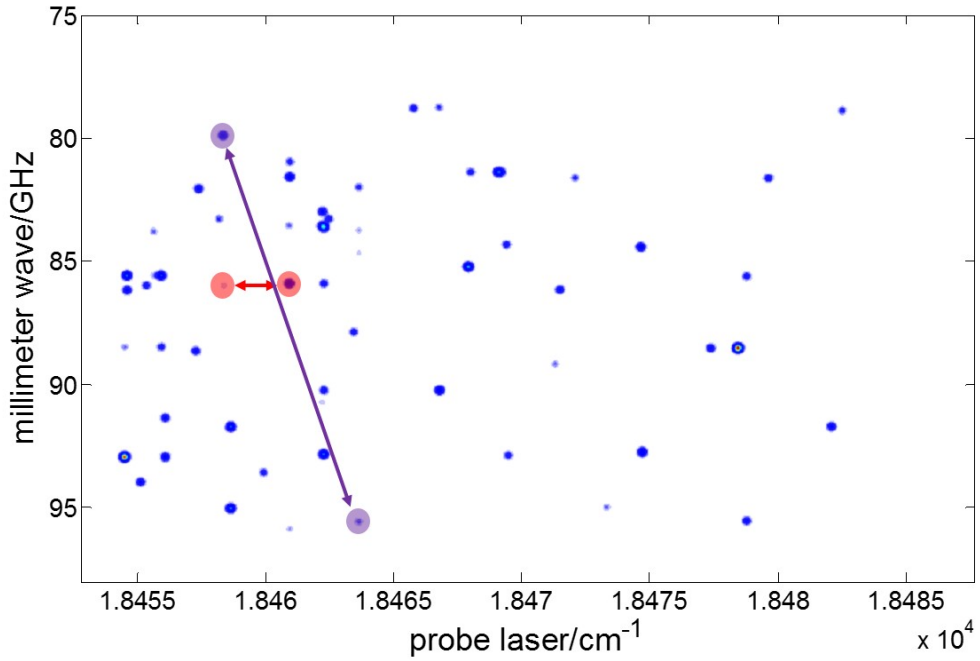

Figure 5-20: Refined laser-millimeter-wave 2D spectrum. The red arrow connects two states with the first type of connection, and the magenta arrow connects two states with the second type of connection. These connections are discussed in Section 5.2.6.

state, has double parity with negligible energy separation (negligible for the probe laser), such approximate transition connections are possible. Figure 5-21, Plot (b) shows the other type of connection via two millimeter-wave photons:

$$f_{laser1} + f_{mmW_1} = f_{laser2} - f_{mmW_2} \rightarrow \Delta f_{laser} = f_{mmW_1} + f_{mmW_2}. \tag{5.4}$$

This connection is not obvious in the 2D spectrum. Similar to the first type of connection, the direction of the millimeter-wave transition with the lower frequency laser transition should be up, and that with higher frequency laser transition should be down. According to Eq.(5.4) and phase measurements, I create Figure 5-22. The dots on the diagonal line satisfy the second type of connection. First and second types of connections can be overlapped. If the intermediate state (state 3 in Figure 5-21, Plot (b)) is a bright state (bright state can be directly populated by the probe laser, dark state cannot), I can split one second type of connection into two first type connections. However, I also find several second type transitions, in which the

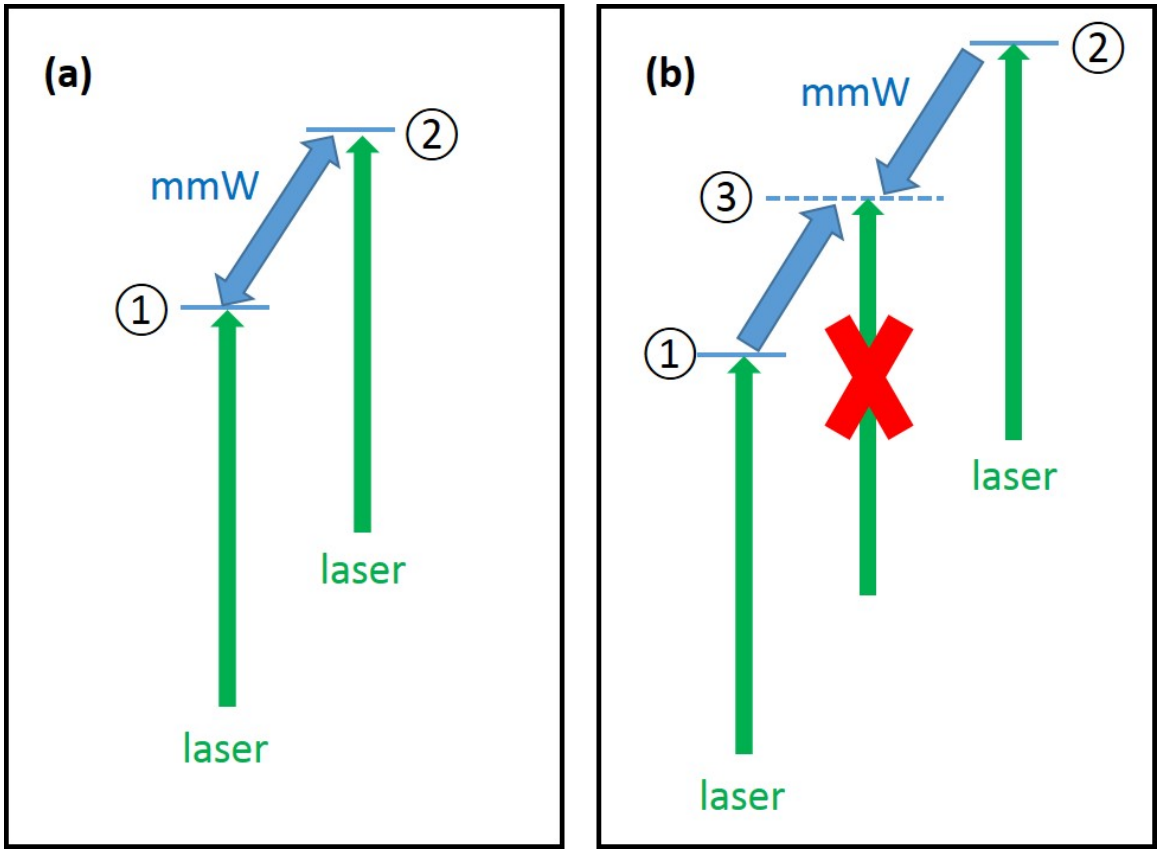

Figure 5-21: Connection of laser wavelengths and millimeter-wave transitions. Plot (a) is a diagram of the first type connection, and Plot (b) is a diagram of the second type connection with a dark intermediate state.

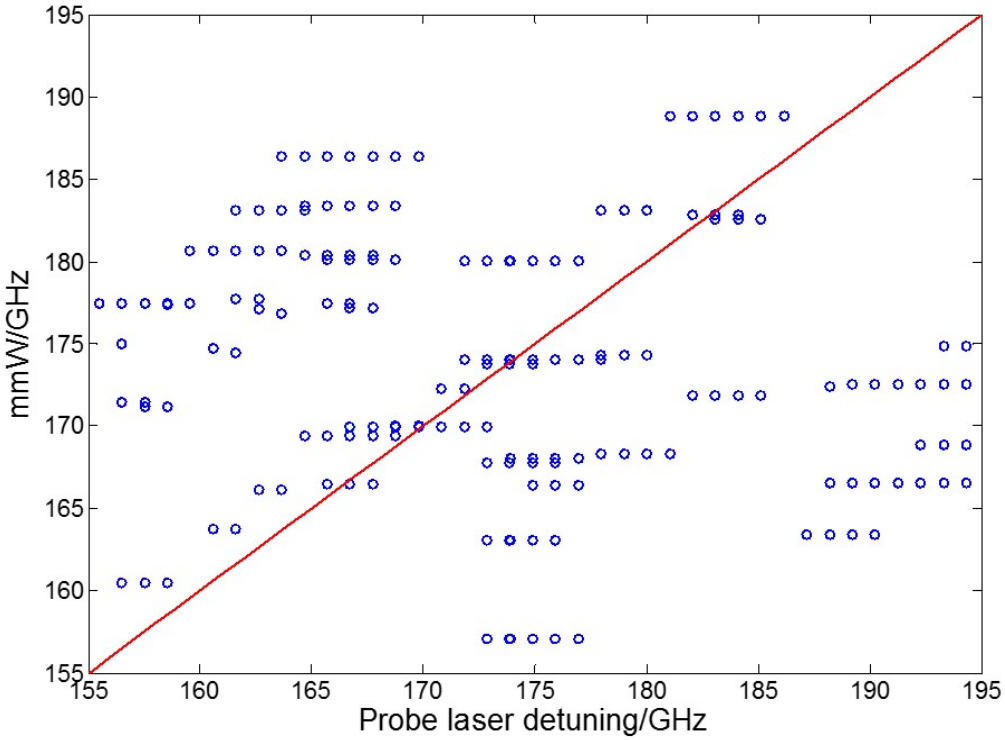

Figure 5-22: The second type connection between the laser wavelengths and millimeter-wave transitions. Due to the relatively large linewidth of the laser transition, two or three neighboring dots with the same millimeter-wave frequency represent the same laser transition.

intermediate state is a dark state. There are two possible explanations: (1) State 3 is an electronic state with single parity, such as Σ^+; (2) State 3 is a core-nonpenetrating state, which cannot be excited by the laser. In Figure 5-20, the red dots show one example of the first type of connection, and the magenta dots show one example of the second type of connection via a dark intermediate state.

5.2.7 Stark demolition

As I mentioned in Section 1.1, molecular core-nonpenetrating (CNP) Rydberg states are a unique and neglected class of matter. I have observed many Rydberg-Rydberg transitions in a 2D spectrum. My work in this section is to isolate the transitions into core-nonpenetrating Rydberg states experimentally. My method, called "Stark

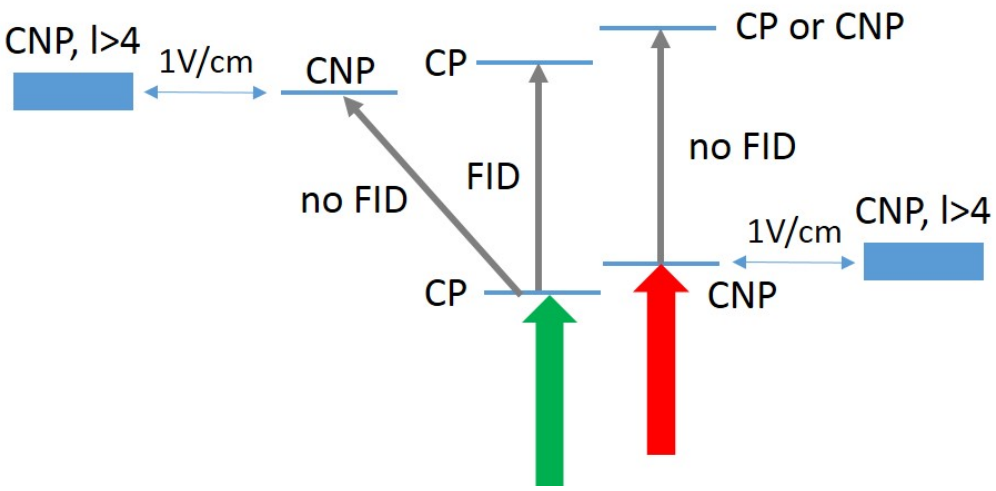

Figure 5-23: Schematic diagram of the "Stark demolition" scheme.

demolition", is based on the super-sensitivity of core-nonpenetrating Rydberg states to an external DC electric field [13]. Figure 5-23 is a schematic diagram of the Stark demolition experiment. A <1 V/cm DC electric field is applied to couple one laser excited "bright" CNP state or a millimeter-wave excited "bright" CNP state, to other "dark" CNP states with high-ℓ (The "bright" states can be populated by probe laser only, or by one probe laser photon and one millimeter-wave photon. The "dark" states can be populated only when a DC field is involved). Due to small quantum defects, all CNP states (with ℓ up to n-1) are nearly degenerate. A small interaction induced by the Stark field can completely mix them. The coherence induced by the chirped millimeter-wave pulse is diluted and dephased into the large number of "dark" CNP states. Therefore, the FID radiation from all CNP-CP or CNP-CNP transitions will be undetectable. However, core-penetrating (CP) states, with their larger quantum defects, are far from the "dark" CNP states and cannot be mixed by a small Stark field. Therefore, the FID radiation from CP-CP transitions can be detected even in the presence of a small Stark field.

The experimental implementation for Stark demolition is simple. Two large mirror-polished stainless steel plates (4" × 6" × 1/16") with 3" separation are inserted into the detection chamber. The plates separated by this large distance (3") do not cause reflections with the millimeter-wave beam, laser beam, or molecular

beam. A pulse generator creates a 0-16 V 10 μs rectangular pulse, which is temporally overlapped with the FT-window of the FID radiation. Figure 5-24 shows the first experimental result of applying Stark demolition to separate CNP states and CP states. With 1 V/cm, the amplitude of FID from a CNP state is reduced by a factor of 5. The non-zero FID signal in CNP Stark demolition comes from the inhomogeneous DC electric field, which is improved in later experiments, discussed here. However, the amplitude of FID from a CP state is only reduced by a factor of 1.5, but its frequency is shifted 10 MHz. The frequency shift is expected, because a Stark effect perturbation by one opposite parity neighboring state could cause a frequency shift. According to second-order perturbation theory, the frequency shift is

$$\Delta f = \frac{(\mu\mathcal{E})^2}{\Delta E} \tag{5.5}$$

where μ is the electric dipole transition moment of the target state and perturbed state ($\sim$2 kD), $\mathcal{E}$ is the amplitude of the Stark field (1 V/cm), ΔE is the energy difference of the target state and perturbing state ($\sim$20 GHz). The expected frequency shift is 40 MHz, which is consistent with the measurement within an order of magnitude. However, I observe a frequency shift but no splitting, which is unexpected. I expect to observe Stark splittings for typical CP states with a significant ℓ-mixing in a polar molecule. Further analysis has not been done.

I have demonstrated that a 1 V/cm Stark field can distinguish CP states and CNP states. However, such separation of CNP and CP states is relative and dependent on the amplitude of the Stark field. A smaller Stark field could have higher separating resolution. For example, in Figure 5-25, both transitions in Plot (a) and Plot (b) are CNP states, as revealed by a 1 V/cm Stark demolition test. However, I can increase the Stark field in small steps and observe the corresponding variation of the lineshape. In Plot (a), several sharp transitions with several MHz frequency shift show up from 0.25 V/cm to 0.75 V/cm. The frequency shifts are nearly linear. However, in Plot (b), there is no sharp peak when the Stark field is larger than 0.25 V/cm. Therefore, the transition in Plot (b) appears to involve core-nonpenetrating with higher-ℓ than

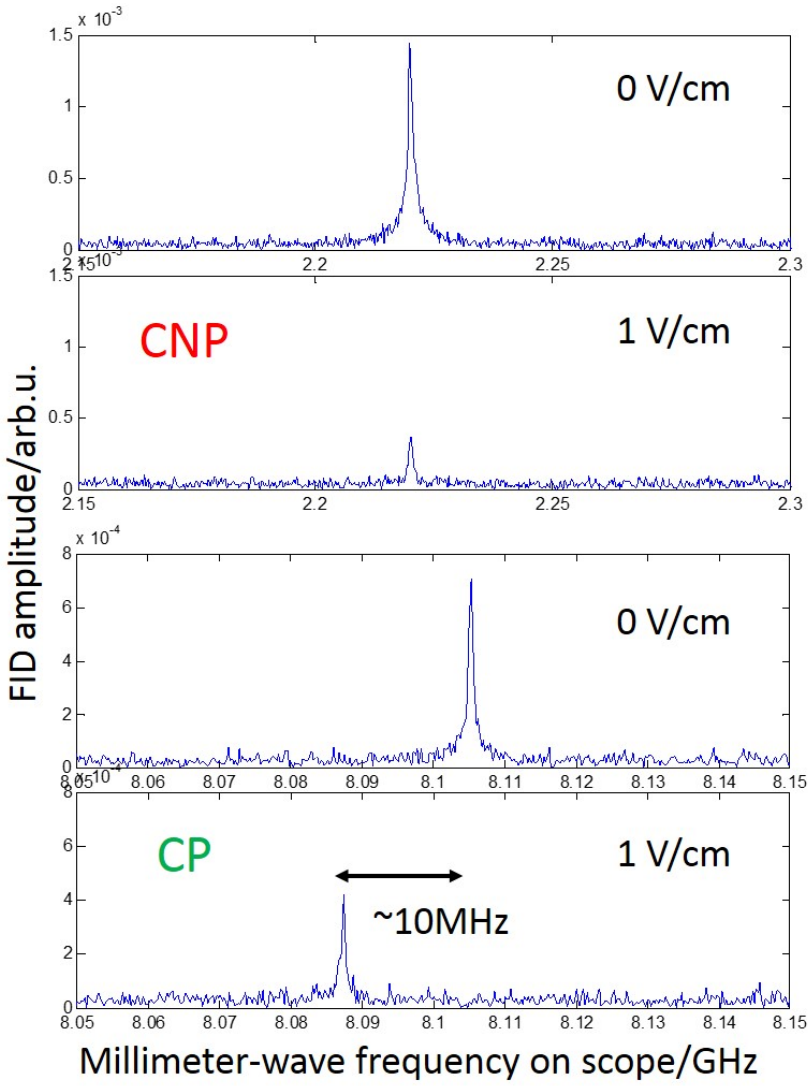

Figure 5-24: Applying Stark demolition to separate CP and CNP states.

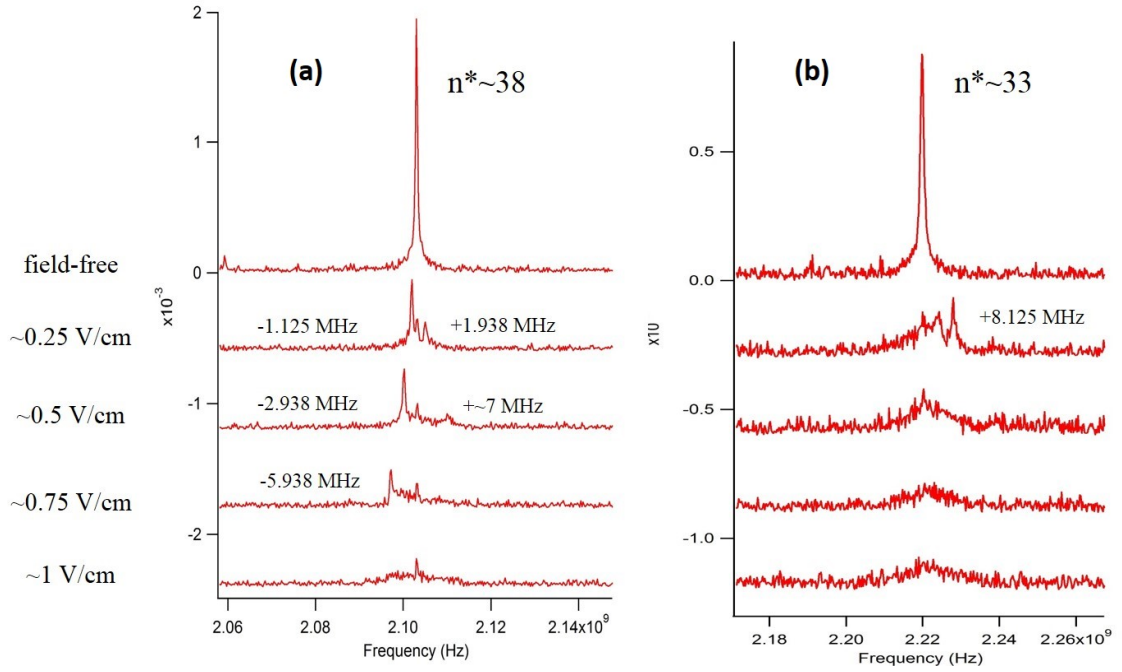

Figure 5-25: A high resolution Stark demolition experiment to separate moderately core-nonpenetrating Rydberg states and highly core-nonpenetrating Rydberg states. Plot (a) shows a transition at $n^*\sim38$. Plot (b) shows a transition at $n^*\sim33$. The transition in Plot (a) has smaller sensitivity of the DC field than the transition in Plot (b).

that in Plot (a). With a series of Stark demolition measurements with small Stark field steps, it is possible to sort all CNP transitions by their quantum defects.

5.2.8 millimeter-wave multiple resonance

In Section 3.2.7, I showed that a millimeter-wave pulse can not only induce FID radiation, but also is sufficiently strong to induce population transfer in an atomic Rydberg system. More than one millimeter-wave photon populates high-ℓ Rydberg states by multiple step resonance excitation. Different from the experiment in Section 3.2.7, I apply a 22 GHz broadband chirp instead of a pulse sequence with several individual single-frequency pulses. Figure 5-26 shows two spectra with different chirp directions. The explanation of an extra transition II in Plot (a) is straightforward: In Plot (a), the increasing frequency chirped pulse sequentially excites transitions I and II. Therefore, the population can be sequentially transferred from state 1 via state 2 to state

3. At the same time, polarizations of both transitions are induced. However, in Plot (b), the decreasing chirped pulse excites transition II earlier than I. The population in state 1 cannot be transferred to state 3 before state 2 is populated. Therefore, the population is only transferred to state 2 and only polarization of transition 1 is induced.

To observe millimeter-wave multiple resonance spectra with more than two photons, I apply more than one chirped pulse, as shown in Figure 5-27 and observe four transitions. To connect these four transitions together: (1) I use a sequence of single frequency pulses (the same as the conventional double resonance method) to judge whether two transitions are sequential or parallel; (2) Extract phase information from the spectra polarized by the pulse sequence of single frequency pulses to obtain the transition directions. Based on such information, I find that five states are involved in this spectrum, and are organized as shown in the inset plot in Figure 5-27.

By the two examples above, I have demonstrated a millimeter-wave multiple resonance technique, which is an efficient method to rapidly detect a complex network of energy levels. However, the data analysis method I am using is preliminary and not elegant. Within a single multiple resonance spectrum, I cannot judge whether the transitions are sequential or parallel. Therefore, the laser-millimeter-wave 2D spectrum, as shown in Figure 5-20, might include many transitions of $\nu_{laser} + \nu_{mmW} + \nu_{mmW}$, which would increase the spectral complexity for analysis. Such information is likely encoded in the phase information and could be extracted directly with an appropriate algorithm.

5.3 Problems and possible solutions

As discussed above, I have demonstrated the successful observation of molecular Rydberg-Rydberg transitions by CPmmW excitation and FID detection in the buffer gas cooled molecular beam. The data collection speed is unprecedented. Many experimental techniques have been developed, such as phase extraction, Stark demolition, multiple resonance, etc. More techniques are under development, such as polariza-

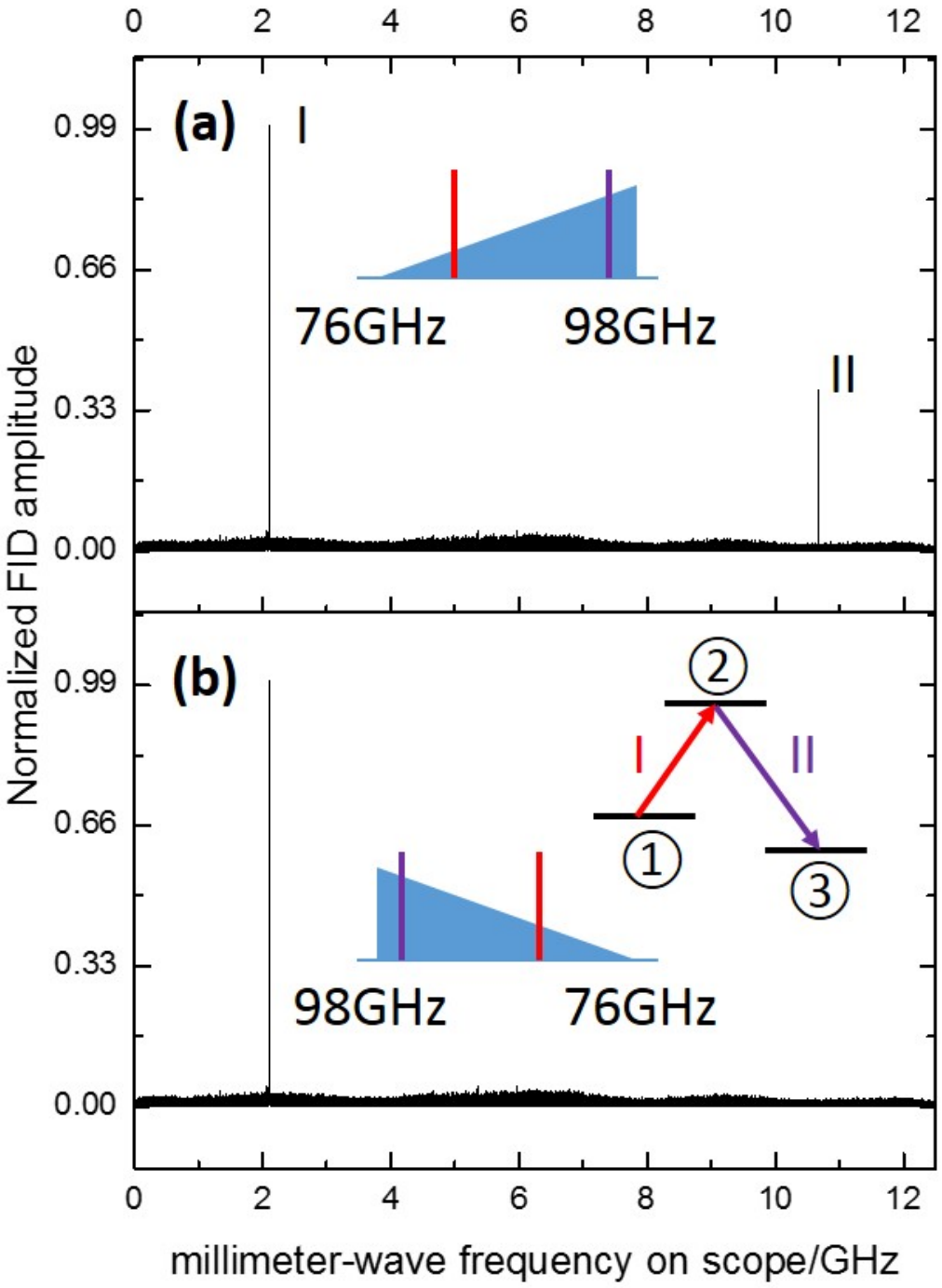

Figure 5-26: millimeter-wave double resonance spectra with a single chirped pulse. Plot (a) shows a spectrum with 76-98 GHz increasing chirped pulse excitation. Two transitions (I and II) are observed. Plot (b) shows a spectrum with 98-76 GHz decreasing chirped pulse excitation. Only one transition (I) is observed. Inset plots show the relationship between the chirped pulses and the energy diagram of the three-level system.

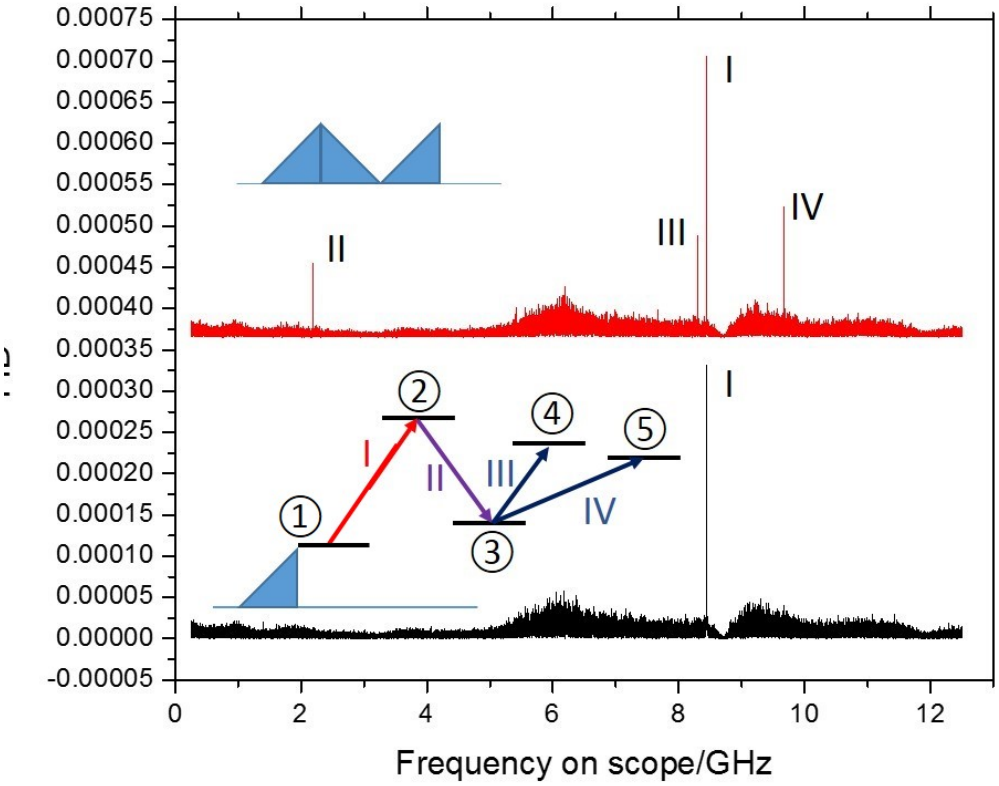

Figure 5-27: millimeter-wave multiple resonance spectra with multiple chirped pulses. The top plot shows a spectrum excited by a pulse sequence with three chirped pulses. The bottom plot shows a spectrum excited by a single chirped pulse. Inset plot shows the connections of the five states involved in this spectrum.

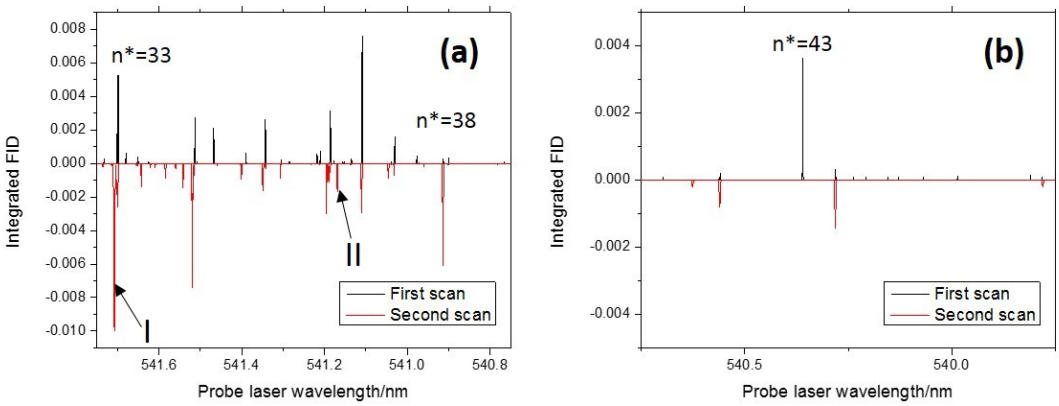

Figure 5-28: Comparing the integrated FID signals in two spectra. Plot (a) shows the integrated FID signals vs. probe laser wavelength from n*=33 to n*=38. Plot (b) shows a much larger spectrum to spectrum vairations in a scheme from n*=39 to n*=50.

tion diagnostic. However, a major obstacle prevents me from applying such wonderful techniques to systematically collect data for detailed analysis. This is the stability of the system. Some FID signals seem to be "randomly" lost. For example, Figure 5-28 shows two sets of data taken in the same day with the same experimental conditions. Plot (a) shows the integrated FID signals vs. probe laser wavelength from n*=33 to n*=38. Most of the integrated FID signals from the two data sets are overlapped. However, the intensity fluctuations of some transitions are very large, and a few integrated FID signals only show up in one data set. This problem seems to be even worse in the region from n*=39 to n*=50 shown in Plot (b). The difference between two spectra is quite large, and the number of signals in the two spectra is much smaller than I expect.

Through several diagnostic experiments, I find that the instability comes from the probe laser. The Sirah Precision Scan pulsed dye laser used as the probe laser, has $\sim$0.03 cm^{-1} short-term linewidth, which is in agreement with its specs. However, its output frequency has a long-term ($\sim$20 s) fluctuation ($\sim$0.06 cm^{-1}). If the linewidth of the Rydberg$\leftarrow$C transition is smaller than the frequency fluctuation, large intensity fluctuations are expected. To measure the linewidth, I scan the probe laser in a small step-size (0.01 cm^{-1}), and plot the integrated FID amplitude, as shown in

Figure 5-29. In Figure 5-29, Plot (a), the black curve shows a broad laser transition (0.08 cm^{-1}, transition I in Figure 5-28). This transition in the two spectra in have similar intensities, as shown in Figure 5-28, and is called "good transition". The FID amplitude does not display large long-term fluctuations, as shown in Figure 5-30, Plot (b). In Figure 5-29, Plot (a), the red curve shows a narrow laser transition (0.04 cm^{-1}, II in Figure 5-28). This transition only shows up in the bottom spectrum, but missed in the top spectrum in Figure 5-28, and is called a "bad transition"). The FID amplitude displays large long-term fluctuations, as shown in Figure 5-30, Plot (a). However, the transition linewidth is not limited by the laser linewidth (1 GHz), natural linewidth (<10 MHz), or Doppler linewidth (<300 MHz). I find that the linewidth is dependent on the laser power, as shown in Figure 5-29, Plot (b). Therefore, the linewidth is determined by the laser power broadening. For the same laser intensity, the transitions with larger electric dipole transition moments have a broader linewidth. If the power broadened linewidth is smaller than the laser long-term frequency fluctuation (0.06 cm^{-1}), the excitation of that transition is not stable. If the power broadened linewidth is smaller than the laser short-term linewidth (0.03 cm^{-1}), the excitation of that transition might be completely missed. This argument can explain the phenomenon of missing most of the transitions in the $n^*\sim43$ region. The expected power broadening linewidth of $n^*\sim43$ can be converted from the linewidth measurement of $n^*\sim33$, as:

$$\Delta\nu_{43} \approx \left(\frac{\mu_{43}}{\mu_{33}}\right)^2 \Delta\nu_{33} \approx \left(\frac{33}{43}\right)^4 \Delta\nu_{33} \tag{5.6}$$

where μ_{43} and μ_{33} are the electric dipole transition moments of $n^*=43$ and $n^*=33$ Rydberg←C state transitions, $\Delta\nu_{33}$ is the power broadening linewidth of $n\sim33$ (0.04 cm^{-1} to 0.08 cm^{-1}). Therefore, the "good transitions" at $n^*=43$ have a 0.03 cm^{-1} linewidth, and the "bad transitions" at $n^*=43$ have a 0.01 cm^{-1} linewidth. Based on the discussions above, the observation of large fluctuations or completely missed lines is understandable.

Therefore, I have two options, stabilizing the laser or broadening the transition

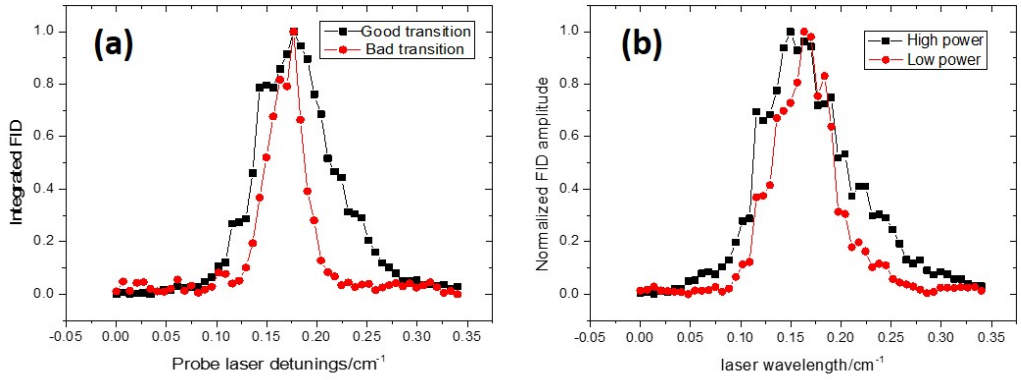

Figure 5-29: Measuring the linewidth of the probe laser transition. Plot (a) shows a comparison of the linewidth between a "good transition" and a "bad transition" at the same laser power. Plot (b) shows a comparison of the linewidth of the same transition at high laser power and low laser power.

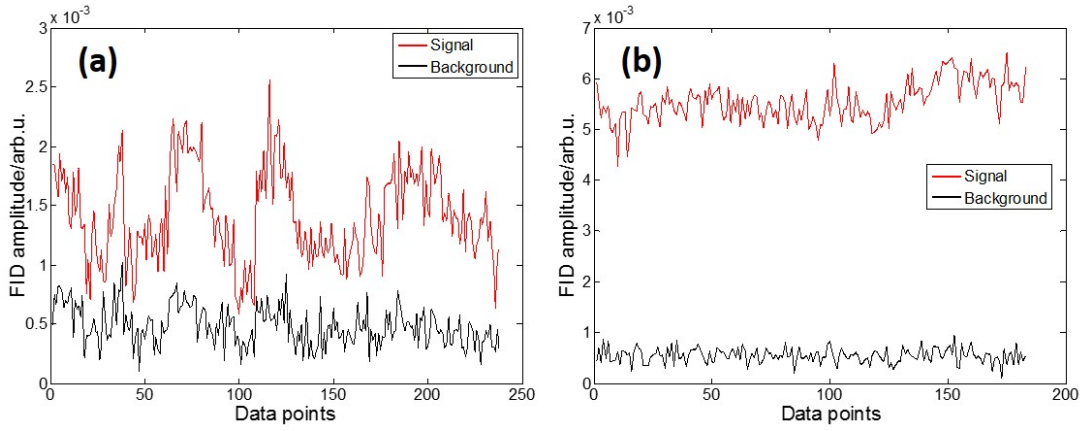

Figure 5-30: Measuring the long-term fluctuations. Plot (a) shows large fluctuations in a "bad transition". Plot (b) shows small fluctuations in a "good transition". The averaging time for each data point is 2 s.

linewidth. To stabilize the laser, I would minimize the long-term drift of the Sirah laser to $\sim$0.03 cm^{-1}, which is the design specification. This might fix the problem at n^*=33, but could not work for n^*=43. Or I could build a pulsed amplified cw laser, which has a $\sim$ 100 MHz linewidth. A narrow band laser would improve the stability and excitation efficiency significantly. To broaden the transition linewidth, I also have several possibilities: (1) I could increase the laser power. However, I might face another problem, multi-photon ionization, at extremely high laser power. (2) I could use another intermediate state instead of the C state. Several experiments have shown evidence that the electric dipole transition moments between the C state and Rydberg states are much smaller than them from another state, such as the D state. (3) I could apply a small electric field to Stark broaden the transition. I hope at least one of these possible solutions will fix the instability problem, especially near n^*=43, in which n^* region 76-98 GHz millimeter-waves induce Δn^*=1 transitions.

Chapter 6

Molecular core-nonpenetrating Rydberg states

Molecular core-nonpenetrating Rydberg states are a unique and neglected class of matter [1, 26, 27, 28, 29], with exceptionally large electric dipole transition moments, polarizabilities, and long lifetimes [13, 30, 19]. In Chapter 5, I demonstrated the preparation of 10^8 BaF core-nonpenetrating Rydberg states by laser excitation and a millimeter-wave pulse sequence. To extend my method to other diatomic molecules or even polyatomic molecules, I have two difficulties: (1) Complicated spectrum of intermediate core-penetrating Rydberg states; (2) Short lifetime of intermediate core-penetrating Rydberg states [25, 100, 101, 102, 103, 104, 105, 106, 107, 108]. In this chapter, I discuss the general properties of molecular core-nonpenetrating Rydberg states first. Then I propose two different experimental strategies, optical-mmW STImulated Raman Adiabatic Passage (STIRAP) and Adiabatically-focused STark-mixed Rydberg Orbitals (ASTRO), for preparing generic molecular core-nonpenetrating Rydberg states. These two methods are demonstrated and analyzed by calculations.

6.1 Molecular core-nonpenetrating Rydberg states

Core-nonpenetrating Rydberg states are defined as having negligible overlap between the wavefunction of the Rydberg electron and that of the ion-core, due to the centrifugal barrier [19]. The effective potential for an electron is:

$$V_l(r) = -\frac{Z^{eff}(r)}{r} + \frac{l(l+1)}{2m_e r^2} \tag{6.1}$$

where $Z^{eff}(r)$ is the r-dependent effective positive charge seen by the Rydberg electron, n and ℓ are the principal quantum number and angular momentum quantum number of the Rydberg electron. At a turning point, $V_l(r_{nl\pm}) = E_{nl} = -R/n^2$, where R is the Rydberg constant (in cm^{-1}). I set $Z^{eff}(r) = 1$, thus

$$r_{nl\pm} = n^2 \left[1 \pm \left(1 - \frac{l(l+1)}{n^2}\right)\right] a.u. \tag{6.2}$$

From equation 6.2, I know that when $n >> l$, the inner turning point position is almost independent of the principal quantum number n, but strongly dependent on the angular momentum quantum number ℓ. The inner turning points of the $3d$, $4f$, and $5g$ orbits can be calculated as 3.17, 6.35, and 10.59 $\AA$, respectively, compared to a typical ion-core diameter of 5 $\AA$. For most diatomic and small polyatomic molecules, states with Rydberg electron angular momentum $\ell \geq 3$, are core-nonpenetrating and can be described by the hydrogenic Rydberg formula, $E_n = 1/2n^2[a.u.]$. The core-nonpenetrating electron is prevented by the centrifugal barrier from penetrating inside the extended electron distribution of the ion-core. All of the *efficient* mechanisms for exchange of energy between the Rydberg electron and the ion-core are turned off [19]. The Rydberg electron is essentially uncoupled from its ion-core, leading to an atom-like electronic structure with "almost good" ℓ quantum numbers and near-degenerate λ components [33, 32, 2, 159, 19].

The Rydberg electron of a molecular core-nonpenetrating state does not interact strongly with the non-spherically symmetric part of the ion-core. Therefore, it is extremely sensitive to an external electric field, which can induce kiloDebye

Table 6.1: Magnitudes of long-range matrix elements of electric dipole, quadrupole, and dipole polarizabilities. Shifts for $n = 40$ and $\lambda = 0$, in MHz, assuming $\mu = -3.36ea_0$, $Q = -0.87ea_0^2$, $\alpha = 12a_0^3$, $\gamma = 9a_0^3$.

Term	$\ell = 3$	$\ell = 4$	$\ell = 5$	$\ell = 6$
Dipole, μ	7369	3350	1804	1082
Quadrupole, Q	-568	-258	-139	-83
Isotropic polarizability, α	-1953	-532	-191	-81
Anisotropic polarizability, γ	-260	-69	-24	-10

dipole moments, GHz cm^2/V^2 polarizabilities, and nearly complete Stark ℓ-mixing at relatively low electric fields ($\approx$1 V/cm) [13]. In addition, due to the long-period Kepler orbit motion of the Rydberg electron and its weak interaction with the non-spherical ion-core, the rate of nonradiative decay of molecular core-nonpenetrating Rydberg states is very slow, scaled by the orbital overlap with the ion-core: as n^{-3} and exponentially decreasing as ℓ increases. Due to the small transition dipole moment for $|\Delta n| > 1$ and small transition frequency for $|\Delta n| \approx 1$, radiative decay of core-nonpenetrating Rydberg state is also slow at high n [13, 25, 19]. Therefore, although molecular core-nonpenetrating Rydberg states have extremely large transition dipole moments and polarizabilities, they are metastable. Their lifetimes can be longer than 10 ms. Molecules in such long-lived, highly polarizable states are useful to researchers working on molecular slowing, cooling, and trapping [14, 15, 16, 17, 18]. For spectroscopists, molecular core-nonpenetrating Rydberg states are also distinctive, because of easily recognizable and predictable patterns that arise from the highly restrictive "pure electronic" transition selection and propensity rules ($\Delta\ell = \pm 1, \Delta N^+ = 0, \Delta v^+ = 0, \Delta N = 0, \pm 1, + \leftrightarrow -$) [19, 30]. However, a simple spectrum does not imply the absence of information. With high-resolution spectroscopic techniques and an analytic perturbative long-range model, measured frequency shifts and intensity deviations from the hydrogenic Rydberg formula yield a complete picture of the electronic structure of the molecular ion-core [31, 1]. Table 6.1 lists the expected frequency shifts caused by the permanent multipole moments and induced dipole polarization of the ion-core from f ($\ell = 3$) to i ($\ell = 6$) states. These frequency shifts are calculated based on the extended long-range model of CaF.

Despite these attractive features, molecular core-nonpenetrating Rydberg states have not been systematically studied nor widely utilized in scientific research. The main obstacle to their use is the lack of an efficient, universal technique for accessing them. For most molecules, preparation of core-nonpenetrating Rydberg states requires jumping over a "zone of death", which are a group of easily accessible molecular core-penetrating Rydberg states with relatively short lifetime (<1 ns) between the low lying valence states and the long-lived molecular core-nonpenetrating Rydberg states. The states in the "zone of death" decay rapidly, by predissociation, autoionization (core-penetrating states have strongly R-dependent quantum defect matrix elements and thus undergo rapid vibrational autoionization), and by Inter-System Crossing and Internal Conversion (for polyatomic molecules) [25, 100, 101, 102, 103, 104, 105, 106, 107, 108]. During a sequential ℓ-climbing excitation scheme with 10 ns optical pulses, almost all of the generated Rydberg molecules are lost to nonradiative decay instead of being excited to molecular core-nonpenetrating Rydberg states. I plan to use either or both of two adiabatic schemes, optical-mmW STImulated Raman Adiabatic Passage (STIRAP) and Adiabatically-focused STark-mixed Rydberg Orbitals (ASTRO) in order to overcome this difficulty. The key physical insight behind both techniques is that by mixing low-ℓ bright state character into high-ℓ states with a DC or AC electric field, I can transfer population while avoiding the brutal decay rates typical of the "zone of death." Experimental implementations of these two methods are under way. The next two sections discuss only the results from the theoretical calculations.

6.2 optical-mmW STImulated Raman Adiabatic Passage (STIRAP)

Stimulated Emission Pumping (SEP)/multiple resonance techniques were invented and widely applied in our research group over the last thirty-five years [160]. In Chapter 3, I showed that, with a pulse sequence of two laser-photons and three mmW-

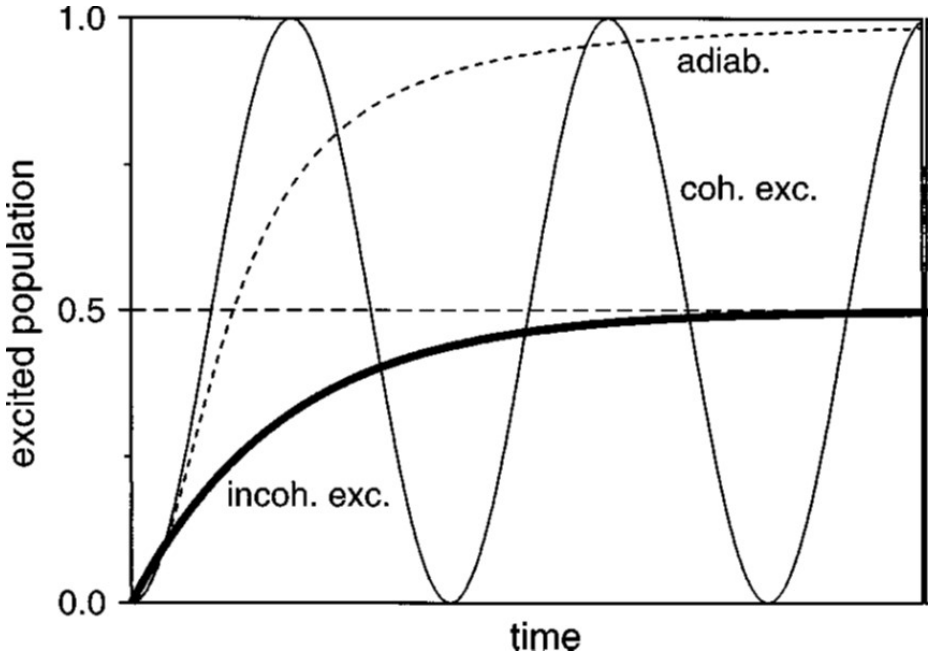

Figure 6-1: Population transfer in a two-level system, driven by a coherent radiation field (thin line), by an incoherent radiation field (heavy line), and by an adiabatic passage process (dashed line).

photons, the h (ℓ=5) Calcium atomic Rydberg state is populated. The efficiency of the multiple resonance technique requires that the lifetimes of intermediate states are longer than the excitation pulse length. However, for most $\ell < 4$ molecular Rydberg states, the lifetimes ($\sim$1 ns) are shorter than both the pulse duration of the tunable Nd:YAG pumped dye laser (7 ns) and the shortest millimeter-wave pulse (10 ns) that I can generate with our CPmmW spectrometer. Fortunately, the STIRAP technique can overcome this difficulty and carry nearly 100% of the population across the "zone of death".

6.2.1 Introduction to STIRAP

STIRAP is a two-photon technique that exploits a coherence between the ground state $|1\rangle$, a short-lived intermediate state $|2\rangle$, and the metastable final state $|3\rangle$ to transfer population directly from the ground state to the final state [161, 162, 163, 164, 165]. The general level diagram of states involved in STIRAP is shown in Figure 6-2, Plot(a). Different from the conventional step-wise multiple-resonance technique,

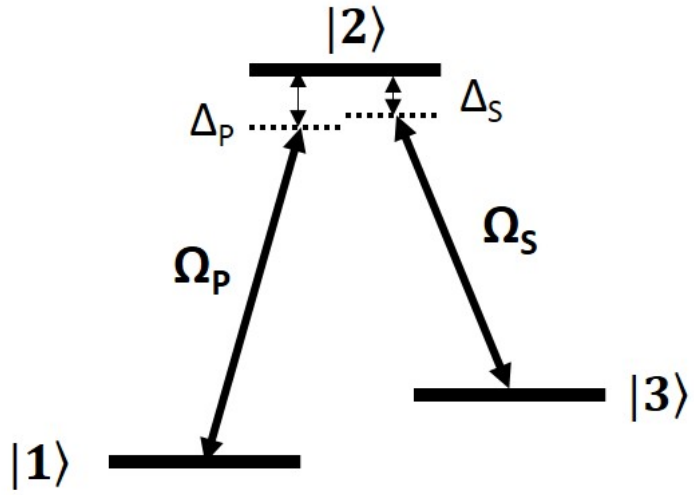

Figure 6-2: Level diagram of STIRAP. The pulse coupling states $|1\rangle$ and $|2\rangle$ is called the Pump pulse, and the pulse coupling states $|2\rangle$ and $|3\rangle$ is called the Stokes pulse. Δ_P and Δ_S are single photon detunings of the Pump pulse and the Stokes pulse.

STIRAP is accomplished with the "counter-intuitive" pulse sequence, where the pulse coupling the intermediate and final states (Stokes pulse) is applied before the pulse coupling the ground and intermediate states (Pump pulse), as shown in Figure 6-3. The Pump pulse and Stokes pulse have significant temporal overlap. Three levels ($|1\rangle$, $|2\rangle$ and $|3\rangle$) are dressed by two (Pump and Stokes) oscillating electromagnetic fields. The two fields couple neighboring states and drive an adiabatic evolution of the system. The time-dependent Hamiltonian in the dressed-atom picture is:

$$H(t) = \frac{\hbar}{2}\begin{bmatrix} 0 & \Omega_P(t) & 0 \\ \Omega_P(t) & 2\Delta_P & \Omega_S(t) \\ 0 & \Omega_S(t) & 2(\Delta_P - \Delta_S) \end{bmatrix}, \tag{6.3}$$

where Ω_P and Ω_S are Rabi frequencies of the Pump and Stokes transitions, Δ_P and Δ_S are the single photon detunings of the Pump and Stokes pulses. Ω_P and Ω_S are time-dependent. $2\Delta_P$ and $2\Delta_S$ are constant for single frequency pulses, and are time-dependent for chirped pulses. The resonant condition for STIRAP is $\Delta_P = \Delta_S = \Delta$. The instantaneous eigenstates can be obtained by diagonalizing the Hamiltonian matrix in Eq.(6.3).

$$\left|a^+\right\rangle = \sin\Theta\sin\Phi\,|1\rangle + \cos\Phi\,|2\rangle + \cos\Theta\sin\Phi\,|3\rangle \tag{6.4a}$$

$$\left|a^0\right\rangle = \cos\Theta\,|1\rangle - \sin\Theta\,|3\rangle \tag{6.4b}$$

$$\left|a^-\right\rangle = \sin\Theta\cos\Phi\,|1\rangle - \sin\Phi\,|2\rangle + \cos\Theta\cos\Phi\,|3\rangle\,, \tag{6.4c}$$

where the mixing angles are:

$$\tan\Theta = \frac{\Omega_P(t)}{\Omega_S(t)} \tag{6.5a}$$

$$\tan 2\Phi = \frac{\sqrt{\Omega_P^2(t) + \Omega_S^2(t)}}{\Delta}. \tag{6.5b}$$

The instantaneous eigen-frequencies of the three instantaneous eigen-states are:

$$\omega^{+} = \Delta_P + \sqrt{\Delta_P^2 + \Omega_P^2 + \Omega_S^2} \tag{6.6a}$$

$$\omega^{0} = 0 \tag{6.6b}$$

$$\omega^{-} = \Delta_P - \sqrt{\Delta_P^2 + \Omega_P^2 + \Omega_S^2}. \tag{6.6c}$$

On resonance, the three instantaneous eigen-states are degenerate at initial and final time, but have large splittings during the STIRAP process, as shown in Figure 6-3, Plot(b). The eigenstate of the semi-stationary state $|a^0\rangle$ with zero eigen-frequency is composed of field-free states $|1\rangle$ and $|3\rangle$, without any admixed character of state $|2\rangle$. STIRAP exploits based on this adiabatic $|a^0\rangle$ state to trap the population in "bright" state $|1\rangle$ and $|3\rangle$, but not in "dark" state $|2\rangle$. For the counter-intuitive pulse ordering, the mixing angle Θ at t=0 is 0 and at t=∞ is $\pi/2$. Therefore, the initial population in state $|1\rangle$ is completely transferred into state $|3\rangle$, as shown in Figure 6-3, Plot(c). Due to the absence of state $|2\rangle$ character in this adiabatic state, even if the state $|2\rangle$ decay rate is fast, there is no possibility of decay.

The discussion above is based on the instantaneous Hamiltonian. However, because the Hamiltonian is explicitly time-dependent, nonadiabatic interactions can couple the adiabatic states causing some mixing of the short-lived "dark" state $|2\rangle$ into the "bright" states. To avoid such a loss process in STIRAP, I must reduce the diabatic interaction to a negligibly small value. The adiabatic condition can be derived from general considerations in time-dependent quantum mechanics. The Hamiltonian matrix element for the nonadiabatic coupling between our state of interest $|a^0\rangle$ and the perturbed state $|a^{\pm}\rangle$ is $\langle a^{+}|\dot{a}^0\rangle$. If the coupling matrix element is much smaller than the field-induced splitting, $|\omega^{\pm} - \omega^0|$, such non-adiabatic interaction can be ignored, as shown in Eq.(6.7a). I substitute Eqs.(6.4) and (6.5) into Eq.(6.7a) and obtain the more practical adiabatic condition, as in Eq.(6.7). If I know the transition

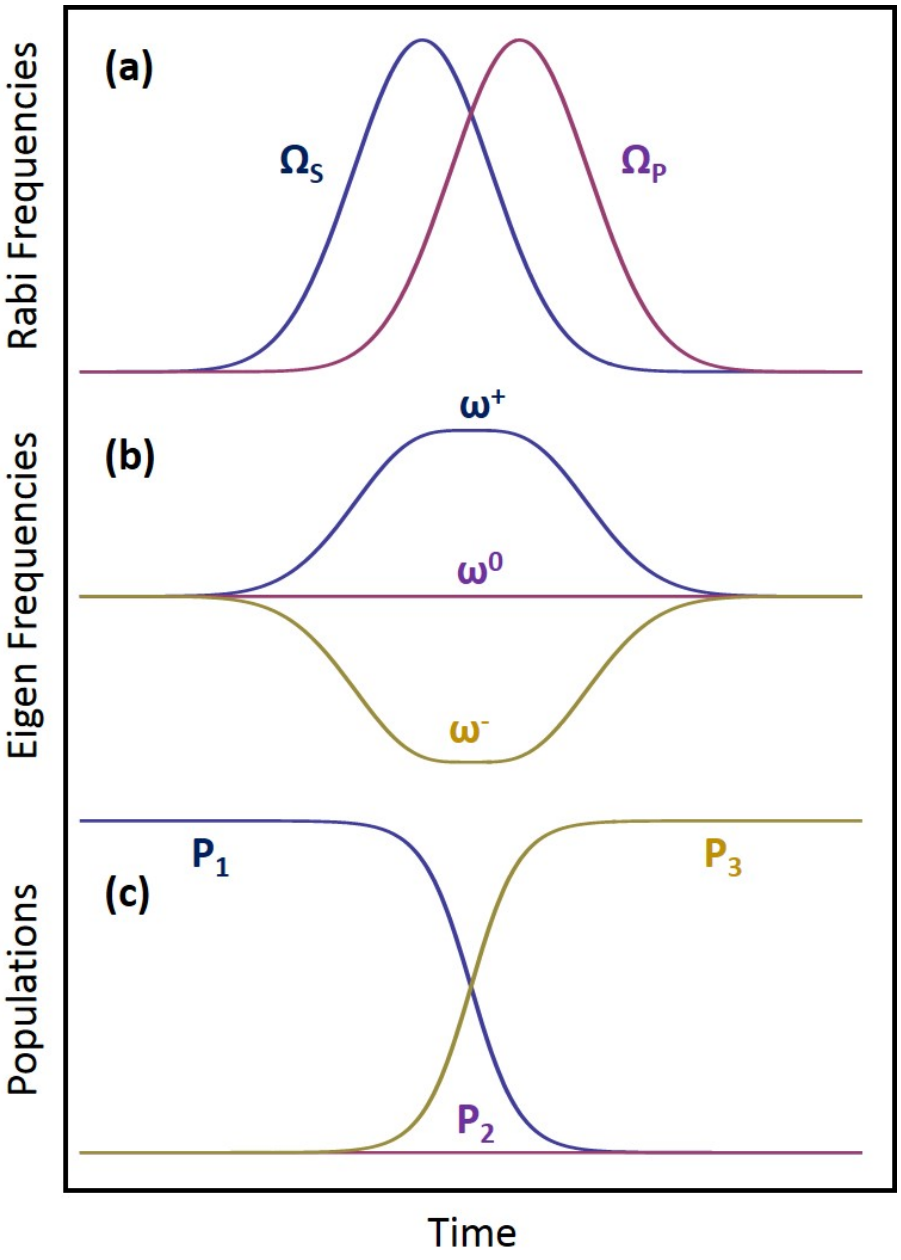

Figure 6-3: Adiabatic evolution in the STIRAP process. Plot (a) shows the counter-intuitive pulse sequence. Plot(b) shows the evolution of the eigen-frequencies of the three eigen-states. Plot (c) shows the population evolution during the STIRAP process. Initial population in $|1\rangle$ is 100% transferred to state $|3\rangle$. No population is moved into State $|2\rangle$.

dipole moments, I can apply Eq.(6.7c) to verify the adiabatic condition.

$$\left|\left\langle a^{+}|\dot{a}^{0}\right\rangle\right| \ll \left|\omega^{\pm}-\omega^{0}\right| \tag{6.7a}$$

$$\left|\dot{\Theta}\right| \ll \left|\omega^{\pm}-\omega^{0}\right| \tag{6.7b}$$

$$\left|\frac{\dot{\Omega}_P\Omega_S-\Omega_P\dot{\Omega}_S}{\Omega_P^2+\Omega_S^2}\right| \ll \left|\omega^{\pm}-\omega^{0}\right|. \tag{6.7c}$$

If the laser pulses that I use have a smooth change in amplitude, such as Gaussian or even triangular, Eq.(6.7c) can be approximately simplified to:

$$\Omega_{eff}^2\Delta\tau > \frac{100}{\Delta\tau}, \tag{6.8}$$

where $\Omega_{eff}=\sqrt{\Omega_P^2+\Omega_S^2}$, and $\Delta\tau$ is the duration of the laser pulse. The left-hand side of this equation is proportional to the laser pulse energy. Eq.(6.7c) is satisfied for completely coherent lasers (FT-limited laser pulse). For most pulsed dye lasers, the output pulses are not FT-limited, and Eq.(6.7c) must be modified to:

$$\Omega_{eff}^2\Delta\tau > \frac{100}{\Delta\tau}\left[1+\left(\frac{\Delta\omega_L}{\Delta\omega_{FT}}\right)^2\right]\Gamma, \tag{6.9}$$

where $\Delta\omega_L$ is the actual bandwidth of the laser pulse, $\Delta\omega_{FT}$ is the FT-limited bandwidth of the laser pulse, and the parameter Γ depends on the spectral profile (Gaussian or Lorentzian) and is approximately unity.

6.2.2 Results of optical-millimeter-wave STIRAP calculation

The STIRAP technique has been widely used in many research communities. The duration and wavelength of the pulse-pairs range from fs-to-s and UV-to-rf [161, 162, 163, 164, 165]. However, in our proposed experiment, to induce transitions from n^*=4, ℓ=2 via $n^*\sim$40, ℓ=3 to $n^*\sim$40, ℓ=4, the Pump pulse is in the visible ($\sim10^{15}$ Hz) region and the Stokes pulse is in the millimeter-wave ($\sim10^{11}$ Hz) region. In this section, the calculations of population transfer efficiency demonstrate quite conclusively the

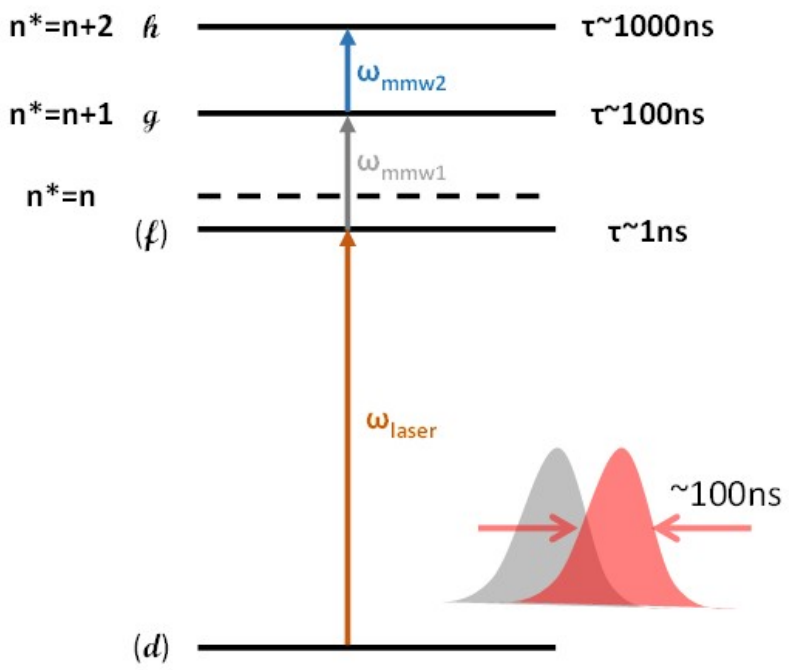

Figure 6-4: Schematic diagram of Rydberg levels involved in a STIRAP experiment. The mmW_2 pulse is added during the STIRAP process to avoid dissociation loss from the g state.

feasibility of our STIRAP experiments. In my calculations, most of the estimated parameters and state structures are based on what is known for the CaF molecule. However, the STIRAP technique is not limited to CaF molecules, but is applicable to Rydberg states of other diatomic and polyatomic molecules.

Figure 6-4 is an energy diagram of our STIRAP system. I start from a nominal "d" state with a relatively long lifetime. One laser and one millimeter-wave pulse are applied to populate a metastable g state via an unstable "f" intermediate state. The lifetimes of such states have not been measured carefully for CaF. Here, I assume that their lifetimes are: $\tau_d = 100$ ns, $\tau_f = 1$ ps to 10 ns, $\tau_g = 100$ ns. Typically, the lifetime of the g state is still not long enough for high resolution millimeter-wave spectroscopy, but it is long enough to excite step-wise through it to a more stable h state.

In this section, I perform two calculations with different sets of parameters. In the first calculation, all parameters are based on the basic setup in our lab, such as

Table 6.2: Parameters for the STIRAP calculations

	Set One	Set Two
μ_{12}	1 Debye	
μ_{23}	5000 Debye	
Laser wavelength	800 nm	
Beam area	5 cm^2	
millimeter-wave frequency	80 GHz	
Laser power	1 mJ	0.1 mJ
Laser pulse duration	10 ns	100 ns
Laser bandwidth	1 GHz	5 MHz
millimeter-wave power	0 dBm	-5 dBm
millimeter-wave duration	10 ns	100 ns
millimeter-wave profile	Rectangular	Gaussian

non-FT limited pulsed dye laser and unshaped rectangular millimeter-wave pulse. In the second calculation, all parameters are based on the new cw amplified FT-limited long-pulse laser (100 ns), which is under construction in our lab, in combination with a Gaussian shaped millimeter-wave pulse. The detailed parameters are listed in Table 6.2.

Pulsed dye laser + rectangular millimeter-wave pulse

In the calculation, the incoherent properties of the non FT-limited ns-pulsed dye laser are taken into account by the colored noise phase fluctuation model [163]. Different from a completely coherent radiation source, the electric field from an incoherent source has extra phase fluctuation terms:

$$\frac{\mu_P E_P(t)}{\hbar} = \Omega_P(t)\cos\left[\omega_{21}t + \alpha(t)\right] \tag{6.10a}$$

$$\frac{\mu_S E_S(t)}{\hbar} = \Omega_S(t)\cos\left[\omega_{23}t + \beta(t)\right], \tag{6.10b}$$

where μ_P and μ_S are the electric dipole transition moments of the Pump and Stokes transitions, E_P and E_S are the electric fields of the Pump and Stoke pulses, Ω_P and Ω_S are the Rabi frequencies of the Pump and Stokes pulses, ω_{21} and ω_{23} are the transition frequencies of the Pump and Stokes transitions, and α and β are the phase fluctuations of the Pump and Stokes pulses. I modify Eq.(6.3) with a partially

incoherent radiation source,

$$H(t) = \frac{\hbar}{2}\begin{bmatrix} 0 & \Omega_P(t)e^{i\alpha(t)} & 0 \\ \Omega_P(t)e^{-i\alpha(t)} & 0 & \Omega_S(t)e^{-i\beta(t)} \\ 0 & \Omega_S(t)e^{i\beta(t)} & 0 \end{bmatrix}. \tag{6.11}$$

The detunings in Eq.(6.11) can be incorporated into the phase fluctuations:

$$\frac{d}{dt}\alpha(t) = -\Delta_P + \varepsilon_\alpha(t) \tag{6.12a}$$

$$\frac{d}{dt}\beta(t) = -\Delta_S + \varepsilon_\beta(t), \tag{6.12b}$$

where ε_α and ε_β are frequency fluctuations of the Pump and Stokes pulses. Such fluctuations are well described by colored noise with the properties:

$$\langle \varepsilon(t) \rangle = 0 \tag{6.13a}$$

$$\langle \varepsilon(t)\varepsilon(s) \rangle = D\Gamma e^{-\Gamma|t-s|}. \tag{6.13b}$$

I apply an algorithm developed by Vemuri et al. [166] to generate colored noise to simulate our dye laser pulses. And, as shown in Figure 2-30, the natural linewidth of the millimeter-wave source is 2 kHz in 1 ms. Its phase noise can be ignored in a 10-100 ns pulse.

Figure 6-5 shows the calculation results for the two-photon and STIRAP population transfer. I find that: (1) The STIRAP has higher population transfer efficiency than the two-photon excitation. (2) The color noise of the dye laser decreases the population transfer efficiency.

In Figure 6-5, Plot (d), I find that the population transfer efficiency without colored noise (ideal efficiency) is much higher than that with colored noise. I try to compensate the laser noise by introducing multiple frequency components in the millimeter-wave pulse. Figure 6-6, Plot (a) shows a similar STIRAP process as in Figure 6-5, Plot (c), but with a 2 GHz linearly chirped millimeter-wave pulse. In

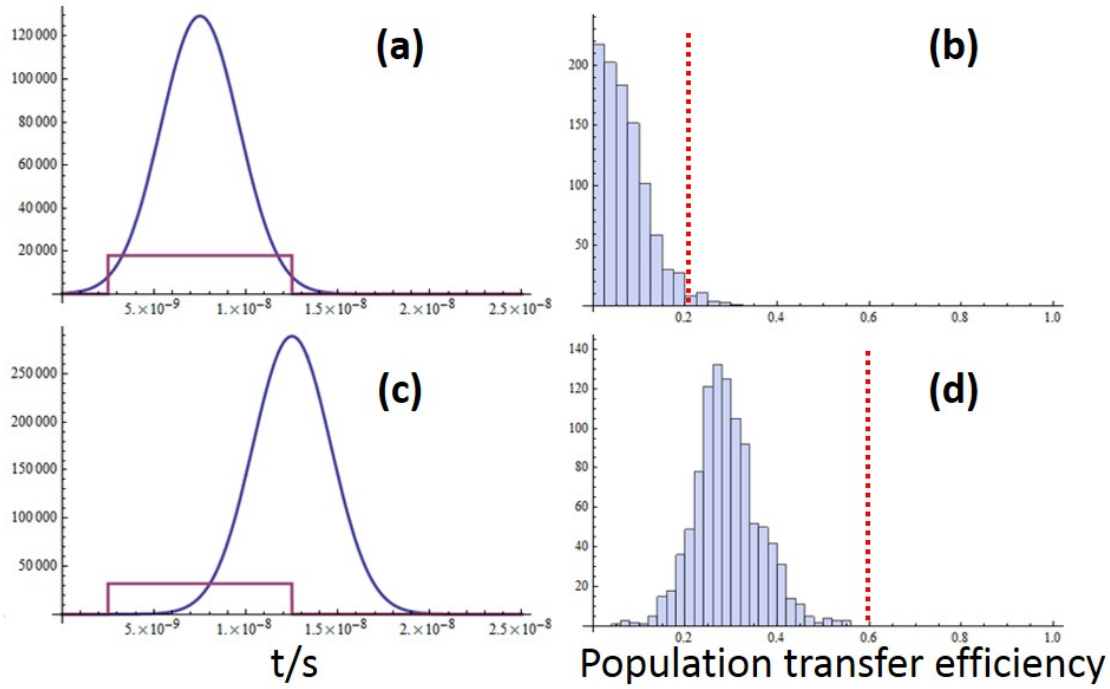

Figure 6-5: Calculation results for two-photon and STIRAP population transfer schemes with a 10 ns pulsed dye laser and rectangular millimeter wave pulse. Plot (a) and Plot (c) show the temporal overlap of the laser pulse and millimeter-wave pulse. Their amplitudes are not scaled. Plot (b) and Plot (d) show the distribution of the population transfer efficiency. The red dotted line shows the population transfer efficiency without the colored noise of the pulsed dye laser.

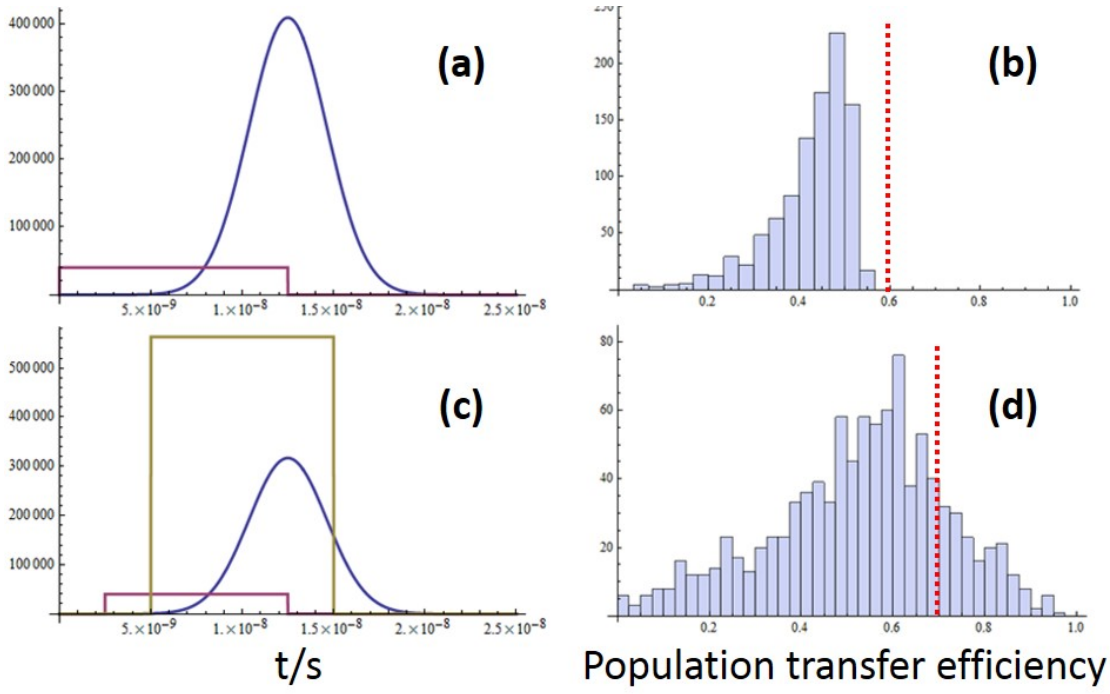

Figure 6-6: Calculation results for the laser+chirped-pulse CHIRAP and laser+double-chirped-pulse CHIRAP population transfer with a 10 ns pulsed dye laser and a rectangular 2 GHz linearly chirped millimeter-wave pulse. Plot (a) and Plot (c) show the temporal overlap of the laser pulse and millimeter-wave pulse. Their amplitudes are not scaled. Plot (b) and Plot (d) show the distribution of the population transfer efficiency. The red dotted line shows the population transfer efficiency without the colored noise of the pulsed dye laser.

Figure 6-6, Plot (b), the average population transfer efficiency moves significantly toward the ideal efficiency significantly. I try to add two chirped millimeter-wave pulses to improve the compensation. With appropriate relative strengths and delay, I can achieve 60% average population transfer efficiency, as shown in Figure 6-6, Plot (d). The ideal efficiency is also increased, because the second chirp also moves the population from the g state to the more stable h state. I name these two methods CHIRAP (CHirped sTimulated Raman Adiabatic Passage). However, due to the complicated light-multi-level matter interactions in CHIRAP, the distribution of the population transfer efficiency is broader.

The calculated population transfer efficiency above is acceptable. However, the population transfer efficiency, even ideal efficiency, is still much lower than that in

typical STIRAP experiments. From Eq.(6.7c), it is not difficult to discover that the sharp edge of the rectangular millimeter-wave pulse induces a significant non-adiabatic interaction. To minimize the population leakage due to such non-adiabatic interactions, it is necessary to change the shape of the millimeter-wave pulse from rectangular to a smoother one, such as Gaussian.

Long pulse FT-limited laser + Gaussian shaped millimeter-wave pulse

Figure 6-7 shows the STIRAP process using a 100 ns FT-limited laser pulse and a Gaussian shaped millimeter-wave pulse, as shown in Plot (a). Plot (b) shows an almost 100% population transfer efficiency. In this calculation, the lifetime of the intermediate state (f) is assumed to be 1 ns. Due to the absence of phase fluctuations in this calculation, the population transfer efficiency is a constant.

In all calculations above, I set the detunings of the Pump and Stokes pulses to zero. To test the tolerance for the detunings, I perform two sets of calculations: (1) Increase both detunings in the same direction and maintain the resonance condition, $\Delta_P = \Delta_S = \Delta$. The population transfer efficiency is almost constant if Δ <5 GHz, and then decreases slowly, as shown in Figure 6-8, Plot (b). (2) Increase the detuning of one photon only. This breaks the resonance condition. The population transfer efficiency decreases abruptly at 0.2 GHz detuning, as shown in Figure 6-8, Plot (a). The comparison shows that I must keep the total frequency of the two photons (sum or difference) in resonance with the energy difference of the initial and final state. A large detuning for the intermediate state is tolerated. More importantly, for a short-lived intermediate state, I always choose a relatively large detuning, $\Delta\sim$2 GHz, to avoid populating the intermediate state by stepwise excitation. With appropriate parameters for the laser pulse and millimeter-wave pulse, I can achieve >20% population transfer efficiency via an intermediate state with a 10 ps lifetime, as shown in Figure 6-9.

From the calculations above, I know that the resonance condition is a very strict requirement. However, Doppler broadening can relax this condition and decrease the population transfer efficiency. Even worse, different from conventional STIRAP, the

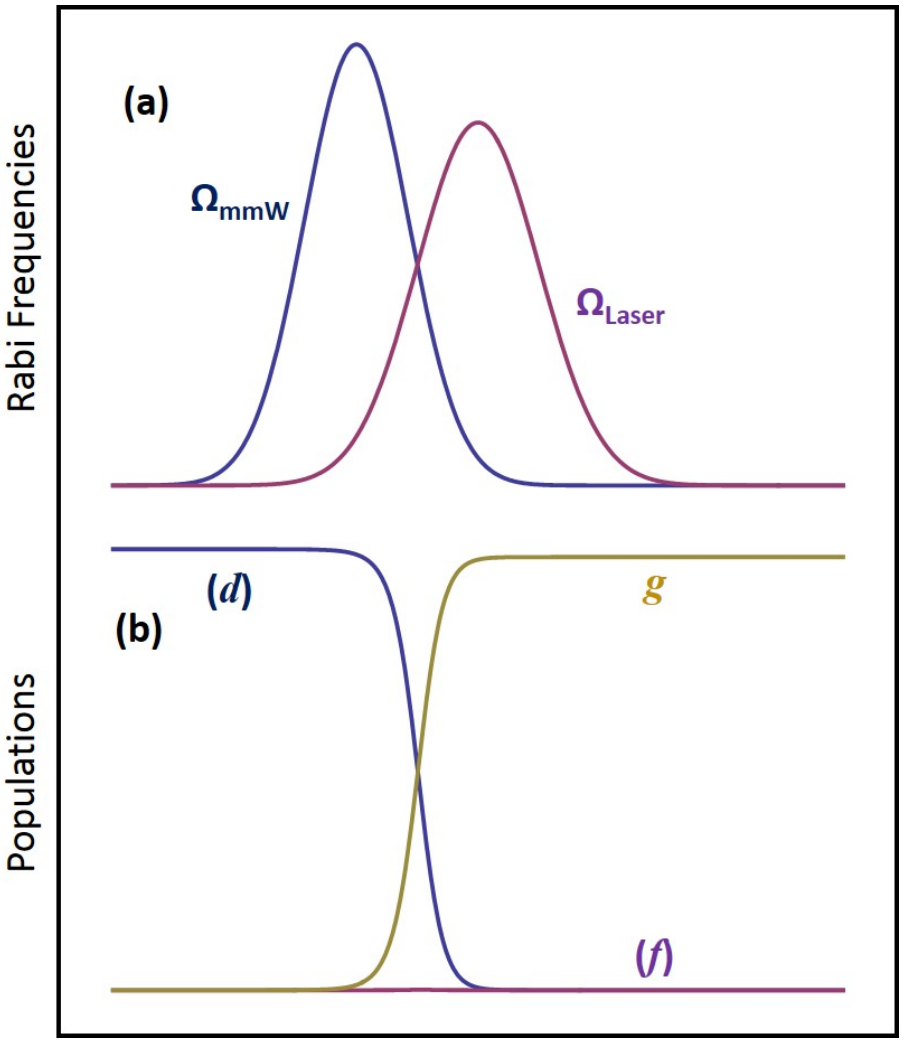

Figure 6-7: Calculation results for the laser-millimeter-wave STIRAP population transfer with a 100 ns FT-limited laser and a Gaussian shaped millimeter-wave pulse. Plot (a) shows the counter-intuitive pulse sequence. Plot(b) shows the population evolution during the STIRAP process. The initial population in state (d) is >95% transferred to state g.

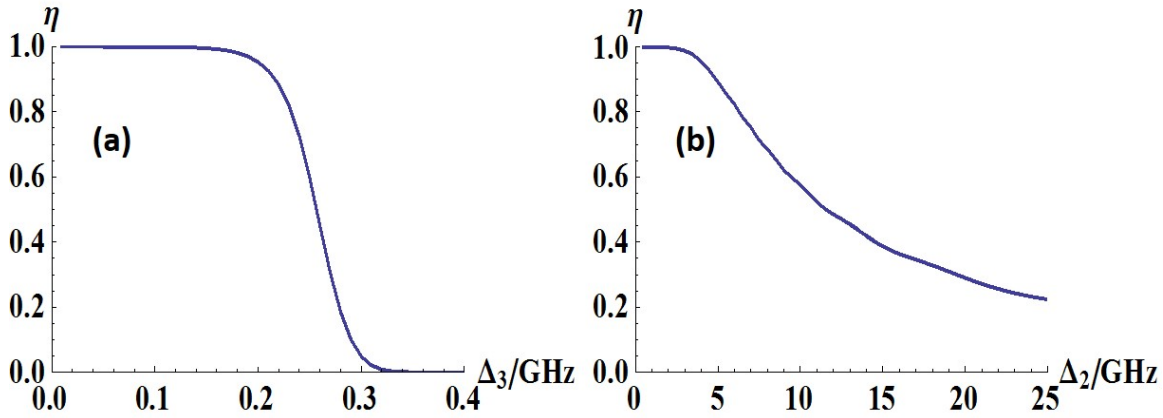

Figure 6-8: Test of the dependence of the population transfer efficiencies and detunings. Plot (a) shows a significant decrease of the population transfer efficiency if the resonance condition is violated. Plot (b) shows a slow decrease of the population transfer efficiency with increasing detuning from the intermediate state, but maintaining the resonance condition.

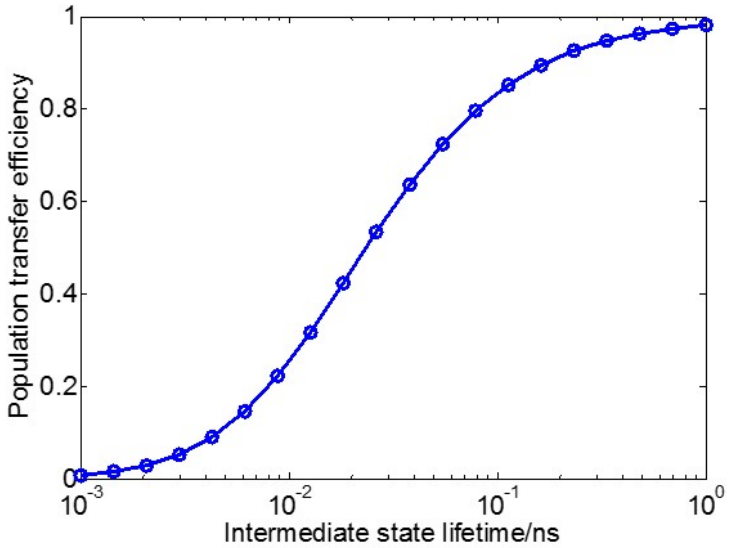

Figure 6-9: The population transfer efficiency between (d) and g states for various lifetimes of the intermediate (f) state.

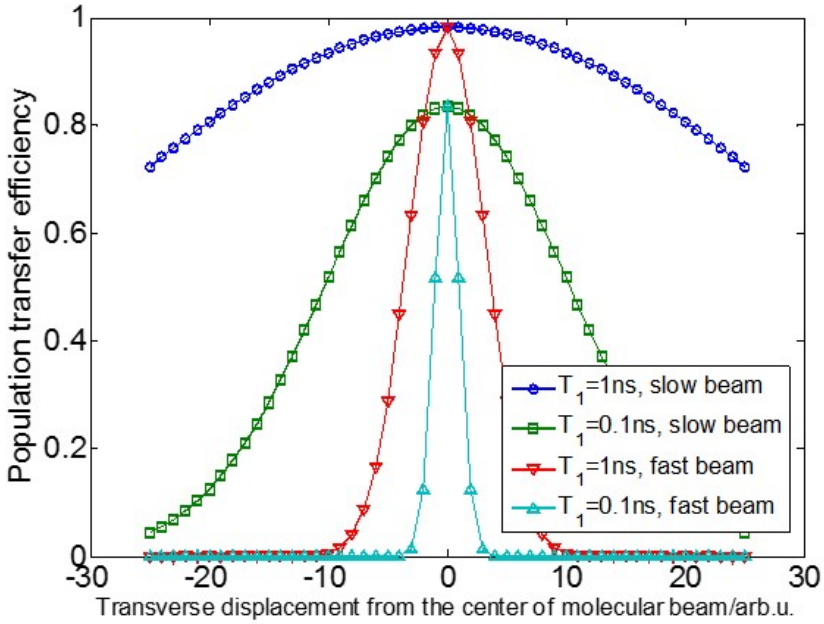

Figure 6-10: The lateral spatial distribution of transfer efficiency in an unskimmed buffer gas cooled slow molecular beam and in a supersonic cooled fast molecular beam.

Doppler widths of the laser (>100 MHz) and millimeter-wave (<1 MHz) transitions are quite different and cannot be canceled by a counter-propagating configuration. I do not have a better solution other than by decreasing the Doppler broadening by using a slow beam. Figure 6-10 shows a comparison of the spatial transfer efficiency distribution for an unskimmed buffer gas cooled slow molecular beam and supersonically cooled fast molecular beam. Transfer efficiencies in the central diameter of the molecular beams are the same. However, due to the different Doppler widths, the slow molecular beam has a more uniform spatial distribution, which is more compatible with the large volume of the CPmmW experiment. To achieve an even better spatial distribution, I can simultaneously apply two or more millimeter-wave pulses with different frequencies, which are used to compensate the laser Doppler shifts.

6.2.3 Unwanted processes

The calculations above demonstrate the feasibility of high efficiency population transfer to high-ℓ core-nonpenetrating Rydberg states. However, two important processes,

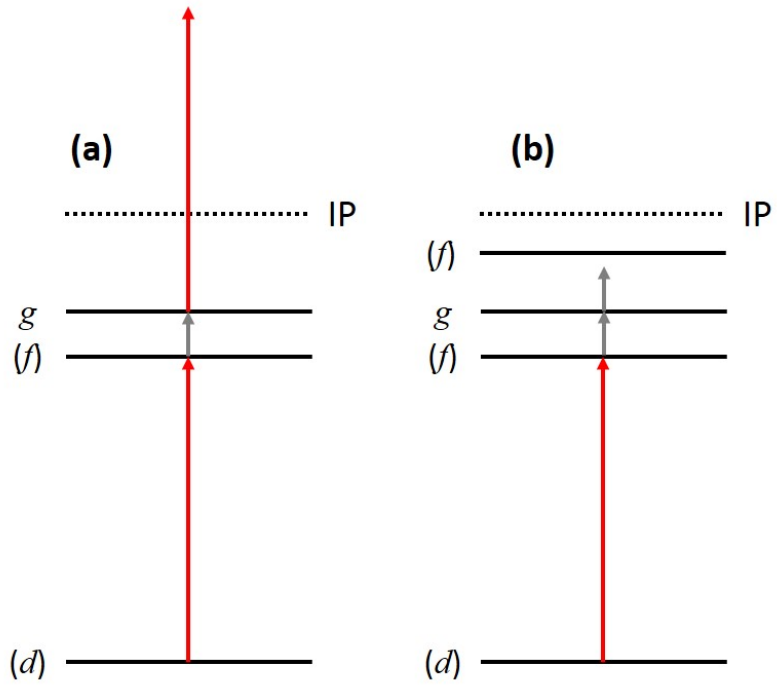

Figure 6-11: Unwanted processes. Plot (a) shows possible ionization of the g state by an intense Pump laser pulse. Plot (b) shows a possible non-resonant excitation to an unstable (f) state by an intense millimeter-wave pulse.

which might decrease the population transfer efficiency significantly, are not included in the calculations. In typical STIRAP experiments, the intensities of both the laser pulse and the millimeter-wave pulse are much higher than in the step-wise double resonance experiment. Intense laser pulses might induce multi-photon ionization, as shown in Figure 6-11, Plot (a). Intense millimeter-wave pulses might induce a non-resonant excitation, as shown in Figure 6-11, Plot (b). The former process causes population loss by creating ions, and the latter process causes population loss by creating unwanted states. In this section, I discuss these two unwanted processes and show that they would not interfere with my experiment with an appropriate setup.

- Laser-Multi-photon ionization

  To avoid multi-photon ionization, I need to derive the dependences of the efficiency of ionization and STIRAP on pulse duration, τ, for a fixed total pulse energy. To evaluate the effective pulse area of a bound-continuum transition, I

need to integrate over the bandwidth of the pulse,

$$A_{eff} \propto \int \left(\frac{M}{\Delta\omega + i\Gamma} E\Delta t \right) d\Delta\omega, \tag{6.14}$$

where M is the matrix element of the transition dipole moment, $\Delta\omega$ is the bandwidth of the laser pulse, Γ is the coherent decay rate of the continuum states, and Δt is the duration of the laser pulse. For continuum final states, $\Gamma >> \Delta\omega$. Therefore, Eq.(6.14) is approximately,

$$A_{eff} \propto \frac{M}{i\Gamma} E\Delta t\Delta\omega, \tag{6.15}$$

where M/iΓ is independent of the laser pulse, and for a FT-limited pulse, $\Delta t\Delta\omega$ is a constant. Therefore, the effective pulse area is only linearly dependent on the electric field, which is inversely proportional to $\sqrt{\Delta t}$ for a fixed total pulse energy, $A_{eff} \propto \sqrt{1/\Delta t}$. The effective pulse area of a bound-bound transition in STIRAP is straightforwardly calculated,

$$A_{STIRAP} \propto \mu E\Delta t \propto \sqrt{\frac{1}{\Delta t}} \Delta t = \sqrt{\Delta t}. \tag{6.16}$$

Therefore, the figure of merit for avoiding ionization scales as τ. In addition to the pulse length, a FT-limited laser pulse is preferred to minimize multi-photon ionization due to its narrow bandwidth, which has smaller overlap with the continuum spectrum. By experiments, I have observed that the pulse energy threshold for two-photon (7 ns non-FT-limited dye laser pulse) ionization is $\approx$100 μJ/mm^2. My proposed experiment use a 100 ns long, <10 μJ/mm^2 FT-limited laser pulse, far below the scaled $\approx$1 mJ/mm^2 multi-photon ionization threshold.

- Non-resonant millimeter-wave excitation

The ratio of the resonant excitation and non-resonant excitation can be evalu-

ated by

$$A_{eff} \propto \frac{M}{\Delta\omega + i\Gamma} \tag{6.17}$$

where $\Delta\omega$ is the off-resonance detunings, and Γ is the radiative lifetime. On resonance, $\Delta\omega \sim 0$ and the matrix element of the transition is inversely proportional to Γ. Off resonance, $\Delta\omega >> \Gamma$ and the matrix element of the transition is inversely proportional to $\Delta\omega$. Therefore, the ratio of the resonant excitation and non-resonant excitation is:

$$\frac{\eta_{res}}{\eta_{non}} = \left(\frac{\Delta\omega}{\Gamma}\right)^2. \tag{6.18}$$

For typical Rydberg states, Γ <1 MHz. For typical nonhydrogenic atomic Rydberg states at n$\sim$40, the frequency distance between an h state and the nearest f state is $\sim$1 GHz. Therefore, non-resonant excitation only contributes $1/10^6$, which can be ignored. However, for molecular Rydberg states, such frequency separations cannot be predicted easily and might be smaller. Therefore, millimeter-wave non-resonant excitation needs to be analyzed carefully in STIRAP experiments on molecular Rydberg states.

6.3 Adiabatically-focused STark-mixed Rydberg Orbitals (ASTRO)

6.3.1 Non-Hermitian Hamiltonian

The non-Hermitian complex Hamiltonian is used to to describe bound-free interactions [19]. Different from the usual Hermitian Hamiltonian, the diagonal matrix elements of the non-Hermitian Hamiltonian can be complex. Therefore, its eigenvalues are also complex. The real part represents the energy of the eigenstate, and the imaginary part represents the lifetime. The Hamiltonian of a two-level system with

finite lifetime can be written as,

$$H_2 = \begin{pmatrix} E_1 & V \\ V & E_2 \end{pmatrix} = \begin{pmatrix} \bar{\varepsilon} - i\bar{\Gamma}/2 & 0 \\ 0 & \bar{\varepsilon} - i\bar{\Gamma}/2 \end{pmatrix} + \begin{pmatrix} \delta\varepsilon - i\delta\Gamma/2 & V \\ V & -\delta\varepsilon + i\delta\Gamma/2 \end{pmatrix} \tag{6.19}$$

The parameters in the Hamiltonian are defined as:

$$E_1 = \varepsilon_1 - i\Gamma_1/2 \tag{6.20a}$$

$$E_2 = \varepsilon_2 - i\Gamma_2/2 \tag{6.20b}$$

$$\bar{\varepsilon} = (\varepsilon_1 + \varepsilon_2)/2 \tag{6.20c}$$

$$\bar{\Gamma} = (\Gamma_1 + \Gamma_2)/2 \tag{6.20d}$$

$$\delta\varepsilon = (\varepsilon_1 - \varepsilon_2)/2 \tag{6.20e}$$

$$\delta\Gamma = (\Gamma_1 - \Gamma_2)/2, \tag{6.20f}$$

where ε_1 and ε_2 are the real energies, Γ_1 and Γ_2 are the decay rates, and V represents the interaction. The eigenvalues of the Hamiltonian are:

$$E_\pm = -i\frac{\bar{\Gamma}}{2} + \bar{\varepsilon} \pm \sqrt{V^2 + \left(\delta\varepsilon - i\frac{\delta\Gamma}{2}\right)^2}. \tag{6.21}$$

For example, in a two-level system, I assume that one state is a completely bound state, and the other one has a 1 GHz decay rate. Their energy spacing is 2 GHz. When I apply a DC electric field to mix the two states, the real energy in Eq.(6.21) represents a Stark splitting, as shown in Figure (6-12), Plot (a). The imaginary energy shows a mixing of the decay rate, as shown in Figure (6-12), Plot (b). It is straightforward to extend this method from a two-level system to a multi-level system, which is used to analyze the ASTRO scheme in the following.

6.3.2 Description of ASTRO

The recipe for preparing core-nonpenetrating states through ASTRO is:

- This is a two-laser 1+1 double resonance excitation scheme. Choose a bright,

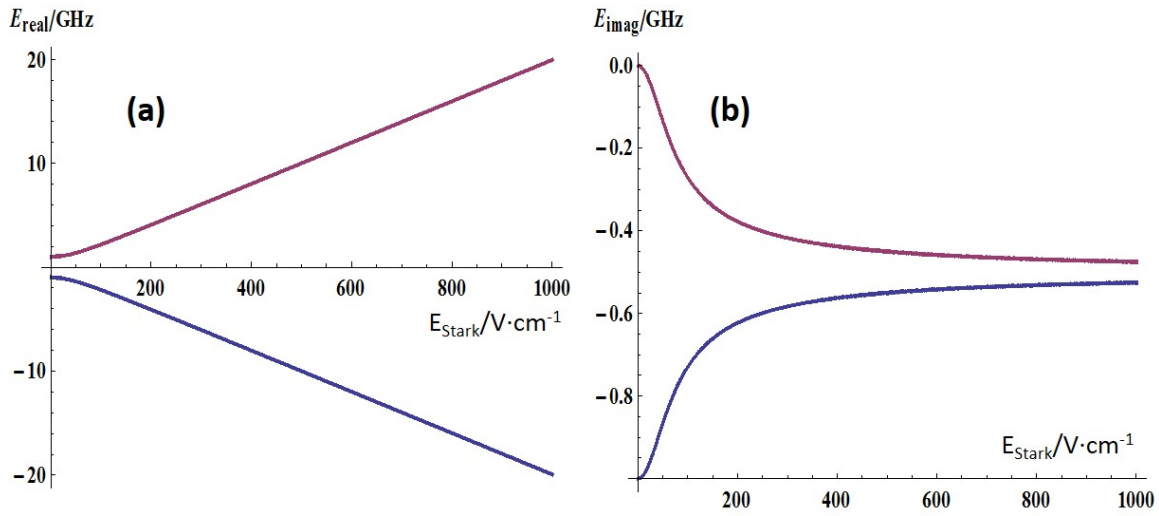

Figure 6-12: Stark mixing of a two-level system

weakly core-penetrating state as the initial state (populated by the second tunable laser), which has relatively strong oscillator strength from the intermediate state (populated by the first tunable laser), relatively pure-ℓ (d or f) character, and small quantum defect, mod(μ)<0.1.

- Turn on a ∼10 V/cm electric field to mix the bright state (f state in CaF) into high-ℓ dark states. I assume Stark mixing only destroys the ℓ quantum numbers, but does not mix λ (projection of ℓ on the molecular axis). This assumption is valid for the Rydberg states that can be described by Hund case d. Detailed discussions of this assumption and a more general calculation method can be found in Petrovic's thesis [167]. With this assumption, all other electronic states with $|\lambda| \neq |\lambda_{initial}|$ or $\ell < |\lambda_{initial}|$ are not involved. Due to the small applied electric field, all states with quantum defect δ >0.2 are excluded from this Stark-mixing process. As mentioned in Section 6.1, the strong propensity rules prevent N^+, v^+ mixing also.

- Selectively populate one Stark state with chosen nominal "ℓ" character using a 10 ns pulsed tunable laser or >100 ns pulse amplified cw diode laser.

- Ramp down the electric field to zero at a maximum rate determined by a simple calculation. The selected "ℓ" state evolves adiabatically to a field-free state with

pure ℓ character.

Several key features of this technique must be emphasized:

- Although bright states with ℓ_{bright} <4 usually have very short lifetimes (e.g., CaF $f\sigma$ state, 1ns), the strong Stark mixing results in dilution of the fast decay rate into nearly all ℓ >4 dark states. This dilution effect increases the effective lifetime approximately by a factor of 100.

- The laser power used to populate Stark-mixed states must be higher than usual, because most Stark states have only a small amount of bright state character. Usually, small $|\ell - \ell_{bright}|$ states have larger bright character. However, if the sign of the quantum defect of a target ℓ state is different from that of the bright state, the mixing angle will be negligibly small (e.g., the $h\phi$, $i\phi$, and $k\phi$ states of CaF have quantum defects opposite in sign to that of $f\phi$, which is predicted by long-range model of CaF). To fill in this gap, I can use a mm/rf pulse to induce transitions into such states during/after the pulsed Stark field.

- As discussed above, the laser powers required for different Stark states compared to that for the field-free bright states are much larger. Based on the discussion in Section 6.2.3, a 10 ns 1 GHz bandwidth pulsed dye laser with sufficient power to populate Stark states might cause significant multi-photon ionization. However, a >100 ns Fourier-Transform limited laser pulse populate the Stark states efficiently with minimal multi-photon ionization. The lifetimes of the Stark states at maximum electric field are sufficiently long to accommodate the long pulse laser excitations.

- The maximum rate at which the electric field must be decreased toward zero depends on nonadiabatic loss and dissociation decay loss. Minimizing both of these loss mechanisms make opposite demands on the ramp rate of the Stark field. The nonadiabatic loss rate is described by the Landau-Zener formula [168], as Eq.(6.22). The nonadiabatic transition probability is smaller if the ramp rate is smaller. The dissociation loss can be calculated by the effective decay rate,

which is determined by the imaginary part of the diagonalized non-Hermitian Hamiltonian. The dissociation loss is smaller if the ramp rate is larger. The ramped rate needs to be a compromise of two opposite considerations,

$$P = \exp\left[-2\pi \frac{|V|^2}{\hbar\,|dE/dt|}\right], \tag{6.22}$$

where V is the Stark interaction matrix element and dE/dt is the rate of change of the Stark energy.

- For most experiments with an external electric field in Rydberg states system, uncompensated stray electric fields limit the ℓ-purity of the final states [55].

6.3.3 Calculation results of ASTRO

In the above section, I describe the recipe for implementing the ASTRO scheme and discuss the general experimental considerations. In this section, I use CaF as a model system to demonstrate the feasibility of ASTRO by calculation [169, 13]. The quantum defects and lifetimes of the $|\lambda| = 1$ Rydberg states of CaF with ℓ=4 to ℓ=7 are listed in Table 6.3. Because of their large quantum detects, states with smaller ℓ cannot be mixed by a 10 V/cm Stark field and are not included in this calculation. States with larger ℓ are degenerate, because μ=0 and have infinite lifetime. The estimated electric dipole transition moments are calculated by a numerical method for non-hydrogenic Rydberg states. Thus, I construct a 32 $\times$ 32 non-Hermitian Hamiltonian for n=35, π states. As described in Section 6.3.1, the energies of the Stark states and their effective lifetimes are obtained from the real and imaginary parts of the diagonalized Hamiltonian, as shown in Figure 6-13. The mixing coefficient of f in each Stark state can be used to estimate the required excitation laser power, as in the fourth column in Table 6.3.

Figure 6-13, Plot (b) shows that: (1) The f state has a much larger dissociation decay rate (off-scale) than the others. (2) The lifetimes of most Stark states are non-linearly dependent on the electric field. I find that in a specific range of the electric

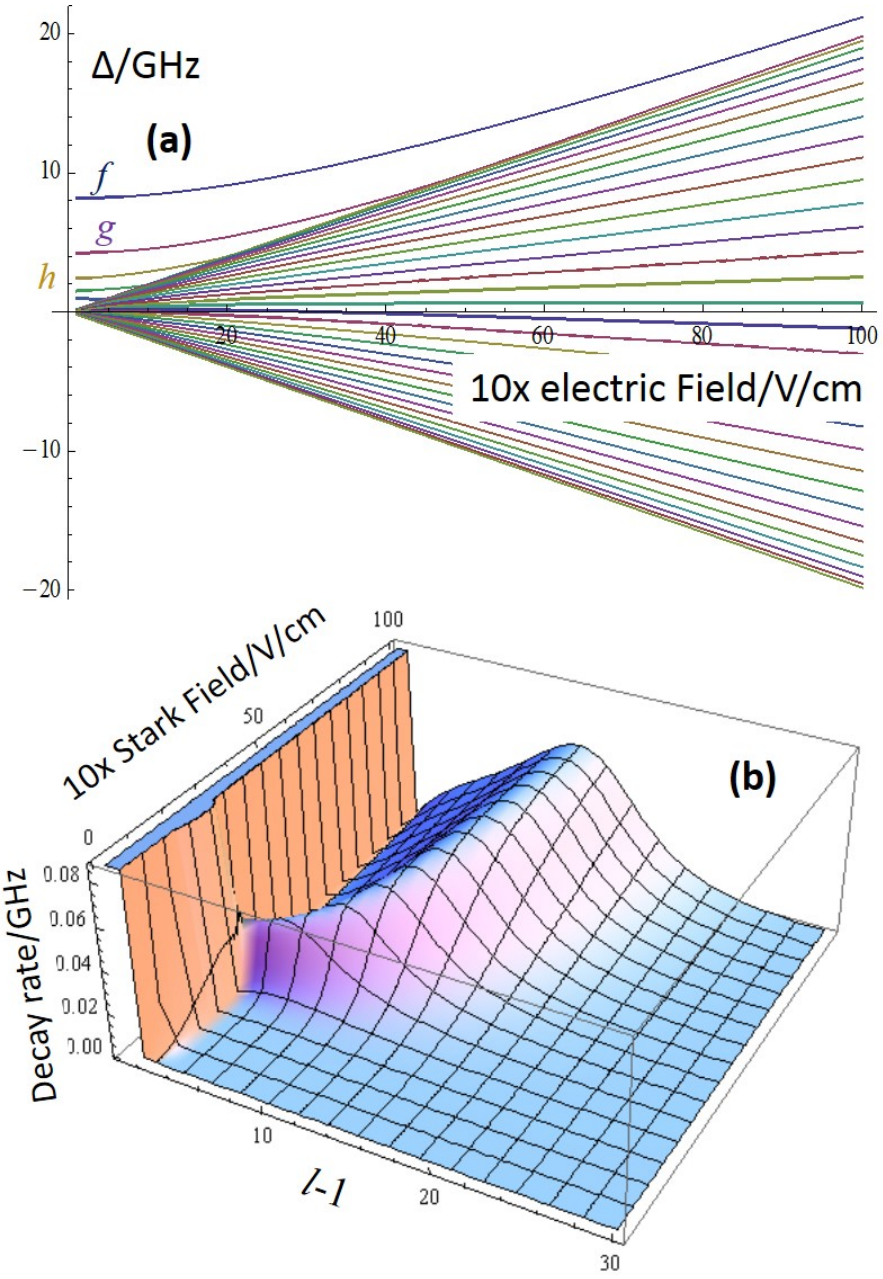

Figure 6-13: Stark states of n=35, π states. Plot (a) shows the energies of Stark states with 0 to 10 V/cm DC electric field. Plot (b) shows the dissociation decay rate of Stark states with 0 to 10 V/cm DC electric field.

	μ^a	$\tau(ns)^b$	Laser^c	lifetime^d	$\eta 1^e$	$\eta 2^f$	Ramp^g	Stray^h
f ($\ell = 3$)	-0.053	1	—	80	—	—	—	—
g ($\ell = 4$)	-0.028	30	x100	>1000	10%	40%	30	100
h ($\ell = 5$)	-0.016	1000	x80	600	20%	80%	100	50
i ($\ell = 6$)	-0.010	10000	x60	400	5%	80%	300	25
k ($\ell = 7$)	-0.006	100000	x40	250	5%	80%	300	13

Table 6.3: **Summary of calculations relevant to the use of Stark mixing and adiabatic focusing to prepare core-nonpenetrating Rydberg states with $\ell = 4$ to $\ell = 7$. (a)** Quantum defects of $|\lambda| = 1$ states calculated by a long-range model [1], **(b)** Estimated field-free lifetimes, **(c)** Laser saturation power ratios for Stark states with E-field=10V/cm relative to field-free f state, **(d)** Lifetimes of the Stark states with E-field=10V/cm in ns **(e)** Population transfer efficiency to the final ℓ state with a linear ramp, **(f)** Population transfer efficiency to the final ℓ state with a nonlinear ramp, **(g)** Total duration of the ramped pulse in ns. **(h)** Maximum tolerable residual stray electric field for each pure ℓ-state after the ramped field is turned off in mV/cm.

field, the dissociation decay rate is very large. In another range, it is almost zero. This suggests designing a non-linearly ramped electric field. The ramped field has a relatively fast ramp rate in the fast dissociation decay regime to avoid dissociation loss, and has a relatively slow ramp rate in the slow dissociation decay regime to avoid nonadiabatic loss. Figure 6-15 shows the relative behaviors of both the nonadiabatic loss rate and the lifetime as a function of field. Compared to a linear ramp, it is more efficient to use a nonlinear ramp that decreases rapidly at large fields, and slowly at smaller fields, in order to obtain the transfer efficiencies shown in the sixth and seventh columns of Table 6.3.

The final discussion in Section 6.3.2 concerns the effects of a stray electric field. The electric field efficiently couples near-degenerate states. If the ASTRO technique is applied to high-ℓ states, the requirement of minimizing the stray electric should be very strict. The last column in Table 6.3 lists the tolerance to stray electric fields for different, accessible ℓ states. For practical experiments, the chosen ℓ state must have a small, but non-zero quantum defect ($0.005 < \mathrm{mod}(\mu) < 0.1$). Thus ASTRO allows access only to those states in which I am most interested: the core nonpenetrating states with relatively small, non-zero quantum defects.

Including all of the considerations above, I ran a complete simulation to display the entire procedure of the ASTRO scheme, as shown in Figure 6-15. I find that: initially, the 10 V/cm DC electric field mixes a wide range of Stark states. With an

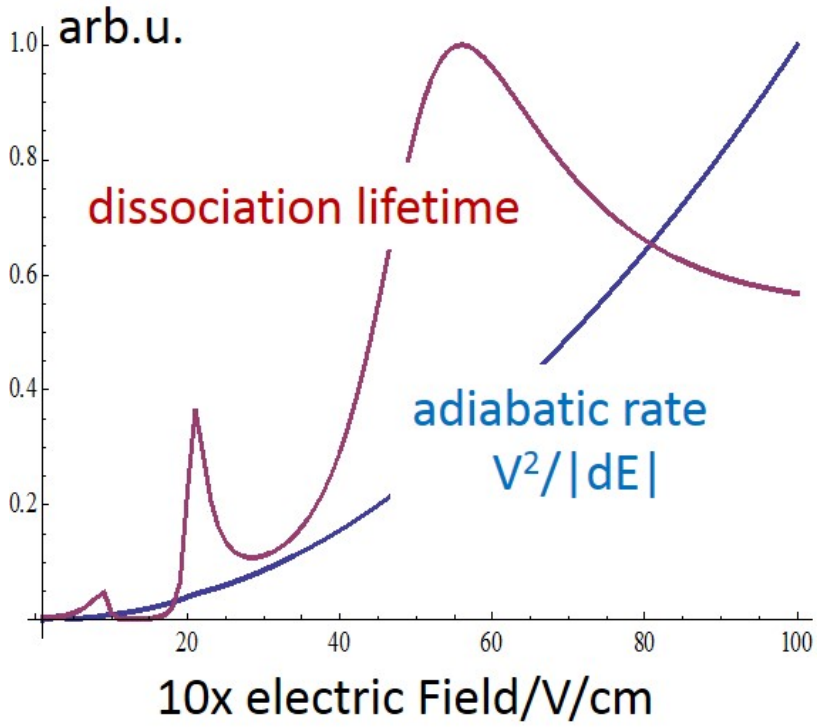

Figure 6-14: Electric field-dependent dissociation lifetime and effective upper limit of the ramp rate for an adiabatic process. These two curves suggest the use of faster ramp at high electric field and a slower ramp rate at low electric field.

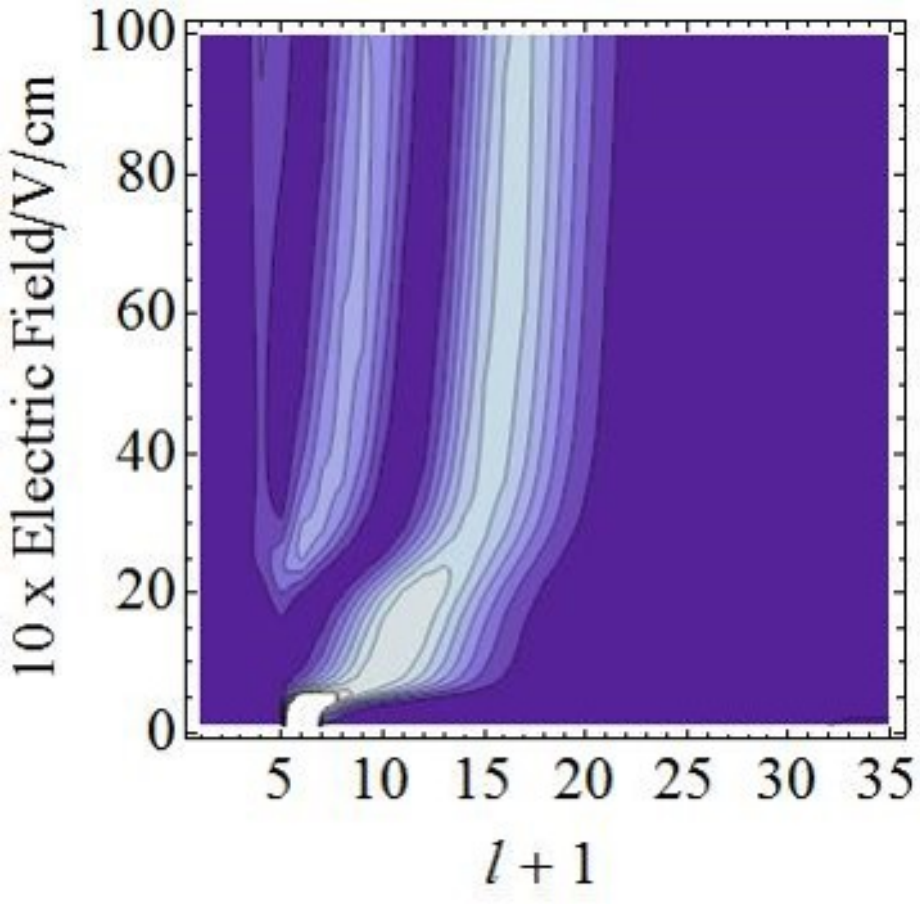

Figure 6-15: Adiabatic focusing from a nominal "h" Stark state at E=10 V/cm into the pure field-free h state.

appropriate non-linear ramped field, multiple Stark states focus to a single field-free core-nonpenetrating Rydberg state. With a moderately fast dissociation decay rate of the f state ($\tau \sim$1 ns), the population transfer efficiency into g, h and i states can be more than 50%.

Appendix A

Rectangular Helmholtz coils

The magnetic field spatial distribution of the rectangular Helmholtz coils can be calculated by integrating Bio-Savart equation:

$$\begin{aligned} B &= \nabla \times A \\ A(r) &= \frac{\mu_0}{4\pi} \int \frac{J(r')}{|r-r'|} d^3 r' \end{aligned} \tag{A.1}$$

where A is vector potential, μ_0 is magnetic permutivity, and J is the current in the coils. The integration is performed along four sides of the coils. One pair of coils are oriented along z axis, as shown in Figure A-1. In this geometrical configuration, $J_z = 0$ and $A_z = 0$. The magnetic field spatial distribution can be obtained analytically as in Eq.(A.2).

$$\begin{aligned} B_x &= -\frac{\partial A_y}{\partial z} \\ B_y &= \frac{\partial A_x}{\partial z} \\ B_z &= \frac{\partial A_y}{\partial x} - \frac{\partial A_x}{\partial y} \end{aligned} \tag{A.2}$$

$$\begin{aligned} A_x &= \frac{\mu_0 I}{4\pi} \left[M_1 - M_2 + M_3 - M_4 \right] \\ A_y &= \frac{\mu_0 I}{4\pi} \left[N_1 - N_2 + N_3 - N_4 \right] \end{aligned} \tag{A.3}$$

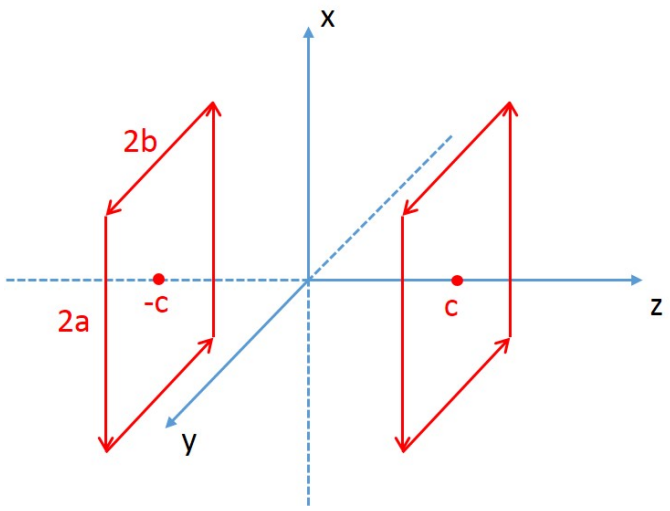

Figure A-1: Geometrical configuration of a pair of rectangular Helmholtz coils.

$$
\begin{aligned}
M_1 &= \int_{-a}^{a} \frac{dx'}{\sqrt{(x-x')^2+(y+b)^2+(z+c)^2}} = \log\left[\frac{\sqrt{(x-a)^2+(y+b)^2+(z+c)^2}-x+a}{\sqrt{(x+a)^2+(y+b)^2+(z+c)^2}-x-a}\right] \\
M_2 &= \int_{-a}^{a} \frac{dx'}{\sqrt{(x-x')^2+(y-b)^2+(z+c)^2}} = \log\left[\frac{\sqrt{(x-a)^2+(y-b)^2+(z+c)^2}-x+a}{\sqrt{(x+a)^2+(y-b)^2+(z+c)^2}-x-a}\right] \\
M_3 &= \int_{-a}^{a} \frac{dx'}{\sqrt{(x-x')^2+(y+b)^2+(z-c)^2}} = \log\left[\frac{\sqrt{(x-a)^2+(y+b)^2+(z-c)^2}-x+a}{\sqrt{(x+a)^2+(y+b)^2+(z-c)^2}-x-a}\right] \\
M_4 &= \int_{-a}^{a} \frac{dx'}{\sqrt{(x-x')^2+(y-b)^2+(z-c)^2}} = \log\left[\frac{\sqrt{(x-a)^2+(y-b)^2+(z-c)^2}-x+a}{\sqrt{(x+a)^2+(y-b)^2+(z-c)^2}-x-a}\right]
\end{aligned}
\tag{A.4}
$$

Appendix B

Design of buffer gas cooling chamber

The design of our buffer gas cooling vacuum chamber is inherited and improved from a similar one in Doyle group at Harvard and DeMille group at Yale. I am very appreciated that John Barry shares the blue print of his design, and David Patterson offers a lot of useful suggestions. All the machining work is reviewed by Andrew Gallant, and done by the team at MIT central machine shop. The original format of this design is in Solidworks 2012 and can be converted to other formats easily, such as AutoCAD. Table B.1 lists all home-built components with their dimensions and materials. The detailed blue prints are not included in this thesis, but can be requested from the author by email.

Table B.1: Buffer gas cooling chamber components list

No.	Name	Materials	Number of pieces	Dimensions (inch)	Notes
1	Source chamber side plate	304 Stainless steel	2	10 × 15 × 0.375	
2	Source chamber side window cover	304 Stainless steel	2	3 × 8 × 0.125	
3	Source chamber front plate	304 Stainless steel	1	10 × 8 × 0.375	
4	Source chamber bottom plate	304 Stainless steel	1	12 × 12 × 0.375	
5	Source chamber back plate	304 Stainless steel	1	10 × 15 × 0.375	
6	Source chamber collar	304 Stainless steel	1	15 × 15 × 4	
7	Source chamber frame	304 Stainless steel	1	12 × 12 × 18	Need welding
8	Probe laser window cover	OFHC Copper	2	0.5 × 0.5 × 0.05	
9	Probe laser extension tube	OFHC Copper	2	0.5 × 0.5 × 1	Need silver soldering
10	Cold cell	OFHC Copper	1	1.5 × 1.5 × 1.5	Need silver soldering
11	Cold cell back window cover	OFHC Copper	1	1.5 × 1.5 × 0.05	
12	Sample cover	OFHC Copper	1	0.85 × 0.85 × 0.05	
13	Cold cell gas inlet	OFHC Copper	1	1.5 × 1.5 × 0.3	Need silver soldering
14	Cold cell output cover	OFHC Copper	1	1.5 × 1.5 × 0.05	
15	Ablation extension tube	OFHC Copper	1	0.85 × 0.85 × 2	Need silver soldering
16	Ablation window cover	OFHC Copper	1	0.85 × 0.85 × 0.05	
17	Radiation shield back window cover	1100 Aluminum	1	1.5 × 1.5 × 0.1	
18	Radiation shield back	1100 Aluminum	1	11 × 7 × 0.25	
19	Radiation shield bottom	1100 Aluminum	1	7.5 × 7.5 × 0.25	
20	Radiation shield collar	1100 Aluminum	1	7 × 7 × 0.25	
21	Radiation shield front	1100 Aluminum	1	11 × 7 × 0.25	
22	Radiation shield side	1100 Aluminum	2	11 × 7 × 0.25	
23	Radiation shield side window cover	1100 Aluminum	2	6 × 1.5 × 0.1	
24	Detection chamber bottom	304 Stainless steel	1	11 × 8.75 × 0.375	
25	Detection chamber cover	304 Stainless steel	1	15 × 8.75 × 0.375	
26	Detection chamber side	304 Stainless steel	2	15 × 6.15 × 0.375	
27	Detection chamber frame	304 Stainless steel	1	8.75 × 6.15 × 16	Need welding
28	Cold cell spacer	304 Stainless steel	1	3.5 × 1.5 × 0.3	
29	Cold copper spacer	OFHC Copper	1	1.5 × 1.5 × 0.5	
30	Cold gas spiral	OFHC Copper	2	R 0.25 × 1.5	
31	Cold plate	OFHC Copper	1	4 × 6 × 0.3	
32	Gas spiral extension	OFHC Copper	1	0.75 × 0.25 × 1.75	
33	Gas spiral spacer	304 Stainless steel	1	0.75 × 0.75 × 0.5	

Bibliography

[1] J. J. Kay, S. L. Coy, V. S. Petrović, B. M. Wong, and R. W. Field, "Separation of long-range and short-range interactions in Rydberg states of diatomic molecules.," *The Journal of Chemical Physics*, vol. 128, pp. 194301 1–20, 2008.

[2] R. W. Field, C. M. Gittins, N. a. Harris, and C. Jungen, "Quantum defect theory of dipole and vibronic mixing in Rydberg states of CaF.," *The Journal of Chemical Physics*, vol. 122, pp. 184314 1–10, May 2005.

[3] S. N. Altunata, S. L. Coy, and R. W. Field, "Properties of nearly one-electron molecules. I. An iterative Green function approach to calculating the reaction matrix.," *The Journal of Chemical Physics*, vol. 123, pp. 084318 1–12, Aug. 2005.

[4] S. N. Altunata, S. L. Coy, and R. W. Field, "Properties of nearly one-electron molecules. II. Application to the Rydberg spectrum of CaF.," *The Journal of Chemical Physics*, vol. 123, pp. 084319 1–12, Aug. 2005.

[5] J. J. Kay, S. L. Coy, B. M. Wong, C. Jungen, and R. W. Field, "A quantum defect model for the s, p, d, and f Rydberg series of CaF," *The Journal of Chemical Physics*, vol. 134, pp. 114313–114321, Mar. 2011.

[6] Cryomech, "http://www.cryomech.com/capacitycurve/PT410_cc.pdf."

[7] T. Gentile, B. Hughey, D. Kleppner, and T. Ducas, "Microwave spectroscopy of calcium Rydberg states," *Physical Review A*, vol. 42, no. 1, pp. 440–451, 1990.

[8] P. R. Berman, "Energy conservation in collective coherent emission by dipole oscillators," *American Journal of Physics*, vol. 78, no. 12, p. 1323, 2010.

[9] M. O. Scully and A. A. Svidzinsky, "Physics. The Lamb shift–yesterday, today, and tomorrow.," *Science*, vol. 328, pp. 1239–41, June 2010.

[10] M. P. Jacobson, S. L. Coy, and R. W. Field, "Extended cross correlation: A technique for spectroscopic pattern recognition," *The Journal of Chemical Physics*, vol. 107, no. 20, p. 8349, 1997.

[11] S. L. Coy, M. P. Jacobson, and R. W. Field, "Identifying patterns in multicomponent signals by extended cross correlation," *The Journal of Chemical Physics*, vol. 107, no. 20, p. 8357, 1997.

[12] J. Rydberg, "XXXIV. On the structure of the line-spectra of the chemical elements," *Philosophical Magazine Series 5*, vol. 29, no. 179, pp. 331–337, 1890.

[13] T. F. Gallagher, *Rydberg Atoms*. Cambridge Monographs on Atomic, Molecular and Chemical Physics, Cambridge University Press, 2005.

[14] S. Hogan, C. Seiler, and F. Merkt, "Rydberg-State-Enabled Deceleration and Trapping of Cold Molecules," *Physical Review Letters*, vol. 103, pp. 123001 1–4, 2009.

[15] S. D. Hogan, C. Seiler, and F. Merkt, "Motional, isotope and quadratic Stark effects in RydbergStark deceleration and electric trapping of H and D," *Journal of Physics B: Atomic, Molecular and Optical Physics*, vol. 46, pp. 045303 1–8, 2013.

[16] S. D. Hogan, P. Allmendinger, H. Saß mannshausen, H. Schmutz, and F. Merkt, "Surface-Electrode Rydberg-Stark Decelerator," *Physical Review Letters*, vol. 108, pp. 1–5, 2012.

[17] E. Vliegen, S. Hogan, H. Schmutz, and F. Merkt, "Stark deceleration and trapping of hydrogen Rydberg atoms," *Physical Review A*, vol. 76, pp. 023405 1–6, Aug. 2007.

[18] C. Seiler, S. D. Hogan, and F. Merkt, "Dynamical processes in Rydberg-Stark deceleration and trapping of atoms and molecules.," *Chimia*, vol. 66, pp. 208–211, 2012.

[19] H. Lefebvre-Brion and R. W. Field, *The spectra and Dynamics of Diatomic Molecules*. Elsevier, 2004.

[20] J. J. Kay, S. Altunata, S. L. Coy, and R. W. Field, "Resonance between electronic and rotational motions in Rydberg states of CaF," *Molecular Physics*, vol. 105, no. 11-12, pp. 1661–1673, 2007.

[21] R. Smith, J. Verlet, E. Boleat, V. Stavros, and H. Fielding, "The dynamics of Rydberg electron wavepackets in NO," *Faraday Discussions*, vol. 115, pp. 63–70, Jan. 2000.

[22] M. Lombardi, P. Labastie, M. C. Bordas, and M. Broyer, "Molecular Rydberg states: Classical chaos and its correspondence in quantum mechanics," *The Journal of Chemical Physics*, vol. 89, no. 6, pp. 3479–3490, 1988.

[23] R. L. Smith, V. G. Stavros, J. R. R. Verlet, H. H. Fielding, D. Townsend, and T. P. Softley, "The role of phase in molecular Rydberg wave packet dynamics," *The Journal of Chemical Physics*, vol. 119, no. 6, pp. 3085–3091, 2003.

[24] P. Labastie, M. C. Bordas, B. Tribollet, and M. Broyer, "Stoboscopic effect between electronic and nuclear motion in highly excited molecular Rydberg states," *Physical Review Letters*, vol. 52, no. May, pp. 1681–1684, 1984.

[25] H. Lefebvre-Brion, "Lifetimes of Rydberg States in Small Molecules: Fluorescence, Predissociation and Autoionization," in *The Role of Rydberg States in Spectroscopy and Photochemistry* (C. Sándorfy, ed.), vol. 20 of *Understanding Chemical Reactivity*, pp. 267–291, Springer Netherlands, 2002.

[26] G. Herzberg and C. Jungen, "High orbital angular momentum states in H2 and D2," *The Journal of Chemical Physics*, vol. 77, no. 12, pp. 5876–5884, 1982.

[27] C. Jungen, I. Dabrowski, G. Herzberg, and D. J. W. Kendall, "High orbital angular momentum states in H2 and D2. II. The 6h5g and 6g5f transitions," *The Journal of Chemical Physics*, vol. 91, no. 7, pp. 3926–3933, 1989.

[28] M. Vervloet, A. L. Roche, and C. Jungen, "Observation of high-l Rydberg states of nitric oxide," *Physical Review A*, vol. 38, pp. 5489–5493, 1988.

[29] W. G. Sturrus, P. E. Sobol, and S. R. Lundeen, "Observation of high-angular-momentum Rydberg states of H_ {2} in a fast beam," *Physical Review Letters*, vol. 54, pp. 792–795, 1985.

[30] E. Eyler, "Autoionization of nonpenetrating Rydberg states in diatomic molecules," *Physical Review A*, vol. 34, no. 4, pp. 2881–2888, 1986.

[31] J. Watson, "Effects of a core electric dipole moment on Rydberg states," *Molecular Physics*, vol. 81, pp. 277–289, Feb. 1994.

[32] M. Child, *Semiclassical Mechanics With Molecular Applications*. International series of monographs on chemical engineering, Oxford University Press, Incorporated, 1991.

[33] J. W. C. Johns and D. W. Lepard, "Calculation of Rotation-Electronic Intensities Energies and Relative Molecules Transition in Diatomic quence the general usefulness of the programs has been greatly increased .," *Journal of Molecular Spectroscopy*, vol. 55, pp. 374–406, 1975.

[34] A. J. Stone, "Distributed polarizabilities," *Molecular Physics*, vol. 56, pp. 1065–1082, Dec. 1985.

[35] A. J. Stone, *The Theory of Intermolecular Forces*. International Series of Monographs on Chemistry, Clarendon Press, 1997.

[36] A. J. STONE and M. ALDERTON, "Distributed multipole analysis Methods and applications," *Molecular Physics*, vol. 100, pp. 221–233, Jan. 2002.

[37] H. Loh, J. Wang, M. Grau, T. S. Yahn, R. W. Field, C. H. Greene, and E. a. Cornell, "Laser-induced fluorescence studies of HfF+ produced by autoionization.," *The Journal of Chemical Physics*, vol. 135, pp. 154308 1–7, Oct. 2011.

[38] H. Loh, R. P. Stutz, T. S. Yahn, H. Looser, R. W. Field, and E. a. Cornell, "REMPI spectroscopy of HfF," *Journal of Molecular Spectroscopy*, vol. 276-277, pp. 49–56, June 2012.

[39] K. C. Cossel, D. N. Gresh, L. C. Sinclair, T. Coffey, L. V. Skripnikov, A. N. Petrov, N. S. Mosyagin, A. V. Titov, R. W. Field, E. R. Meyer, E. a. Cornell, and J. Ye, "Broadband velocity modulation spectroscopy of HfF+: Towards a measurement of the electron electric dipole moment," *Chemical Physics Letters*, vol. 546, pp. 1–11, Sept. 2012.

[40] M. Arif, C. Jungen, and A. L. Roche, "The Rydberg spectrum of CaF and BaF: Calculation by R-matrix and generalized quantum defect theory," *The Journal of Chemical Physics*, vol. 106, no. 10, pp. 4102–4118, 1997.

[41] N. Harris and C. Jungen, "Rydberg states of calcium fluoride.," *Physical review letters*, vol. 70, pp. 2549–2552, Apr. 1993.

[42] C. Fabre, S. Haroche, and P. Goy, "Millimeter spectroscopy in sodium Rydberg states: Quantum-defect, fine-structure, and polarizability measurements," *Phys. Rev. A*, vol. 18, pp. 229–237, July 1978.

[43] L. Moi, C. Fabre, P. Goy, and M. Gross, "Heterodyne detection of Rydberg atom maser emission," *Optics Communications*, vol. 33, no. 1, pp. 47–50, 1980.

[44] P. Goy, J. M. Raimond, G. Vitrant, and S. Haroche, "Millimeter-wave spectroscopy in cesium Rydberg states. Quantum defects, fine- and hyperfine-structure measurements," *Phys. Rev. A*, vol. 26, pp. 2733–2742, Nov. 1982.

[45] F. Merkt and A. Osterwalder, "Millimetre wave spectroscopy of high Rydberg states," *International Reviews in Physical Chemistry*, vol. 21, pp. 385–403, July 2002.

[46] E. Murgu, J. D. D. Martin, and T. F. Gallagher, "Resonant enhancement of pulsed-field ionization zero-kinetic-energy photoelectron spectra using microwave fields," *The Journal of Chemical Physics*, vol. 113, no. 4, pp. 1321–1324, 2000.

[47] E. Murgu, J. D. D. Martin, and T. F. Gallagher, "Stabilization of predissociating nitric oxide Rydberg molecules using microwave and radio-frequency fields," *The Journal of Chemical Physics*, vol. 115, no. 15, pp. 7032–7040, 2001.

[48] F. C. De Lucia, "The submillimeter: A spectroscopists view," *Journal of Molecular Spectroscopy*, vol. 261, pp. 1–17, May 2010.

[49] J. M. Brown and A. Carrington, "Rotational Spectroscopy of Diatomic Molecules," in *Cambridge Molecular Science Series*, Cambridge, UK: Cambridge University Press, 2003.

[50] W. Gordy and R. L. Cook, *Microwave Molecular Spectra*. New York: Wiley, 1984.

[51] J. Demaisen, K. Sarka, and E. A. Cohen, "Spectroscopy From Space," in *NATO Science Series: II. Mathematics, Physics and Chemistry*, Dordrecht, The Netherlands: Kluwer Academic, 2000.

[52] A. P. Colombo, Y. Zhou, K. Prozument, S. L. Coy, and R. W. Field, "Chirped-pulse millimeter-wave spectroscopy: Spectrum, dynamics, and manipulation of RydbergRydberg transitions," *The Journal of Chemical Physics*, vol. 138, no. 1, pp. 014301 1–9, 2013.

[53] K. Prozument, A. Colombo, Y. Zhou, G. Park, V. Petrović, S. Coy, and R. W. Field, "Chirped-Pulse Millimeter-Wave Spectroscopy of Rydberg-Rydberg Transitions," *Physical Review Letters*, vol. 107, pp. 1–4, 2011.

[54] A. Vaidyanathan, W. Spencer, J. Rubbmark, H. Kuiper, C. Fabre, D. Kleppner, and T. Ducas, "Experimental study of nonadiabatic core interactions in Rydberg states of calcium," *Physical Review A*, vol. 26, no. 6, pp. 3346–3350, 1982.

[55] A. Osterwalder and F. Merkt, "Using High Rydberg States as Electric Field Sensors," *Physical Review Letters*, vol. 82, pp. 1831–1834, Mar. 1999.

[56] T. Balle and W. Flygare, "FabryPerot cavity pulsed Fourier transform microwave spectrometer with a pulsed nozzle particle source," *Review of Scientific Instruments*, vol. 52, no. 1, pp. 33–45, 1980.

[57] G. G. Brown, B. C. Dian, K. O. Douglass, S. M. Geyer, S. T. Shipman, and B. H. Pate, "A broadband Fourier transform microwave spectrometer based on chirped pulse excitation.," *The Review of Scientific Instruments*, vol. 79, pp. 053103 1–13, May 2008.

[58] B. C. Dian, G. G. Brown, K. O. Douglass, and B. H. Pate, "Measuring picosecond isomerization kinetics via broadband microwave spectroscopy.," *Science (New York, N.Y.)*, vol. 320, pp. 924–8, May 2008.

[59] G. B. Park, A. H. Steeves, K. Kuyanov-Prozument, J. L. Neill, and R. W. Field, "Design and evaluation of a pulsed-jet chirped-pulse millimeter-wave spectrometer for the 70-102 GHz region.," *The Journal of Chemical Physics*, vol. 135, pp. 024202 1–10, July 2011.

[60] K. Prozument, R. G. Shaver, M. a. Ciuba, J. S. Muenter, G. B. Park, J. F. Stanton, H. Guo, B. M. Wong, D. S. Perry, and R. W. Field, "A new approach toward transition state spectroscopy," *Faraday Discussions*, vol. 163, pp. 33–57, 2013.

[61] M. Morse, "Supersonic Beam Sources," *Experimental Methods in the Physical Sciences*, vol. 29B, pp. 21–47, 1996.

[62] M. A. Duncan, "Invited review article: laser vaporization cluster sources.," *The Review of Scientific Instruments*, vol. 83, pp. 041101 1–19, Apr. 2012.

[63] J. K. Messer and F. C. Delucia, "Measurement Of Pressure-Broadening Parameters for the Co-He System at 4-K," *Physical Review Letters*, vol. 53, no. 27, pp. 2555–2558, 1984.

[64] C. D. Ball, F. C. DeLucia, D. Risal, A. Ruch, H. Sheng, Y. Abebe, P. A. Farina, and A. W. Mantz, "Performance characteristics of a low temperature cell for collisional cooling experiments," *Proceedings of the Society of Photo-Optical Instrumentaion Engineers*, vol. 2834, pp. 102–109, 1996.

[65] D. Patterson, *Buffer Gas Cooled Beams and Cold Molecular Collisions*. PhD thesis, Harvard University, 2010.

[66] S. E. Maxwell, *Buffer gas cooled atoms and molecules: production, collisional studies, and applications*. PhD thesis, 2007.

[67] J. F. Barry, E. S. Shuman, and D. DeMille, "A bright, slow cryogenic molecular beam source for free radicals.," *Physical Chemistry Chemical Physics*, vol. 13, pp. 18936–47, Nov. 2011.

[68] S. E. Maxwell, N. Brahms, R. DeCarvalho, D. R. Glenn, J. S. Helton, S. V. Nguyen, D. Patterson, J. Petricka, D. DeMille, and J. M. Doyle, "High-Flux Beam Source for Cold, Slow Atoms or Molecules," *Physical Review Letters*, vol. 95, pp. 1–4, 2005.

[69] H.-I. Lu, J. Rasmussen, M. J. Wright, D. Patterson, and J. M. Doyle, "A cold and slow molecular beam.," *Physical chemistry chemical physics : PCCP*, vol. 13, pp. 18986–90, Nov. 2011.

[70] N. R. Hutzler, H.-I. Lu, and J. M. Doyle, "The Buffer Gas Beam: An Intense, Cold, and Slow Source for Atoms and Molecules.," *Chemical Reviews*, vol. 112, pp. 4803–4827, May 2012.

[71] N. R. Hutzler, M. F. Parsons, Y. V. Gurevich, P. W. Hess, E. Petrik, B. Spaun, A. C. Vutha, D. Demille, G. Gabrielse, and J. M. Doyle, "A cryogenic beam of refractory, chemically reactive molecules with expansion cooling.," *Physical Chemistry Chemical Physics*, vol. 13, pp. 18976–85, June 2011.

[72] E. S. Shuman, J. F. Barry, and D. Demille, "Laser cooling of a diatomic molecule.," *Nature*, vol. 467, pp. 820–823, Oct. 2010.

[73] E. S. Shuman, J. F. Barry, D. R. Glenn, and D. DeMille, "Radiative Force from Optical Cycling on a Diatomic Molecule," *Physical Review Letters*, vol. 103, pp. 223001 1–4, Nov. 2009.

[74] A. Buchleitner, D. Delande, and J. Zakrzewski, "Non-dispersive wave packets in periodically driven quantum systems," *Physics Reports*, vol. 368, pp. 409–547, 2002.

[75] H. Maeda and T. F. Gallagher, "Nondispersing wave packets," *Physical Review A*, vol. 75, pp. 1–11, Mar. 2007.

[76] H. Maeda, J. Gurian, and T. F. Gallagher, "Nondispersing Bohr Wave Packets," *Physical Review Letters*, vol. 102, pp. 2–5, Mar. 2009.

[77] H. Maeda and T. F. Gallagher, "Nondispersing Wave Packets," *Physical Review Letters*, vol. 92, pp. 2–5, Apr. 2004.

[78] H. Maeda, D. Norum, and T. F. Gallagher, "Microwave manipulation of an atomic electron in a classical orbit," *Science*, vol. 307, no. 5716, pp. 1757–1760, 2005.

[79] B. Wyker, S. Ye, F. Dunning, S. Yoshida, C. Reinhold, and J. Burgdörfer, "Creating and Transporting Trojan Wave Packets," *Physical Review Letters*, vol. 108, pp. 1–5, Jan. 2012.

[80] J. Rost, J. Griffin, B. Friedrich, and D. Herschbach, "Pendular states and spectra of oriented linear molecules," *Physical review letters*, vol. 68, no. 9, pp. 1299–1302, 1992.

[81] B. Friedrich and D. Herschbach, "Alignment and trapping of molecules in intense laser fields," *Physical review letters*, vol. 74, no. 23, pp. 4623–4626, 1995.

[82] B. Friedrich, "Alignment and orientation of rotationally cool molecules," *The Journal of Physical Chemistry*, no. 6, pp. 8118–8129, 1991.

[83] B. Friedrich and D. Herschbach, "Enhanced orientation of polar molecules by combined electrostatic and nonresonant induced dipole forces," *The Journal of Chemical Physics*, vol. 111, no. 14, p. 6157, 1999.

[84] B. Schmidt and B. Friedrich, "Topology of surfaces for molecular Stark energy, alignment, and orientation generated by combined permanent and induced electric dipole interactions.," *The Journal of chemical physics*, vol. 140, p. 064317, Feb. 2014.

[85] A. Salam, "Intermolecular interactions in a radiation field via the method of induced moments," *Phys. Rev. A*, vol. 73, p. 13406, Jan. 2006.

[86] a. H. Safavi-Naeini, T. P. Mayer Alegre, J. Chan, M. Eichenfield, M. Winger, Q. Lin, J. T. Hill, D. E. Chang, and O. Painter, "Electromagnetically induced transparency and slow light with optomechanics.," *Nature*, vol. 472, pp. 69–73, Apr. 2011.

[87] C. Liu, Z. Dutton, C. H. Behroozi, and L. V. Hau, "Observation of coherent optical information storage in an atomic medium using halted light pulses.," *Nature*, vol. 409, pp. 490–493, Jan. 2001.

[88] T. Hong, A. Gorshkov, D. Patterson, A. Zibrov, J. Doyle, M. Lukin, and M. Prentiss, "Realization of coherent optically dense media via buffer-gas cooling," *Physical Review A*, vol. 79, pp. 2–5, Jan. 2009.

[89] V. Sautenkov, van Kampen H, E. Eliel, and J. Woerdman, "Dipole-Dipole Broadened Line Shape in a Partially Excited Dense Atomic Gas.," *Physical review letters*, vol. 77, pp. 3327–3330, Oct. 1996.

[90] H. van Kampen, V. Sautenkov, a. Shalagin, E. Eliel, and J. Woerdman, "Dipole-dipole collision-induced transport of resonance excitation in a high-density atomic vapor," *Physical Review A*, vol. 56, pp. 3569–3575, Nov. 1997.

[91] H. Park, P. J. Tanner, B. J. Claessens, E. S. Shuman, and T. F. Gallagher, "Dipole-dipole broadening of Rb nsnp microwave transitions," *Physical Review A*, vol. 84, p. 022704, Aug. 2011.

[92] H. Park and T. F. Gallagher, "Measurement of the dipole-dipole interaction of Rb nsnp states by microwave Ramsey interferometry," *Physical Review A*, vol. 86, p. 052510, Nov. 2012.

[93] J. Clevenger, *Spectra and dynamics of calcium monochloride*. PhD thesis, MIT, 2002.

[94] G. Scoles, D. Bassi, U. Buck, and D. C. Laine, *Atomic and Molecular Beam Methods: Volume 1*. Oxford University Press, 1988.

[95] M. A. . Duncan, "Infrared spectroscopy to probe structure and dynamics in metal ion-molecule complexes," *International Reviews in Physical Chemistry*, vol. 22, pp. 407–435, Apr. 2003.

[96] M. a. Duncan, "Spectroscopy of metal ion complexes: gas-phase models for solvation.," *Annual review of physical chemistry*, vol. 48, pp. 69–93, Jan. 1997.

[97] W. C. Campbell, T. V. Tscherbul, H.-I. Lu, E. Tsikata, R. V. Krems, and J. M. Doyle, "Mechanism of Collisional Spin Relaxation in $^3\Sigma$ Molecules," *Phys. Rev. Lett.*, vol. 102, p. 13003, Jan. 2009.

[98] C. Effantin, A. Bernard, J. D'Incan, G. Wannous, J. Verges, and R. F. Barrow, "Studies of the electronic states of the BaF molecule," *Molecular Physics*, vol. 70, no. 5, pp. 735–745, 1990.

[99] M. Stafe, A. Marcu, and N. Puscas, *Pulsed Laser Ablation of Solids: Basics, Theory and Applications*. Springer, 2013.

[100] W. Chupka, "Factors affecting lifetimes and resolution of Rydberg states observed in zeroelectronkineticenergy spectroscopy," *The Journal of Chemical Physics*, vol. 98, no. 6, pp. 4520–4530, 1993.

[101] M. Vrakking, "Lifetimes of Rydberg states in ZEKE experiments. III. Calculations of the dc electric field dependence of predissociation lifetimes of NO," *The Journal of Chemical Physics*, vol. 105, no. 17, pp. 7336–7347, 1996.

[102] M. J. J. Vrakking and Y. T. Lee, "Lifetimes of Rydberg states in zero-electron-kinetic-energy experiments. I. Electric field induced and collisional enhancement of NO predissociation lifetimes," *The Journal of Chemical Physics*, vol. 102, pp. 8818–8832, June 1995.

[103] M. J. J. Vrakking and Y. T. Lee, "Lifetimes of Rydberg states in zero-electron-kinetic-energy experiments. II. Electric field induced and collisional enhancement of Xe autoionization lifetimes," *The Journal of Chemical Physics*, vol. 102, pp. 8833–8841, June 1995.

[104] H. Park and R. N. Zare, "Rotationally resolved photoelectron spectra from vibrational autoionization of NO Rydberg levels," *The Journal of Chemical Physics*, vol. 106, no. 6, pp. 2239–2247, 1997.

[105] R. Zhao, I. M. Konen, and R. N. Zare, "Optical-optical double resonance photoionization spectroscopy of nf Rydberg states of nitric oxide.," *The Journal of Chemical Physics*, vol. 121, pp. 9938–47, Nov. 2004.

[106] H. Park, D. Leahy, and R. Zare, "Extensive electron-nuclear angular momentum exchange in vibrational autoionization of np and nf Rydberg states of NO.," *Physical Review Letters*, vol. 76, pp. 1591–1594, Mar. 1996.

[107] A. Staib, W. Domcke, and A. Sobolewski, "MQDT analysis of radiationless decay rates of autoionizing rydberg states of polyatomic molecules," *Chemical Physics Letters*, vol. 162, no. 4, pp. 336–341, 1989.

[108] C. Jungen and S. T. Pratt, "Vibrational autoionization in polyatomic molecules," *The Journal of Chemical Physics*, vol. 106, pp. 9529–9538, 1997.

[109] J. MacGillivray and M. Feld, "Theory of superradiance in an extended, optically thick medium," *Physical Review A*, vol. 14, no. 3, pp. 1169–1189, 1976.

[110] R. Dicke, "Coherence in spontaneous radiation processes," *Physical Review*, vol. 93, no. 1, pp. 99–110, 1954.

[111] R. Bonifacio and L. Lugiato, "Cooperative radiation processes in two-level systems: superfluorescence," *Physical Review A*, vol. 11, no. 5, pp. 1507–1521, 1975.

[112] T. Wang, S. F. Yelin, R. Côté, E. E. Eyler, S. M. Farooqi, P. L. Gould, M. Kostrun, D. Tong, and D. Vrinceanu, "Superradiance in ultracold Rydberg gases," *Physical Review A*, vol. 75, p. 33802, Mar. 2007.

[113] I. I. Rabi, "Space Quantization in a Gyrating Magnetic Field," *Physical Review*, vol. 51, pp. 652 LP – 654, Apr. 1937.

[114] J. McGurk, T. Schmalz, and W. Flygare, "Fast passage in rotational spectroscopy: Theory and experiment," *The Journal of Chemical Physics*, vol. 60, no. May 2009, p. 4181, 1974.

[115] J. Rubbmark, M. Kash, M. Littman, and D. Kleppner, "Dynamical effects at avoided level crossings: A study of the Landau-Zener effect using Rydberg atoms," *Physical Review A*, vol. 23, no. 6, pp. 3107–3117, 1981.

[116] A. Colombo, *Chirped-Pulse Millimeter-Wave Spectroscopy, Dynamics, and Manipulation of RydbergRydberg Transitions*. PhD thesis, MIT, 2013.

[117] N. A. Kurnit, I. D. Abella, and S. R. Hartmann, "Observation of a Photon Echo," *Physical Review Letters*, vol. 13, pp. 567–568, Nov. 1964.

[118] E. L. Hahn, "Spin Echoes," *Physical Review*, vol. 80, pp. 580–594, Nov. 1950.

[119] R. Brewer and A. Genack, "Optical Coherent Transients by Laser Frequency Switching," *Physical Review Letters*, vol. 36, no. 16, pp. 959–962, 1976.

[120] R. Brewer and R. Shoemaker, "Photo echo and optical nutation in molecules," *Physical Review Letters*, vol. 27, no. 10, pp. 631–634, 1971.

[121] R. G. Brewer and E. L. Hahn, "Coherent Raman Beats," *Physical Review A*, vol. 8, pp. 464 LP – 472, July 1973.

[122] G. Banfi and R. Bonifacio, "Superfluorescence and cooperative frequency shift," *Physical Review A*, vol. 12, no. 5, pp. 2068–2082, 1975.

[123] N. Skribanowitz, I. Herman, J. MacGillivray, and M. Feld, "Observation of Dicke Superradiance in Optically Pumped HF Gas," *Physical Review Letters*, vol. 30, pp. 309–312, Feb. 1973.

[124] S. McCall and E. Hahn, "Self-induced transparency by pulsed coherent light," *Physical Review Letters*, vol. 18, no. 21, pp. 908–911, 1967.

[125] S. McCall and E. Hahn, "Self-induced transparency," *Physical Review*, vol. 183, no. 2, pp. 457–485, 1969.

[126] R. Slusher and H. Gibbs, "Self-induced transparency in atomic rubidium," *Physical Review A*, vol. 5, no. 4, pp. 1634–1659, 1972.

[127] A. A. Soares and L. E. E. de Araujo, "AutlerTownes doublet and electromagnetically induced transparency resonance probed by an ultrashort pulse train," *Journal of Physics B: Atomic, Molecular and Optical Physics*, vol. 43, no. 8, p. 85003, 2010.

[128] S. H. Autler and C. H. Townes, "Stark Effect in Rapidly Varying Fields," *Phys. Rev.*, vol. 100, pp. 703–722, Oct. 1955.

[129] N. N. Bogoliubov and D. V. Shirkov, *The Theory of Quantized Fields*. New York: Interscience, 1959.

[130] M. Gross and S. Haroche, "Superradiance: An essay on the theory of collective spontaneous emission," *Physics Reports*, vol. 93, pp. 301–396, Dec. 1982.

[131] F. Bloch, "Nuclear Induction," *Physical Review*, vol. 70, pp. 460 LP – 474, Oct. 1946.

[132] A. Icsevgi and W. Lamb, "Propagation of light pulses in a laser amplifier," *Physical Review*, vol. 185, no. 2, pp. 517–545, 1969.

[133] Y. Zhou, "Cooperative effects in a dense Rydberg gas," *Molecular Physics*, vol. 110, no. 15-16, pp. 1909–1915, 2012.

[134] D. M. Kim, M. O. Scully, and W. E. Lamb, "Quantum Theory of an Optical Maser. V. Atomic Motion and Recoil," *Physical Review A*, vol. 2, pp. 2534 LP – 2541, Dec. 1970.

[135] M. O. Scully, D. M. Kim, and W. E. Lamb, "Quantum Theory of an Optical Maser. IV. Generalization to Include Finite Temperature and Cavity Detuning," *Physical Review A*, vol. 2, pp. 2529 LP – 2533, Dec. 1970.

[136] M. O. Scully and W. E. Lamb, "Quantum Theory of an Optical Maser. II. Spectral Profile," *Physical Review*, vol. 166, pp. 246 LP – 249, Feb. 1968.

[137] M. O. Scully and W. E. Lamb, "Quantum Theory of an Optical Maser. I. General Theory," *Physical Review*, vol. 159, pp. 208 LP – 226, July 1967.

[138] M. O. SCULLY and W. E. LAMB, "Quantum Theory of an Optical Maser. III. Theory of Photoelectron Counting Statistics," *Physical Review*, vol. 179, pp. 368 LP – 374, Mar. 1969.

[139] B. Mollow and M. Miller, "The damped driven two-level atom," *Annals of Physics*, vol. 52, no. 3, pp. 464–478, 1969.

[140] B. R. Mollow, "Power Spectrum of Light Scattered by Two-Level Systems," *Physical Review*, vol. 188, pp. 1969 LP – 1975, Dec. 1969.

[141] M. O. Scully and A. a. Svidzinsky, "Physics. The super of superradiance.," *Science (New York, N.Y.)*, vol. 325, pp. 1510–1, Sept. 2009.

[142] M. Scully, "Collective Lamb Shift in Single Photon Dicke Superradiance," *Physical Review Letters*, vol. 102, pp. 1–4, Apr. 2009.

[143] F. Hopf, R. Shea, and M. Scully, "Theory of Optical Free-Induction Decay and Two-Photon Superradiance," *Physical Review A*, vol. 7, no. 6, pp. 2105–2110, 1973.

[144] A. a. Svidzinsky, J.-T. Chang, and M. O. Scully, "Cooperative spontaneous emission of N atoms: Many-body eigenstates, the effect of virtual Lamb shift processes, and analogy with radiation of N classical oscillators," *Physical Review A*, vol. 81, pp. 1–15, May 2010.

[145] J. B. French and V. F. Weisskopf, "The Electromagnetic Shift of Energy Levels," *Physical Review*, vol. 75, pp. 1240–1248, Apr. 1949.

[146] W. E. Lamb and R. C. Retherford, "Fine Structure of the Hydrogen Atom by a Microwave Method," *Physical Review*, vol. 72, pp. 241 LP – 243, Aug. 1947.

[147] R. Röhlsberger, K. Schlage, B. Sahoo, S. Couet, and R. Rüffer, "Collective Lamb shift in single-photon superradiance.," *Science (New York, N.Y.)*, vol. 328, pp. 1248–51, June 2010.

[148] R. Friedberg, S. Hartmann, and J. Manassah, "Frequency shifts in emission and absorption by resonant systems ot two-level atoms," *Physics Reports*, vol. 7, pp. 101–179, Mar. 1973.

[149] R. Friedberg and J. T. Manassah, "Cooperative Lamb shift in an ellipsoid," *Physical Review A*, vol. 81, pp. 063822 1–7, June 2010.

[150] E. Kuznetsova, R. Rajapakse, and S. F. Yelin, "Enhanced index of refraction in four-wave-mixing media," *Phys. Rev. A*, vol. 88, p. 33850, Sept. 2013.

[151] Z. J. Jakubek, N. a. Harris, R. W. Field, J. a. Gardner, and E. Murad, "Ionization potentials of CaF and BaF," *The Journal of Chemical Physics*, vol. 100, no. 1, pp. 622–627, 1994.

[152] Z. J. Jakubek and R. W. Field, "Rydberg series of BaF: peturbation-facilitated studies of core-nonpenetrating states," *Philosophical Transactions of the Royal Society A: Mathematical, Physical and Engineering Sciences*, vol. 355, pp. 1507–1526, Aug. 1997.

[153] Z. J. Jakubek and R. W. Field, "Core-Penetrating Rydberg Series of BaF: Single-State and Two-State Fits of New Electronic States in the $4.4 \leq n^* \leq 14.3$ Region.," *Journal of Molecular Spectroscopy*, vol. 205, pp. 197–220, Feb. 2001.

[154] Z. J. Jakubek and R. W. Field, "Core-Penetrating Rydberg Series of BaF: s$\sim$p$\sim$d$\sim$f Supercomplexes," *Physical Review*, vol. 72, no. 14, pp. 2167–2170, 1994.

[155] Z. J. Jakubek and R. W. Field, "Core-Penetrating Rydberg Series of BaF : New Electronic States in the $n^*\sim4$ Region," *Journal of Molecular Spectroscopy*, vol. 179, pp. 99–124, 1996.

[156] C. M. Gittins, *Electronic Structure and Electronic-Vibrational Energy Exchange in Rydberg States of Calcium Monofluoride*. PhD thesis, MIT, 1995.

[157] M. P. Jacobson, *Spectroscopic Patterns Encode Unimolecular Dynamics*. PhD thesis, MIT, 1999.

[158] A. F. Ruckstuhl, M. P. Jacobson, R. W. Field, and J. a. Dodd, "Baseline subtraction using robust local regression estimation," *Journal of Quantitative Spectroscopy and Radiative Transfer*, vol. 68, pp. 179–193, Jan. 2001.

[159] D. Dill and C. Jungen, "Quantum-defect functions. Interconverters of electronic and nuclear motion," *The Journal of Physical Chemistry*, vol. 2122, no. 64, pp. 2116–2122, 1980.

[160] C. Hamilton, J. Kinsey, and R. W. Field, "Stimulated emission pumping: new methods in spectroscopy and molecular dynamics," *Annual Review of Physical ...*, vol. 37, pp. 493–524, 1986.

[161] Y. B. Band, "Chirped adiabatic passage with temporally delayed pulses," *Physical Review A*, vol. 50, pp. 584–594, 1994.

[162] K. Bergmann, H. Theuer, and B. Shore, "Coherent population transfer among quantum states of atoms and molecules," *Reviews of Modern Physics*, vol. 70, no. 3, pp. 1003–1025, 1998.

[163] A. Kuhn, G. W. Coulston, G. Z. He, S. Schiemann, K. Bergmann, and W. S. Warren, "Population transfer by stimulated Raman scattering with delayed pulses using spectrally broad light," *The Journal of Chemical Physics*, vol. 96, no. 6, pp. 4215–4223, 1992.

[164] J. R. Kuklinski, U. Gaubatz, F. T. Hioe, and K. Bergmann, "Adiabatic population transfer in a three-level system driven by delayed laser pulses," *Physical Review A*, vol. 40, pp. 6741–6744, 1989.

[165] B. Shore, J. Martin, M. Fewell, and K. Bergmann, "Coherent population transfer in multilevel systems with magnetic sublevels. I. Numerical studies.," *Physical Review A*, vol. 52, pp. 566–582, July 1995.

[166] R. Fox, I. Gatland, R. Roy, and G. Vemuri, "Fast, accurate algorithm for numerical simulation of exponentially correlated colored noise.," Dec. 1988.

[167] V. S. Petrovic, *Toward Pure Electronic Spectroscopy*. PhD thesis, MIT, 2008.

[168] C. Wittig, "The Landau-Zener formula.," *The Journal of Physical Chemistry B*, vol. 109, pp. 8428–30, May 2005.

[169] V. Petrović, J. Kay, S. Coy, and R. Field, "The Stark effect in Rydberg states of a highly polar diatomic molecule: CaF," *The Journal of Chemical Physics*, vol. 131, pp. 064301 1–14, 2009.